National Technical University of Athens
School of Mechanical Engineering
Mechanical Design and Control Systems Division
Dynamics and Acoustics Laboratory (DAL)

Local and Global Active Noise Control Systems in Vehicle Cabins

DOCTORAL DISSERTATION

by
DIMITRIOS E. MYLONAS
M.Eng. Electrical and Computer Engineer

SUPERVISOR:
Dr. IOANNIS A. ANTONIADIS
NTUA Professor

ATHENS, July 2024

Εθνικό Μετσόβιο Πολυτεχνείο
Σχολή Μηχανολόγων Μηχανικών
Τομέας Μηχανολογογικών Κατασκευών
και Αυτομάτου Ελέγχου
Εργαστήριο Δυναμικής και Ακουστικής (ΕΔΑ)

Συστήματα Τοπικού και Ολικού Ενεργητικού Ελέγχου Θορύβου σε Οχήματα

ΔΙΔΑΚΤΟΡΙΚΗ ΔΙΑΤΡΙΒΗ

ΔΗΜΗΤΡΙΟΥ Ε. ΜΥΛΩΝΑ
Διπλωματούχου Ηλεκτρολόγου Μηχανικού και Μηχανικού Ηλεκτρονικών Υπολογιστών Ε.Μ.Π.

ΕΠΙΒΛΕΠΩΝ:
Δρ. ΙΩΑΝΝΗΣ Α. ΑΝΤΩΝΙΑΔΗΣ
Καθηγητής ΕΜΠ

ΑΘΗΝΑ, Ιούλιος 2024

National Technical University of Athens
School of Mechanical Engineering
Mechanical Design and Control Systems Division
Dynamics and Acoustics Laboratory (DAL)

Local and Global Active Noise Control Systems in Vehicle Cabins

DOCTORAL DISSERTATION

DIMITRIOS E. MYLONAS
M.Eng. Automation Systems,
Diploma in Electrical and Computer Engineering N.T.U.A

ADVISORY COMMITTEE:

- Dr. Ioannis A. Antoniadis, Professor, NTUA
- Dr. Christophoros Provatidis, Professor, NTUA
- Dr. Dimitrios Koulocheris, Associate Professor, NTUA

EXAMINATION COMMITTEE:

- Dr. Ioannis A. Antoniadis, Professor, NTUA
- Dr. Christophoros Provatidis, Professor, NTUA
- Dr. Dimitrios Koulocheris, Professor, NTUA
- Dr. Konstantinos Kyriakopoulos, Professor, NTUA
- Dr. Vasilios Spitas, Professor, NTUA
- Dr. Dimitrios Saravanos, Professor, University of Patras
- Dr. Nikolaos Chrysochoidis, Assistant Professor, University of Patras

ATHENS, July 2024

Ἡ έγκριση της διδακτορικής διατριβής από την Ανώτατη Σχολή Μηχανολόγων Μηχανικών του Ε.Μ. Πολυτεχνείου δεν υποδηλώνει αποδοχή των γνωμών του συγγραφέα (Ν. 5343/1932. Άρθρο 202)¨.

Acknowledgements

First of all, I would like to express my deepest gratitude to my supervisor, Professor Ioannis Antoniadis, for his invaluable guidance, support, and encouragement throughout my PhD journey. His expertise and dedication have been instrumental in shaping this dissertation, and his mentorship has greatly enriched my academic and professional development. I am also profoundly grateful to my Doctoral Advisory Committee members, Professors Christoforos Provatidis and Dimitrios Koulocheris. Their insightful feedback, constructive criticism, and unwavering support have been crucial in refining my research and enhancing the quality of this work.

A special thank you goes to Dr. Christos Yiakopoulos, for trusting me and sharing his scientific expertise. His collaboration and insights have significantly contributed to the advancement of my research. I would also like to acknowledge my colleagues Alberto Erspamer, for his great contribution to the scientific papers included in this dissertation, Moris Kalderon, for his valuable advice and feedback, and Kostas Fouskas, for his support in everyday life in the office and his encouragement during challenging periods for the completion of this dissertation.

My sincere thanks to the Doctoral Examination Committee, consisting of Professors Konstantinos Kyriakopoulos, Vasilios Spitas, Dimitrios Saravanos, and Nikolaos Chrysochoidis, for their time, effort, and valuable input during the evaluation of my dissertation.

Additionally, I would like to extend my heartfelt thanks to my family and friends for their constant encouragement and understanding throughout this demanding process. Their patience and support have been a source of strength for me.Finally, I acknowledge the support of my institution and the funding bodies that have contributed to my research.

Thank you all for your invaluable contributions!

Abstract

Excessive noise in vehicle cabins, particularly from the propulsion systems and their interaction with the environment (e.g., wind, road, waves), significantly diminishes the acoustic comfort of passengers. At low frequencies, where acoustic energy is typically concentrated in these disturbances, the feasibility of using conventional passive sound insulation techniques is limited due to the increased weight and thickness of these structures as the wavelength of the acoustic disturbances increases. The primary objective of this doctoral thesis is to devise and evaluate innovative systems for global and local active noise control in the cabins of small aircraft and yachts. The proposed methods focus on enhancing the performance of existing techniques, while also exploring the potential for integration into real-world applications.

Initially, the focus is on developing a local active noise control system, known as the active headrest, which is installed at the front headrest of the passenger seat. The purpose of this system is to create a quiet zone around the ears, where a substantial reduction in sound pressure level is achieved, and the zone must be large enough to allow for gentle head movements while maintaining the reduced noise level. The development of this system involved an initial evaluation of a low-complexity linear adaptive control algorithm, with the aim of facilitating its implementation in digital signal processing systems and enabling the operation of multiple such systems, without requiring powerful processors. The mixed error FxLMS algorithm, an alternative to the multichannel FxLMS algorithm, was found to be an effective solution for local noise control systems, as it reduced computational complexity without significantly impacting performance.

In the second phase of the system's development, a method for estimating acoustic pressure in the passenger's ears was incorporated, using microphones positioned a few centimeters away. This method, based on linear extrapolation, allowed for the relocation of the quiet zone to the desired location without the need for physical microphones, which are often constrained by spatial limitations. Finally, to achieve greater sound level reduction, a nonlinear algorithm was employed, based on a simple single-level functional link neural network. This algorithm combined mixed error and linear extrapolation techniques, offering the benefits previously mentioned. The system demonstrated improved

performance, particularly for real-world acoustic disturbances recorded in vehicle cabins.

In the last part of this thesis, an investigation was conducted into the sound field of the entire cabin when multiple local control systems were operational simultaneously. The findings revealed that although quiet zones persisted in front of the headrest, the sound levels in the sub-regions of the cabin remained high. To address this issue, a global active noise control system was devised, which utilized active sound absorbers. The examination of this system demonstrated that by strategically positioning the absorbers, a reduction of over 10 dB in sound pressure levels could be attained in all areas of a small cabin.

Keywords: Local Active Noise Control, Global Active Noise Control, Aircraft Cabin Noise, Noise Cancellation, Active Sound Absorber, Filtered-x Least Mean Squares, Functional Link Neural Network, Quiet Zones, Active Headrest.

Σύνοψη

Ο θόρυβος στις καμπίνες των μέσων μεταφοράς, που προέρχεται κυρίως από τα συστήματα πρόωσης καθώς και την αλληλεπίδραση τους με το περιβάλλον (π.χ. άνεμος, δρόμος, κύματα), αποτελεί έναν σημαντικό παράγοντα που υποβαθμίζει την ακουστική άνεση των επιβατών. Ειδικά στις χαμηλές συχνότητες, όπου συνήθως είναι συγκεντρωμένη η ακουστική ενέργεια στις εν λόγω διαταραχές, η δυνατότητα χρήσης συμβατικών παθητικών τεχνικών ηχομόνωσης είναι μειωμένη, μιας και το βάρος και το πάχος αυτών των παθητικών δομών αυξάνεται με την αύξηση του μήκους κύματος των ακουστικών διαταραχών. Σκοπός της παρούσας διδακτορικής διατριβής είναι η ανάπτυξη και η αξιολόγηση καινοτόμων συστημάτων ολικού και τοπικού ενεργητικού ελέγχου θορύβου σε καμπίνες μικρών αεροσκαφών και σκαφών αναψυχής.

Οι προτεινόμενες μέθοδοι, εστιάζουν αφενός στη βελτίωση της απόδοσης των υπαρχόντων τεχνικών και αφετέρου στη δυνατότητα ενσωμάτωσης σε πραγματικές εφαρμογές. Έτσι, αρχικά δίνεται έμφαση στην ανάπτυξη ενός συστήματος τοπικού ελέγχου θορύβου, το οποίο εγκαθίσταται στο προσκέφαλο της θέσης του επιβάτη (ενεργό προσκέφαλο). Σκοπός του συστήματος αυτού είναι η δημιουργία μιας περιοχή γύρω από τα αυτιά, όπου επιτυγχάνεται σημαντική μείωση της ηχοστάθμης. Επιπλέον, η περιοχή αυτή, η οποία ονομάζεται ζώνη ησυχίας πρέπει να είναι αρκετά μεγάλη, ώστε να επιτρέπει ήπιες κινήσεις του κεφαλιού του επιβάτη, διατηρώντας τη μειωμένη στάθμη θορύβου.

Το πρώτο στάδιο της ανάπτυξης του συστήματος αυτού περιελάμβανε την αξιολόγηση ενός γραμμικού προσαρμοστικού αλγορίθμου ελέγχου με χαμηλή υπολογιστική πολυπλοκότητα, ώστε να είναι πιο εύκολη η υλοποίηση σε ενσωματωμένα ψηφιακά συστήματα καθώς και η παράλληλη λειτουργία πολλών τέτοιων συστημάτων χωρίς να υπάρχει ανάγκη για ισχυρούς επεξεργαστές ψηφιακού σήματος που θα ανέβαζαν το κόστος της εφαρμογής. Πράγματι, ο αλγόριθμος αυτός που ονομάζεται FxLMS μικτού σφάλματος και αποτελεί εναλλακτική του πολυκαναλικού αλγορίθμου FxLMS, φάνηκε ότι αποτελεί έναν αλγόριθμο που μπορεί να χρησιμοποιηθεί στην υλοποίηση τοπικών συστημάτων ελέγχου θορύβου μειώνοντας την υπολογιστική πολυπλοκότητα, χωρίς να επηρεάζεται ιδιαίτερα η απόδοση.

Έπειτα, στο δεύτερο στάδιο ανάπτυξης του συστήματος τοπικού ελέγχου θορύβου, ενσωματώθηκε μια μέθοδος εκτίμησης της ακουστικής πίεσης στα αυτιά του επιβάτη, με τη χρήση

μικροφώνων που βρίσκονται σε απόσταση μερικών εκατοστών από αυτά. Η μέθοδος αυτή που βασίζεται στη γραμμική παρέκταση, δίνει τη δυνατότητα μεταφοράς της ζώνης ησυχίας στο σημείο ενδιαφέροντος, χωρίς την τοποθέτηση φυσικών μικροφώνων, το οποίο συνήθως αντιμετωπίζει χωροταξικούς περιορισμούς. Τέλος, για να επιτευχθεί μεγαλύτερη μείωση της ηχοστάθμης χρησιμοποιήθηκε ένας μη γραμμικός αλγόριθμος βασισμένος σε ένα απλό νευρωνικό δίκτυο ενός επιπέδου (FLNN). Στον αλγόριθμο αυτό ενσωματώθηκαν οι τεχνικές του μικτού σφάλματος και της γραμμικής παρέκτασης προσφέροντας τα πλεονεκτήματα που αναφέρθηκαν παραπάνω. Έτσι, παρατηρήθηκε καλύτερη απόδοση ιδιαίτερα για πραγματικές ακουστικές διαταραχές που ηχογραφήθηκαν σε καμπίνες μέσων μεταφοράς.

Στο τελευταίο κομμάτι της παρούσας διδακτορικής διατριβής, μελετήθηκε το ακουστικό πεδίο ολόκληρης της καμπίνας, όταν λειτουργούν ταυτόχρονα πολλά συστήματα τοπικού ελέγχου θορύβου, διαπιστώνοντας ότι ενώ οι ζώνες ησυχίας εξακολουθούν να υπάρχουν μπροστά στο προσκέφαλο, η ηχοστάθμη παραμένει υψηλή στις υπόλοιπες περιοχές της καμπίνας. Έτσι δημιουργήθηκε η ανάγκη ανάπτυξης ενός συστήματος συνολικού ελέγχου του ηχητικού πεδίου, που βασίζεται σε ενεργούς απορροφητές ήχου. Η μελέτη του συστήματος αυτού έδειξε ότι με κατάλληλη τοποθέτηση των απορροφητών, μπορεί να επιτευχθεί μείωση της ηχοστάθμης μεγαλύτερης των 10 dB σε όλες της περιοχές μιας μικρής καμπίνας.

Λέξεις κλειδιά: Τοπικός Ενεργητικός Έλεγχος Θορύβου, Ολικός Ενεργητικός Έλεγχος Θορύβου, Θόρυβος Καμπίνας Αεροσκάφους, Ακύρωση Θορύβου, Ενεργητικός Απορροφητής Ήχου, Filtered-x Least Mean Squares, Functional Link Neural Network, Ζώνες Ησυχίας, Ενεργό Προσκέφαλο.

Contents

List of Figures

List of Tables

Abbreviations

This section provides a list of abbreviations used throughout the thesis. It serves as a reference for the reader to understand the shorthand terms and acronyms used in the document.

Abbreviation	**Full Form**
ANC	Active Noise Control
NC	Noise Cancellation
ASA	Active Sound Absorption
LMS	Least Mean Squares
FxLMS	Filtered x Least Mean Squares
VEM-FxLMS	Virtual Error Mixed FxLMS
FLNN	Functional Link Neural Network
SPL	Sound Pressure Level
QZ	Quite Zone
BPF	Blade Passage Frequency
VMT	Virtual Microphone Technique
RMT	Remote Microphone Technique
VMC	Virtual Microphone Control
DSP	Digital Signal Processor
PML	Perfectly Matched Layer
Eq./Eqs.	Equation/Equations

CHAPTER 1

Introduction

1.1 Context and Motivation

Active Noise Control (ANC) is a group of techniques used to mitigate acoustic pressure and unlike passive conventional methods, they do not use physical barriers for this purpose. Instead, they rely on the generation of acoustic waves that result in the cancellation or absorption of unwanted disturbances. Thus, we can divide ANC methods into those based on noise cancellation (NC) and those based on sound absorption. The concept of active NC was first patented by Paul Lueg [1] early in 1933. It is based on the idea that a sound wave can be cancelled by producing an antinoise wave of same amplitude and opposite phase, resulting to wave destructive interference. However, technological limitations did not allow its widespread application [2], until Olson and May proposed the concept of Active Sound absorber [3] based on Lueg's idea. The breakthrough in this field came from Widrow with the introduction of the LMS [4] and FxLMS [5] algorithms in 1975 and 1981 respectively, which even today are still a benchmark for Active NC systems.

Nowadays, many NC systems are incorporated into commercially available headphones and earbuds. In the future it seems that such systems will be integrated into a variety of devices such as noise cancelling headrests [6], [7], active windows [8] and active noise barriers [9]. On the other hand, Active Sound Absorption (ASA) techniques [10]–[13] are designed to change the acoustic impedance of a boundary in order to achieve sound absorption, which can result in the reduction of acoustic pressure in an enclosure. A variety of methods have been proposed to modify the acoustic impedance, including altering the electric load of the loudspeaker or changing the absorption coefficient by computing and minimizing the reflected component of a sound wave in front of a loudspeaker that

acts as a sound absorber. Finally, there is a category of methods known as Active Vibration Control (AVC) [14], [15], which aim to decrease acoustic pressure by diminishing structure-borne sound. Although these techniques are noteworthy, they will not be the focus of this dissertation.

An application of ANC which is gaining increasing interest in both academia and industry is the use of such systems to reduce acoustic pressure in vehicle cabins.The issue of excessive noise levels within these enclosures has emerged as a significant problem that diminishes passenger comfort. The main sources of acoustic disturbances are the vehicle engines as well as the air or waves in the case of boats. Traditional strategies to mitigate this issue involve the utilization of passive insulation and sound-absorbing structures, such as fibrous materials, foams, and puffed materials [16]. However, a crucial drawback of these passive methods is their limited effectiveness in attenuating low-frequency sounds that are often present in cabin acoustic disturbances.

In order to enhance their efficiency, the deployment of structures with substantial thickness and weight is necessary. In particular, the $\lambda/4$ rule applies to the thickness of passive noise barriers, which stipulates that the thickness must be at least one-quarter of the wavelength of the lowest harmonic component of the acoustic disturbance in order to achieve absorption. This approach, however, conflicts with the general objective of manufacturers to minimize the weight and the cost of vehicles. Reducing the weight of the fuselage is a critical factor in the aircraft industry, as it is directly linked to a reduction in fuel consumption and CO_2 emissions [17]. As a result, active noise control methods are increasingly being considered for controlling noise within vehicle cabins.

Since many scientific researches have focused on ANC systems in cars [18], [19], the emphasis of this dissertation is laid on aircraft and yacht cabins, which have not been extensively studied. In particular, the study examines ANC in tilt rotors [20], [21] and conventional propeller-driven aircraft, as well as in yacht cabins. The primary target of the ANC system is the harmonic acoustic disturbances and noise generated by various sources, particularly in low frequencies, which are dominated by the Blade Passage Frequency of the propeller or rotor and its harmonics [17], [22]. In the case of yacht cabins, the emphasis was on the acoustic disturbances produced by electric generators [23], [24], which can be a significant source of discomfort for passengers during the night.

In addition to broadband harmonic sound components, this study also examines the chaotic components of acoustic disturbances, which pose challenges for their mitigation with active methods. However, since these chaotic characteristics contribute less as we move lower in the frequency spectrum, they do not significantly impact the performance of the ANC system [22]. A small attenuation of these chaotic components can still provide an advantage to the ANC method that achieves it. Beyond the reduction in acoustic pressure achieved by an ANC system, the size of the area where this reduction is achieved is also important. Therefore, this dissertation focuses on methods that can extend the size

of the quiet zones, whether local or global, throughout an enclosure. Finally, practicality issues such as computational complexity and suitability for installation in small cabins are also considered in the study of these systems.

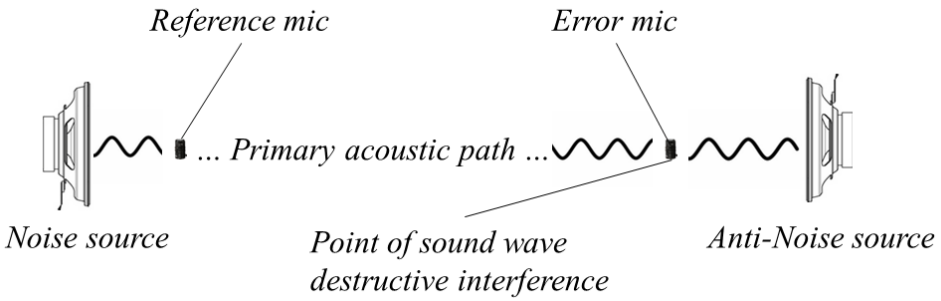

Figure 1.1: Working principle of a single-input single-output feedforward Active NC system

Year	Authors	Contribution	Reference
1936	Lueg	First patent in ANC	[1]
1953	Olson & May	ANC headrest	[3]
1955	Simshauser & Hawley	ANC headphones	[25]
1981	Widrow & Shur & Shaffer	FxLMS algorithm	[5]
1987	Elliot & Stothers & Nelson	Multiple Error FxLMS	[26]
1989	Dorling & Eatwell & Hutchins et al.	Aircraft cabin ANC	[27]
1992	Orduña-Bustamante & Nelson	FxLMS for Active Absorption	[28]
2004	Das & Panda	FsLMS algorithm	[29]
2005	Zhou & Zhang & Li & Gan	Back Propagation ANC	[30]
2018	Elliot & Jung & Cheer	Head-tracking active headrest	[31]

Table 1.1: Timeline of ANC

1.2 State-of-the-art

The concept of the active headrest refers to a device that uses speakers, microphones and a Digital Signal Processor (DSP) to create QZs around a vehicle occupant's ears, where a reduction in acoustic pressure is achieved [6], [32]–[34]. An NC algorithm is implemented in the DSP, with FxLMS being the benchmark for all other algorithms. Although numerous studies on active headrests utilize feedforward FxLMS, significant progress is being made to propose more efficient control algorithms that can better reduce acoustic pressure and computational complexity, making these systems more suitable

for practical applications. As a result, various algorithms, such as the Kalman filter [32], Recursive least squares (RLS) [35], [36], and feedback [37] and hybrid versions of FxLMS [38], have been proposed, but have not yet achieved significant improvements in both acoustic pressure reduction and computing speed. Non-linear algorithms, on the other hand, have shown more promising results in terms of noise reduction [39]. These algorithms, which are primarily based on Volterra series [40], [41] and Functional Link Neural Networks with sinusoidal expansion [29], [42], effectively model the non-linearities present in individual electroacoustic systems and can more accurately predict the sound disturbance reaching the passenger's ear. This enables the reproduction of antinoise signals that achieve better cancellation. Furthermore, an extension of the Volterra-based algorithm, known as Bilinear FxLMS [43], [44], has been proposed, which incorporates a feedback path from the controller output. Finally, a convex combination approach [45], which combines filters derived from both linear and non-linear algorithms, has been tested to optimize the performance of FxLMS in certain scenarios.

The techniques detailed herein follow an adaptive approach to ANC, where the weights of the generated filters are updated in real time in response to changes in acoustic disturbances. In recent years, a shift towards ANC systems based on pretrained neural network models [46] has been observed due to advancements in machine learning-based techniques [47], [48]. Although these systems, which are non-adaptive, exhibit superior performance compared to previously mentioned systems, their non-adaptive behaviour and high computational complexity have limited their widespread application in both research and commercial settings.

Despite these challenges, the constant advances in technology, including the increasing computing power of DSPs and the evolution of machine learning algorithms, have made it possible to implement practical systems that can be utilized in real-world applications. As a result, systems based primarily on Recurrent [49] and Convolutional Neural Networks [50] have been proposed, which demonstrate a substantial improvement in performance compared to conventional FxLMS systems. To address the limitation of non adaptive behaviour in machine learning-based systems, another interesting idea is to develop a pool of models that have been trained with various datasets of acoustic disturbances. By employing a pattern matching algorithm, an appropriate model can be selected to facilitate active noise control. This technique, known as Selective ANC [34], [51], can pave the way for incorporating neural network algorithms into active noise control systems, achieving good performance for various acoustic disturbances.

Apart from the control algorithm, the design of an ANC system for an active headrest depends on several factors, including the size and location of the quiet zone to be created. The parameters that affect the size of the quiet zone are the number of loudspeakers and microphones that make up the ANC system, the diameter of the loudspeaker diaphragm, and the distance of the microphone position from the diaphragm [52]. It is important to

note that a conventional noise-cancelling system with one loudspeaker and one microphone can only cancel the acoustic disturbance at points and cannot create an extended zone of acoustic disturbance mitigation [53]. Therefore, such a system is suitable only for headphone applications and not for applications that require the creation of a quiet zone. In contrast, an ANC system for active headrest typically relies on two speakers and two microphones, and an algorithm that combines the signals from the microphones to produce the signals that drive the speakers. Additionally, several studies have found that the larger the diameter of the speakers used in an active headrest, the larger the quiet zone produced. Therefore, the design of an ANC system involves selecting secondary sources (loudspeakers) of appropriate diameter to increase the active area of the source without excessively increasing the added weight. Thus, some researchers have suggested the use of lightweight transducers for this purpose [54], [55]. Finally, the position of the microphones in relation to the diaphragm of the loudspeakers may increase the quiet zone radius, if the microphones are placed away from the diaphragm, but without obstructing the movement of the head. Thus, it is sometimes selected to place the microphones at the edges of the loudspeakers or to place the loudspeakers in a cavity of a wall, where the ANC is placed.

Regarding the location of the quiet zone, it normally extends like a sphere centred on the cancelling microphone, which is often inconvenient for an active headrest since the locations where the reduction of acoustic pressure is needed are usually far away from the microphones. Thus, various techniques referred to as Virtual Sensing Techniques have been developed, which move the silent zone to positions far from the microphones [56]. These methods may involve the extrapolation of acoustic pressure or the modeling of acoustic paths, allowing the prediction of acoustic pressure at locations without a microphone. Two such algorithms are the Virtual Microphone Technique (VMT) [57], [58] and Remote Microphone Technique (RMT) [59], [60], which have demonstrated the ability to transfer the quiet zone to the desired location. The primary disadvantages of the last two algorithms are their instability, especially when there is movement of the human head, and their impracticality due to the need for a modeling phase of the acoustic paths before implementation. Another challenge that Virtual Sensing techniques face relates to relocating the area where the cancellation of acoustic interference is required, as the ears of a user of an active headrest move. A potential solution to this issue has been suggested through the use of head-tracking systems [31], [32], which monitor the head position and choose an appropriate acoustic system model from a pre-trained filter bank. However, the substantial increase in computational complexity is a major limitation of this approach.

The reduction of computational requirements is another important aspect in applications where several parallel systems have to be implemented, such as in the cabin of an aircraft since the implementation of complex algorithms leads to the use of more powerful digital signal processors which in turn increases both the cost and power consumption of

a large application. Thus, many papers propose either alternative algorithms, which are usually variants of FxLMS, which are more computationally efficient [61]–[63] or different implementations utilizing DSP platforms like FPGAs [64], [65]. Also other papers suggest reducing the number of actuators and sensors involved in the system without particularly affecting its performance [66]. Finally, the global approach of ANC, where the quiet zones are not limited around the headrests of the seats of an aircraft cabin or yacht, but instead extend throughout the enclosure, is possible to contribute to the reduction of transducers and consequently to the reduction of the system complexity [12].

Implementing global Active Noise Control (ANC) in an enclosure involves two primary methods. The first method entails placing speakers and microphones in strategic positions throughout the enclosure to achieve global attenuation of acoustic pressure [52], [67]. A multichannel algorithm is then applied to minimize the sound energy in areas of interest, where microphones are typically placed. This approach typically results in a global effect throughout the cabin, provided that the speakers are placed in locations that do not excite annoying acoustic modes [68], and the microphones are not placed at antinodes of acoustic modes that are intended to be cancelled. Therefore, the placement of transducers must be carefully considered in such systems. Such approaches have primarily been used in small aircraft cabins.

On the other hand, an alternative approach is based on the placement of sound absorbers [69] at points that dampen the acoustic modes of an enclosure [70]. These absorbers can be shunt loudspeakers, active electroacoustic absorbers [71], or adaptive sound absorbers that adjust the acoustic impedance of a barrier to minimize reflection [28]. All three types of absorbers can be a promising solution for attenuating low frequency acoustic disturbance components in aircraft and ship cabins.

1.3 Background Concepts

In the subsequent sections, the fundamental principles of ANC systems will be introduced, serving as the basis for the implementation of the systems outlined in the remainder of this thesis.

1.3.1 Feedforward ANC

The primary objective of a NC system is to model an unknown plant, which lies between the noise source and the point of cancellation, in order to predict the acoustic disturbance and to produce the anti-noise signal. This process is typically performed by an adaptive filter W(z). A distinguishing feature of a feedforward system is the presence of a reference sensor situated in close proximity to the noise source, which captures the reference signal. The reference signal is subsequently utilized in the calculation of the coefficients of W(z).

The process of computing the filter coefficients involves the minimization of a cost function, commonly the mean squared error (MSE), resulting from the superposition of the acoustic disturbance and the antinoise sound wave generated by the ANC system at the point of cancellation. The error signal is obtained by a microphone placed at that point, and through an adaptive algorithm, the cost function is minimized, and the taps of W(z) are calculated. The most prevalent adaptive algorithm for feedforward ANC systems is FxLMS (Figure 1.2a), because of its good performance and robustness. It derives from Least Mean Squares (LMS) algorithm, except that the reference signal is filtered by a secondary path model before the calculation of adaptive filter coefficient [53].

$$y(n) = \mathbf{w}(n) * \mathbf{x}(n) \tag{1.1}$$

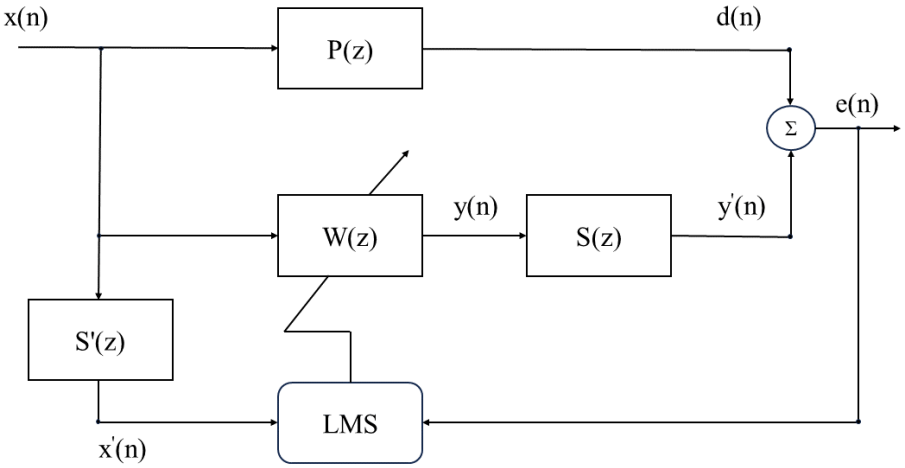

(a)

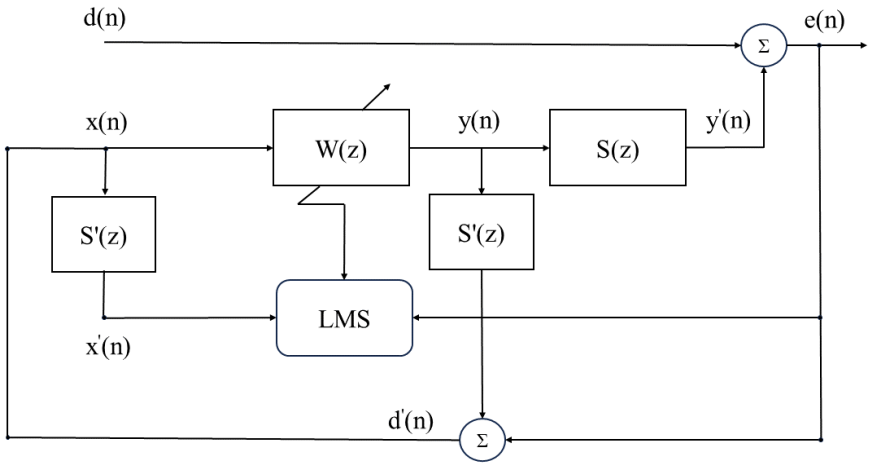

(b)

Figure 1.2: Block diagrams of single-input single-output (a) feedforward and (b) a feedback ANC systems performing NC. The control algorithm in both systems is FxLMS.

At this point we must mention that the secondary path, denoted by $S(z)$, comprises a collection of electroacoustic systems that are located between the error microphone and the controller, which is responsible for generating the anti-noise signal. It usually includes the acoustic paths between the anti-noise source and the error microphone, as well as the noise source and the reference microphone the Analog to Digital and Digital to Analog converters and the cables. Thus, the optimal adaptive filter can be described by the transfer function of Eq. 1.2 as it is can be derived from Figure 1.2a.

$$W^o(z) = \frac{P(z)}{S(z)} \tag{1.2}$$

where P(z) is the transfer function of the primary path while S(z) is the transfer function of the secondary path. Finally, the adaptive FIR filter coefficients that derive from FxLMS are given by Eq. 1.3 and the antinoise signal by Eq. 1.4.

$$\mathbf{w}(n+1) = \mathbf{w}(n) - \mu \mathbf{x}^{'}(n)e(n) \tag{1.3}$$

and

$$\mathbf{x}^{'}(n) = \mathbf{x}(n) * s^{'}(n) \tag{1.4}$$

where $\mathbf{w}$ is a vector that contains the coefficients of the FIR adaptive filter, μ is the step size, which determines the speed of cost function minimization process, and $\mathbf{x}^{'}(n)$ is a vector that contains the latest values of reference signal filtered by a model of secondary path impulse response $s^{'}(n)$ as described by Eq. 1.4. Typically, the symbol $*$ denotes the convolution operation, while the bold font is used to represent a vector. Furthermore, the model of the secondary path, is usually obtained during a preliminary identification stage, when LMS is used for system identification task. Finally as long as $\mathbf{w}(n)$ is computed the antinoise signal derives from Eq. 1.1.

1.3.2 Feedback ANC

The basic difference between feedforward and feedback ANC systems lies in the absence of reference sensor. Thus, in the case of feedback ANC, the reference signal is an estimation of the acoustic disturbance $d(n)$, which is obtained by subtracting the antinoise signal filtered by the secondary path model from the error signal (Eq. 1.5).

$$x(n) = d(n) = e(n) - y(n) * s^{'}(n) \tag{1.5}$$

The primary benefit of the technique illustrated in Figure 1.2b is that it relies on internal model control (IMC) [72], [73] and does not necessitate a reference sensor in close proximity to the noise source, which is not always feasible in various applications. In addition, a

common challenge with feedforward systems is the low correlation between the reference signal and the error signal, which can negatively impact their performance. However, this issue is resolved in feedback systems, often resulting in enhanced performance.

On the other hand, a drawback of these systems has to do with their robustness, since due to feedback, instability problems are more often generated. Thus, special attention should be paid to ensure the stability of such systems. Also, another issue of IMC based ANC is the increase in computational complexity due to the convolution of the anti-noise signal $y(n)$ with the secondary path model. Therefore, the development of advanced methods to reduce computational demands has been proposed. Finally, another category of ANC systems, referred to as hybrid, integrates feedback and feedforward systems to augment the magnitude and frequency range of acoustic pressure attenuation. In conclusion, the decision to employ a specific type of ANC is impacted by several considerations, including the computational requirements, the feasibility of deploying a reference sensor with a strong correlation to the noise source, and the desired level of acoustic pressure attenuation.

1.3.3 Broadband and Narrowband ANC

The term broadband refers to ANC systems that are designed to control acoustic disturbances with a broad frequency range. These systems, depicted in Figure 1.2, are capable of canceling out broadband signals, which can either be captured by the reference microphone or synthesized using the IMC in the feedback configuration. The specific frequency range that these systems are effective in attenuating depends on both the control algorithm and parameters such as the number of coefficients in the adaptive filter. It has been observed that filters with a greater number of coefficients tend to be more effective in mitigating broadband disturbances. Additionally, algorithms based on neural networks have shown promising results in addressing broadband noise.

On the other hand, narrowband systems [74]–[76] are designed to target single frequency disturbances. These systems typically employ adaptive notch filters and an algorithm that identifies the dominant frequencies present in an acoustic disturbance, which are then used as a reference for the notch filter. By combining these filters in parallel, multiple frequencies can be attenuated, although it is important to note that these systems are not able to reduce non-harmonic elements. A similar system was implemented in the Dynamics and Acoustics Laboratory during this PhD thesis, which uses 4 speakers and 3 error microphones to attenuate the Blade Passage Frequency (BPF) of a small aircraft (Figure 1.3). Each speaker is driven by an adaptive notch filter and the BPF is detected by the ESPRIT frequency estimation method [77]. Although this system was effective for single frequency attenuation, it did not perform well for multi-frequency attenuation due to the increase in complexity resulting from the many parallel filters and therefore

broadband algorithms were eventually adopted.

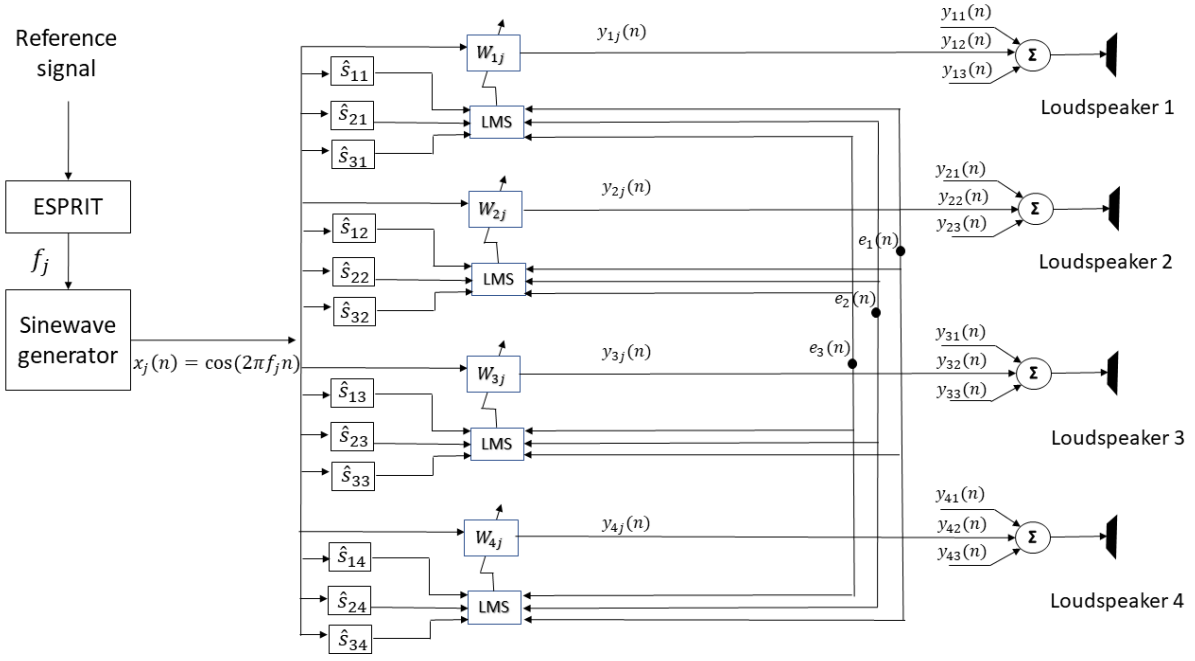

Figure 1.3: Multichannel narrowband ANC system used for attenuating single frequency acoustic disturbances. It consists of four adaptive notch filters using FxLMS algorithm to update their coefficients.

1.3.4 Virtual sensing algorithms and Quite Zones

One of the main challenges in ANC systems designed for seat headrests is the development of large areas where acoustic pressure is significantly reduced, known as Quiet Zones (QZs). A common benchmark for the reduction of sound pressure level (SPL) required in these zones is 10 dB. However, single-channel systems that consist of a single speaker and an error microphone typically produce relatively small QZs that are located around the error microphone, making them insufficient for active headrest applications.

Consequently, multichannel algorithms are employed in such cases, using multiple speakers and microphones, in combination with larger speaker diaphragms. Furthermore, virtual sensing techniques are usually used. These techniques estimate the acoustic pressure at the ear of the seat occupant without placing physical microphones at that point, which is usually impractical in real-world applications. Therefore, in such systems the physical microphones are typically placed near to the headrest and close to the system's speakers (Figure 1.4a). This approach has twofold benefits: firstly, it eliminates the need to place physical microphones near the ears of the seat occupant, and secondly, it increases the distance between the virtual error microphone and the speaker diaphragm, resulting in an expansion of the QZ. Additionally, virtual techniques enable the integration of head-tracking systems that move the virtual sensor and, consequently, the QZ according to the

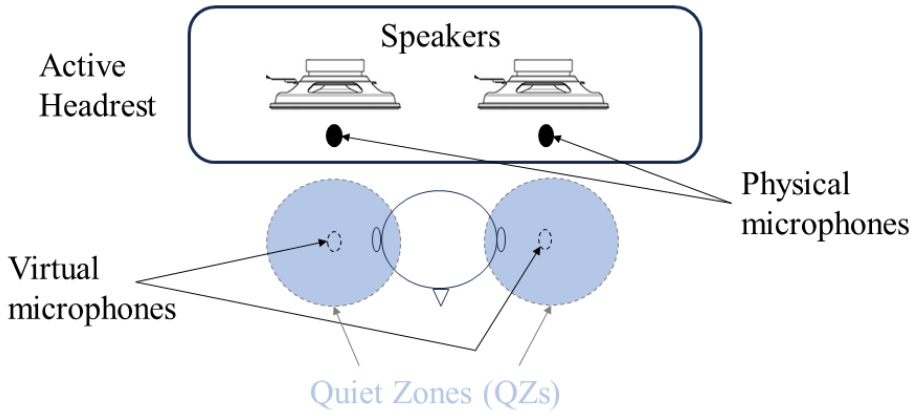

(a)

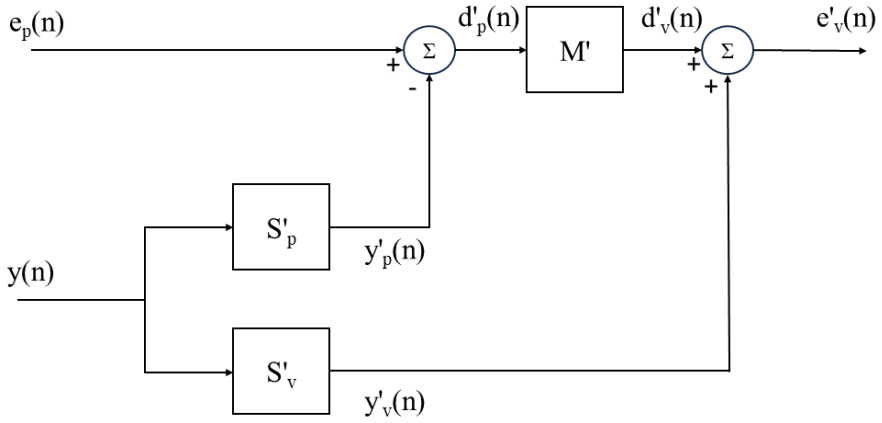

(b)

Figure 1.4: a) Top view of an active headrest and the forming quiet zones. b) Block diagram of the remote microphone technique for the estimation of the acoustic pressure at a remote location.

position of the head.

A common virtual sensing technique, with significant advantages is remote microphone technique (RMT) which aims to estimate the acoustic pressure at the virtual location (passenger's ear) using the models of the electroacoustic path between the secondary sources (speakers) and the locations of physical and virtual microphones. The block diagram of RMT is depicted in Figure 1.4b. The error signal at the virtual position (e'_v) is computed from the estimations of the acoustic disturbance (d'_v) and the control signal (y'_v) at the virtual location. In order to make this computation, the secondary paths between the physical (S'_p) as well as the virtual microphone (S'_v) and the speakers are modeled during a preliminary identification stage. In addition, the acoustic path between the physical and the virtual microphone (M') is also modeled. Although, this technique can accurately estimate the acoustic pressure at the virtual location, it increases the

system complexity and also it requires a extra stage for the identification of electroacoustic paths. Furthermore, it inserts a feedback loop by using $y(n)$, which can affect system's robustness. In the following Chapters of this dissertation a simpler alternative virtual sensing technique is used, which is effective for low frequency acoustic disturbances, and is based on linear extrapolation.

1.3.5 Acoustic disturbances in vehicle cabins

High acoustic pressure in vehicle cabins can be a major factor that degrades passenger comfort. The acoustic disturbances in such enclosures are usually caused by the vehicle engine, the interaction with the surface, where the vehicle moves, as well as the interaction with the air. For instance, in cars the main sources of low-frequency noise ($< 500Hz$) are the engine and the air, while the noise produced due to the interaction between the road surface and the tires is characterized by higher frequencies. Moreover, regarding the case of acoustic disturbances in train cars, it comes from a variety of sources related to propulsion system, auxiliary equipment, aerodynamic noise at high speeds and rolling noise.

In propeller-driven aircraft cabins, the acoustic spectrum consists of a series of discrete frequency components at the Blade Passage Frequency (BPF) and its harmonics, superimposed on a broadband background [17], [78]. The broadband noise was found to correspond to aerodynamic pressure fluctuations associated with external attached and separated boundary layers [22]. In addition, it has been found that the levels of the higher order BPF harmonics are much higher when the airplane is stationary than it is when moving forward. Thus, the low-frequency components of the BPF are dominant in propeller-driven aircraft during flight. On the other hand, in turbojet-powered commercial aircraft with cruise speeds substantially greater than those of propeller-driven airplanes, the cabin acoustic disturbance is mainly due to turbulent boundary layer noise, or aerodynamic noise. Interior noise generated by the external turbulent boundary layer is usually important in frequencies bigger than 400 Hz. Therefore, active noise control methods have been mainly used for low frequency BPF harmonic mitigation in small propeller-driven aircraft.

Finally in boat cabins, including yachts, the acoustic disturbances usually come from machinery and propellers as well as local sources, which can be the HVAC (Heating, Ventilation and Air Conditioning) systems and the local resonance of furniture. Machinery noise is typically characterized by both low frequency broadband noise and tonal components, which vary depending on the operating conditions. Similarly, propeller noise also features broadband noise and tonal components, albeit at lower frequencies than engine noise due to the lower rotating speed of propellers. Lastly, electric power generators on yachts can be a significant source of annoying noise, characterized by the low frequency

harmonics of the rotating speed of the generator. These frequency components usually range between 50 Hz and 250 Hz and can be disturbing when the background environmental noise level is low [[23], [24]. Consequently, the application of active noise control techniques can be advantageous in this situation.

1.3.6 Active noise control in enclosures

The active headrest is a system that falls under the category of local ANC, as it aims to reduce acoustic pressure locally, around the headrest area of a seat. In contrast, global ANC aims to mitigate acoustic pressure throughout the entire cabin. In this case, the acoustic modes of the enclosure are significant because they are responsible for the shape of the enclosed sound field. Therefore, knowledge of the mode shapes is essential for effective global noise control in vehicle cabins. Actually, acoustic modes are standing waves that occur between the boundaries of an enclosure at certain frequencies that depend on its geometric characteristics. For instance, in a rectangular room the acoustic modes are characterized as axial (one dimensional), tangential (two-dimensional) and oblique (three-dimensional). The three mode categories for a rectangular enclosure are depicted in Figure 1.5. At this point we must mention that the mode shapes change when the enclosure is not rectangular, and as a result the shape of the enclosure is an important parameter in order to decide the architecture of a global ANC system.

A common approach to global ANC in enclosures is based on placing the speakers in antinodes of the acoustic modes excited by the acoustic disturbance, since only then is it possible to cancel them. In addition, error microphones must also be placed away from nodes in order to detect the oscillation modes responsible for the disturbing acoustic pressure. Due to the fact that the acoustic pressure distribution is not always easy to determine in an enclosed sound field, several techniques are used that involve genetic algorithms to coalesce the optimal position of speakers and microphones in an enclosure. If the enclosure is cubic, things are usually straightforward, since maximum noise attenuation is achieved when the speakers are placed at the four corners. In more complex geometries, however, special care must be taken in the placement strategy for sensors and actuators. An alternative approach for ANC in enclosures is based on the placement of active sound absorbers to damp low frequency acoustic modes. The global system for aircraft cabins proposed in this thesis is also based on this approach. In the next paragraph some introductory concepts about the concept of active sound absorber are given.

1.3.7 The concept of Active Sound Absorber

An active sound absorber is usually a loudspeaker, that can modify the acoustic impedance of the diaphragm in order to maximize the absorption coefficient and perform perfect absorption in a specific frequency band. Many techniques have been proposed in order to

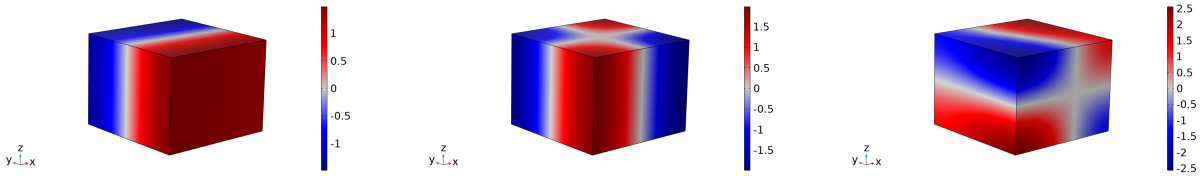

(a) axial (b) tangential (c) oblique

Figure 1.5: Acoustic modes of a rectangular enclosure.

implement an active absorber. Some methods rely on the the feedback of a combination of sound pressure and diaphragm velocity, resulting in a broadband acoustic impedance control. Other methods use an electric resistance loading the electric terminals of the loudspeaker. This device, which is usually called shunt loudspeaker can perform as sound absorber, however it is not active as the resistance must be preselected in order to absorb a specific frequency band, which is usually narrow. Furthermore, another method uses adaptive algorithm like LMS in order to minimize the reflected part of a sound wave at a loudspeaker's diaphragm. This, technique requires the separation of the sound wave into incident and reflected component, which can be achieved with sound intensity p-p method, using two closely spaced microphones. Finally, hybrid active/passive sound absorbers have been proposed that perform active control of the impedance at the rear face of a porous material panel so that the front face impedance takes on a desired value. Various sound absorbing devices have been implemented by combining the aforementioned methods and have been used for modal equalization of rooms as well as the mitigation of low frequency acoustic disturbances in small enclosures. In this dissertation, they are effectively employed for the global mitigation of low frequency acoustic disturbances in a small aircraft cabin mockup.

1.4 Original contributions

Summarizing the current state-of-the-art, it is evident that there is considerable interest in advanced ANC systems that effectively suppress low frequency acoustic disturbances in vehicle cabins, such as those found in small aircraft and yachts. The primary challenges associated with these systems involve:

- The performance of the control algorithm in terms of acoustic pressure attenuation.
- The system's computational efficiency and practicality.
- The size and relocation of the quiet zone when employing local control strategies.
- The global attenuation of low frequency acoustic modes, using a limited number of sensors and actuators.

This thesis has attempted to answer the challenges herein:

- Adapting an algorithm more computationally efficient than multichannel FxLMS to an active headrest. This algorithm, referred to as mixed-error FxLMS, was applied to a local ANC system designed for a single seat headrest, as well as to a system covering two adjacent seats. By doing so, the computational load was further reduced, as were the number of loudspeakers and microphones required.

- Incorporating a technique based on linear extrapolation of the acoustic pressure to increase and relocate the quiet zone. The main novelty lays in the combination of mixed-error approach with linear extrapolation, to form a new method.

- Proposing a nonlinear control algorithm that improves the performance of conventional FxLMS in attenuating low frequency components of a small aircraft cabin acoustic disturbance. This algorithm is based on a Functional Link Neural Network with sinusoidal expansion and incorporates both mixed-error approach and the ability to relocate the quiet zone.

- Giving an insight on the operation of multiple stand-alone ANC systems in the same cabin. This study was made by implementing several simulation models using FEM as well as through experimental evaluation.

- Presenting a novel method for global ANC in an aircraft cabin mockup using active sound absorbers. This method, that has never been employed in an aircraft cabin, tries to damp the significant acoustic modes of the enclosure, in order to reduce SPL throughout the cabin.

1.5 Outline of the dissertation

The doctoral dissertation comprises five chapters, wherein the fundamental techniques and systems for local and global active noise control in vehicle cabins are developed. The first section of each Chapter provides background information on the subject matter. Subsequently, the analytical models, simulations, and experimental tests conducted for the methods outlined in each Chapter are detailed. Each Chapter concludes with a section summarizing the findings. The final Chapter offers an overall conclusion based on the research conducted throughout the thesis. Finally, the Appendix provides comprehensive details on the implementation of the simulation models and experimental setups, as well as relevant codes implemented on embedded digital signal processors. The remainder of this section describes the structure and purpose of each chapter:

Chapter 2: Herein, an algorithm known as mixed-error FxLMS is examined. This algorithm serves as a viable alternative to the traditional multichannel FxLMS and one of

its primary advantage is the reduced computational complexity, making it an attractive option for large-scale, real-world applications. Subsequently, the mixed error FxLMS is evaluated for local ANC applications via FEM simulations. Furthermore, the experimental evaluation of a novel ANC system for two adjacent aircraft seats is presented. The results show that the mixed-error version can achieve significant attenuation of the SPL while saving computational resources.

Chapter 3: A major challenge of local ANC systems is to create an area of reduced SPL around the ears of the seat occupant, using methods to relocate the quiet zone, which normally extends around the error microphones. Therefore, this chapter presents a novel algorithm, called VEM-FxLMS that combines the mixed-error approach with the linear extrapolation employed for the prediction of acoustic pressure at passenger's ears. The proposed method was evaluated through simulations using k-space pseudospectral method and tested experimentally in a cabin mockup installed in the Dynamics and Acoustics Laboratory. Finally, a system with 2 inputs and 1 output based on this method was successfully installed on the deck of a yacht, in order to cancel the acoustic produced by the yacht' electric generators.

Chapter 4: In chapter 4, another novel method is introduced, based on a Functional Link Neural Network with sinusoidal functional expansion. Firstly, simulations of convergence as well as acoustic simulations based on FEM are presented. Subsequently, the experimental evaluation of the proposed method used included the mitigation of a real-world acoustic disturbance captured in the cabin of a small tilt-rotor aircraft and the comparison with conventional FxLMS. The comparison demonstrated that the FLNN based algorithm outperforms the FxLMS in terms of BPF harmonic attenuation. Good results were also obtained when the novel system was employed for the mitigation of other real-world acoustic disturbances, that comprised of yacht cabin noise while sailing, as well as cabin noise from a propeller driven aircraft and a helicopter, captured during flight.

Chapter 5: After investigating the operation of stand-alone local ANC systems, it became necessary to determine their behavior when operating simultaneously in an enclosure. Thus, the interaction of either four or six separate systems was studied, through simulations and experiments. Initially, two-dimensional simulation of the concurrent function of six systems either in a cooperating or a stand-alone mode is presented. Subsequently, a section implementing three-dimensional simulations discusses the size of the quiet zones that are shaped throughout the cabin, as well as the sound field between the quiet zones after the ANC activation. The final section of Chapter 5 discusses the experimental test, which employed four stand-alone single channel local ANC systems to study the enclosed sound field both in front of the loudspeakers and the areas between them.

Chapter 6: In this section of the thesis, the global control of the enclosed sound field of the cabin is attempted using active sound absorbers based on the wave separation method in incident and reflected. The evaluation of the method is done through three-dimensional

FEM simulations for various low frequency harmonic disturbances that can be encountered in a cabin of a small tilt-rotor aircraft. Furthermore, experimental tests performed on the cabin mockup in the laboratory confirmed the effectiveness of the method and are listed at the end of the chapter.

1.6 List of publications

International Scientific Journals

1. D. Mylonas, A. Erspamer, C. Yiakopoulos and I. Antoniadis. *Global control of propeller-induced aircraft cabin noise using active sound absorbers*. Journal of Sound and Vibration, Volume 573, Number 118213, 2024. https://doi.org/10.1016/j.jsv.2023.118213.

2. D. Mylonas, A. Erspamer, C. Yiakopoulos and I. Antoniadis. *A Virtual Sensing Active Noise Control System Based on a Functional Link Neural Network for an Aircraft Seat Headrest*. Journal of Vibration Engineering and Technologies, Volume 12, Pages 3857-3872, 2024. https://doi.org/10.1007/s42417-023-01090-5.

3. D. Mylonas, A. Erspamer, C. Yiakopoulos and I. Antoniadis. *An extrapolation-based virtual sensing technique of improving the control performance of the FxLMS algorithm in a maritime environment*. Applied Acoustics, Volume 193, Number 108756, 2022. https://doi.org/10.1016/j.apacoust.2022.108756.

International Scientific Conferences

1. D. Mylonas, A. Erspamer, C. Yiakopoulos and I. Antoniadis. *A low computational complexity local Active Noise Control system for adjacent aircraft seats*, in Proceedings of Forum Acusticum, FA2023, Torino, Italy, 2023, doi:10.61782/fa.2023.0022,https://dael.euracoustics.org/confs/fa2023/data/articles/000022.pdf.

2. D. Mylonas, A. Erspamer, C. Yiakopoulos and I. Antoniadis.*Global noise attenuation through the combination of local Active Noise Control systems in the cabin of an aircraft*, in Proceedings of 29^{th} International Congress of Sound and Vibrations, ICSV29, Prague, Czech Republic, 2023, https://iiav.org/content/archives_icsv_last/2023_icsv29/content/papers/papers/full_paper_141_20230606140344328.pdf.

3. D. Mylonas, A. Erspamer, C. Yiakopoulos and I. Antoniadis. *A Non-linear ANC system for an aircraft's seat headrest*, in Proceedings of National Conference in Acoustics, Thessaloniki, Greece, 2022.

4. D. Mylonas, A. Erspamer, C. Yiakopoulos and I. Antoniadis. *A narrowband virtual sensing Active Noise Control system using ESPRIT for an aircraft interior*, in Proceedings of EuroNoise, Madeira, Portugal, 2021,`https://documentacion.sea-acustica.es/publicaciones/Madeira21/ID104.pdf`.

5. D. Mylonas, A. Erspamer, A. Paradisiotis, C. Yiakopoulos and I. Antoniadis. *A local active noise control system based on a nonlinear sensing technique for yacht applications*, in Proceedings of the International Conference on Structural Dynamic, EURODYN, 2020, Athens, Greece. `https://eurodyn2020.org/proceedings/pdf/19996.pdf`.

CHAPTER 2

Multichannel algorithms for active headrests

2.1 Introductory notes

In the introduction of this thesis, the concept of an active headrest was introduced as an ANC system that is installed on the headrest of a passenger's seat, generally in a means of transportation, with the aim of creating areas of reduced acoustic pressure around the ears. Previous research has proposed methods for implementing such systems. This Chapter begins by discussing the multichannel FxLMS algorithm, which is commonly used in such systems and serves as a benchmark for their performance. Subsequently, the mixed error FxLMS algorithm is presented, which exhibits reduced computational complexity. Lastly, the chapter examines ANC architectures that have been tailored for use in active headrest applications using mixed error FxLMS.

2.2 Single-Reference/Multichannel FxLMS algorithm

The multichannel FxLMS algorithm, with one reference signal, K loudspeakers and M microphones based on the analysis of Kuo and Morgan [79], is depicted in Figure 2.1.

The adaptive multichannel FxLMS algorithm computes the weights of K adaptive FIR filters $\mathbf{w_k}(n)$. Thus, we obtain the vector $\mathbf{w}(n)$ with dimensions $K \times L$, where L is the number of coefficients for each adaptive filter, which is typically referred to as the filter length.

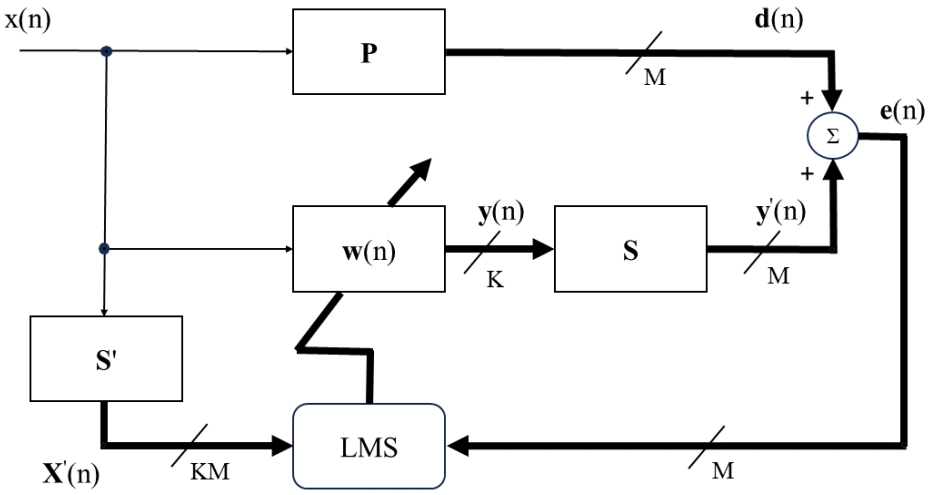

Figure 2.1: Multichannel FxLMS with single reference signal, K loudspeakers and M microphones.

$$\mathbf{w}(n) = [\mathbf{w}_1^T(n) \quad \mathbf{w}_2^T(n) \quad \cdots \quad \mathbf{w}_K^T(n)]^T \tag{2.1}$$

where

$$\mathbf{w}_k(n) = [w_{k,0}(n) \quad w_{k,1}(n) \quad \cdots \quad w_{k,L-1}(n)]^T, \quad k = 1, 2, ..., K \tag{2.2}$$

Furthermore, the antinoise signal for each loudspeaker is computed by the dot product between the reference signal and the corresponding adaptive filter (Eq. 2.3)

$$y_k(n) = \mathbf{w}_k^T(n)\mathbf{x}(n) \tag{2.3}$$

where

$$\mathbf{x}(n) = [x(n) \quad x(n-1) \quad \cdots \quad x(n-L+1)]^T \tag{2.4}$$

The error signal vector $\mathbf{e}$(n) of M error microphones is also given by Eq. 2.5:

$$\mathbf{e}(n) = \mathbf{d}(n) + \mathbf{y}'(n) \tag{2.5}$$

where

$$\mathbf{y}'(n) = \mathbf{S}(n) * \mathbf{y}(n) \tag{2.6}$$

and $\mathbf{S}(n)$ is a K x M matrix that contains all the secondary paths between K loudspeakers and M microphones

$$\mathbf{S}(n) = \begin{bmatrix} s_{11}(n) & s_{12}(n) & \cdots & s_{1K}(n) \\ s_{11}(n) & s_{12}(n) & \cdots & s_{1K}(n) \\ \vdots & \vdots & \ddots & \vdots \\ s_{M1}(n) & s_{M2}(n) & \cdots & s_{MK}(n) \end{bmatrix} \tag{2.7}$$

At this point, it is essential to emphasize that in Eq. 2.5 we employ the sum rather than the subtraction of the two signals, which is used in the original analysis of Kuo and Morgan. This is because we presume that the antinoise signal y(n) incorporates the phase inversion when it is calculated by the adaptive algorithm. Moreover, this assumption forms the basis for the code implementation utilized in the controllers implemented for this dissertation.

The antinoise signal that reaches the m^{th} microphone is obtained by Eq. 2.8.

$$y'_m(n) = \sum_{k=1}^{K} s_{mk}(n) * y_k(n), \quad m = 1, 2, ..., M \tag{2.8}$$

Combining Eqs. 2.3, 2.5 and 2.6 we can write in matrix form:

$$\mathbf{e}(n) = \mathbf{d}(n) + \mathbf{S}(n) * \mathbf{y}(n) = \mathbf{d}(n) + \mathbf{S}(n) * [\mathbf{X}^T(n)\mathbf{w}(n)] \tag{2.9}$$

where $\mathbf{X}(n)$ is a KL x K block-diagonal matrix, that contains the same reference signal in its diagonal.

In addition, the cost function is the mean-squared error of M error signals:

$$J(n) = \sum_{m=1}^{M} E[e_m^2(n)], \quad m = 1, 2, ..., M \tag{2.10}$$

According to LMS algorithm, the mean squared error can be approximated by the instantaneous squared error. Therefore, the cost function of Eq. 2.10 can be rewritten as:

$$J(n) = \sum_{m=1}^{M} e_m^2(n), \quad m = 1, 2, ..., M \tag{2.11}$$

Employing the gradient descent method, the adaptive weight vector $\mathbf{w}(n)$ is updated by Eq. 2.12:

$$\mathbf{w}(n+1) = \mathbf{w}(n) - \frac{\mu}{2}\nabla J(n) \tag{2.12}$$

First the gradient of the cost function of Eq. 2.11 will be calculated with respect to the k^{th} weight subvector $\mathbf{w_k}(n)$ at time n. By combining Eqs. 2.3, 2.5 and 2.8 we obtain:

$$\nabla_k J(n) = \nabla_k \sum_{m=1}^{M} e_m^2(n) = 2 \sum_{m=1}^{M} [s_{mk}(n) * \mathbf{x}(n)] e_m(n), \quad k = 1, 2, ..., K \tag{2.13}$$

Thus we can write the gradient of the cost function in matrix form:

$$\nabla J(n) = 2 \begin{bmatrix} s_{11}(n) * \mathbf{x}(n) & s_{21}(n) * \mathbf{x}(n) & \cdots & s_{M1}(n) * \mathbf{x}(n) \\ s_{11}(n) * \mathbf{x}(n) & s_{21}(n) * \mathbf{x}(n) & \cdots & s_{M2}(n) * \mathbf{x}(n) \\ \vdots & \vdots & \ddots & \vdots \\ s_{1K}(n) * \mathbf{x}(n) & s_{2K}(n) * \mathbf{x}(n) & \cdots & s_{MK}(n) * \mathbf{x}(n) \end{bmatrix} \mathbf{e}(n) = \tag{2.14}$$

$$= 2[\mathbf{S}^T(n) \circledast \mathbf{X}(n)]\mathbf{e}(n)$$

where $\circledast$ denotes the Kronecker product convolution.

In the implementation of FxLMS in practical systems, secondary paths are typically unavailable. Consequently, we rely on the models obtained during a preliminary identification stage [53]. During this stage, the k^{th} loudspeaker emits white noise, which is captured by the m^{th} microphone to create the model $s_{km}(n)$ of the secondary path. By employing LMS, we obtain the model $s'_{km}(n)$ of the secondary path, and we form the matrix $\mathbf{S}'(n)$ respectively. Therefore, Eq. 2.14 becomes:

$$\nabla_k J(n) = 2[\mathbf{S}'^T(n) \circledast \mathbf{X}(n)]\mathbf{e}(n) = 2\mathbf{X}'(n)\mathbf{e}(n) \tag{2.15}$$

Finally, from Eqs. 2.12 and 2.14 we obtain the update equation of the coefficients of the K adaptive filters:

$$\mathbf{w}_k(n+1) = \mathbf{w}_k(n) - \mu \sum_{m=1}^{M} \mathbf{x}'_{km}(n) e_m(n), \quad k = 1, 2, ..., K. \tag{2.16}$$

which in matrix form becomes:

$$\mathbf{w}_k(n+1) = \mathbf{w}_k(n) - \mu \mathbf{X}'(n)\mathbf{e}(n) \tag{2.17}$$

2.3 The need of an algorithm of lower complexity

The multichannel FxLMS algorithm possesses several advantages, including its ability to effectively attenuate acoustic disturbances, create larger silence bands, and achieve

rapid convergence. Additionally, it is highly effective in broadband disturbances. Despite these advantages, the high computational complexity of the algorithm poses a challenge for its practical implementation. This complexity stems primarily from the numerous convolution operations required between the secondary paths connecting the speakers and microphones with the reference signal. As the number of sensors and actuators increases, the number of these operations also increases, necessitating the use of powerful digital signal processors (DSPs) to implement the algorithm in large environments such as aircraft cabins or ships. This increase in cost is undesirable for manufacturers of these vehicles, which is one reason why multichannel active noise control systems have not been widely adopted in commercial applications. To address this issue, numerous research studies have focused on developing methods to reduce the computational requirements of multichannel ANC systems.

Douglas et al. proposed an alternative implementation of the conventional FxLMS algorithm that can save operations and memory storage in multichannel case [80]. In addition, a computationally efficient architecture based on multiple-parallel-branch was implemented in an FPGA controller [81]. Furthermore, some papers present alternative approaches to the implementation of multichannel ANC that aim to reduce convolution operations, either by replacing high-order global secondary path estimate with multiple low-order local estimates [63], or by reducing the secondary path models involved in the computation of the filtered reference signals [82]. Moreover, there are works that apply modifications that lead to algorithms which have the same optimal control as the standard multichannel FxLMS but with lower computational demands. Shi et al. proposed a system based on the adjoint least mean square algorithm [83], while proving that its multichannel version has a significantly lower computation cost than the FxLMS, while Ho et al. presented a method to split the reference signal into different time slots, in order to reduce the signals from multiple reference microphones [84].

Another attempt to reduce the computational cost involved in using the conventional multichannel FxLMS was made by Murao et al. who proposed a cost function involving the mean square of the sum of the error signals instead of the sum of the mean square errors [85]. This algorithm was used for an active window application, where loudspeakers and microphones were placed in front of the opening surface, in order to reduce the acoustic pressure entering a room from outside. Experimental evaluation demonstrated that this algorithm exhibits similar performance to the conventional FxLMS in terms of SPL reduction while significantly reducing the computational complexity. The remainder of this chapter will analyze this algorithm called mixed error FxLMS and two applications for active headrest based on it will be presented.

2.4 Mixed-error FxLMS algorithm

The mixed error FxLMS algorithm, initially introduced by T. Murao, C. Shi, W.S. Gan, and M. Nishimura, presents an alternative approach to single-reference multichannel ANC systems employing K loudspeakers and M microphones. It has been used for an active window application [8] and it is distinguished by its notably reduced computational complexity. Moreover, the algorithm operates under the assumption that the acoustic pressure observed at each error microphone is nearly identical. The original research elucidates through mathematical analysis that under conditions, where this assumption is valid, the mixed error algorithm converges to the same global minimum as the conventional multichannel FxLMS algorithm. Consequently, this approach proves particularly advantageous in mitigating low-frequency acoustic disturbances, where spatial variations in acoustic pressure are small because of the large wavelengths. The block diagram of mixed-error FxLMS algorithm is depicted in Figure 2.2. In this algorithm, we use the mixed error (Eq. 2.18) instead of the separate errors of each microphone.

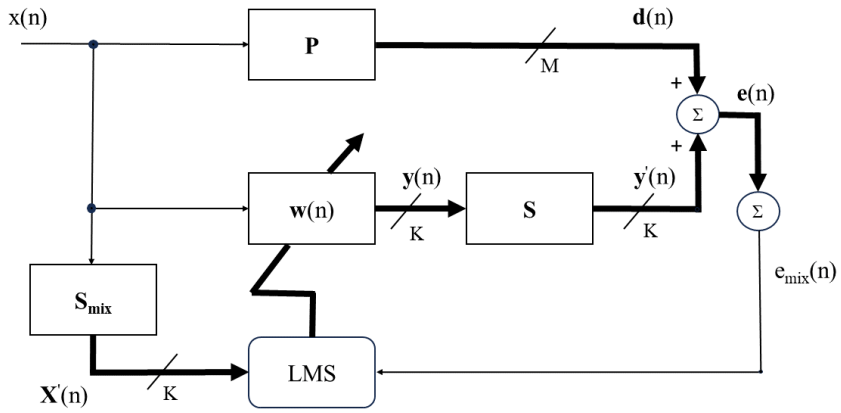

Figure 2.2: Mixed-error FxLMS with single reference signal, K loudspeakers and M microphones.

$$e_{mix}(n) = \sum_{m=1}^{M} e_m(n), \quad m = 1, 2, ..., K. \tag{2.18}$$

In addition, the k^{th} mixed secondary path is computed during a preliminary identification stage, which is described in Figure 2.3. During this process, the corresponding loudspeaker reproduces band limited white noise, which is used as reference signal for the LMS algorithm. In addition, the M error microphones record the acoustic pressure at the cancellation area. Subsequently, the mixed error is computed by summing the separate error signals. The coefficients of the filter obtained by the LMS algorithm are

updated with respect to the mixed error, producing the model of the mixed secondary path. The whole procedure of k^{th} mixed secondary path modeling is depicted in Figure 2.3. Therefore, we form the block vector $\mathbf{S}_{mix}$ of K mixed secondary paths, expressed by Eq. 2.19.

$$\mathbf{S}_{mix} = [\mathbf{s}_{1,mix} \quad \mathbf{s}_{2,mix} \quad \cdots \quad \mathbf{s}_{K,mix}] \tag{2.19}$$

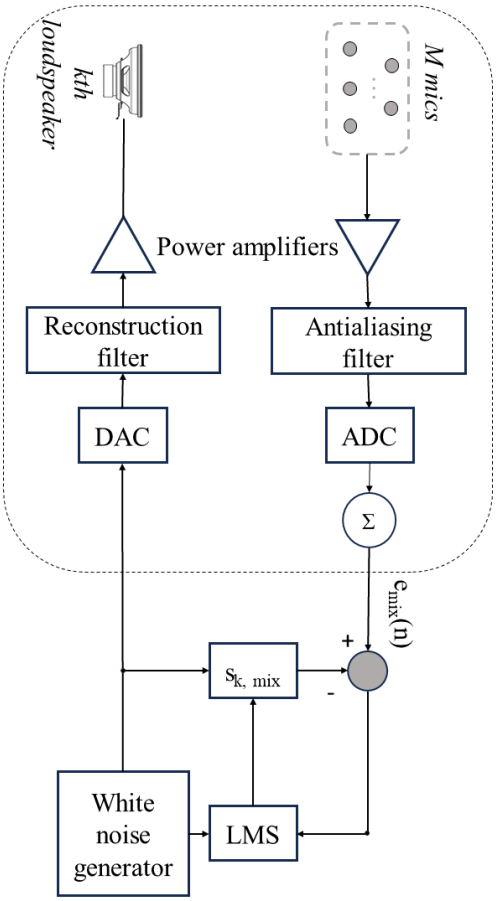

Figure 2.3: Block diagram of preliminary identification stage of k^{th} mixed secondary path.

Subsequently, the filtered reference block vector is computed by Eq.2.20:

$$\mathbf{X}'(n) = [\mathbf{s}_{1,mix} * \mathbf{x}(n) \quad \mathbf{s}_{2,mix} * \mathbf{x}(n) \quad \cdots \quad \mathbf{s}_{K,mix} * \mathbf{x}(n)] \tag{2.20}$$

$$= [\mathbf{x}'_{1,mix}(n) \quad \mathbf{x}'_{2,mix}(n) \quad \cdots \quad \mathbf{x}'_{K,mix}(n)]$$

Thus, the kth adaptive filter coefficients are updated by Eq. 2.21. Subsequently, the antinoise signal is computed similarly to Eq. 2.3.

$$\mathbf{w}_k(n+1) = \mathbf{w}_k(n) - \mu \mathbf{x'}_{k,mix}(n) e_{mix}(n), \quad k = 1, 2, ..., K. \tag{2.21}$$

2.5 Mixed-error algorithm for active headrests

The majority of headrest applications usually incorporate two or three microphones and two loudspeakers. Consequently, the mixed-error algorithm analysis that follows is based on these configurations. As already mentioned in section 2.4, the original research that employed this algorithm to create a noise-canceling window presupposed that the acoustic pressure at the locations of the error microphones was nearly identical. However, this assumption may not always be valid in active headrest applications. Therefore, the objective of this analysis is to extend the capabilities of the algorithm to situations where the acoustic pressure differs between the two error microphones.

2.5.1 2 input-2 output mixed error FxLMS

To begin with, the anti-noise signal that drives the system's loudspeakers is represented by the following equation:

$$y_k(n) = \mathbf{w}_k^T(n)\mathbf{x}(n), \quad k = 1, 2 \tag{2.22}$$

where x is the reference signal obtained by a sensor close to the noise source and w is a vector of adaptive filter coefficients computed by Eq. 2.23, corresponding to k^{th} loudspeaker.
The vectors are also denoted with bold letters, just like the analysis in previous paragraphs.

$$\mathbf{w}_k(n) = [w_{k,0}(n) \quad w_{k,1}(n) \quad \cdots \quad w_{k,L-1}(n)], \quad k = 1, 2, ..., K \tag{2.23}$$

where L is the adaptive filter length.
In addition, the mixed-error cost function that has to be minimized is the instantaneous squared sum of the 2 error signals given by Eq. 2.24.

$$J_{mix}(n) = e_{mix}^2(n) = \left(\sum_{m=1}^{2} e_m(n) \right)^2 = (e_1)^2 + (e_2)^2 + 2e_1e_2 \tag{2.24}$$

The gradient of the cost function is given by Eq. 2.25

$$\nabla J_{mix}(n) = 2[\nabla e_{mix}(n)] e_{mix}(n) \tag{2.25}$$

In addition, the error signal of each microphone is given by Eq. 2.26.

$$e_i(n) = d_i(n) + \sum_{k=1}^{2} \mathbf{s}_{ki}(n) * [\mathbf{w}_k^T(n)\mathbf{x}(n)], \quad i = 1, 2. \tag{2.26}$$

where d_i is the acoustic disturbance at the i^{th} microphone, $\mathbf{s}_{ki}$ is the secondary path from k^{th} loudspeaker to the i^{th} microphone and * denotes the convolution operator. Furthermore, the gradient of the mixed error is given by Eq. 2.27. As we differentiate with respect to $\mathbf{w}_k$ the mixed error derivative will be different for each loudspeaker.

$$\begin{aligned} \nabla e_{mix_k}(n) &= \nabla\Bigg(\sum_{i=1}^{2} e_i(n)\Bigg) \overset{(5)}{=} \nabla\Bigg(\sum_{i=1}^{2}\Big(d_i(n) + \sum_{k=1}^{2} \mathbf{s}_{ki}(n) * [\mathbf{w}_k^T(n)\mathbf{x}(n)]\Big)\Bigg) \Rightarrow \\ \nabla e_{mix_k}(n) &= \Bigg(\sum_{i=1}^{2} \mathbf{s}_{ki}(n)\Bigg) * \mathbf{x}(n) = \mathbf{s}_k(n) * \mathbf{x}(n) = \mathbf{x}'_k(n) \end{aligned} \tag{2.27}$$

where s_k is the parallel combination of the 2 secondary paths from one loudspeaker to each error microphone in the active headrest. This assumption can be made as the distance between the loudspeakers and the microphones is relatively small comparing to the wavelength of low frequency acoustic disturbances. As a result, it can be assumed that during the secondary path identification stage, the acoustic path through the air is common to all microphones. The only thing that changes is the electrical path involving the DAC, ADC and cables. Finally, the coefficients of the adaptive filters, which produce the output signal of each loudspeaker derive from Eq. 2.28.

$$\begin{aligned} \mathbf{w}_k(n+1) &= \mathbf{w}_k(n) - \frac{\mu}{2}\nabla J_{mix}(n) \Rightarrow \\ \mathbf{w}_k(n+1) &= \mathbf{w}_k(n) - \mu \mathbf{x}'_k(n) e_{mix}(n) \end{aligned} \tag{2.28}$$

where μ is the step size of the minimization process.

As already mentioned, the mixed-error algorithm converges to the same optimum control filters as those of the normal multichannel FxLMS algorithm, when the output of every error microphone is almost identical [85]. However, this condition is not always valid in the case of an active headrest. If we assume that the acoustic disturbance consists of low frequency harmonic components, we can make the assumption that their wavelength is sufficiently longer than the distance between the microphones, which are part of the active headrest. As a result, the acoustic pressure at the midpoints between them can be described by a linear equation given by Eq. 2.29.

$$e_{mid_{12}}(n) = \frac{e_1(n) + e_2(n)}{2} \tag{2.29}$$

where $e_{mid_{12}}$ is the acoustic pressure at the midpoint between the two error microphones of

the active headrest and e_1, e_2 are the acoustic pressures at these microphones. In addition, the cost function resulting from the conventional multichannel FxLMS for minimizing the acoustic pressure at the midpoints between the microphones is obtained from Eq. 2.30.

$$J_{mid}(n) = e^2_{mid_{12}}(n) = \left(\frac{e_1(n) + e_2(n)}{2}\right)^2 = \frac{1}{4} J_{mix}(n) \tag{2.30}$$

Thus, the relationship between the gradient of the conventional FxLMS algorithm for minimizing the acoustic pressure at the midpoint between the two error microphones and the gradient of the mixed-error cost function is described by equation 10.

$$\nabla J_{mid}(n) = \frac{1}{4} \nabla J_{mix} \tag{2.31}$$

Thus, we can conclude that the 2 input-2 output mixed-error algorithm converges to the optimum control filters as those of the normal multichannel FxLMS algorithm, minimizing the acoustic pressure at the midpoints between the actual error microphones of the active headrest when the assumption made in Eq. 2.27 is valid and $e_1 \neq e_2$. The only parameter that changes is the convergence rate, as indicated in Eqs. 2.30, 2.31.

Simulation results

The three-dimensional simulations of the active headrest system were conducted using time domain FEM in Comsol Multiphysics®, in order to evaluate its performance in terms of acoustic pressure attenuation and the size of the quiet zone. The geometry of the model used for the simulation purposes consisted of a cuboid air domain, which is surrounded by a PML in order to simulate free space. The loudspeaker diaphragms were simulated as circles with a normal acceleration boundary condition, while the microphones were domain point probes. Two different configurations for the loudspeaker setup were evaluated. In the first configuration, the noise source was positioned opposite to the active headrest. Conversely, in the second configuration, the noise source was aligned with the headrest. The driving signals of the loudspeakers were inserted into the model by adding global equations, that control the normal acceleration of the circular boundaries that model their diaphragm. Each of these equations included a Matlab function implementing the desired control algorithm. In addition, the communication between Comsol and Matlab was achieved via Matlab Livelink® for each iteration of the time dependent solver. Finally, the noise source, which was also simulated as a circle with a normal acceleration boundary condition, consisted of three sinusoidal components at 72 Hz, 96 Hz, and 120 Hz. Further details on this simulation model are also given in Appendix A.2.1.

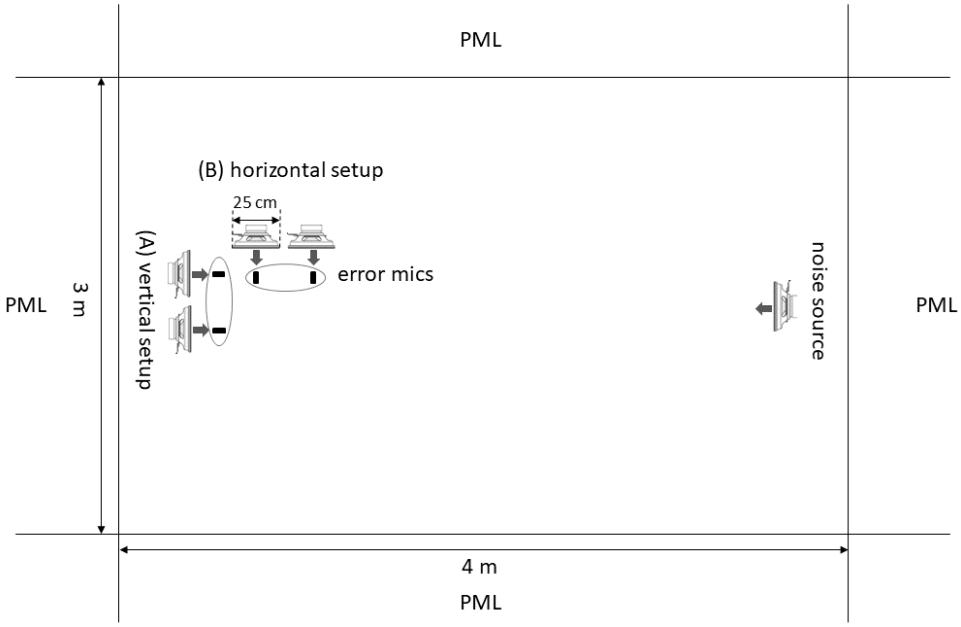

Figure 2.4: Top view of the geometry used during FEM simulations of the active headrest, with the two different loudspeaker setups (vertical or horizontal).

Vertical loudspeaker setup

In these simulations, corresponding to A loudspeaker setup of Figure 2.4, the loudspeakers of the active headrest were placed opposite to the noise source, so that the acoustic pressure at the points, where the error microphones were placed is almost the same. This is due to the long wavelength of the harmonic components of the acoustic disturbance and the fact that there is a PML around the air domain, resulting in absence of reflections. In addition, the distance between the error microphones was set to 30 cm, and the distance between the loudspeaker diaphragm and the corresponding error microphone to 10 cm.

Initially, the conventional multichannel FxLMS with 2 inputs and 2 outputs was employed to mitigate acoustic pressure in front of the active headrest. Figure 2.5 illustrates the SPL distribution before and after the ANC activation, as well as the shape of the quiet zones that were shaped in front of the system's loudspeakers. Therefore, we can observe that the largest SPL reduction is located around the position where the error microphones are placed and reaches 25 dB. In contrast, in the area between them, the reduction is 10 dB (Figure 2.5b. These results are expected for conventional multichannel FxLMS, which creates quiet zones around the error microphones.

Furthermore, when the mixed error FxLMS was employed as control algorithm, the SPL distribution remained the same as in the conventional FxLMS as illustrated in Figure 2.5c. Thus, we confirm the analysis of section 2.5.1 that the mixed error FxLMS has similar behavior to conventional FxLMS, when the output of every error microphone is almost identical. In such cases, therefore, the use of the mixed error version leads to similar performance as the conventional version with reduced computational complexity

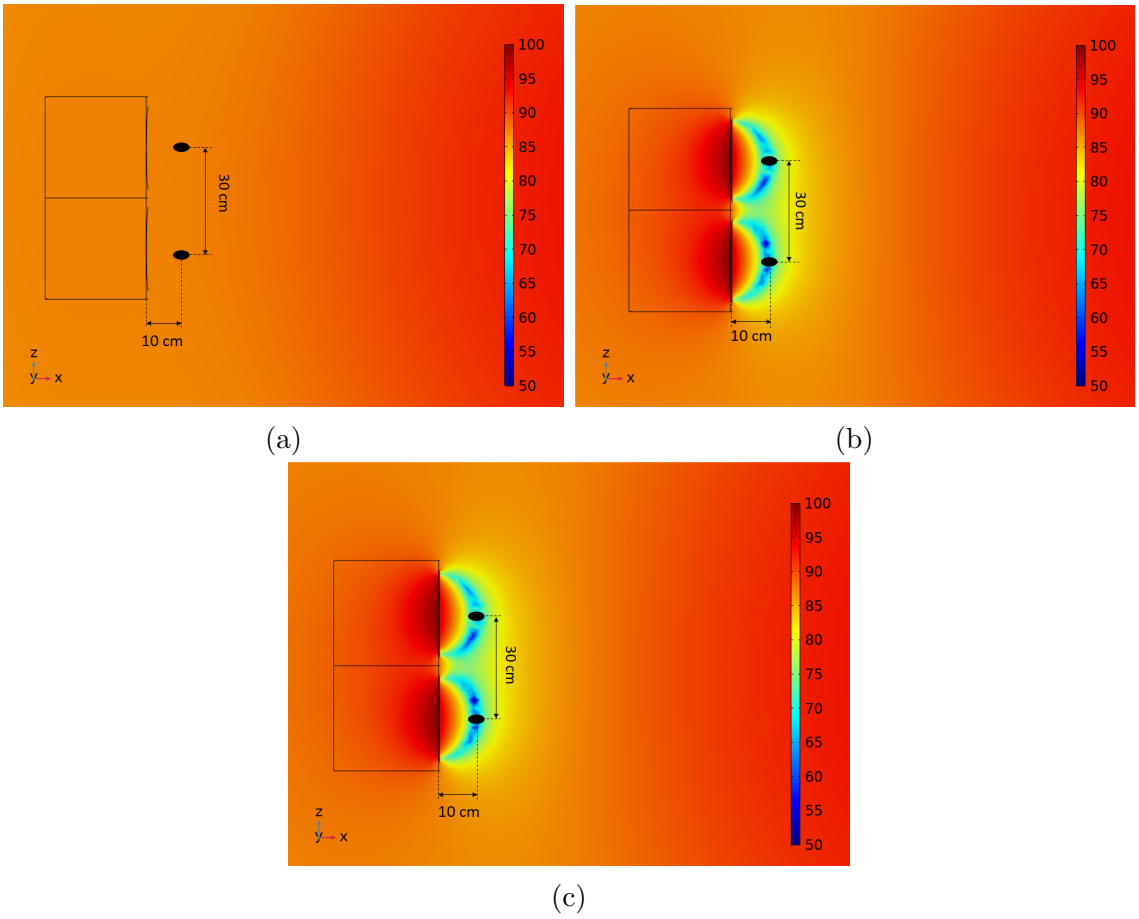

Figure 2.5: a) SPL distribution at a measurement plane at the middle of the loudspeaker diaphragm for vertical loudspeaker setup when a) the ANC is off, b) the conventional multichannel FxLMS is used, c) the mixed error FxLMS is used.

since the convolution operations are significantly reduced.

Horizontal loudspeaker setup

The horizontal loudspeaker setup corresponds to the configuration B that is illustrated in Figure 2.4. In this configuration, the acoustic pressure at the midpoint between the two error microphones is given by Eq. 2.29 for acoustic disturbances with large wavelengths compared to the microphone distance. For instance the wavelength of a 72 Hz sound wave at $25°C$ is $\lambda = 4.5m$. Thus, the error microphone distance is $\lambda/15$, which supports the assumption made in the derivation of Eq. 2.29.

According to Figure 2.6c, it can be seen that the conventional multichannel FxLMS algorithm achieved the maximum SPL attenuation at the positions of the error microphones. On the other hand, the mixed error algorithm produced a quiet zone where the SPL was significantly lower in the area between the error microphones. This can be particularly observed when the distance between the error microphones is 50 cm, as depicted in Figure 2.7b. In this case, the SPL attenuation at the midpoint reached 20 dB, while at

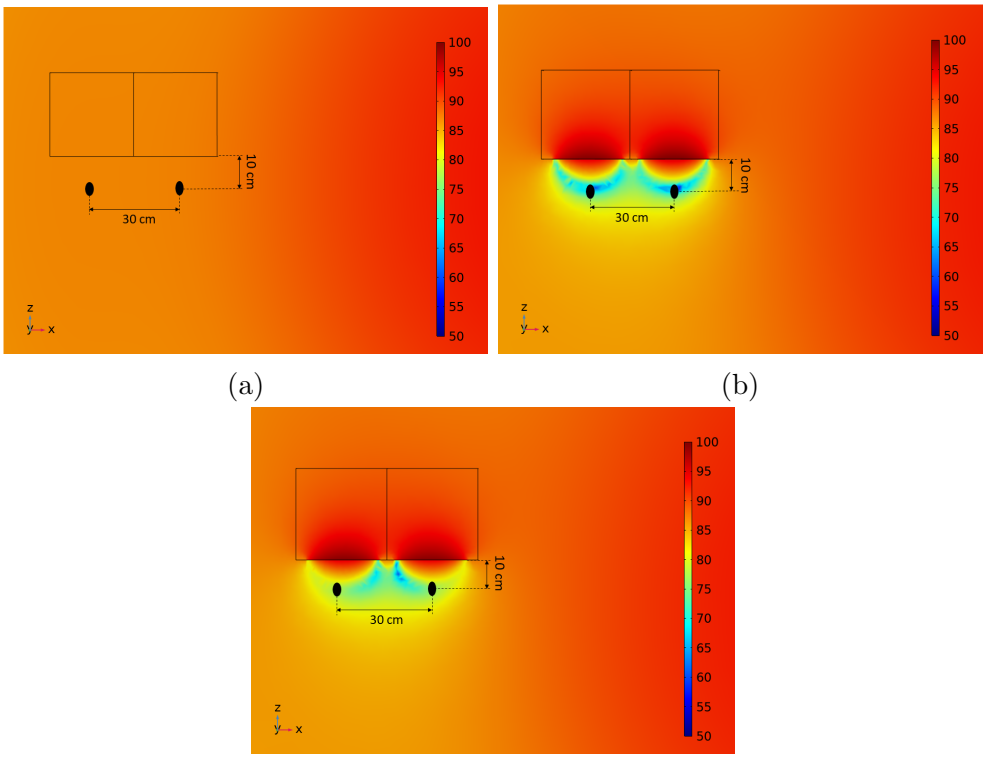

(a) (b)

(c)

Figure 2.6: a) SPL distribution at a measurement plane at the middle of the loudspeaker diaphragm for horizontal loudspeaker setup when a) the ANC is off, b) the conventional multichannel FxLMS is used, c) the mixed error FxLMS is used.

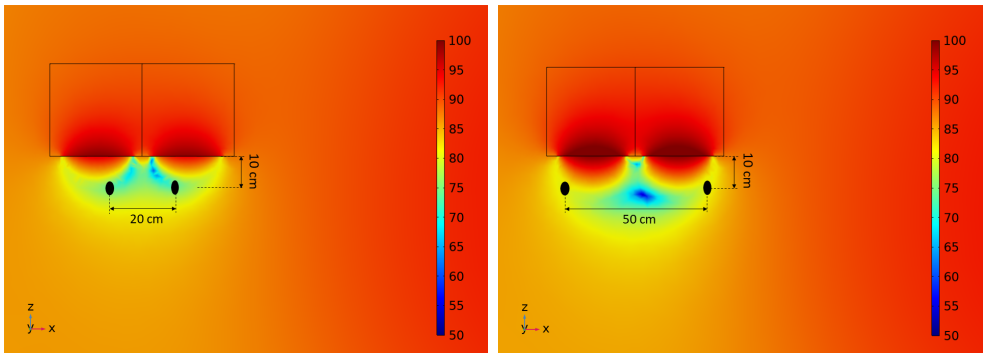

(a) (b)

Figure 2.7: a) SPL distribution at a measurement plane at the middle of the loudspeaker diaphragm for vertical loudspeaker setup when the distance between the error microphones was a) 20 cm and b) 50 cm.

the error microphone positions it was 10 dB. Furthermore, when the microphone distance was 30 cm and 20 cm (Figs. 2.6c, 2.7a), the SPL distribution did not change significantly when the ANC was activated. The SPL attenuation at the midpoint was 15 dB, while at the error microphone positions it remained at 10 dB.

Thus, we observe that if the acoustic pressure captured by the error microphones is different, the maximum SPL attenuation is achieved at the midpoint between the error

microphones instead of the positions where they are located, assuming that we use mixed error FxLMS as control algorithm and the wavelengths of the acoustic disturbance is much larger than the distance between the error microphones. This finding can lead us to choose different speaker and microphone layouts in order to bring the maximum SPL reduction to the passenger's ears. However, even if this condition does not exist, noise mitigation is in most cases sufficient to make it worth the small decline in performance, in order to reduce computational complexity. In the following paragraph, the configuration of loudspeaker and microphones along with the mixed error FxLMS were combined for the implementation of an ANC system for adjacent aircraft seats characterized by low computational complexity.

2.5.2 3 input-2 output mixed error FxLMS

The ANC system that aims to create a quiet zone in front of two adjacent airplane seats consists of two secondary sources (subwoofers) and three microphones, as illustrated in Figure 2.8. The driving signal (anti-noise signal), which is the same for the two secondary sources, derives from Eq. 2.32. In the following equations, the vectors are denoted by bold letters.

$$y(n) = \mathbf{w}^T(n)\mathbf{x}(n) \tag{2.32}$$

where x is the reference signal obtained by a sensor close to the noise source and w is a vector of adaptive filter coefficients computed by Eq. 2.21, as shown in Eq. 2.33.

$$\mathbf{w}(n) = [w_1(n)\, w_2(n)\, w_3(n) \ldots w_L(n)] \tag{2.33}$$

where L is the filter length.

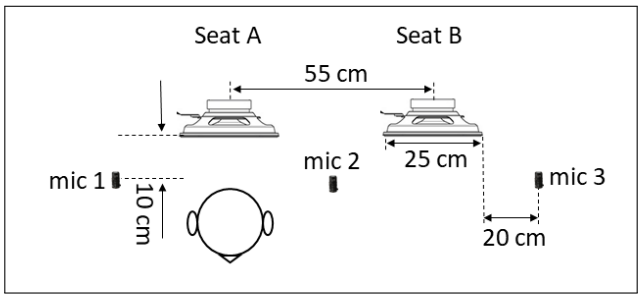

Figure 2.8: The ANC setup for two adjacent seats that consists of two subwoofers and three microphones.

The mixed error FxLMS algorithm is used to compute **w**, because of its low computational complexity. The cost function that has to be minimized is the instantaneous squared sum of the three error signals, given by Eq. 2.34.

$$J(n) = [e_1(n) + e_2(n) + e_3(n)]^2 = e_{mix}^2 \tag{2.34}$$

Then the analysis is similar to the 2 input-2 output system described in the previous paragraph. Except from the mixed error, that consists of three error signals, another difference has to do with the mixed error secondary path model, which is computed with respect to three error microphone, instead of two.

Simulation results

The three-dimensional simulations of the proposed ANC headrest were conducted using time domain FEM in Comsol Multiphysics®. The cabin mockup of the aircraft was designed to be identical to the one installed in the laboratory for the system's experimental testing. More details on the dimensions of the cabin mockup as well as on the model developed for the simulation purposes are given in the Appendix section.

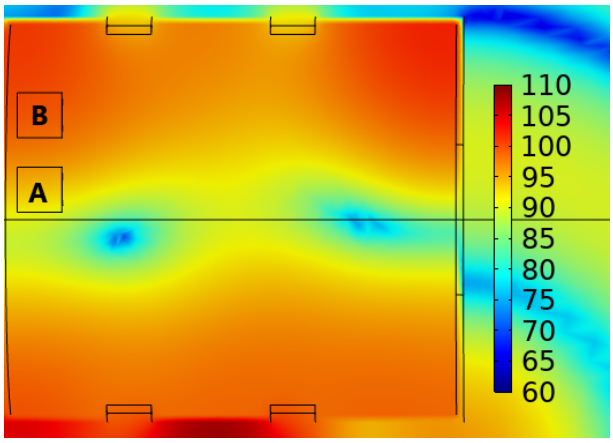

(a)

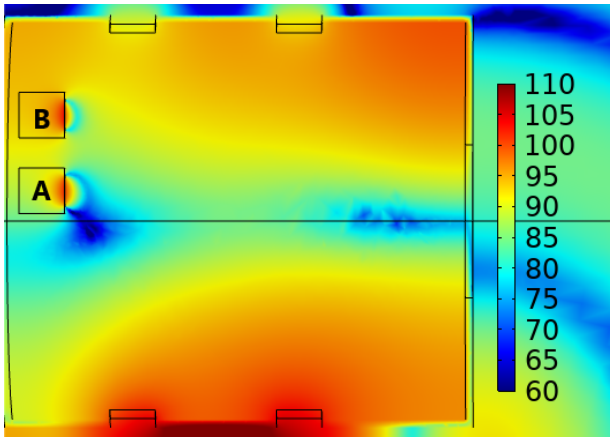

(b)

Figure 2.9: Top view of the cabin mockup modeled using FEM (a) before and (b) after the activation of the ANC system.

The driving signal of the loudspeakers was again inserted into the model by adding global equations, which control the normal acceleration of the boundaries that model the

diaphragms. A loudspeaker that was placed one meter away from the cabin was used as the noise source. It was driven by a synthetic signal consisting of three 24 Hz BPF harmonics at 72 Hz, 96 Hz, and 120 Hz.

Figure 2.9 illustrates the SPL distribution at a plane parallel to the cabin's floor, at the height of the center of the loudspeaker's diaphragm. When the ANC was activated (Figure 2.9b, the SPL attenuation reached 18 dB in front of seat A and 20 dB in front of seat B. In addition, the maximum attenuation was achieved 10 cm to 15 cm far from the surface of the subwoofers. The quiet zone had a surface area of $30cm \times 30cm$ in front of both seats, and over the area between them. Furthermore, the rest of the cabin was not negatively affected by the system's activation. Instead, the acoustic pressure was reduced in the vicinity of the subwoofers. At this point, we have to mention that the results refer to the plane along the z axis with height 120 cm, which coincides with the z coordinate of the center of the subwoofers. Similar results were obtained for heights between 105 cm and 135 cm. As a result, the generated quiet zone is adequate for gentle head movements by passengers of various heights. Moreover, the mixed error algorithm proves to be an effective solution for a 3-input-2-output system, demonstrating a lack of significant impact on performance as a result of the assumptions made during the algorithm analysis.

Experimental Evaluation

The experimental set-up consisted of two Pioneer TS-A250S4 subwoofers, which were utilized to reproduce the low frequencies necessary for the application, and three Shure MX 183 microphones as shown in Figure 2.10. The control algorithm was implemented on a National Instruments CRIO-9030 microcontroller. Moreover, in order to take advantage of the parallel data processing capabilities of the FPGA, specifically the Xilinx Kintex-7, and the Labview® platform was used.

The synthesized acoustic disturbance was generated through the combination of three sinusoidal components at 72 Hz, 96 Hz, and 120 Hz, as well as low-amplitude white noise. The noise source was placed in proximity to the cabin mockup, and a microphone placed 5 cm away from the source captured the reference signal. A total of 16 microphones, arranged in a grid covering an area of 30 cm by 25 cm, were used to measure the acoustic pressure in front of the two seats. Linear interpolation was additionally utilized to estimate the acoustic pressure levels at points between the measurement locations. More details on the measurement microphone setup are given on the Appendix D of this dissertation.

For both seats, the maximum SPL attenuation was achieved 10 cm away from the error microphones, which coincides with the simulation results. It reached 15.5 dB in front of seat A (see Figure 2.11a), and 13 dB in front of seat B (see Figure 2.11b). However, the surface of the zone where this attenuation was maintained differed between the two headrests. At seat A there was a quiet zone, which is 20 cm wider than seat B. Although the highest SPL attenuation is not achieved in a large quiet zone in the case

Figure 2.10: The 3-input-2-output ANC system for two adjacent seats installed in the cabin mockup.

of seat B, the amplitude of the 72 Hz and 96 Hz harmonics is reduced by more than 10 dB for all measurement points (see Table 2.1). However, efficient reduction in some areas is not achieved in the case of the 120 HZ harmonic, resulting in a decline in system's performance around microphone D. Finally, for the four measuring microphones, the average attenuation was greater for the 96 Hz harmonic, reaching 18.25 dB, and smaller for the 120 Hz harmonic, reaching 8.25 dB.

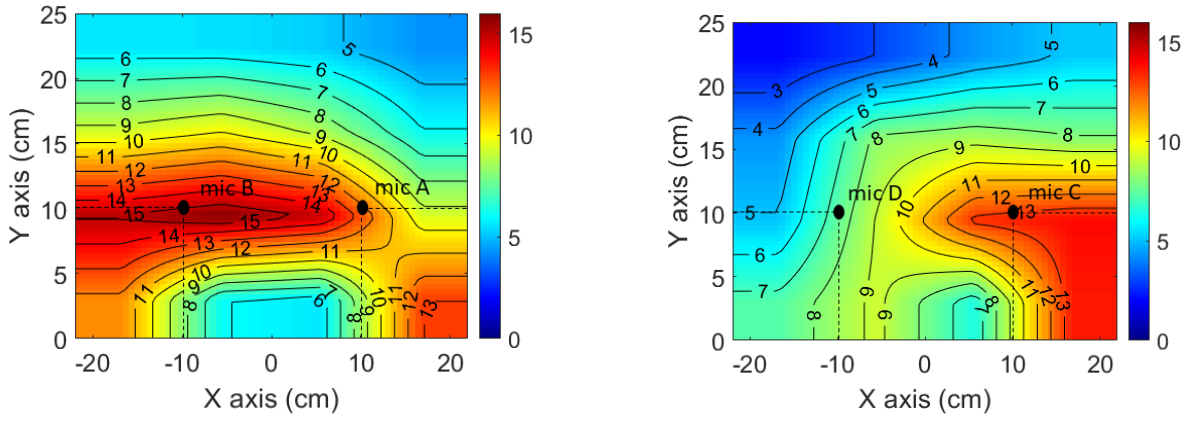

(a) (b)

Figure 2.11: Attenuation of the SPL in front of a) seat A and b) seat B. The error microphones are located at the zero level of the y-axis. Measurement microphones A and C correspond to the passenger's right ear, while microphones B and D to the passenger's left ear.

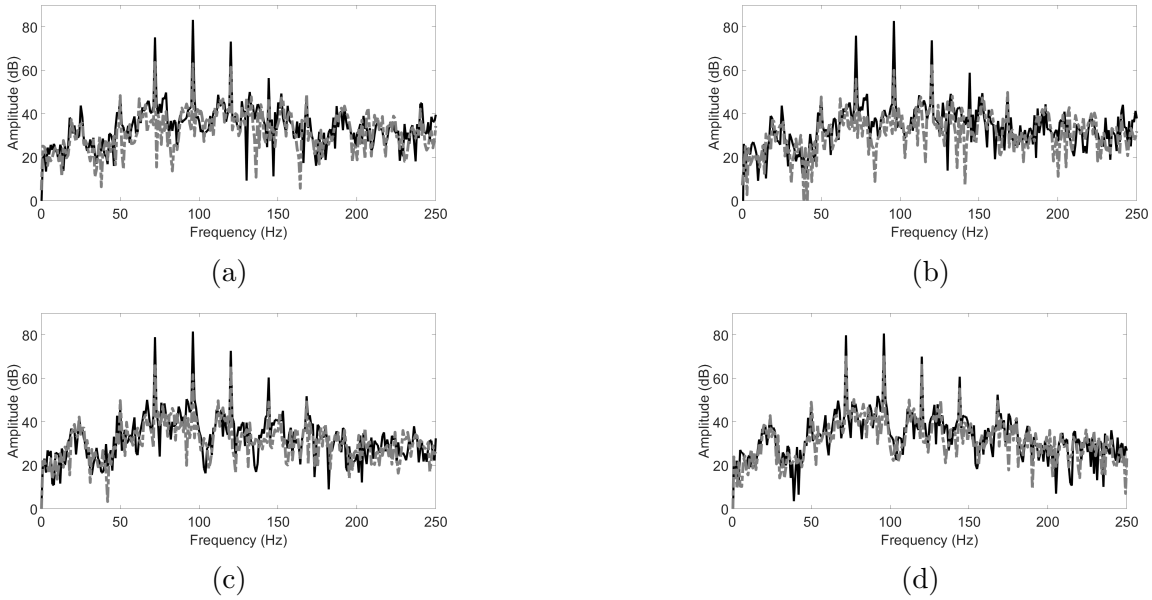

Figure 2.12: Frequency spectrums captured by a) microphone A, b) microphone B, c) microphone C and d) microphone D demonstrated in Figs. 2.11a and 2.11b before (black line) and after (gray dotted line) the ANC activation.

Frequency (Hz)	SPL Attenuation (dB)				
	micA	micB	micC	micD	Average
72	12	20	13	9	13.5
96	20	22	20	11	18.25
120	12	10	7	4	8.25

Table 2.1: Attenuation of three BPF harmonics' amplitudes after the activation of the proposed ANC system.

2.5.3 Computational complexity

The computational complexity of the conventional multichannel FxLMS as well as the mixed-error approach is summarized in the study of Shi et al. [81]. For an ANC setup with 1 reference signal, K loudspeakers and M microphones, the Multiply-Accumulate (MAC) operations for multichannel FxLMS are $(2M+1)KL+M$, where L is the number of taps of both the secondary path and the adaptive filter $\mathbf{w(n)}$. On the other hand, the MAC operations for the mixed-error FxLMS are $3KL+1$. Therefore, in the case of a 2-input-2-output setup, assuming $L = 250$ we have 2502 MAC operations for conventional FxLMS and 1501 MAC operations for the mixed-error approach. When we have a 3-input-2-output, the MAC operations are 3503 and 1501 respectively. We see that the computational complexity of the mixed-error FxLMS remains the same while the number of microphones increases, as there are no convolution operations between the reference signal and the secondary path that corresponds to each error microphone. Thus, the computational advantage of this approach is significant, especially when we implement

large-scale applications.

2.6 Concluding remarks

The application of the mixed-error approach of the multichannel FxLMS algorithm to local ANC applications of low-frequency acoustic disturbances was examined in this Chapter. Compared to the conventional version, this approach offers a significant computational advantage, especially when the number of microphones is increased. The SPL reduction achieved by this method is greater than 10 dB in a range that covers light head movements of the seat occupant. Interestingly, the points where a larger SPL attenuation is observed are identical to those of the conventional algorithm when the acoustic pressures in the error microphones are equal. Otherwise, the maximum SPL attenuation is located in the middle of the microphones. This characteristic can be exploited to design special ANC configurations, such as the 3-inputs and 2-outputs configuration intended for the headrests of adjacent aircraft seats. By adopting this approach, both hardware and computing resources can be utilized more efficiently.

CHAPTER 3

Virtual sensing for local ANC systems

3.1 Introductory notes

The previous chapter discussed the mixed error FxLMS algorithm, which is characterized by low computational complexity, making it well-suited for practical applications. Moreover, this algorithm was applied to local ANC systems achieving comparable performance and stability to conventional FxLMS. As mentioned in the thesis introduction, these systems face a significant issue in that the maximum attenuation of acoustic disturbance occurs around the error microphones. However, in most cases of active headrests, it is challenging to place microphones around the passenger's ears due to spatial constraints. As a result, the quiet zone where the maximum attenuation of sound pressure level occurs is located at distance from the passenger ears. Furthermore, the placement of the physical error microphones near the loudspeaker diaphragm results in the reduction in the size of the generated quiet zone, as it is contingent upon the distance between the error microphone and the diaphragm surface.

In order to address this issue, many systems take advantage of several virtual microphone techniques that have been proposed in recent years. These techniques aim to estimate the acoustic pressure at a remote location, near to he passenger's seat occupant's head, without placing physical microphones. In [37], [86], a Virtual Microphone Technique (VMT) has been used to relocate the quiet zones around the points of interest, while in [87], [88] the Remote Microphone Technique (RMT) in combination with a head tracking system have been developed for the same purpose. Another algorithm called

Virtual Microphone Control (VMC) [6], developed in a multiple input multiple output (MIMO) format, has managed to move the maximum attenuation of the acoustic pressure around the passenger ears. Recently [89] proposed a virtual sensing method that combines Additional Filter and Remote Microphone methods for a headrest application, improving system's performance and robustness.

However, the main disadvantage of the aforementioned techniques lies in the complexity that is introduced during the computation of the antinoise signal, while they also need to compute the additional filters in an additional identification stage. In addition, as it is mentioned in [57], a head tracking system is needed to ensure stability and the 10 dB quiet zone is obtained for acoustic disturbances with relatively small bandwidth (100 Hz) and big filter lengths. Other approaches that also use head tracking systems for the relocation of the quiet zone have been proposed in [7], [32]. Finally, in [90] the error microphones are mounted on a hat, that is applied on people's head. However, this approach could be inconvenient for some applications (e.g. seats in vehicles).

Another approach to virtual sensing methods is to extrapolate the acoustic pressure using a polynomial [56], [58], [91]. The simplest version is linear extrapolation, which uses a straight line in order to approximate the acoustic pressure at a short distance from the physical microphones [92]. Usually two or more physical microphones are used in order to approximate the virtual acoustic pressure. Finally, another method uses both the pressure and the velocity of the air molecules to make a better estimate of the sound wave at the remote location and improve the performance of the ANC [93]. Certainly, the method of simple linear extrapolation has been demonstrated to be the most computationally effective in reducing low frequency acoustic disturbances, as it requires minimal calculations and delivers superior results in terms of noise reduction and the size of the quiet band. Thus, the subsequent paragraphs details a system that integrates mixed error FxLMS with linear extrapolation and present simulation results, as well as the experimental evaluation.

3.2 VEM-FxLMS method

This section discusses an innovative method for active headrest applications combining mixed error FxLMS with linear extrapolation. This method (VEM-FxLMS) was originally proposed in [23] and was used for the attenuation of the acoustic disturbance produced by the electric generators of luxury yacht, both in the cabins and on the deck.

For a system with two virtual microphones (Figure 3.1), the estimated acoustic pressures can be approximated by the first-order finite difference estimate (Eq. 3.1), assuming that the wavelength is much larger than the distance between the physical microphones:

$$e_{vk}(n) = \frac{e_{pk2}(n) - e_{pk1}(n)}{a} x + e_{pk2}(n), \quad \text{for k=1,2} \tag{3.1}$$

where e_{vk} is the estimated virtual acoustic pressure at the point of interest, $e_{pk1,2}$ are the signals captured by the physical microphones, a is the distance between the physical microphones and x is the distance between the farthest physical microphones and the point where the virtual acoustic pressure is estimated.

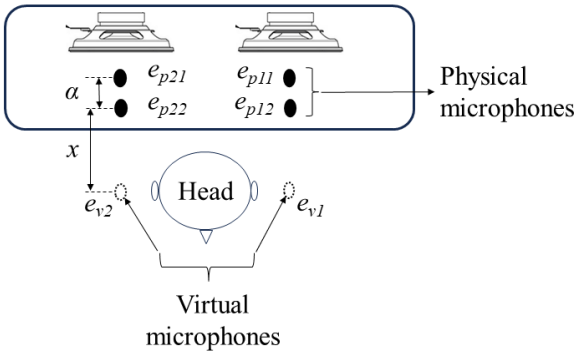

Figure 3.1: Top view of active headrest consisting of 2 loudspeakers and 4 physical microphones, which are use for the estimation of the acoustic pressure at two virtual locations.

Then the virtual mixed error derives as the sum of the virtual errors:

$$\begin{gathered} e_{v,mix}(n) = \sum_{k=1}^{2} e_{vk}(n) = \\ \frac{e_{p12}(n) + e_{p22}(n) - e_{p11}(n) - e_{p21}(n)}{a} x + e_{p12}(n) + e_{p22}(n) = \\ \frac{e_{p2,mix}(n) - e_{p1,mix}(n)}{a} x + e_{p2,mix}(n) \end{gathered} \tag{3.2}$$

In order to derive the update equation for the adaptive filter coefficients, we need to estimate the virtual mixed secondary path, which corresponds to the virtual locations. However, this is not straightforward as there are no physical microphones at these locations. As demonstrated in the publication in [23], the virtual mixed secondary path can be approximated from the mixed secondary path that corresponds to $e_{p2,mix}(n)$, using the procedure described in Section 2.5. Practically, we assume that the acoustic path between the farthest physical microphones and the points of NC (virtual microphones) can be ignored during the secondary path modeling, without significant deterioration in system performance and stability. This assumption is only valid for acoustic disturbances with high power spectral density at lower frequencies and low spatial change of acoustic pressure due to long wavelengths. In addition, the physical microphones of each pair must be close to one another ($a \leq 5cm$) and the extrapolation distance relative small ($x \leq 30cm$). As a result, the formula for the computation of the filter weights is demonstrated in Eq. 3.3, which is practically Eq. 2.28 incorporating linear extrapolation:

$$\mathbf{w}_k(n+1) = \mathbf{w}_k(n) - \mu \mathbf{x'}_{k,mix}(n) e_{v,mix}(n), \quad k = 1, 2, ..., K. \tag{3.3}$$

where μ represents the step size of the algorithm, $e_{v,mix}(n)$ is the virtual mixed error defined in (Eq. 3.2) and $x'_{k,mix}$ is the reference vector filtered by the virtual mixed secondary path that correspond to k^{th} secondary source with respect to mixed error signal $e_{p12}(n) + e_{p22}(n)$. Therefore, the antinoise signal is given by Eq. 2.22, as in the simple mixed-error FxLMS.

3.3 Computer simulation analysis

During the computer simulation analysis of the VEM-FxLMS, two ANC architectures were employed. The first utilized one loudspeaker and four physical microphones (4-input-1-output), while the second used two loudspeakers and four physical microphones (4-input-2-output). Furthermore, the k-Wave MATLAB toolbox [94] was used to simulate the sound pressure in a free field. The acoustic modelling is based on the solution of three coupled first-order partial differential equations, which are equivalent to a generalized form of the Westervelt equation. The equations are solved using a k-space pseudo-spectral method where spatial gradients are calculated using a Fourier collocation scheme, and temporal gradients are calculated using a k-space corrected finite-difference scheme. More details on this method and Matlab toolbox are given in Appendix A.1.

A narrowband synthesized signal characterized by harmonic tones at $f_1 = 55Hz$ and $f_2 = 110Hz$ was generated by the primary source. The SPL in front of the loudspeakers reached 85 dB when the ANC system was disabled. The primary acoustic pressure field was assumed to be uniform in the x-y plane. Note that changing the directions of the incident plane wave has a small effect at the low frequencies of interest. The simulations were performed in two-dimensions using a grid point spacing in the x and y directions $dx = dy = 0.01m$, a grid size of $(N_x = 300) \times (N_y = 300)$ grid points or $3m \times 3m$, a time step of $dt = 8.596e^{-6}sec$, a total simulation time of $T = 2sec$, medium density $p_0 = 1.2Kg/m^3$, and sound speed $c_0 = 349m/sec$.

The microphones were assumed as one grid point sensors, while the loudspeakers were configured as arcs. The reference sensor was located close to the noise source. The diameter of the subwoofer was $D_w = 0.26m$ (Figure 3.2), while the diameter of the medium-sized loudspeakers was $D_s = 0.125m$ (Figure 3.3). Moreover, the coordinates of the mid-point of the loudspeaker/s were defined as $(N_x/10 + 32, N_y/4 + 32)$. The spacing between the error sensors at a microphone array was $h = 0.04m$ (Figure 3.3b). Similarly, the distance between the loudspeaker/s edge and the microphone array in the x direction was $r = 0.04m$ in the case of 4-input-1-output configuration and $r = 0.06m$ in case of 4-input-2-output configuration (Figure 3.3b), respectively. The noise source was located at $(N_x/2, N_y/10)$ and it was expressed as one grid point source. The ears (basic points of interest) were placed 0.1 m away from the control box edge, while the desired quiet zone (DQZ) was located 0.05 m away from the audio box edge. As presented in Figure 3.3, the

DQZ was assumed to be an area of $0.6 \times 0.15m^2$.

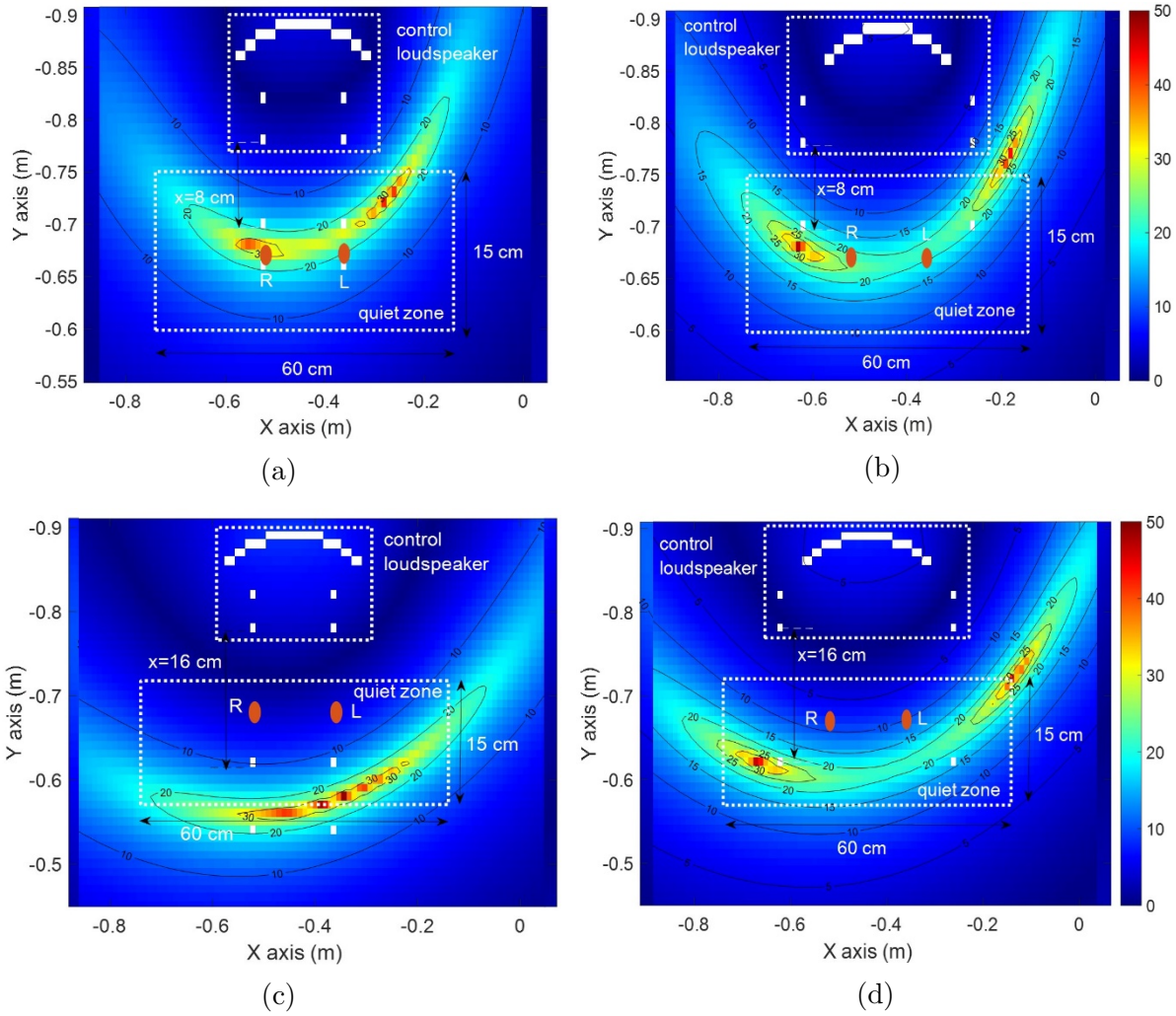

Figure 3.2: Total SPL reduction in the presence of a simulated primary noise generated by k-wave Matlab toolkit applying the proposed ANC scheme for different values of x: (a), (b) x=8cm (c), (d) x=16 cm and for different distances between the two pairs of error sensors (a), (c) 16 cm and (b), (d) 36 cm. The brown ellipse represents the basic locations of the right (R) ear and left (L) ears.

The ANC system was modelled by incorporating the extrapolation-based virtual sensing technique discussed in Section 3.2 into the acoustic modelling. To test the validity of the method, the noise reduction performance was measured under both system configurations. For comparison, the conventional single channel FxLMS was also applied as control algorithm. For modeling purposes, the filter length was chosen equal to be $L = 100$ taps and the step size was set as $\mu = 3e^{-10}$. The preliminary step was to model the mixed secondary path with respect to mixed error signal $e_{p12}(n) + e_{p22}(n)$, for each loudspeaker, using Gaussian white noise as it has been described in Section 2.4. Then the VEM-FxLMS algorithm was tested for the two setups.

The simulation results demonstrated that a significant noise attenuation up to 30 dB is

achieved throughout an area far from the physical error microphone location that depends on the parameter x which is the distance of the virtual microphone from the farthest physical microphone. At this point, we must note that the conventional FxLMS achieves a similar noise attenuation at an area close to the physical error microphone location when it is used both with 4-input-1-output and 4-input-2-output scheme. However, the noise attenuation does not reach the passenger ears and therefore the produced quiet zone is not located at the desired place.

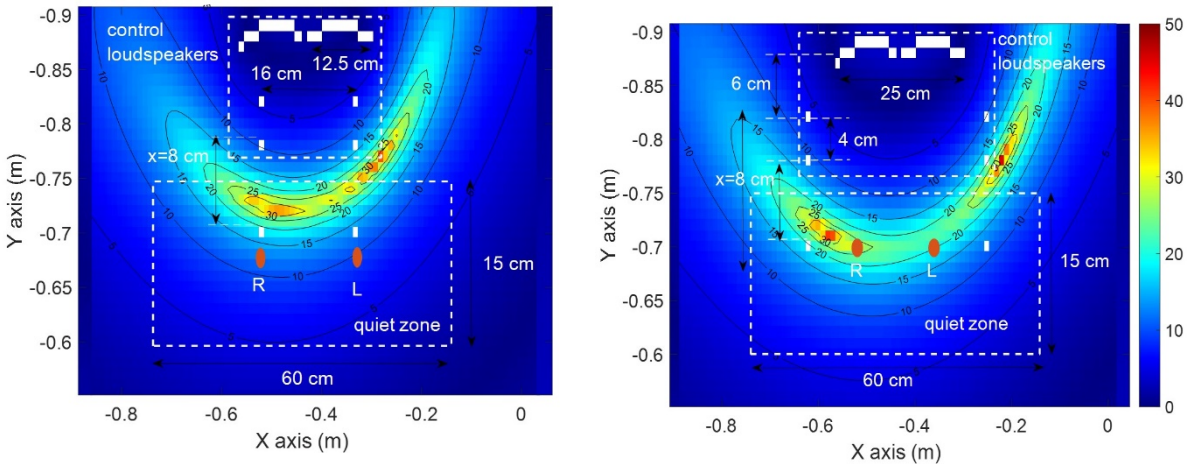

Figure 3.3: Total SPL reduction in the presence of a simulated primary noise generated by k-wave Matlab toolkit applying the proposed ANC scheme using two loudspeakers for x=8 cm, for distance between the two pairs of error sensors (a) 16 cm and (b) 36 cm. The brown ellipse represents the basic locations of the right (R) ear and left (L) ear.

Consequently, the influence of the ANC configuration as well as the topology of the physical error sensors on the control performance of the VEM-FxLMS to the DQZ and the 10dB-quiet zone (QZ10) were investigated. The results of the 4-input-1-output system simulation setup are illustrated in Figure 3.2. The virtual sensors can be virtually placed anywhere in the DQZ. Hence, the variable x of the extrapolation technique is set to $8cm$ in order to relocate the quiet zone close to the ears. This means that the virtual sensors are placed at $x = 0.08m$ away from the audio box. In order to investigate the effect of the physical sensors topology located in front of the control source, the space between the error microphone arrays is chosen to be (a) smaller (Figs. 3.2a, 3.2c) and (b) larger (Figs. 3.2b, 3.2d) than the diameter D_w of the subwoofer. It is observed in Figs. 3.2a and 3.2b, where parameter x has been chosen to be $8cm$, that any noise attenuation at the ears is now much higher than at the error microphones. The noise attenuation reaches up to 30 dB directly to the ears. As demonstrated in Figs. 3.2a and 3.2b, the 4-input-1-output setup can ensure comfort to the passenger for head movements inside the DQZ, while the QZ10 is extended when the space between the microphone arrays is larger than the diameter D_w of the subwoofer. Moreover, the passenger can experience reasonable

noise suppression for lateral head movements outside the DQZ. But, the noise attenuation outside the DQZ drops faster until reaching the 5 dB zone that extends over all practical forward head movements. Note that the non-symmetry of the produced silence zone is due to the location of the primary source.

3.4 Experimental evaluation

Subsequently, the ANC system configurations described in the previous paragraph (Figure 3.4) were experimentally evaluated in the Dynamics and Acoustics Laboratory for synthesized acoustic disturbances that simulated the ones encountered in real-world conditions.

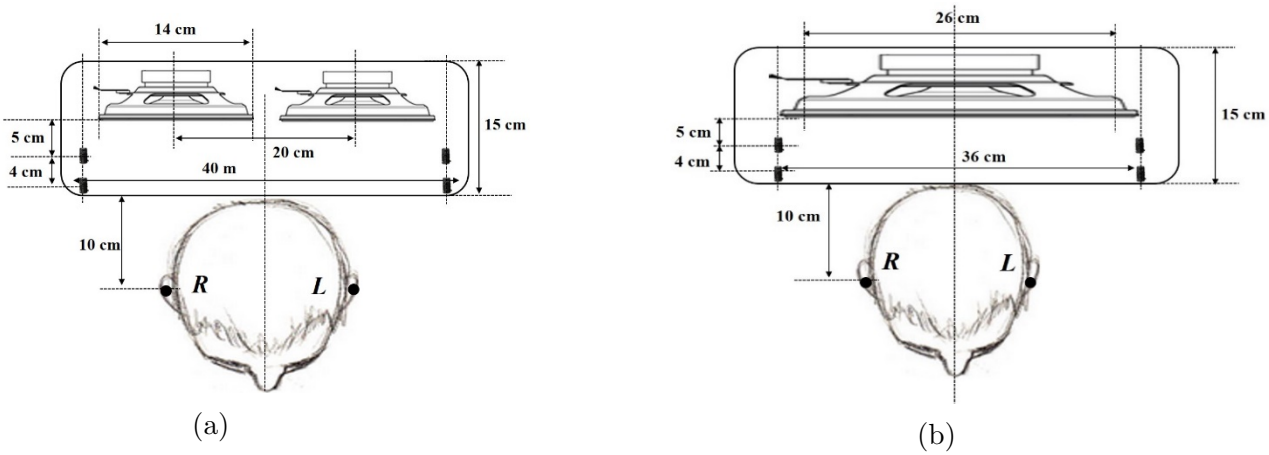

Figure 3.4: Headrest configuration for (a) 4 input-2 output and (b) 4 input-1 output ANC scheme.

The experiments were taken place either in the cabin mockup or freely in the laboratory's room. The 4 input-2 output system consisted of 4 Shure® MX-183 microphones and two Visaton® FR 6.5" loudspeakers. Furthermore, a handmade, lightweight amplifier was employed to amplify their signal. On the other hand, in the 4 input-1 output system, the two loudspeakers were substituted by an Omnitronix® BX 1250 subwoofer. The primary noise signal was generated using Labview®, and it was reproduced through the sound card of a desktop computer and a subwoofer. A Behringer® KM750 amplifier was also used to amplify the primary noise signal. The selection of the woofer was made because a low frequency acoustic disturbance, captured in the cabin of a yacht was used for the evaluation of the 4-input-1-output system setup. It consisted of a 55 Hz harmonic, which was the most prevalent one measured onboard when the electric generators were in operation. The SPL distribution on a horizontal and flat testing area was determined by placing observation microphones on a wooden grille and calculating the results. In order to create a three-dimensional measurement grid, the grille was raised vertically, resulting in five flat planes with a separation distance of 5 centimeters between them. It is impor-

tant to note that plane C intersects with the center of the control loudspeakers, which is at a level that corresponds to a passenger ear. The distance between the center of the cone and the floor was 1.20 meters.

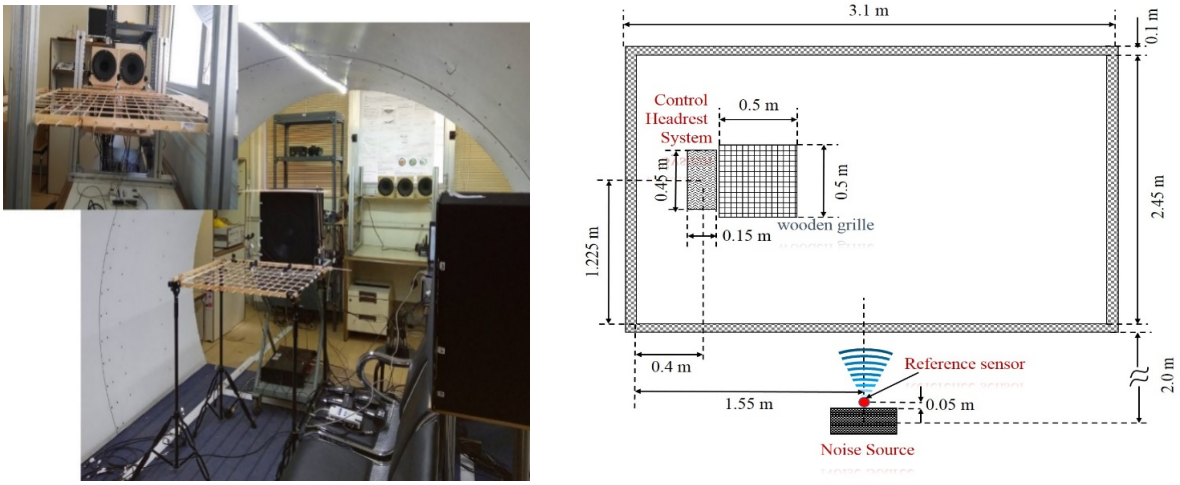

(a) (b)

Figure 3.5: (a) The hardware configuration of the 4-input-2-output (upper left) and the 4-input-1-output ANC systems. (b) A 2D sketch of the experimental setup for the 4-input-1-output system evaluation.

3.4.1 4-input-2-output system

In the case of the 4-input-2-output system, the acoustic disturbance was a multi-tonal synthetic signal contaminated by a 30 dB white noise. When the ANC was disabled, the SPL ranged from 80 to 85 dB at each of the five measurement planes. The noise attenuation was determined by measuring the difference in SPL when the ANC system was turned on and off. After applying the extrapolation-based virtual sensing technique, the ANC was activated to relocate the $QZ_1 0$ close to the ears. The SPL attenuation for five measurement planes, using the proposed scheme for $x = 32cm$, are illustrated in Figure 3.6.

It can be observed that the SPL reduction varies from 17 to 24 dB directly at the ears at planes B, C, D, and E, while it is approximately 9 dB at plane A. The QZ_{10} not only encompassed the entire DQZ, but it has also been significantly expanded beyond the DQZ. The SPL reduction ranged from 10 to 24 dB for a distance of approximately 20 cm beyond the DQZ at planes B, C, and D. The analysis in Figure 3.6 indicates that the 4-input-2-output system allows head movements within an area of volume $SV_{32} = 0.4{\times}0.3^{+}{\times}0.15^{++}$. The symbol + denotes a larger dimension in certain areas of the DQZ. The outcomes of this real-time experiment were intriguing because the VEM-FxLMS system was not expected to extend the QZ_{10}, but only to relocate it, as discussed in Section 3.3.

When the parameter x was selected to be $8cm$, the passenger can experience acceptable noise reduction within the DQZ in every fixed flat plane. The noise attenuation varies from 8 to 15 dB directly at the ears at the standard/initial locations. The QZ_{10} covers nearly the entire DQZ at planes A, B, and C. However, the proposed ANC system for a distance of $x = 8cm$ exhibits poor noise reduction at plane E. Furthermore, the noise attenuation for a distance of $x = 5cm$ outside the DQZ drops to 5 dB. The proposed system for $x = 8cm$ enables head movement within a silence volume of $SV_8 = 0.4{\times}0.15{\times}0.15m^3 (= W{\times}L{\times}H)$, creating a quiet environment for the passenger.

Moreover, when x was selected to be $16cm$, it is noted that the QZ_{10} not only encompassed the entire DQZ but also expanded considerably beyond. Consequently, for forward head movements, the noise attenuation varies from 10 to 21 dB for a distance of at least 10 centimeters beyond the DQZ at planes A, B, C, and D. The noise reduction is approximately 20 dB directly at the ears at planes B, C, and D, and around 12 dB at planes A and E. Additionally, the 4-input-2-output system for an extrapolation distance of 16 centimeters allows for head movement within a silence volume of $SV_{16} = 0.4 \times 0.25 \times 0.15m^3$. In conclusion, as the parameter x increases, we observe an enlargement of the quiet zone, so that when it becomes $32cm$ we obtain the largest QZ_{10} and an adequate SPL attenuation at passenger ears.

3.4.2 4-input-1-output system

The 4-input-1-output system was experimentally evaluated in the wooden cabin mockup ('cabin setup'), installed in the Dynamics and Acoustics Laboratory, in order to simulate the acoustic environment of a small enclosure as well as outside of it ('deck setup'). More details on the construction and the acoustic characteristics of this cabin are given in Appendix B of this dissertation. Furthermore, the acoustic disturbance was selected to be a signal captured in a cabin of a luxury yacht, while the electric generators were working. Then the measured signal was reproduced in the laboratory, following the procedure described in Section 3.4.1. Therefore, the acoustic disturbance consisted of 55 Hz harmonic as well as broadband noise.

When the 'cabin setup' was implemented, the obtained SPL distribution of the 3D measurement grid when the proposed ANC system was off varied from 73 to 77 dBA. The A-weighted sound pressure level was about 73 dBA directly at the ears, at the standard position at all the planes. Initially, the conventional single channel FxLMS was performed. However, the desired noise attenuation didn't reach to the ears, as it was limited around the error microphone positions. Thus, the overall attenuation results obtained from the classic FxLMS algorithm were poor. The SPL attenuation did not exceed 3 dBA in the areas of interest, around the passenger ears. Then, the proposed 4-input-1-output VEM-FxLMS algorithm was applied for an extrapolation distance of $x = 8cm$. The results

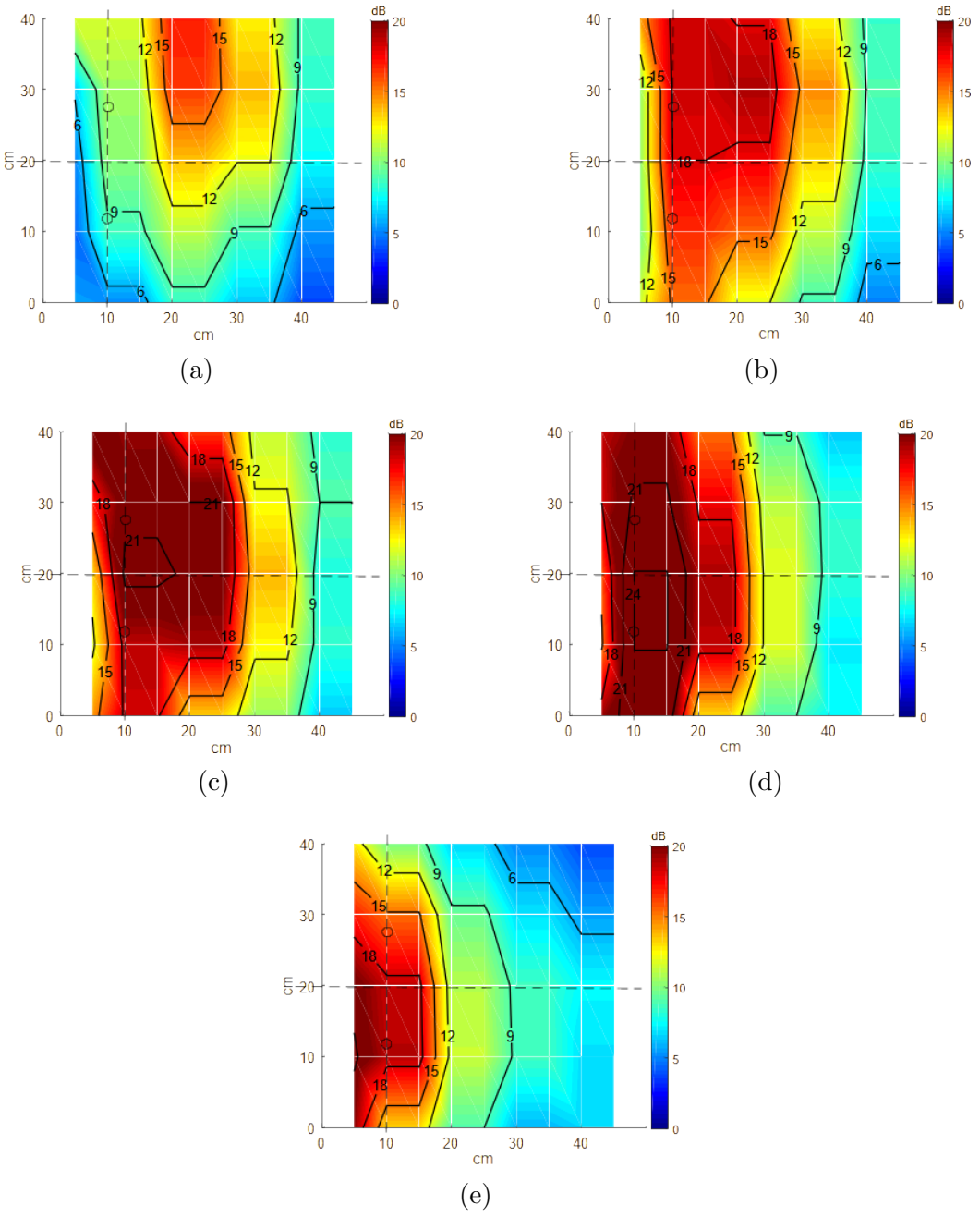

Figure 3.6: Total SPL attenuation at five different horizontal planes when the proposed 4-input-2-output scheme was applied with $x = 32cm$: (a) A plane, (b) B plane, (c) C plane, (d) D plane and (e) E plane.

are presented in Figure 3.7. The SPL attenuation varied from 8 to 12 dBA directly at the ears at the standard locations at the planes A, B and C. In addition, the control performance was poor at the plane E. In case of forward head movements, the noise attenuation varied from 9 to 12 dBA for a distance up to 10 cm far from the standard ear locations throughout the planes A and B. Thus, based on the analysis in Figure 3.7, for the value of parameter x being 8 cm the proposed system allowed a head movement in a silence volume that equals to $SV_8 = 0.40 \times 0.15 \times 0.10^{+}m^3$.

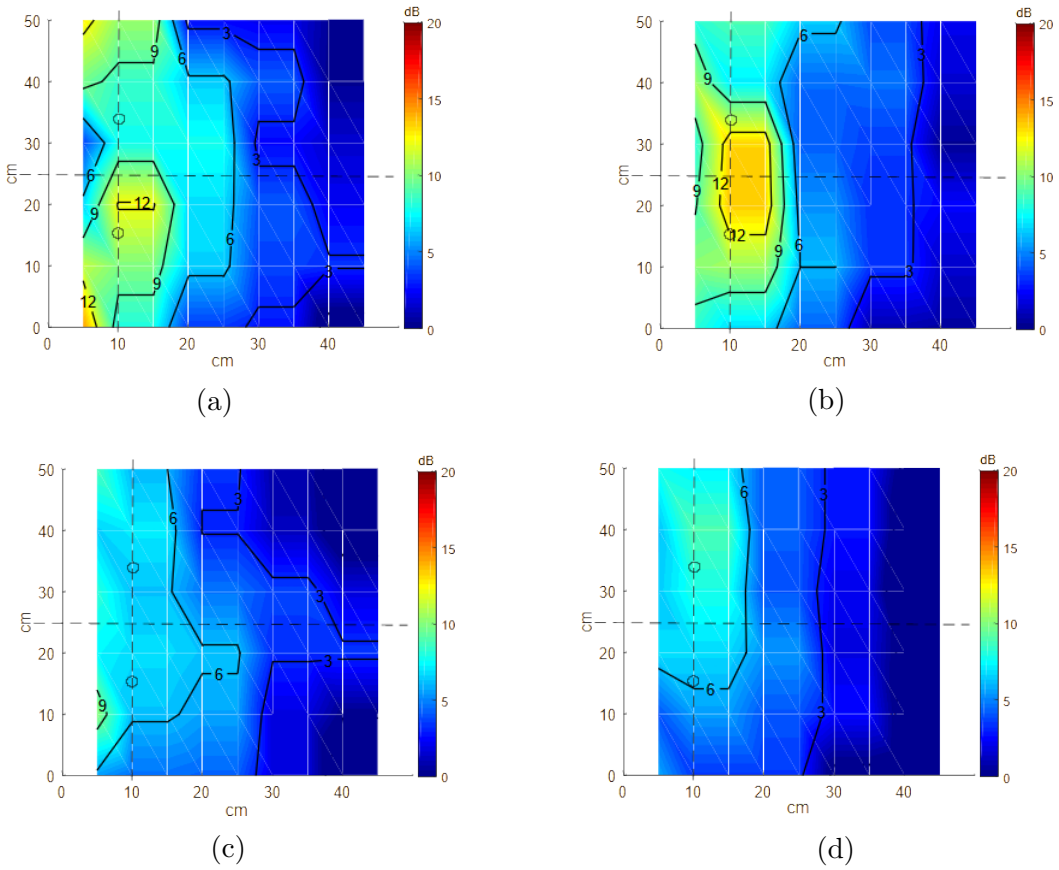

Figure 3.7: Total SPL attenuation profile at different horizontal contours in the case of 'cabin setup' applying the proposed ANC scheme: (a) A plane, (b) B plane, (c) C plane and (d) D plane. The 'o' indicates the basic location of the ears

Finally, in this stage of the experimental evaluation, the 4-input-1-output system was placed in the laboratory's room far from the walls, in order to simulate a more open space without many reflections. Therefore, this configuration will be referred to as 'deck setup'. Again, the proposed technique was performed for a distance $x = 8cm$. When the ANC system was off, the SPL distribution at all the planes varied from 70 to 75 dBA. Initially, the conventional FxLMS was applied. It should be noted that the results are close to those obtained in the test with the 'cabin setup'. The SPL reduction did not exceed 3 dBA in the areas of interest at all the planes. At the same time, in contrast to the conventional FxLMS, the proposed VEM-FxLMS achieved to expand the QZ10 to the DQZ and provide significant noise attenuation. As illustrated in Figure 3.8, the noise reduction varied from 9 to 15 dBA directly at the ears at the standard locations at all the planes. In case of forward head movements, the noise attenuation varied from 9 to 15 dBA for a distance up to 15 cm beyond the standard ear locations in the planes B, C and D. Hence, based on the analysis in Figure 3.8, the proposed methodology allows a head movement in a silence volume $SV_8 = 0.40 \times 0.20 \times 0.15^{+}m^3$.

Moreover, Figure 3.9 illustrates the comparison of the frequency spectrums at the

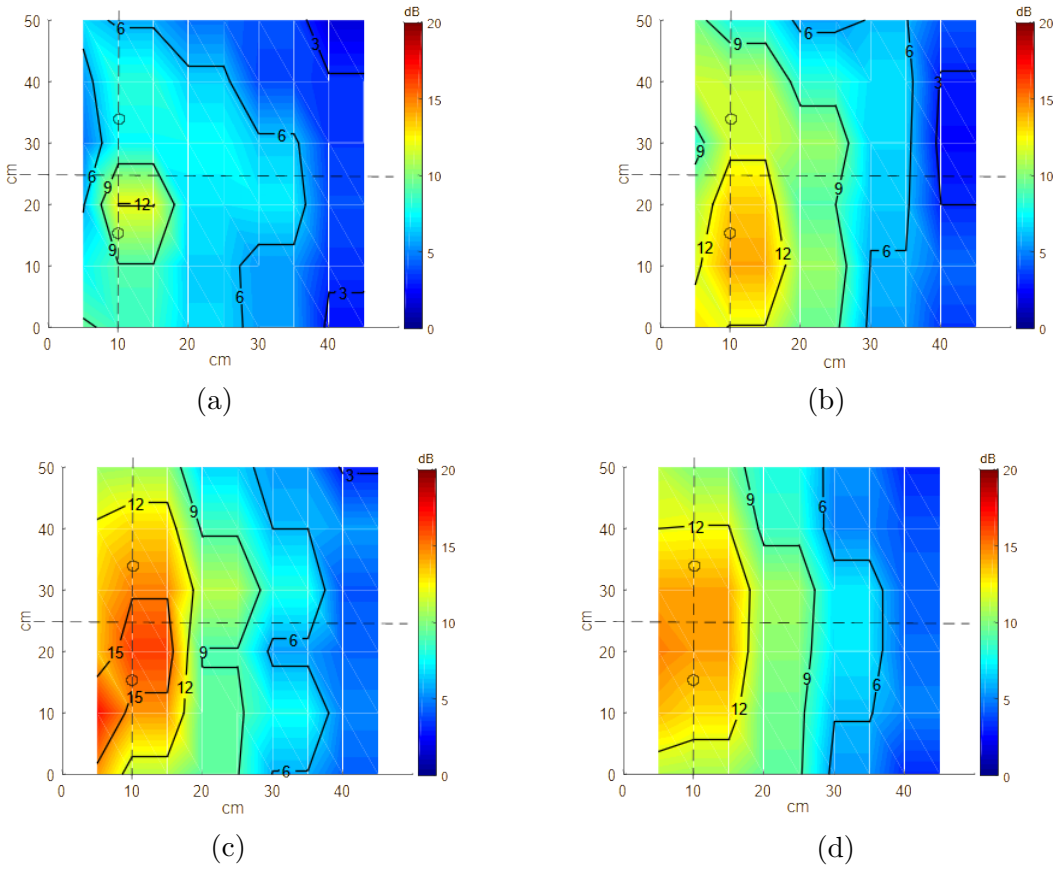

Figure 3.8: Total SPL attenuation profile at different horizontal contours in the case of 'deck setup' applying the proposed ANC scheme: (a) A plane, (b) B plane, (c) C plane and (d) D plane. The 'o' indicates the basic location of the ears

locations of passenger ears for the 'deck setup', when the ANC was enabled and disabled. We observe that the attenuation of 55 Hz harmonic was 10.89 and 10. 94 dBA at right and left ears respectively, which is due to the relocation of the quiet zone achieved by the acoustic pressure prediction technique, based on linear extrapolation. In addition, smaller but significant amplitude attenuation was observed for other harmonics like the one at 164 Hz. The achievement of greater than 10 dBA attenuation is of paramount importance, as it corresponds to a level of reduction that is discernible to the human ear and can have a substantial impact on the acoustic comfort of passengers in settings, such as yachts.

3.5 Yacht application

The 4-input-1-output system was installed on the deck of a yacht, as illustrated in Figure 3.10a, in order to mitigate the acoustic disturbance produced by one of the electric generators. The control algorithm was feedforward VEM-FxLMS using an Omnitronix® BX 1250 subwoofer as secondary source and four 4 Shure® MX-183 microphones, arranged in

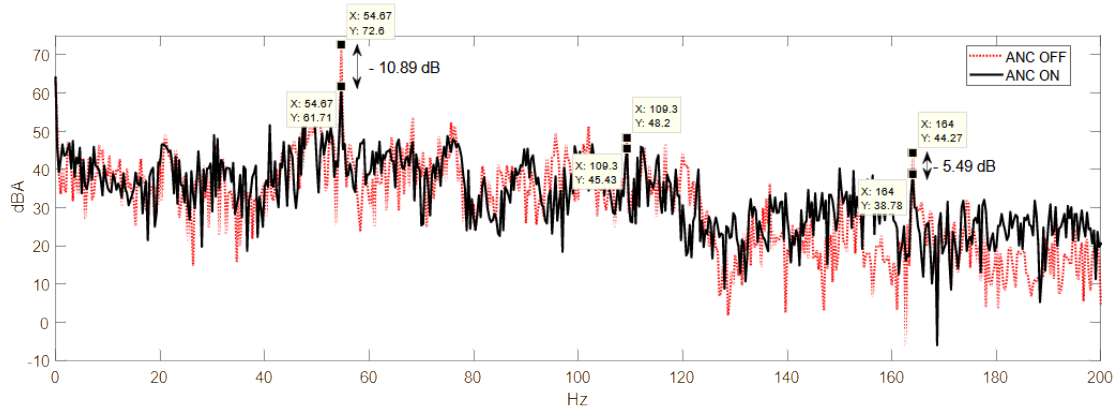

(a)

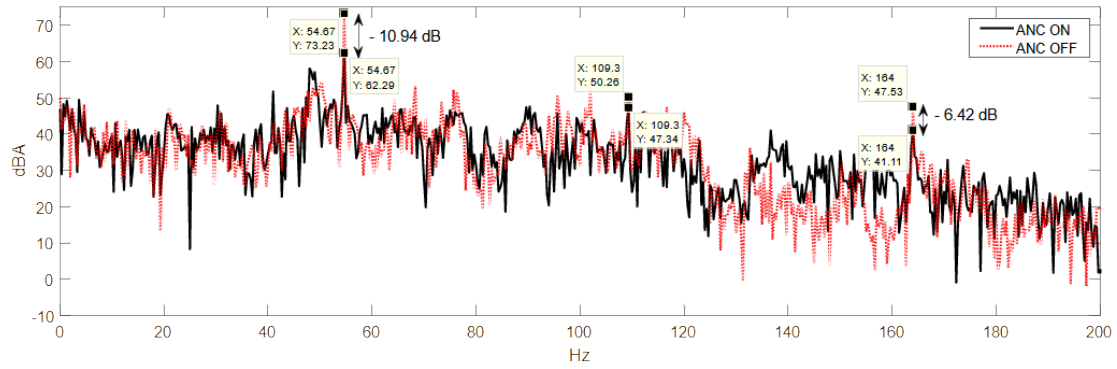

(b)

Figure 3.9: Spectrums of monitoring signal measured in B plane close to a) the right ear and b) the left ear while the ANC system using the proposed methodology is disabled (red dot line) and enabled (black line).

pairs in order to implement the forward difference prediction technique. Additionally, the reference microphone was strategically positioned in the engine room, between the two electric generators (Figure 3.10b), to ensure a strong correlation between the reference signal and the noise source. The engine room was located below the deck, which could potentially create a causality constraint issue for the FxLMS algorithm. Nevertheless, the algorithm's implementation was designed to be efficient enough to prevent any such issues from arising.

To assess the system's performance with respect to both SPL attenuation and the size of the quiet zone, measurements were taken at 84 points in front of the secondary source, with the data collected both when the ANC was activated and when it was deactivated. The measurement points were organized into three height levels that corresponded to the middle of the subwoofer, the bottom, and the top. Each height level comprised 28 measurement points arranged in four rows, with seven points in each row. The distance between points in the same row was 10 cm, and the distance between rows was 15 cm. As a result, the measurement volume had dimensions of $60cm \times 45cm \times 40cm$.

The measurement microphone, situated in front of the woofer's diaphragm and 0 cm

(a) (b)

Figure 3.10: a) The active headrest system implemented on the yachts deck, b) the engine room, with two electric generators (ONAN 17 KW), where the reference microphone was placed.

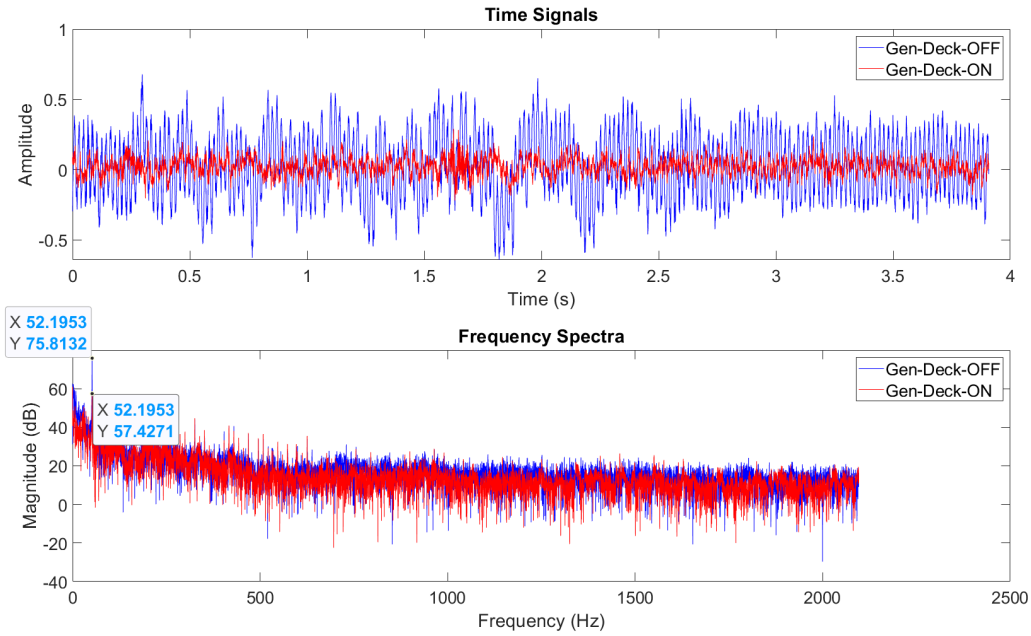

Figure 3.11: Time domain signals and frequency spectrums when the VEM-FxLMS based ANC operated on the deck of a yacht in real-world conditions. The distance between the error and the measurement microphone along the z-axis was 0 cm.

away from the error microphones, recorded both the time signal and frequency spectrum when the ANC was activated and deactivated. These results are depicted in Figure 3.11. Our analysis indicates that the attenuation of the 52 Hz harmonic magnitude reached 18 dB. Furthermore, we observe increased attenuation of the low-frequency broadband components of the acoustic disturbance. When the distance from the error microphone was 15 cm, the magnitude attenuation reached its maximum value, which was 25 dB

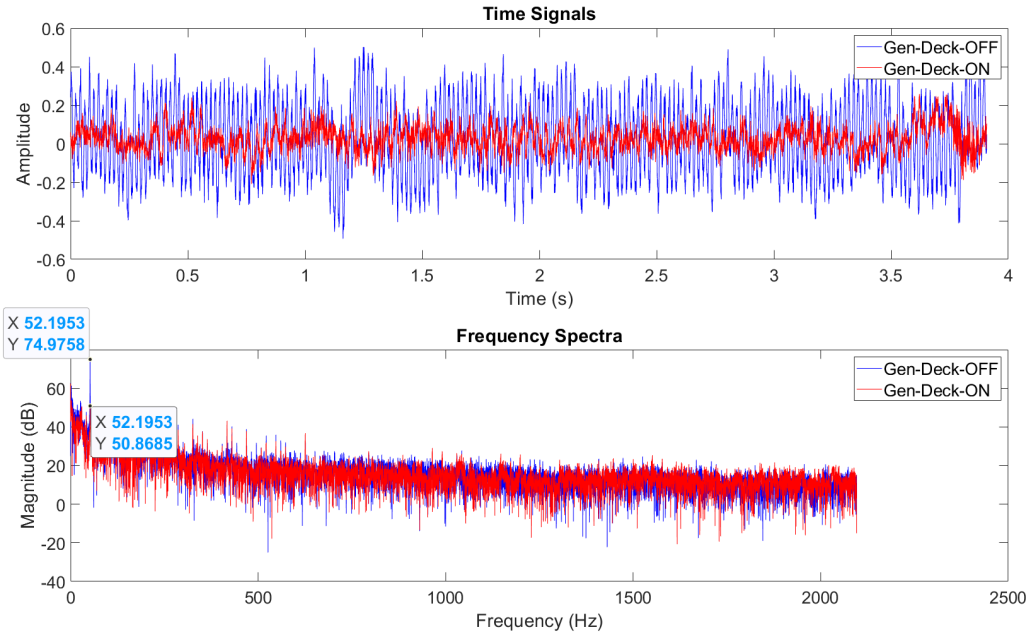

Figure 3.12: Time domain signals and frequency spectrums when the VEM-FxLMS based ANC operated on the deck of a yacht in real-world conditions. The distance between the error and the measurement microphone along the z-axis was 15 cm.

(Figure 3.12). This is related to the parameter x of Eq. 3.3 representing the first-order finite difference estimation of acoustic pressure, which was set at 15 cm.

When the distance from the error microphone became 30 cm the magnitude attenuation reached 15 dB and finally at 45 cm the magnitude attenuation reduced to 10 dB. As a result the 10 dB quiet zone, when employing the VEM-FxLMS algorithm, extended from the positions of the error microphones up to 45 cm far from them. In addition, similar measurements were recorded for the measurement planes up and down from the medium plane, resulting at a 10 dB quiet zone of 40 cm at the y-axis. Furthermore, the woofer's diaphragm diameter was 30cm, and the SPL attenuation along the diaphragm was similar to the measurements done for the central microphone. In addition, the 10 dB SPL attenuation was attained 10 cm left and right from the diaphragm's end. As a result, we observe an $40cm \times 40cm \times 45cm$ area of more than 10 dB magnitude attenuation, which shows the ability of VEM-FxLMS to relocate and expand the quiet zone due to the linear prediction technique of the acoustic pressure.

3.6 Concluding remarks

The main objective of this chapter was to introduce a new algorithm, VEM-FxLMS, which integrates the mixed-error method discussed in Chapter 2 with linear extrapolation of the acoustic pressure to relocate the quiet zone. The algorithm was evaluated through both computer simulations and experimental tests, which showed that the SPL reduction

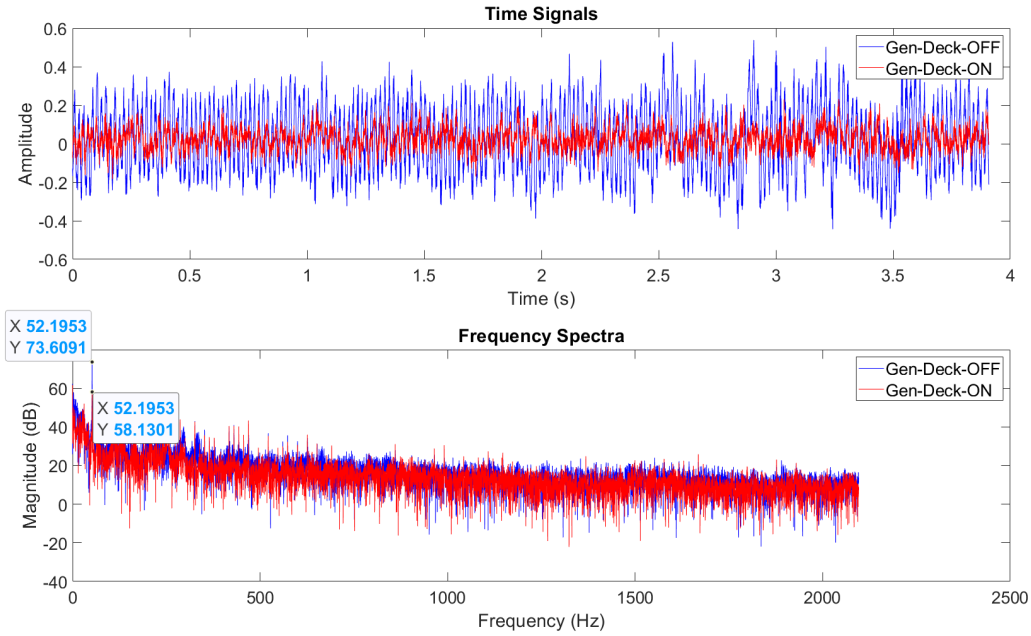

Figure 3.13: Time domain signals and frequency spectrums when the VEM-FxLMS based ANC operated on the deck of a yacht in real-world conditions. The distance between the error and the measurement microphone along the z-axis was 30 cm.

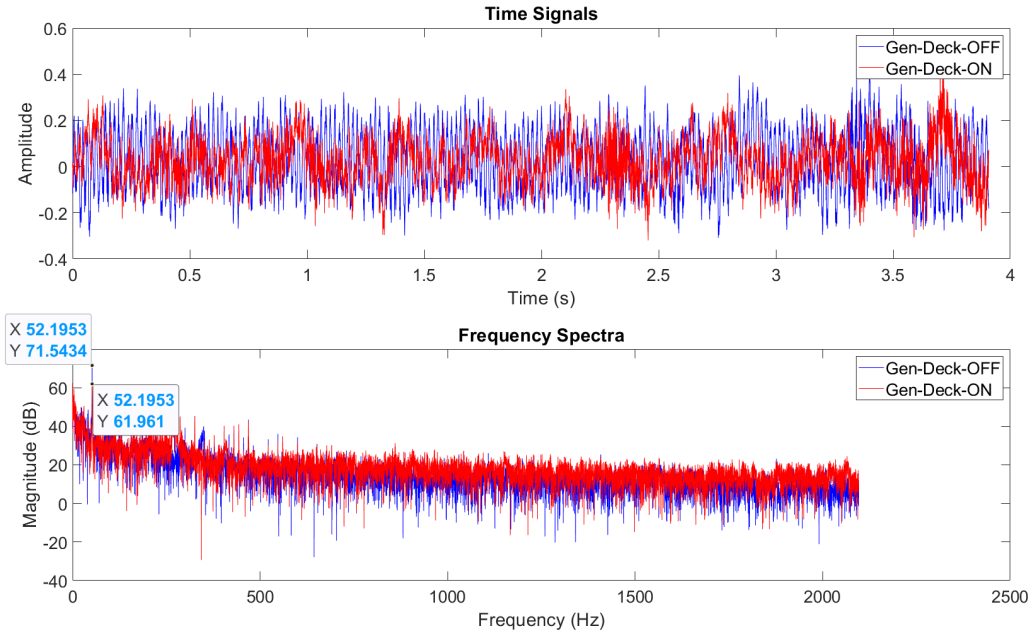

Figure 3.14: Time domain signals and frequency spectrums when the VEM-FxLMS based ANC operated on the deck of a yacht in real-world conditions. The distance between the error and the measurement microphone along the z-axis was 45 cm.

is contingent on the distance between the second error microphone of each pair and the desired noise cancellation location, as determined by the parameter x. The system's effectiveness was maintained in both small enclosures and larger rooms, and it achieved

an additional SPL reduction of more than 10 dB with both a 4-input-2-output and a 4-input-1-output setup. This reduction is significant because it is an acoustic pressure difference that is easily perceptible to the human ear. The 4-input-1-output system, which performed slightly better in laboratory tests, was installed on the open deck of a yacht and successfully reduced the amplitude of the 52 Hz harmonic generated by the yacht's diesel generators by 25 dB at the positions where the ears were thought to be located. This demonstrates that the proposed system is effective in both laboratory and real-world conditions, and the results are particularly noteworthy since they indicate that the system can perform well in both environments.

CHAPTER 4

FLNN based non-linear ANC

4.1 Introductory notes

In the previous chapters, linear algorithms for ANC systems were discussed, and particular attention was given to reducing computational complexity and creating and relocating the areas where acoustic pressure reduction is achieved to a satisfactory extent. However, algorithms based on FxLMS are inherently linear and usually have reduced performance when used to model electroacoustic systems where strong nonlinearities are present [95] or when solving tasks which involve the prediction of time series that are a mixture of harmonic and chaotic elements. The non-linearities in ANC systems can arise from the sensors, actuators, or amplifiers employed in the system, usually in the secondary path. The presence of high amplitude levels in the primary noise may cause saturation in low-power devices like the reference and error microphones. The effect of non-linearities due to the components in the secondary paths on the FxLMS algorithm has been studied in [96], which shows that the presence of even a small non-linearity may affect the noise mitigation capacity [97].

Another issue that can degrade the performance of the ANC is the non-minimum phase behavior of secondary paths. In this situation, the system's response moves to a different direction than the system's input, causing difficulty in modeling by linear algorithms. A typical example of a system with non-minimum phase is the aircraft pitching-up action, which is used to increase the altitude. Systems with similar behavior can be usually met in electroacoustic systems. Furthermore, it has been reported that the noise generated by a fan in a duct shows a chaotic behavior and can be modelled by a nonlinear and deterministic process [98]. Acoustic disturbances with similar characteristics are usually

present in vehicle cabins and mainly in aircraft. The effect of this type of noise on the controller behavior, when an ANC system is employed for controlling such sound, has also been studied in [98]. In real-world applications and in particular in vehicles such phenomena are very frequent, resulting in a reduction of the SPL reduction achieved by ANC systems [99].

A solution to this problem has been given by non-linear adaptive filters, which are more effective in attenuating broadband acoustic disturbances characterized by the combination of harmonic and chaotic components, that propagate through non-linear electroacoustic paths. Several researches have focused on non-linear controllers based on Volterra series [40], [41] and bilinear filters [43], [44], while others have been utilized architectures that employ the convex combination of non-linear and linear filters [45]. Moreover, Functional Link Neural Networks with several functional expansions is another solution that has been employed by several researches [100]–[102].

In case of sinusoidal functional expansion, Das et al. proposed a non-linear FsLMS algorithm [29], that is a single layer Functional Link Neural Network (FLNN) with trigonometric functional expansion to enhance ANC system performance. In [42], a modified version of the algorithm has achieved better performance in noise cancellation, when the primary path is non-linear. Moreover, a combination of FsLMS and Remote Microphone Technique was presented in [103] for the relocation of the quiet zone far from the physical microphones, forming a virtual version of the FsLMS. This version was used in a headrest system [104], achieving better performance than conventional FxLMS when non-linearities are present either at primary and secondary paths, or at cancelling loudspeakers (distorted speaker). However, this system is characterized by uncertainties in the computation of virtual error that can lead to robustness issues [87] and by high computational complexity. In this Chapter, the FsLMS is combined with the mixed error approach, discussed in Chapter 2 and with the linear extrapolation of acoustic pressure, to form a novel method that is applied in a headrest application.

4.2 Filtered-s Least Mean Squares algorithm

FLNN [105] is a type of neural network that aims to address the complexity issue commonly associated with conventional neural networks that employ backpropagation for training. The operation of FLNNs is built upon the functional expansion of the original input layer using specific functions, such as trigonometric [106], Chebyshev [107] and Lagrange [108], to enable the modeling of nonlinearities. One of the key advantages of FLNNs is their reduced complexity, which enables online training and real-time monitoring of changes in the modeled problem. FLNNs have been effectively utilized in the areas of system identification [109], [110] and time-series prediction [35], [111].

Although it appears that various algorithms, particularly neural networks, have the

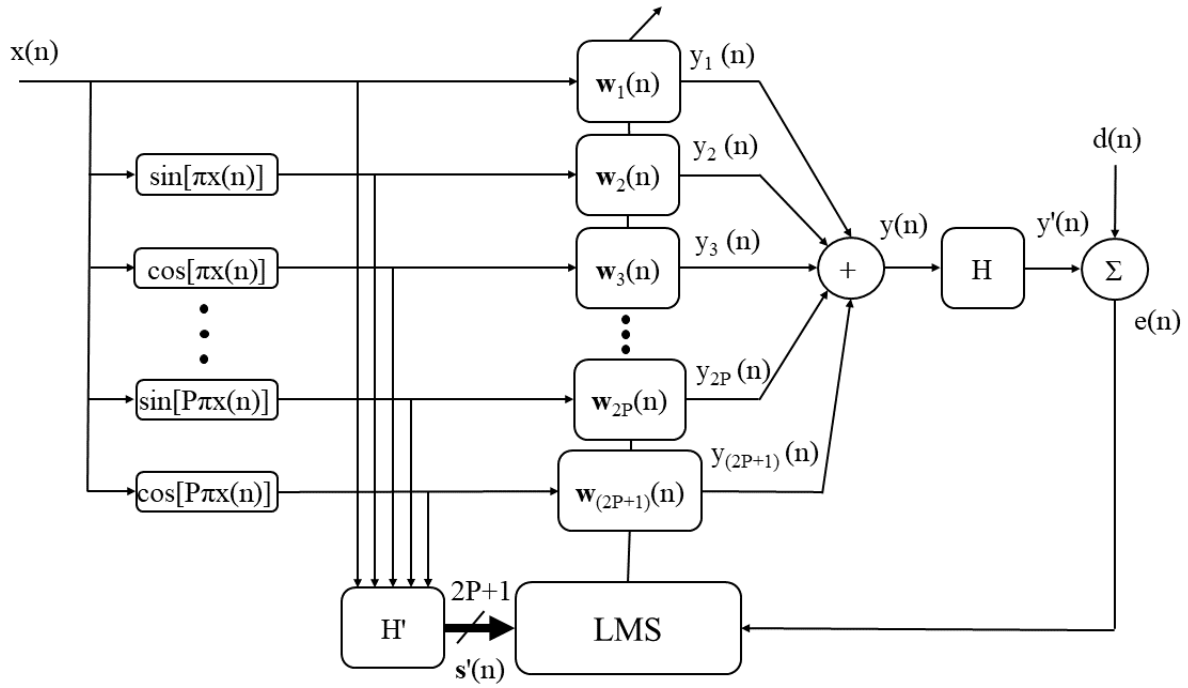

Figure 4.1: Block diagram of a single-channel FsLMS algorithm. The functionally expanded reference signal filtered by the model of the secondary path H' is denoted by $s'(n)$.

potential to improve the performance of the original FxLMS especially in real-world applications, there is a subtle issue that continuously presents challenges. Specifically, the existence of the secondary path after the output of the digital signal processor, where the control algorithm is implemented, poses difficulties in defining the training task. This system filters the signal that is being computed, which can hinder the ability of the noise-cancelling task to perform as it was trained to. As a result, the impact of the secondary path must be considered in any algorithm that aims to achieve NC. In the case of the FLNN algorithm, the effect of the secondary path was introduced by the FsLMS algorithm, whose filter bank implementation is shown in Figure 4.1.

In single-channel FsLMS the functionally expanded reference signal described by Eq. 4.2 is employed. The reference signal $\mathbf{x}(n)$ (Eq. 4.1) is obtained by a reference sensor located near to the noise source, similarly to the conventional FxLMS. Then $\mathbf{s}(n)$ is calculated by passing $\mathbf{x}$(n) as input to sinusoidal functions. Furthermore, the model of the secondary path H' is obtained similarly to the FxLMS, during a preliminary identification stage.

$$\mathbf{x}(n) = [x(n) \quad x(n-1) \quad \cdots \quad x(n-L+1)]^T \tag{4.1}$$

$$s_i(n) = \begin{cases} x(n), & \text{if } i = 1 \\ sin(l\pi x(n)), & \text{if i is even} \\ cos(l\pi x(n)), & \text{if i is odd} \end{cases} \tag{4.2}$$

for $1 \leq l \leq P$ and $1 \leq \ i \leq 2P + 1$, assuming that P is the FLNN order.

Therefore, we obtain:

$$\mathbf{s}(n) = [s(n) \quad s(n-1) \quad \cdots \quad s(n-L+1)]^T \tag{4.3}$$

In a filter bank implementation of FsLMS, where a separate filter is computed for each component of the trigonometrically expanded reference signal, the weights of the non-linear adaptive filter derive from Eq. 4.4:

$$\mathbf{w}_i(n+1) = \mathbf{w}_i(n) - \mu \mathbf{s}'_i(n) e(n) \tag{4.4}$$

where w represents the weights vector, μ the step size of the algorithm, and $\mathbf{s}'_i(n)$ the functionally expanded reference signal filtered by the model of the secondary path H'. Then, the antinoise signal is obtained by summing the outputs of the filters in the filter bank.

$$y(n) = \sum_{n=1}^{2P+1} y_i(n) \tag{4.5}$$

where

$$y_i(n) = \mathbf{w_i}^T(n)\mathbf{s}(n) \tag{4.6}$$

4.3 Mixed-error FsLMS

The mixed-error FsLMS algorithm is an extension of the algorithm presented in section 2.4. Again, it employs the mixed error of Eq. 2.18 in order to update the weight coefficients of the *kth* non-linear adaptive filter, that drives the *kth* loudspeaker (Figure 4.2). Therefore, for a multichannel ANC system with K loudspeakers and M microphones the update equation of the adaptive filter coefficient

$$\mathbf{w}_{ik}(n+1) = \mathbf{w}_{ik}(n) - \mu \mathbf{s'}_{k,mix}(n) e_{mix}(n), \quad k = 1, 2, ..., K. \tag{4.7}$$

where μ is the step size of the algorithm, and $\mathbf{s'}_{k,mix}(n)$ the functionally expanded reference signal, filtered by the model of the mixed error secondary path $H'_{k,mix}$ corresponding to *kth* and the sum of M error signals. Thus, the antinoise signal for the *kth* loudspeaker is

computed by Eq. 4.8.

$$y_k(n) = \sum_{n=1}^{2P+1} y_{ik}(n) \tag{4.8}$$

where

$$y_{ik}(n) = \mathbf{w}_{ik}^T(n)\mathbf{s}(n), \quad k = 1, 2, ..., K. \tag{4.9}$$

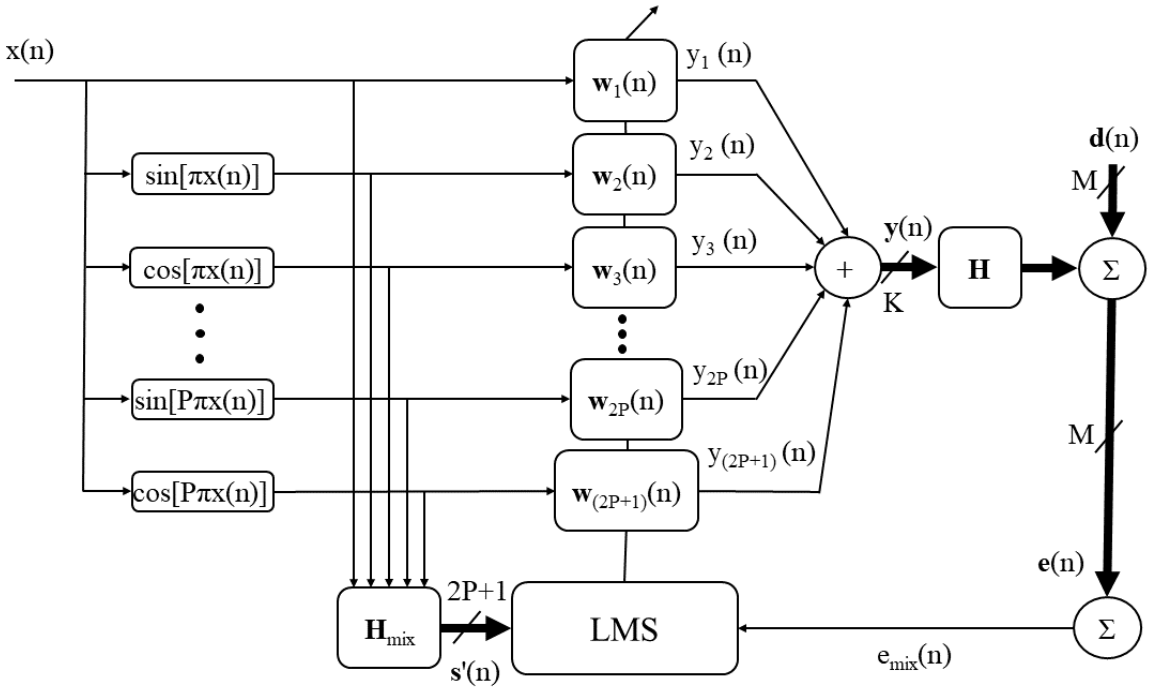

Figure 4.2: Block diagram of mixed-error FsLMS algorithm for a multichannel ANC with k loudspeakers and M microphones. The functionally expanded reference signal filtered by the mixed secondary path H_{mix} is denoted by $s'(n)$.

As in the VEM-FxLMS of section 3.2, we can integrate the first-order finite difference technique to estimate the acoustic pressure at the ears of the seat occupant and therefore to relocate the quiet zone in a more significant area for the passenger comfort. At this point we would like to reiterate that this particular method of acoustic pressure estimation is only effective at low frequencies ($< 500Hz$), due to its relatively small spatial variation, which in turn is due to the long wavelengths of these acoustic disturbances.

$$\mathbf{w}_{ik}(n+1) = \mathbf{w}_{ik}(n) - \mu \mathbf{s'}_{k,mix}(n) e_{v,mix}(n), \quad k = 1, 2, ..., K. \tag{4.10}$$

where $e_{v,mix}(n)$ for a system with two error microphones is computed by Eq. 3.2. In addition, the functionally expanded reference signal is filtered by the mixed secondary path H_{mix} that corresponds to the furthest microphone pair as, described in section 3.2 and depicted in Figure 4.3. Subsequently, the antinoise signal is computed by Eqs. 4.8, 4.9.

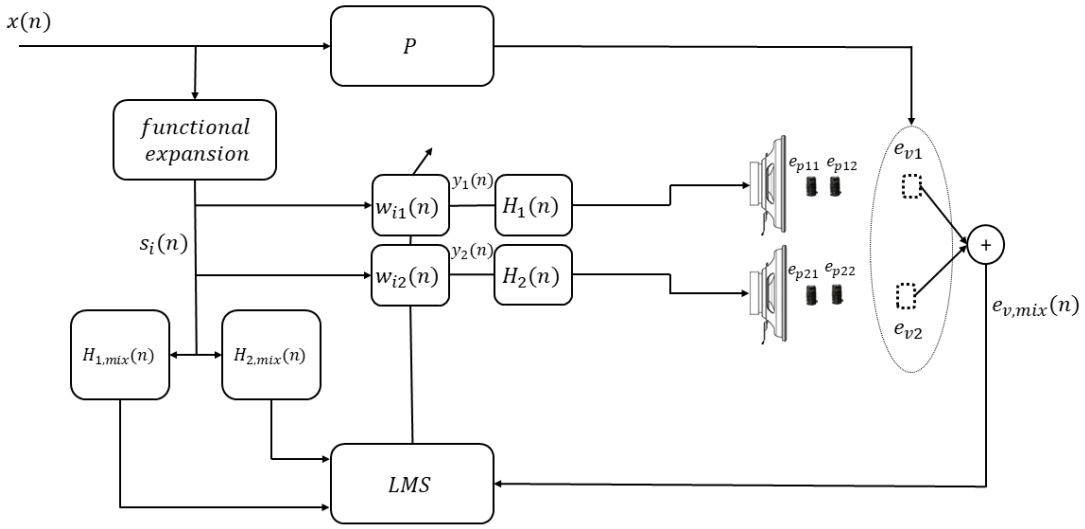

Figure 4.3: Block diagram of the FLNN based algorithm using 2 loudspeakers and 2 physical microphone pairs in order to estimate virtual error signals e_{v1}, e_{v2}.

.

4.3.1 Computational complexity

The computational complexity of a single iteration of the proposed algorithm is detailed in Table 4.1. The algorithm is designed to operate on a sample-by-sample basis; hence, determining the computational load per iteration and the sampling frequency provides comprehensive information regarding the requirements for the digital signal processor. It is assumed that the ANC system features two outputs and two inputs, which serve as virtual error signals. Furthermore, a FIR filter of length L is utilized to model the mixed error secondary path. The vectors w_{ik} have a length of N, and P denotes the order of the FLNN. The mixed error secondary path is identified during a preliminary stage using the conventional LMS algorithm, resulting in low computational complexity during this phase.

The low computational load during the control stage is attributable to both the mixed error approach of the multichannel FLNN and the simplicity of the first-order prediction technique. The benefits of these methods are realized if the assumptions outlined in Sections 2.1 and 2.2 are satisfied. The mixed error approach minimizes the number of convolution operations, as demonstrated by the comparison between Eqs. 1.1 and 1.5. According to [112], the traditional multichannel FLNN, with an equivalent number of inputs and outputs, requires $2(2P+1)(3N+4L)$, which results in $2(2P+1)(N+3L)-2$ more multiplications than the proposed algorithm. Similarly, we can derive that the number of additions is reduced by $2(2P+1)(N+3L-4)-1$. Finally, the publication[57]

demonstrates that the number of multiplications increases significantly when any of the VMT, RMT, or VMC virtual sensing techniques is applied. Conversely, the integration of the first-order prediction technique introduces only two additional multiplications per iteration.

An example with $P = 1$ and $L = N = 250$ demonstrates the computational efficiency of the proposed algorithm. In this scenario, the total number of additions is 4,501, and the total number of multiplications is 4,502 during the control stage. In contrast, the FLNN described in [104] for a headrest application, which incorporates the Remote Microphone Technique, requires 7,020 multiplications and 7,008 additions to compute the output signals. This discrepancy becomes significant when multiple systems are implemented. For instance, in the cabin of a small airplane with six seats, fewer digital signal processors would be needed, leading to reduced hardware and lower cost. Moreover, the low computational complexity allows for the addition of more input and output signals, potentially enhancing the system's overall performance.

Computation	Multiplications	Additions	$sin(.)/$ $cos(.)$
y_{ij}	$2N(2P+1)$	$2N(2P+1)$	$4P$
$e_{v,mix}$	2	3	-
$s'_{ij,mix}$	$2L(2P+1)$	$2L(2P+1)-2$	-
w_{ij}	$2N(2P+1)$	$2N(2P+1)$	-
Total	$2(2P+1)(2N+L)+2$	$2(2P+1)(2N+L)+1$	$4P$

Table 4.1: Number of computations for 1 iteration of the control algorithm, with 2 inputs, 2 outputs. L and N denote the length of $H_{k,mix}$ and w_{ik} respectively. P is the order of the FLNN.

4.4 Computer simulations analysis

Two types of numerical simulations were conducted. The first examined the proposed algorithm's convergence and stability in comparison to the linear FxLMS. The second simulated the acoustic behavior of the ANC system when placed in an aircraft cabin.

Both the FLNN and the FxLMS algorithms were implemented in Matlab® to evaluate their convergence and stability, as well as to compare their performance. The instantaneous squared error was used as the criterion. For the purpose of this study, three types of reference signals were used: 1) two signals recorded in the cabin of a tilt-rotor aircraft during a measurement campaign for the PIANO project [113]; 2) a synthetic logistic chaotic signal; and 3) a mixture of three tonal components (48 Hz, 72 Hz, 96 Hz) added with white Gaussian noise at a signal-to-noise ratio of 30 dB. The real-world signals correspond to flight at 10 kft and 20 kft with speeds of 150 kts and 200 kts, respectively. These signals consist of harmonics of the BPF of the aircraft's rotor and background

noise, which has chaotic characteristics, as demonstrated in subsequent sections. The logistic chaotic acoustic disturbance is described by Eq. 4.11 and has been used in many previous works [29], [112], [114], [115] for the evaluation of non-linear ANC algorithms based on trigonometric FLNN due to its effectiveness at detecting the presence of chaotic characteristics in acoustic disturbances.

$$x(n+1) = \lambda x(n)[1 - x(n)] \tag{4.11}$$

where $\lambda = 4$ and $x(0) = 9$.

Moreover, the primary electroacoustic paths between the reference microphone and the four error microphones (Eq. 4.12), as well as the secondary paths between the secondary sources and the two furthest error microphones (Figure 4.4), are identical to the actual systems in the laboratory and align with the experimental analysis paths. These paths were modeled using the LMS algorithm for the purpose of the simulation.

$$\begin{aligned}
p_{11} = [&-0.0025\ -0.0028\ -0.0014\ -0.0003\ -0.0009\ -0.0014\ -0.0001 \\
&0.0020\ 0.0032\ -0.0004] \\
p_{12} = [&-0.0021\ -0.0030\ -0.0014\ -0.0001\ -0.0007\ -0.0016\ -0.0006 \\
&0.0019\ 0.0035\ -0.0008] \\
p_{21} = [&-0.0015\ -0.0026\ -0.0011\ -0.0005\ -0.0002\ -0.0015\ -0.0010 \\
&0.0011\ 0.0026\ -0.0017] \\
p_{22} = [&-0.0015\ -0.0024\ -0.0075\ 0.0007\ -0.000017\ -0.0015\ -0.0009 \\
&0.0012\ 0.0029\ -0.0022]
\end{aligned} \tag{4.12}$$

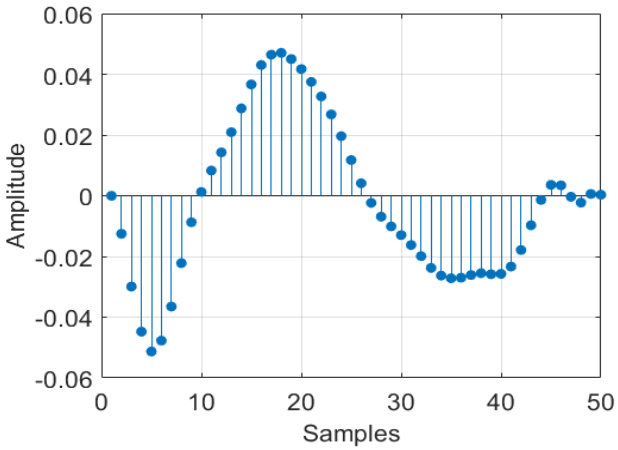

Figure 4.4: Impulse response of one loudspeaker's mixed error secondary path.

The minimization of the instantaneous error for both FxLMS, first order FLNN and second order FLNN is demonstrated in Figure 4.5. The performance of the second or-

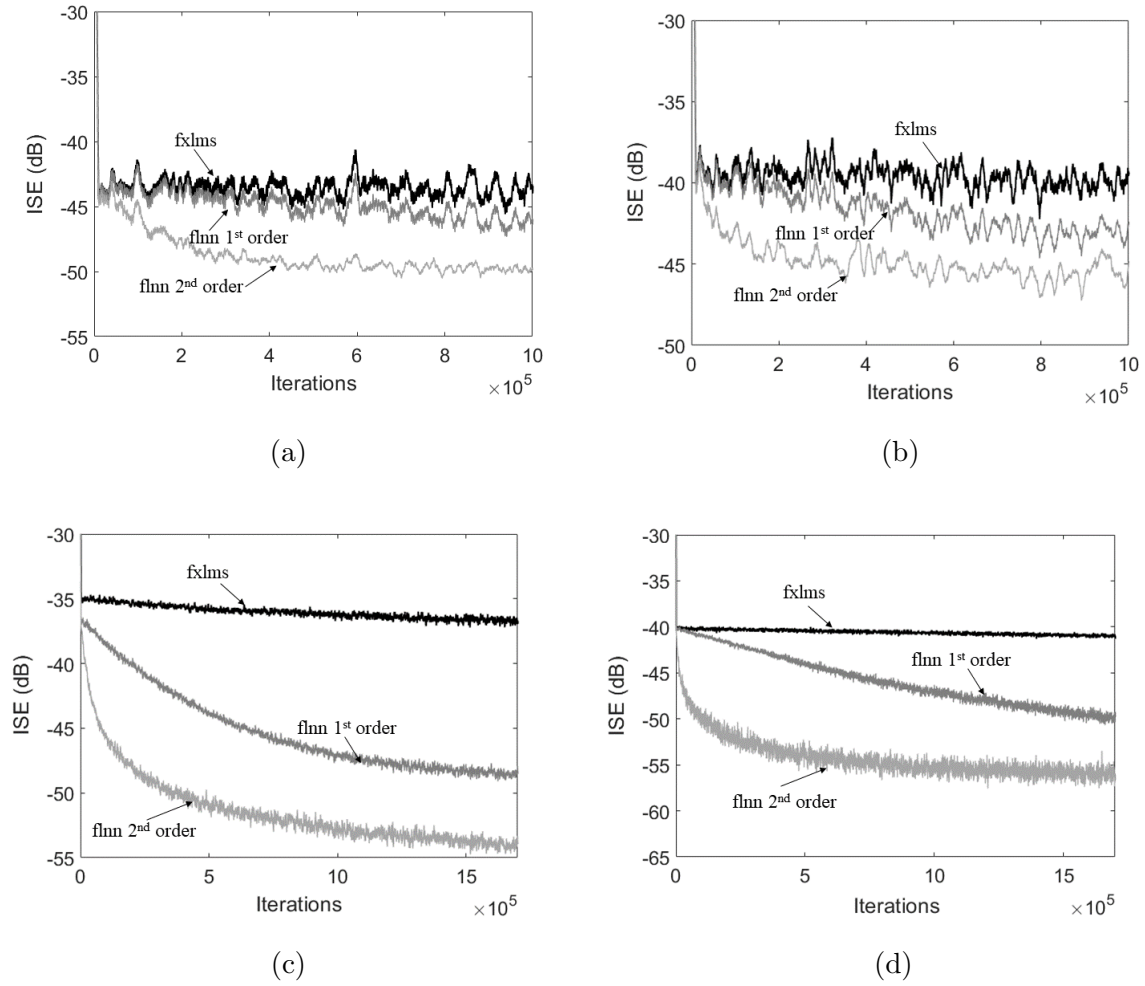

Figure 4.5: Instantaneous Squared Error of the FxLMS and FLNN of first and second order when the reference signal is (a) the acoustic disturbance captured during flight at 10 kft with speed of 150 kts, (b) the acoustic disturbance captured during flight at 10 kft with speed of 200 kts, (c) the logistic chaotic noise described by Eq. 4.11 and (d) the mixture of tonal components and the Gaussian white noise.

der FLNN surpasses that of the other algorithms for both four signals. For the logistic chaotic signal (Figure 4.5c), the difference between linear and non-linear systems is more pronounced, indicating that the trigonometric FLNN is a better predictor in the presence of chaotic characteristics. When using recorded real-world signals as reference (Figs. 4.5a, 4.5b), the difference between the three algorithms is smaller, which can be attributed to their strong harmonic characteristics. However, chaotic characteristics are also present, as indicated by the method based on the computation of Lyapunov exponent λ [116]. For the signal corresponding to 150 kts, $\lambda = 0.0314$, and for the signal corresponding to 200 kts, $\lambda = 0.0718$. This suggests the presence of chaos in these time series, which can explain the improvement in performance when non-linear algorithms are employed. Moreover, the non-minimum phase behavior of the secondary paths, as depicted in Figure 4.4, is better modeled by a trigonometric FLNN, as previously mentioned in [29]. The

non-minimum phase behavior of the secondary paths used in the convergence simulation can also account for the superior performance of the FLNN in the case of the signal with tonal and noisy components (Figure 4.5d). Finally, the presence of noise can make non-linear control more effective in time series prediction than linear control.

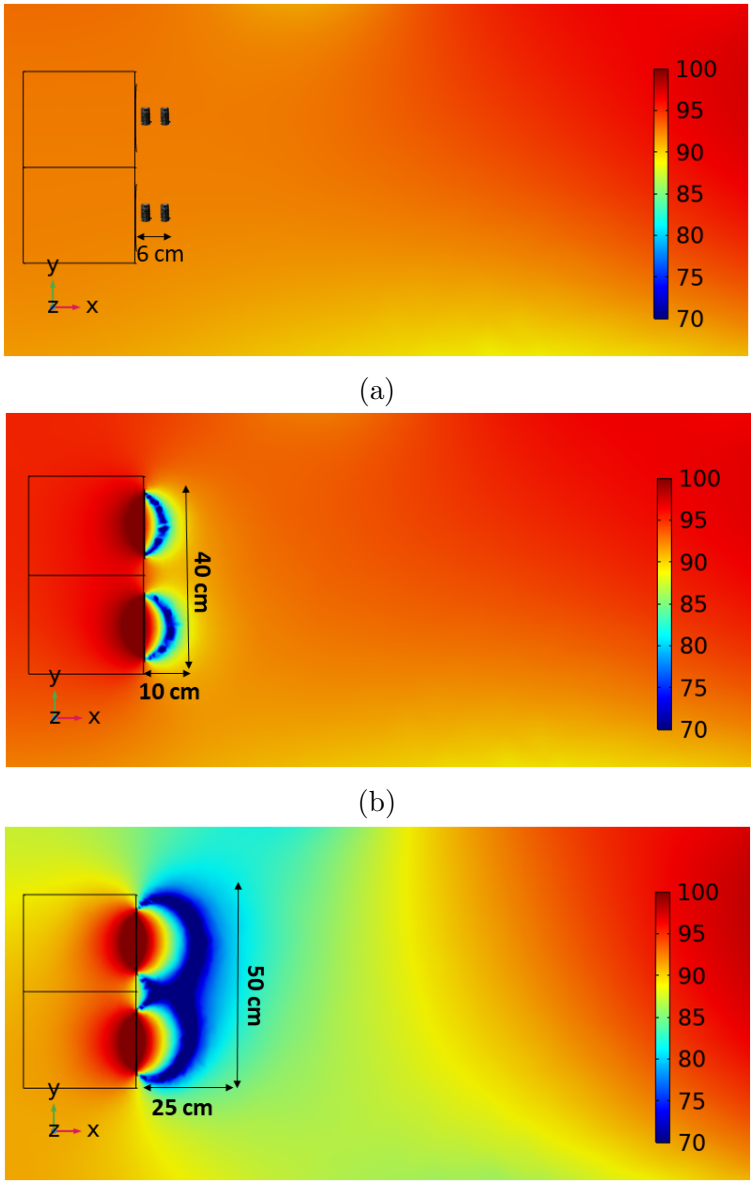

Figure 4.6: Sound Pressure Level around the loudspeakers of the ANC headrest system based on second order FLNN. The simulations were conducted using time domain FEM when (a) ANC is deactivated, (b) ANC is activated and x= 0 cm, and (c) ANC is activated and x=6 cm

Apart from conducting convergence simulations, acoustic simulations were executed using the FEM. These simulations were performed in the Acoustics module of Comsol Multiphysics®. Additional information pertaining to these simulations, along with details on other simulations conducted in this dissertation, can be found in Appendix A.2.3. In

Figure 4.6, the SPL distribution in front of the headrest is presented. In Figure 4.6a, the system was inactive, while in Figs. 4.6b and 4.6c, the ANC based on the second-order FLNN algorithm was activated. The second-order algorithm was selected for deployment due to its superior performance in the convergence simulations. Moreover, in the case of Figure 4.6b, the value of the parameter x in the extrapolation method was set to 0 cm, while in the case of Figure 4.6c, it was set to 6 cm. The difference in size between the shaped quiet zones is considerable.

Their dimensions are 10 cm x 40 cm without acoustic pressure's prediction at the passenger ears and 25 cm x 50 cm with it. As a result, the first order prediction technique manages to extend the quiet zone far from the surface of the headrest and around the passenger head, making the system suitable for an aircraft headrest application. In addition, for a synthesized acoustic disturbance consisting of three harmonics of the BPF at 48 Hz, 72 Hz, and 96 Hz, the maximum attenuation of the sound pressure level reached 25 dB (from around 93 dB to 68 dB). Similar results have also been demonstrated during the evaluation of VEM-FxLMS, thus showing that the non-linear nature of the method proposed in this Chapter is compatible with linear extrapolation of acoustic pressure.

4.5 Experimental evaluation

The experimental evaluation of the FLNN-based ANC system was held in the interior of the aircraft cabin mock-up, similar to the experiments discussed in the previous Chapters. Further details on the construction and the acoustic characteristics of the cabin are given in Appendix section of this dissertation. In addition, a sketch of the top view of the cabin mockup is demonstrated in Figure 4.7a.

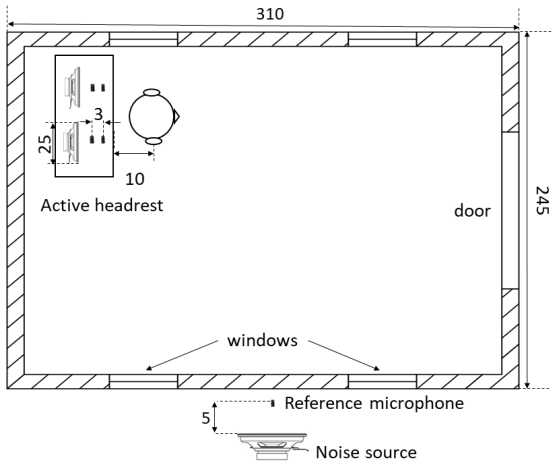

(a)

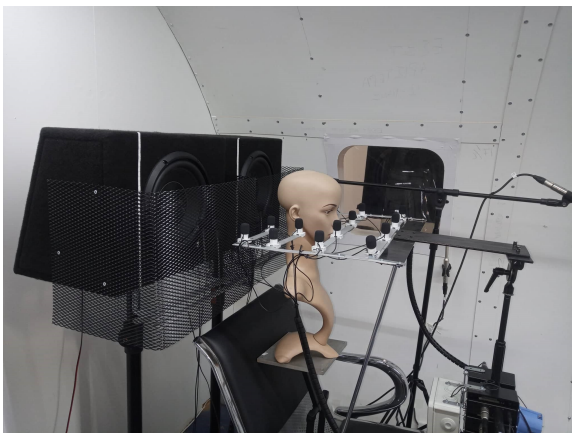

(b)

Figure 4.7: a) Sketch of the top view of the aircraft cabin mockup installed in the Dynamics and Acoustics laboratory. b) Active headrest setup employed the proposed FLNN algorithm.

The choice of an enclosure instead of an anechoic chamber for the experimental evaluation of the active headrest, derives from the need to simulate as much as possible the real electro-acoustic paths that exist in an aircraft, which are characterized by non-linearities and non-minimum phase behaviour, like most real-world systems. Furthermore, the Active Headrest is depicted in Figure 4.7b. It comprised two subwoofers (Visaton WS 25E) and four microphones (Shure MX 183). The utilization of subwoofers rather than conventional loudspeakers aimed to minimize low frequencies, and the frequency response of the subwoofers was suitable for this purpose. The development of the control algorithm involved the use of a National Instruments® cRIO 9030 controller, which integrates an embedded FPGA (Xilinx® Kintex-7) with a dual-core CPU (Intel atom) operating at 1.33 GHz. The core of the FLNN algorithm was constructed within the FPGA part of the cRIO 9030 controller using the Labview® FPGA development platform. The cRIO 9030 was connected to the reference and error microphones via an ADC (NI 9220) and to the secondary sources through a DAC (NI 9264). Lastly, the system's microphone preamplifiers and the amplifiers used to drive the loudspeakers were integrated into a lightweight, handcrafted electronic board that adheres to the weight and size constraints of an aircraft application.

The experimental evaluation of the ANC system was conducted using acoustic disturbances that were recorded within the cabins of a tilt-rotor aircraft, a small propeller driven one and a helicopter during flight as well as the yacht mentioned in Chapter 3. The disturbance from the tilt-rotor was also utilized in the convergence simulations described in Section 4.4. To reproduce the original signal's spectral characteristics, the acoustic disturbance was played through a subwoofer (Omnitronix BX 1250) that was driven by a power amplifier (Behringer KM750) in a laboratory setting. An omnidirectional microphone (t-Bone MM-1) was used to record the reference signal, which was placed 5 centimeters in front of the primary source, as depicted in Figure 4.7a.

A series of measurements were taken to determine the SPL around a passenger's head when the ANC was either enabled or disabled. These measurements were conducted using a sophisticated measurement system that incorporated 16 microphones mounted on a grille (see Figure 4.7b). The construction of this measurement system is further detailed in the Appendix section. Additionally, the accuracy of the measurements was validated using a sound level meter (RION NL-52).

Two stages were necessary for the system activation. Initially, a preliminary identification stage was carried out to model the mixed secondary path of each secondary source $H_{k,mix}$. In this process, the step size and filter length of the LMS algorithm were chosen to be $\mu_{iden} = 0.001$ and N=250 taps, respectively. The reference signal was white noise, which was replicated by the corresponding secondary source. The error signal was the sum of the signals obtained from the farthest error microphones of each pair for both secondary paths (as illustrated in Figure 4.3).

After the identification stage was completed, the control stage calculates the noise-canceling signal for each secondary source. The step size for adapting the linear terms in the filter bank, which is shown in Figure 4.2, was $\mu_{linear} = 0.0001$ and for the non-linear terms it was $\mu_{non\_linear} = 0.0005$. The total number of taps in all sub-filters was set to 250, as longer filter lengths can significantly improve the mitigation of broadband acoustic disturbances, as demonstrated in [117]. The reference signal was recorded by a microphone placed in front of the noise source, which is shown in Figure 4.7a. In a real-world application, the position of the reference microphone must be selected to ensure the maximum correlation between the reference and the error signal while meeting the causality constraint. The control algorithm was implemented using a mixed error approach and the first-order prediction technique for estimating the acoustic pressure at the passenger's ears according to Eq. 4.10. Both the distance between the error microphones of each pair and the distance between the secondary sources and the nearest microphones was set to 3 cm. Finally, the sampling frequency for both identification and control stages was $f_s = 2kHz$.

4.5.1 Tilt-rotor aircraft cabin noise

Evaluation of the linear prediction technique

While the linear prediction technique presented in section 3.2 has been thoroughly studied in [23], [92], [93], to the best of the author's knowledge, it has never been combined with an FLNN. In this experiment, the changes of the SPL in front of the headrest have been investigated, while changing the parameter x of Eq. 6.9. The acoustic disturbance recorded in the aircraft cabin and reproduced in the laboratory is shown in Figure 4.10 with the black line.

The lower frequency band is dominated by the harmonics of the rotor's BPF at 24 Hz. As a result, there are peaks at 48 Hz, 72 Hz, 96 Hz and 119 Hz along with broadband noise. The proposed control algorithm was tested for various values of parameter x in order to evaluate the effectiveness of the acoustic pressure prediction technique. Figure 4.8 depicts the shifting of the quiet zone for x= 0, 4, 8, 12, and 16 cm. The area between 0 and 5 cm in the y direction is empty because the ears are usually positioned 5 cm in front of the headrest even when the head touches it. We observe that the control algorithm converges for all values of x, and the relocation of the QZ is accurate enough for the current application, which aims to attenuate low frequencies.

It is obvious that the maximum attenuation of the SPL is observed near to the y coordinate that is defined by parameter x. When x is selected to be 0 cm, the SPL reduction at the points with coordinates (-5,10) and (5,10) that correspond to the possible positions of the passenger ears is 2-3 dB, given that before the system activation the overall SPL varied between 86.5 and 88.5 dB (Figure 4.8a). The best performance is achieved for

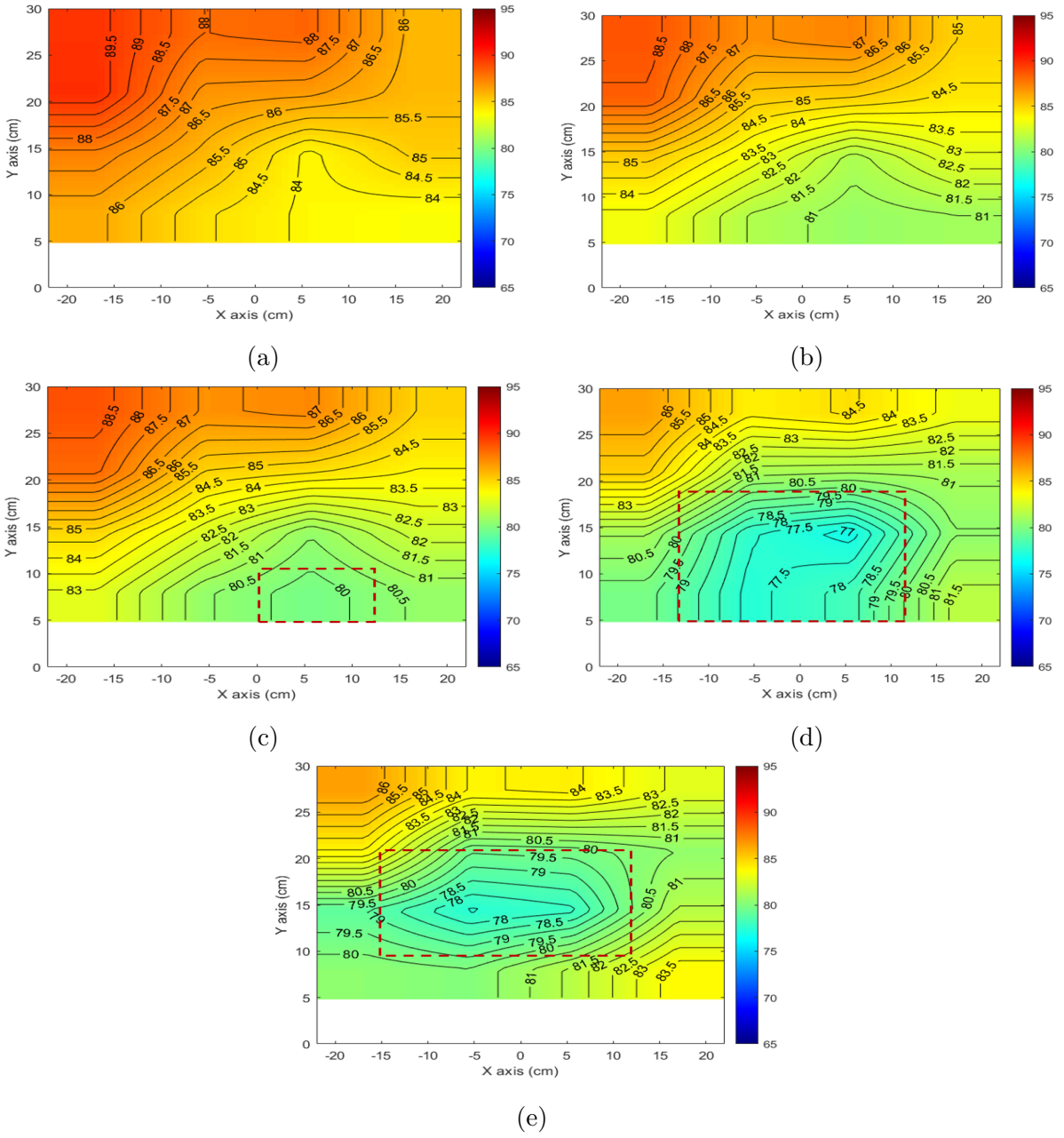

Figure 4.8: Sound Pressure Level at the measurement area for different values of parameter x: a) x=0 cm, b) x=4 cm, c) x=8 cm, d) x=12 cm, and e) x=16 cm. The dotted rectangle denotes the area with SPL attenuation greater than or equal to 7 dB.

x=12 cm (Figure 4.8d), where the 10 dB attenuation is reached near the passenger ears. Finally, when x=16 cm a good performance is achieved at most points of measurement (Figure 4.8e). However, the attenuation does not reach the threshold of 10 dB. Thus, we can say that when the quiet zone is shifted far from the microphone pairs, the overall SPL is attenuated over a larger area but the performance slightly decreases. This is due to a decline in the accuracy of acoustic pressure prediction. As previously stated, the accuracy is determined by the spectral characteristics of the acoustic disturbance and the parameter x. As a result, this method is more effective for low-frequency disturbances

and short distances between the physical and virtual error microphones.

Evaluation of algorithm's noise attenuation performance

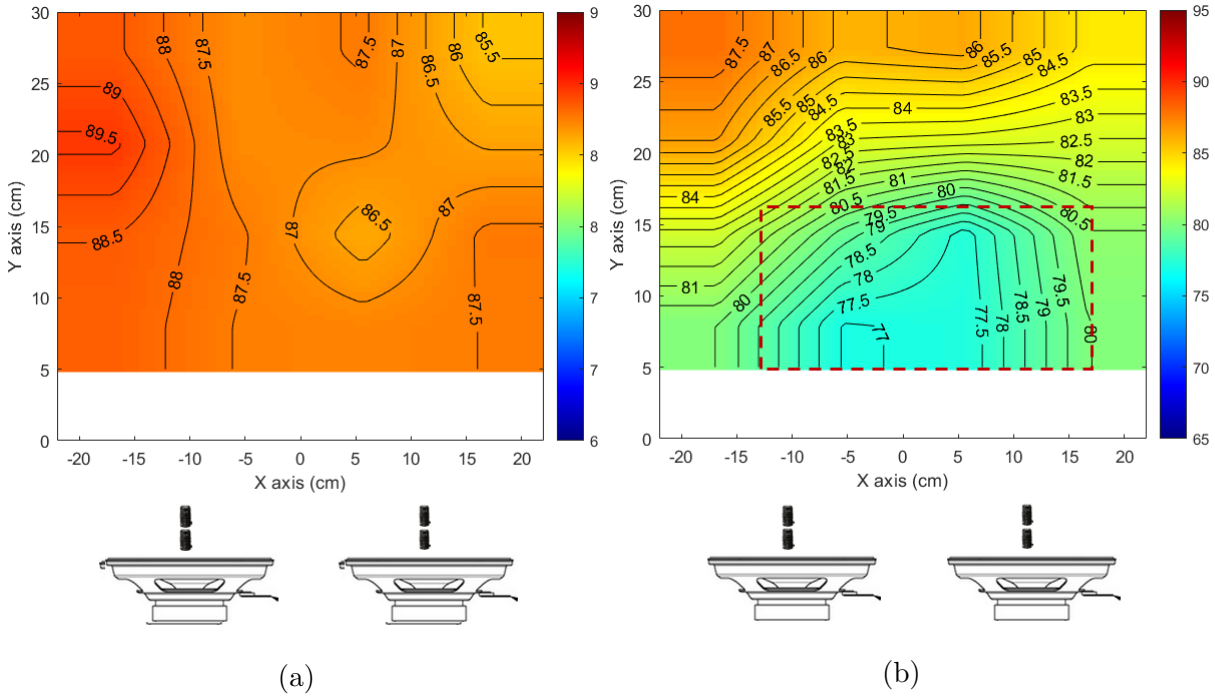

(a) (b)

Figure 4.9: Sound Pressure Level in the vicinity of the active headrest for real-world acoustic disturbance at a height of 110 cm from the cabin's floor when (a) ANC is deactivated, an (b) the ANC based on second order FLNN is activated. The dotted rectangle denotes the area with SPL attenuation greater than or equal to 7 dB.

For the evaluation of the algorithm's performance in mitigating noise, the parameter x was set to 10 cm in order to achieve the maximum attenuation of acoustic pressure between 5 cm and 10 cm from the surface of the headrest. In this way, the maximum SPL reduction is achieved around the ears when the passenger's head touches the seat's headrest. Figure 4.9 shows the SPL map before and after ANC activation. We can see that from 87 dB to 88 dB 5cm - 10 cm away from the surface of the headrest, the SPL drops to 77dB - 77.5 dB, corresponding to a 10 dB noise reduction. Although this reduction in SPL is significant for an aircraft application, it is smaller than the 25 dB observed in the acoustic simulation. This is due to the broadband characteristics of the real world acoustic disturbance and the existence of background noise, which inserts extra difficulty in the prediction problem. Consequently, the size of the 10 dB quiet zone is limited comparing to the simulation results, covering a surface of (15x15) cm^2. However, it can cover the passengers' ears when the head touches the headrest. In addition, a significant attenuation of 8 dB is achieved in a 30 cm x 17 cm area.

Furthermore, the frequency spectrums before and after the ANC activation were recorded by measurement microphones with coordinates (-5,10) and (5,10), which cor-

respond to the passenger's ears and are depicted in Figure 4.10. The most significant BPF harmonics were attenuated by 12 dB to 23 dB (Table 4.2). In addition, at the frequency range between 50 Hz and 150 Hz the frequency spectrum is flattened, showing the broadband noise attenuation capabilities of the proposed algorithm. As a result, the proposed system can achieve significant amplitude reduction for low frequency harmonics, which can be extremely annoying in an aircraft cabin and are difficult to mitigate using passive sound absorption techniques.

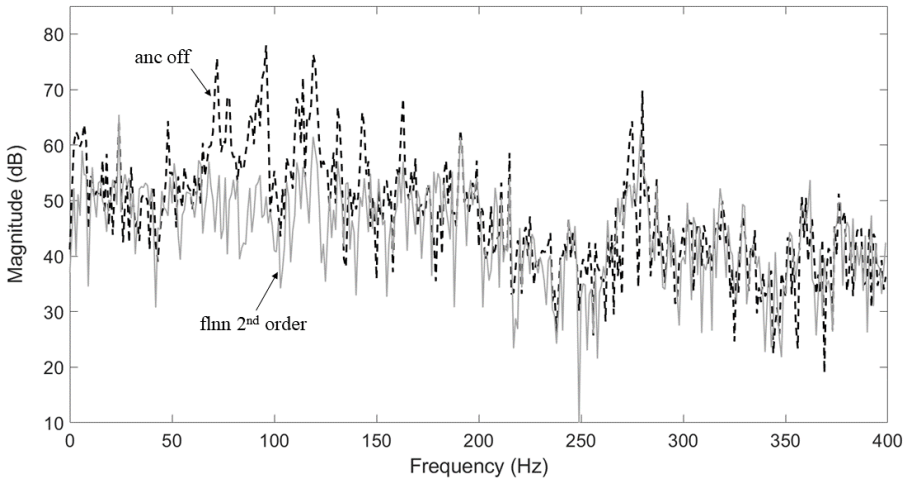

(a)

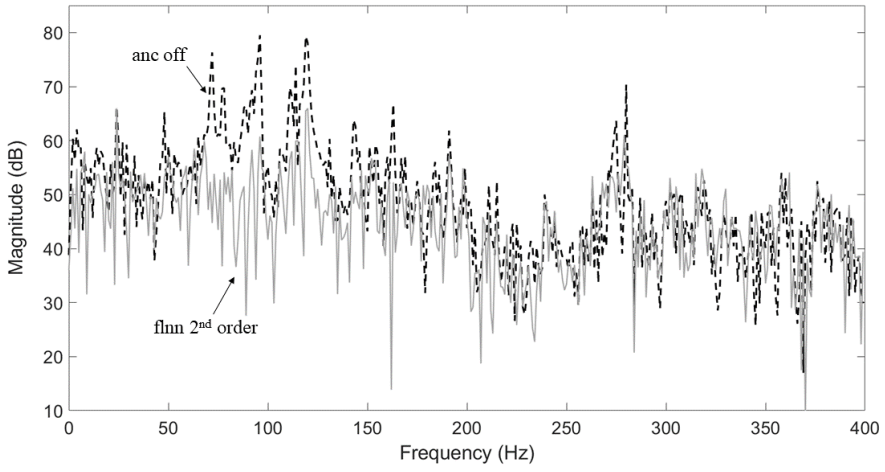

(b)

Figure 4.10: Frequency spectrums before and after the ANC activation. They were recorded by the measurement microphones which were placed 10 cm far from the headrest's surface and 110 cm from the cabin's floor corresponding to the (a)left and (b)right ear of the seat's occupant.

Comparison with the FxLMS algorithm

In section 4.4, it was demonstrated through convergence simulations that the ANC system based on the second order FLNN performs better than the similar systems based on first order FLNN and FxLMS, with respect to the minimization of the instantaneous squared mixed error for the acoustic disturbances of a tilt-rotor aircraft. When the performance criteria are SPL attenuation in different 1/3 octave bands (Figure 4.11) and harmonic amplitude mitigation, the second order FLNN also outperforms.

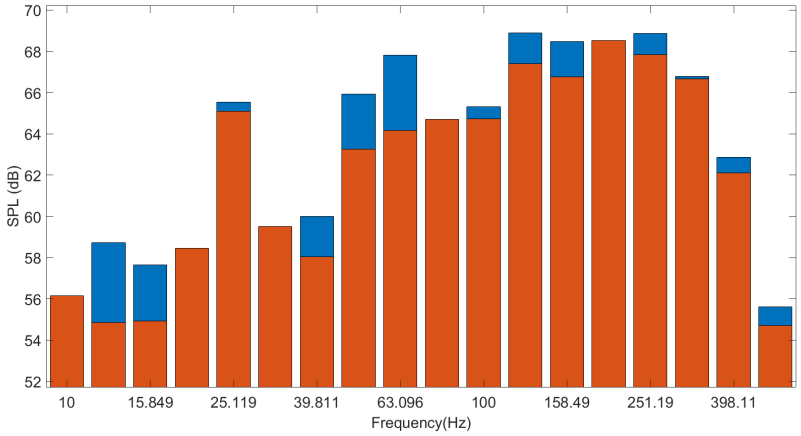

(a)

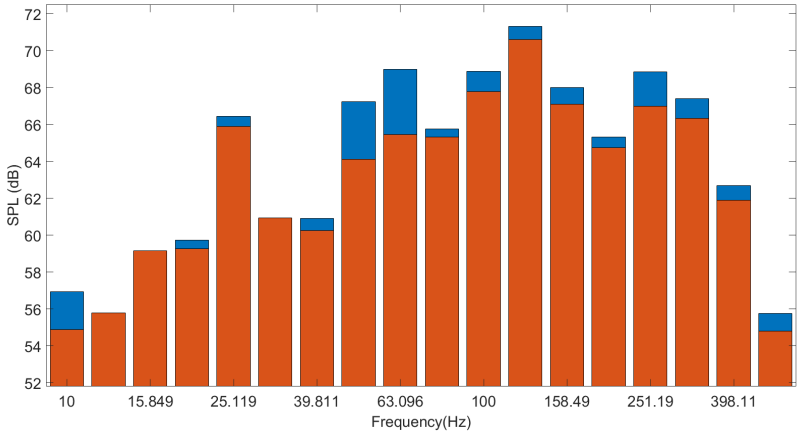

(b)

Figure 4.11: SPL for different 1/3 octave bands, after the ANC activation at the (a)left and (b)right ear of the seat's occupant. The blue columns correspond to FxLMS and the orange to second order FLNN.

The greatest difference is observed in the 1/3 octave bands with central frequencies of 53 Hz and 60 Hz, where the second order FLNN achieves a 3-4dB higher SPL attenuation. This difference derives from the bigger reduction of some harmonics (Table 4.2) and the mitigation of chaotic components. The amplitude of 48 Hz harmonic was reduced by 12 dB and 17 dB at the right and left ear respectively when second order FLNN was used as control algorithm instead of 1 dB when FxLMS was applied. In addition, the performance

Frequency (Hz)	Attenuation (dB)			
	FxLMS		2^{nd} order FLNN	
	Left	Right	Left	Right
48	1	1	12	17
72	21	19	23	21
96	17	27	19	27
119	15	14	13	15
163	8	7	14	12
280	3	2	15	12

Table 4.2: Comparison of the attenuation achieved by the FxLMS and the second order FLNN algorithms for different harmonics of the real-world acoustic disturbance. The measurements correspond to the left and right ear measurement microphones.

of the FLNN is superior in the case of frequencies at 163 Hz and 280 Hz, where there are peaks in the frequency spectrum (Figure 4.10a). The FLNN's superior performance is due to its ability to predict chaotic disturbances and better model physical systems with non-linearities, as stated in section 4.4. Finally, the advantages of the FLNN may be even more significant for acoustic systems with stronger nonlinearities, which will be investigated in future research.

4.5.2 Propeller-driven aircraft cabin noise

To further investigate the performance of the FLNN based ANC system, a signal recorded inside a small aircraft illustrated in Figure 4.12 was used as a noise source. The acoustic energy of this signal, as well as that in the cabin of the tilt-rotor, is concentrated in low frequency bands, namely from 60 Hz to 200 Hz. We also observe two harmonic components at 62 and 124 Hz which are related to the BPF of the propeller. In addition, up to 500 Hz there is broadband noise which is at a much lower level than the harmonic components. Thus, before activation of the ANC the magnitudes of the harmonics at 62 Hz and 124 Hz were 78 and 83 dB respectively in the right ear of the passenger and 79 and 81 dB in the left ear. The passenger ears were also assumed to be 10 cm in front of the error microphones.

As the ANC was activated, a significant reduction in the magnitude of the frequency spectrum from 60 to 140 Hz was observed, for both measurement points corresponding to the two passenger ears. The largest reductions were observed in the 62 and 124 Hz components, which were 14 and 17 dB respectively for the right ear (Figure 4.13b) and 14 and 15 dB for the left ear (Figure 4.13a). In addition, the other peaks of the frequency spectrum up to 500 Hz also subjected to a reduction, leading to a flattening of the spectrum.

Figure 4.12: Small propeller-driven aircraft (Pipistrel Alpha Trainer), where the cabin-noise was recorded.

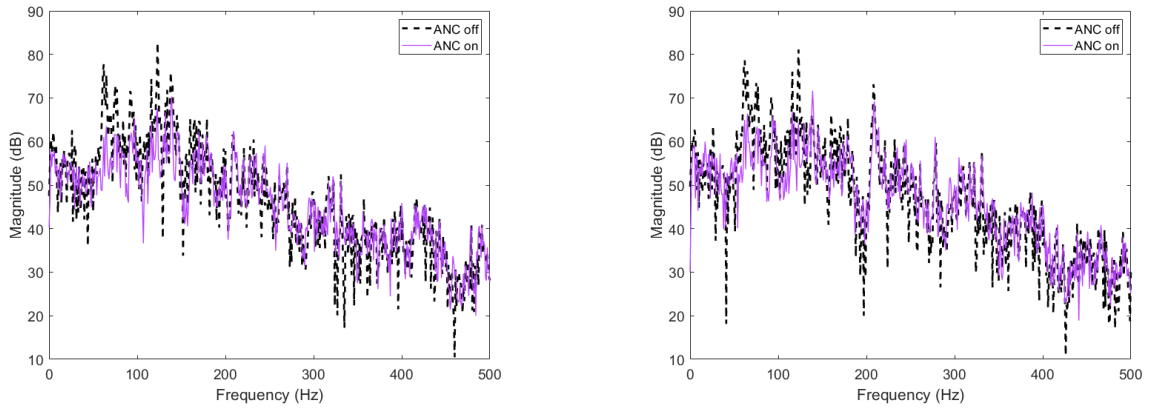

(a) (b)

Figure 4.13: Frequency spectrums at the aircraft cabin mockup, using a recorded signal from the cabin of a propeller-driven aircraft as noise source; a) left passenger ear when ANC is enabled and disabled (dotted line), b) right passenger ear when ANC is enabled and disabled (dotted line).

4.5.3 Helicopter cabin noise

The evaluation process was continued using a noise recording from a helicopter cabin as the noise source. In the frequency spectrum of the acoustic disturbance, harmonics of 26 Hz as well as a frequency component at 115 Hz were observed, along with a concentration of energy in the low frequencies, similar to the case of small propeller-driven aircraft. The 26 Hz harmonic is related to the BPF of the helicopter, which is much lower than the propeller driven aircraft. Furthermore, the magnitude of the individual harmonic elements ranged from 76 to 84 dB at the passenger's ears prior to the activation of the ANC system.

Following the ANC activation, the amplitude of the 26 Hz harmonic was reduced by 3 dB in the left ear and 1 dB in the right ear. Although the reduction in BPF amplitude was small, it did not negatively impact the system's performance, as the human ear has limited perceptual capability for frequencies below 50 Hz, except in cases where the amplitude

(a)

(b)

Figure 4.14: a) Helicopter and b) yacht cabin, where the acoustic disturbances used for the evaluation of the FLNN based ANC system were recorded.

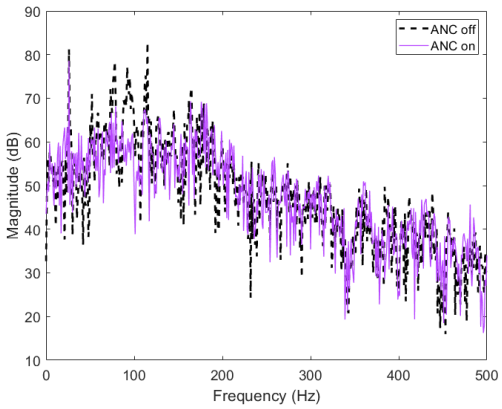

(a)

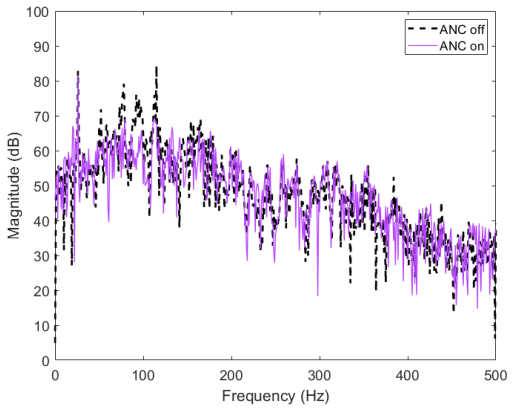

(b)

Figure 4.15: Frequency spectrums at the aircraft cabin mockup, using a recorded signal from the cabin of a helicopter as noise source; a) left passenger ear when ANC is enabled and disabled (dotted line), b) right passenger ear when ANC is enabled and disabled (dotted line).

is very large. The SPL reduction was larger for higher harmonic components like the harmonic at 52 Hz which showed an attenuation of 11 dB. In addition, the magnitude reduction was 14 dB at the left ear and 15 dB at the right ear of the passenger at 78 Hz. Additionally, the harmonics at 92 and 115 Hz showed an amplitude drop of 19 and 18 dB in the left ear and 16 and 22 dB in the right ear, respectively. Finally, it is worth noting that there was a general decrease in broadband noise up to 200 Hz in this case as well.

4.5.4 Yacht cabin noise

Finally, the FLNN-based ANC system was employed to attenuate an acoustic disturbance recorded in one of the yacht's cabins while one of the electric generators was operating.

Thus, the frequency spectrum consisted of a harmonic component at 55 Hz and broadband noise. As for the harmonic at 55 Hz before the ANC was activated it reached 78 and 77 dB at the right and left ear of the passenger respectively. When the ANC was activated, a reduction in amplitude of 16 and 14 dB respectively was achieved. In addition, a slight reduction in the broadband noise level was observed.

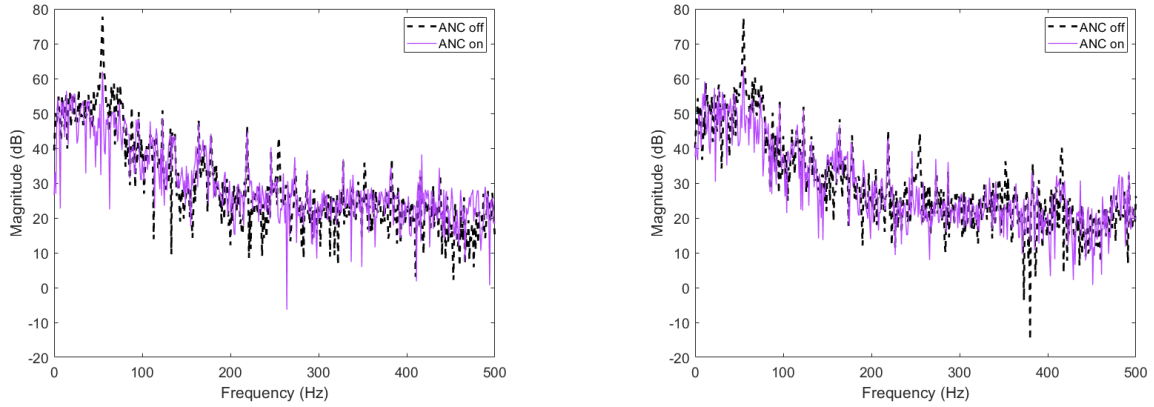

(a) (b)

Figure 4.16: Frequency spectrums at the aircraft cabin mockup, using a recorded signal from yacht cabin as noise source; a) left passenger ear when ANC is enabled and disabled (dotted line), b) right passenger ear when ANC is enabled and disabled (dotted line).

4.6 Concluding remarks

In this Chapter, the methods presented in this dissertation are expanded upon by a non-linear algorithm that aims to be more efficient than conventional FxLMS for real-world acoustic disturbances. The algorithm combines a second-order Functional Link Neural Network with sinusoidal functional expansion, the mixed error approach presented in Chapter 2, and the linear prediction technique of the acoustic pressure at the passenger ears presented in Chapter 3. The algorithm was evaluated through simulations and experimental tests at the cabin mockup installed in the laboratory, achieving significant attenuation of SPL over a QZ of adequate size for gentle passenger movements. Furthermore, convergence simulations revealed that the proposed FLNN outperforms the FxLMS algorithm in terms of instantaneous squared error minimization, resulting in greater harmonic attenuation during experimental tests. Acoustic simulations using FEM and experimental tests have also demonstrated that the system remains stable, when the distance between physical microphones and the area of acoustic pressure prediction is relatively small. Moreover, the proposed algorithm maintains low computational complexity, making it suitable for real-world applications. At the end of the Chapter, the proposed system was also tested for noise sources such as helicopter cabin noise, yacht cabin noise, and small propeller-driven aircraft cabin noise, achieving the mitigation of the majority of

main harmonic components for more than 15 dB. In addition, it demonstrated the ability to attenuate low-frequency broadband noise.

CHAPTER 5

Interaction of local ANC systems in small enclosures

5.1 Introductory notes

Previous chapters of this dissertation have focused on ANC system architectures and algorithms that are suitable for an active headrest system in vehicles, such as small aircraft and yachts, to mitigate acoustic disturbances around the passenger's head. This approach relies on the local effect of separate systems, as the attenuation of acoustic pressure occurs within a specific quiet zone. Consequently, this approach is referred to as local ANC. However, randomly placing many local ANC systems in a small enclosure, like a boat or aircraft cabin may not guarantee how it will affect the sound field at other locations within the enclosure, which are far from the quiet zones. To address this issue, P.A. Nelson and S.J. Elliot have thoroughly described the principles that govern the placement of loudspeakers and microphones to minimize the total potential acoustic energy in the enclosure [52]. At first, it is crucial that the error microphones detect the acoustic modes, and their placement must avoid the nodes of the modes that are intended to be canceled. Another principle involves the placement of loudspeakers, which must be positioned near a pressure maximum of at least one mode to achieve maximum attenuation of that specific mode.

While this approach can provide a solution for the placement of sensors and actuators, which can also be optimized using appropriate algorithms, it may not always be compatible with multiple active headrests, as the seat headrest may be located in a suboptimal position for minimizing potential acoustic energy. Additionally, even if an optimized place-

ment is achieved, there may still be locations where acoustic pressure increases. Therefore, it is important to study the interaction of separate local ANC systems in an enclosure, if this type of ANC architecture is selected to avoid extreme acoustic pressure in certain areas of the cabin or instability issues resulting from the interaction of adjacent systems.

In this chapter, we utilize FEM simulations to investigate the interactions between local ANC systems. Specifically, we evaluate two architectures: one in which each seat has a dedicated ANC system (Figure 5.1b), and another in which adjacent seats share a multichannel system (Figure 5.1a). Our analysis draws conclusions about the advantages and disadvantages of each architecture. Furthermore, we present experimental results that assess the stability of the systems and the distribution of SPL attenuation in a cabin mockup installed in our laboratory.

5.2 Computer simulation analysis

For the purpose of simulation, two models were created in the Acoustics module of Comsol Multiphysics®, both in 2 and 3 dimensions. The dimensions of the cabin were identical to those of a small tilt rotor aircraft cabin. Further details regarding the model may be found in Appendix A.2, similar to the other simulations discussed in this dissertation. Additionally, two ANC architectures were simulated. In the first scenario, which is depicted in Figure 5.1b, a multichannel system with two inputs and one output was assigned to every seat, while in the second scenario, which is depicted in Figure 5.1a an ANC system with two inputs and two outputs was responsible for creating quiet zones in front of adjacent seats. In other words, in the second case, the adjacent loudspeakers collaborated with each other, reducing the need for additional hardware and computing power. Each system utilized a mixed error FsLMS algorithm, which was analyzed in Chapter 4, combined with a first-order forward difference method for predicting the acoustic pressure far from the passenger's ears. This resulted in the relocation of the quiet zone, and thus, microphone pairs were employed instead of single microphones.

5.2.1 2D models

The two-dimensional model incorporated a total of six loudspeakers, with each one specifically designed for active noise control tasks in the vicinity of each seat's headrest. The simulations involving the 2 input-2 output ANC architecture (Figure 5.1a), which utilized collaborating adjacent loudspeakers, also incorporated 24 microphones, which corresponded to two microphones per seat. Conversely, the model simulating the 2 input-1 output architecture (Figure 5.1b), which was designed for seat-dedicated systems, utilized 4 microphones per seat.

The virtual acoustic pressures at the passenger's ears have been estimated using the

first order extrapolation technique and two microphone pairs, as discussed Chapter 3. The distance between the microphones of each pair and between the first microphone and the loudspeaker's surface was set to 3 cm. In addition, the distance between the centers of two adjacent loudspeakers was set to 65 cm and the distance between two opposites to 1.8 m. Finally, due to the fact that second order FsLMS algorithm is feedforward, a reference microphone is needed. The reference signal must be highly correlated with the signal of the error microphones in order to achieve a good ANC performance. In these simulations, the reference microphone was placed in front of a hypothetical noise source at the rear end of the cabin. In real application, tests should be made for the determination of the reference sensor's position in order to achieve the best performance.

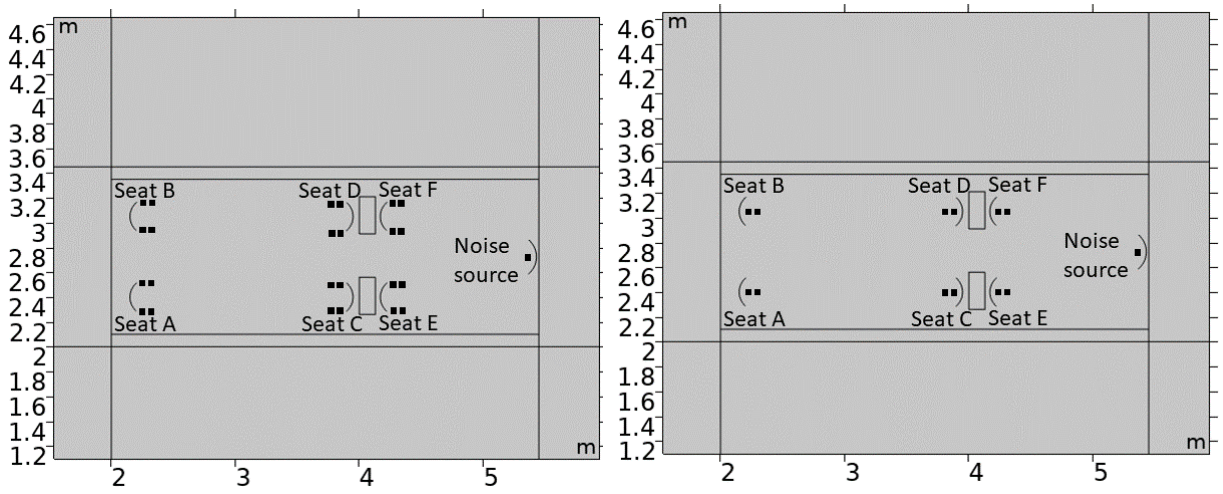

Figure 5.1: The two different system setups investigated during the 2D simulations. (a) At the first setup, every system consisted of 2 microphone pairs (black rectangles) and 1 loudspeaker (arc) dedicated to one seat. (b) At the second setup every system consisted of 2 microphone pairs and 2 loudspeakers which cooperated to attenuate noise in front of adjacent seats.

Figure 5.2 illustrates the SPL within the cabin when the six active headrests were activated. The measurement of SPL occurred six seconds after the activation time. The acoustic disturbance generated in the Comsol platform comprised four harmonics at 48 Hz, 72 Hz, 96 Hz, and 119 Hz, resembling the actual measurement taken inside the aircraft. Moreover, low-frequency pink noise was added to enhance the realism of the simulation. Prior to the activation of the ANC, the SPL levels in front of seats A and B were 96 dB, in front of seats C and D were 93 dB, and in front of seats E and F were 96 dB (refer to Figure 5.2a). Upon activation of the six separate active headrests, six quiet zones were established in front of the headrests (as shown in Figure 5.2b). The attenuation in SPL between seats A and B varied between 7 and 18 dB, as indicated by the blue color, and the quiet zone covered an area measuring approximately 20 cm in width (x-axis) and 45

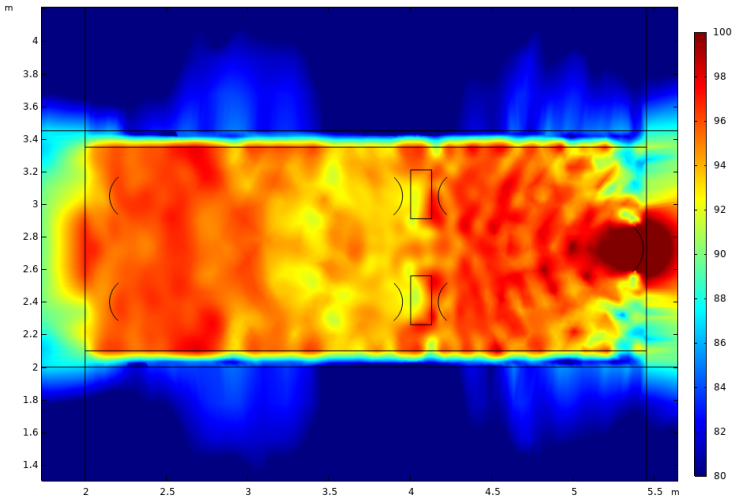

(a)

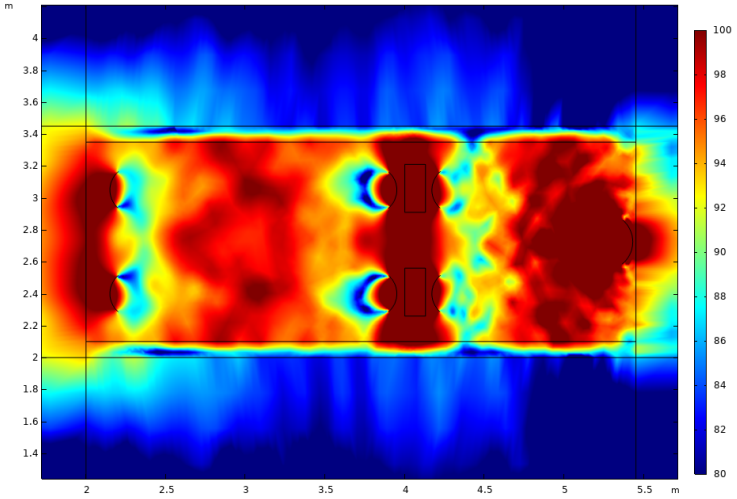

(b)

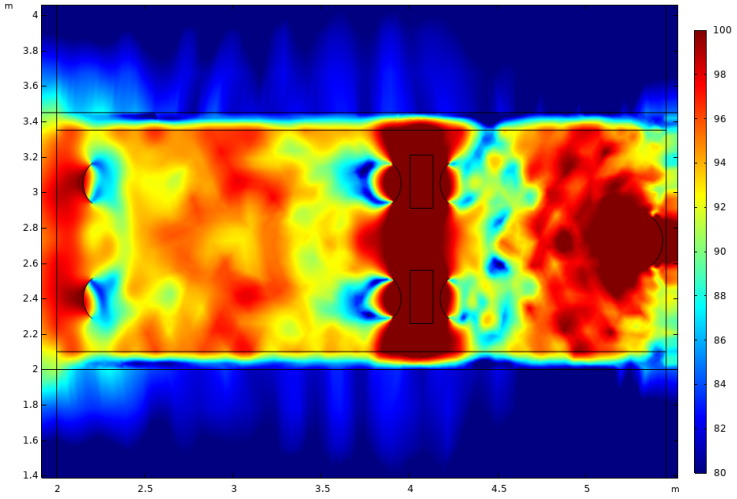

(c)

Figure 5.2: SPL distribution in the 2-dimensional enclosure, when a) the ANC is off, b) the 2-input-1-output architecture is employed, with standalone systems, c) the 2-input-2-output architecture is employed, with cooperating adjacent systems.

cm in length (y-axis).

In the case of seats C and D, the SPL reduction ranged from 8 to 19 dB, which is similar to the values obtained for seats A and D. However, the zone of high acoustic pressure attenuation was larger, thus providing better coverage for the passengers' ears. The dimensions of each quiet zone was approximately 25 cm in width and 30 centimeters in length. In contrast, the attenuation of acoustic pressure was worse in front of seats E and F, as evidenced by the SPL difference ranging from 6 to 11 dB within a quiet zone of surface 12 cm by 15 cm. This decline in the system's performance is attributed to the small distance between the active headrest of these seats and the reference sensor, which results in an intense feedback phenomenon. Nevertheless, the overall reduction in SPL around the passengers' ears is approximately 9 dB, which is deemed satisfactory. As a result, no feedback neutralization technique was employed to minimize the computational complexity of the algorithm.

In the case of adjacent cooperative loudspeakers belonging to the same multichannel system with 2-inputs and 2-outputs, the distribution of SPL can be observed in Figure 5.2c. Compared to the ANC architecture of six stand-alone systems, the quiet zones in front of seats A, B, E, and F are larger and more uniform. Moreover, the 10 dB quiet zone is more extensive, and areas with increased SPL no longer exist. Additionally, the quiet zone in front of seats C and D has expanded over the area between the two headrests, resulting in a reduction of 6 dB in the SPL. As a consequence, the performance of the total ANC system is significantly better than in the case of six stand-alone systems. This improvement is accompanied by a decrease in the computational resources required for the system's implementation, as the number of FsLMS algorithms running simultaneously was reduced by 3.

Furthermore, the overall behavior of the system was better aligned with a global approach to noise control of the cabin, as the acoustic conditions inside the enclosure have been enhanced. Moreover, in addition to the significant reduction of the SPL, which is a crucial factor for the overall performance of the system, the enhancement of the acoustic environment becomes apparent from the frequency spectra at the passenger's ears, which are depicted in Figure 5.3. For instance, in the case of seat A (as shown in Figure 5.3a), which shares similarities with seat B due to symmetry, the attenuation of various harmonics is comparable to the solution provided by stand-alone systems. The primary improvement in this case is the decrease in noise level between 150 Hz and 200 Hz. A similar conclusion can be drawn for the case of seat C. The 2-input-2-output architecture offers the most significant improvement in seat E, where the attenuation of the 48 Hz harmonic reaches 11 dB, and no amplified harmonics are present (as depicted in Figure 5.3e). A comprehensive comparison between the two architectures is provided in Table 5.1

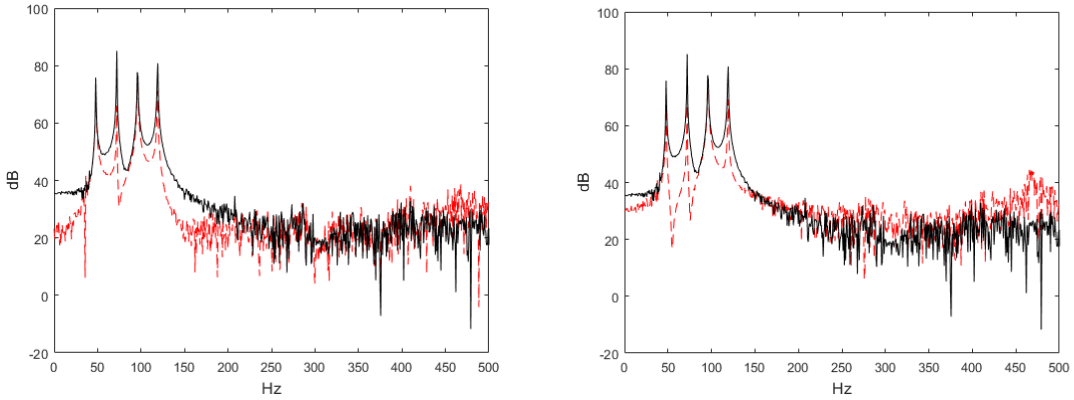

(a)

(b)

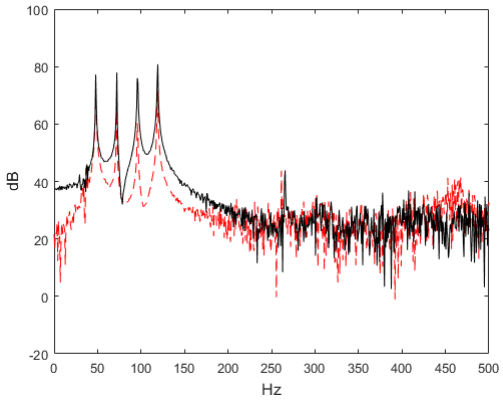

(c)

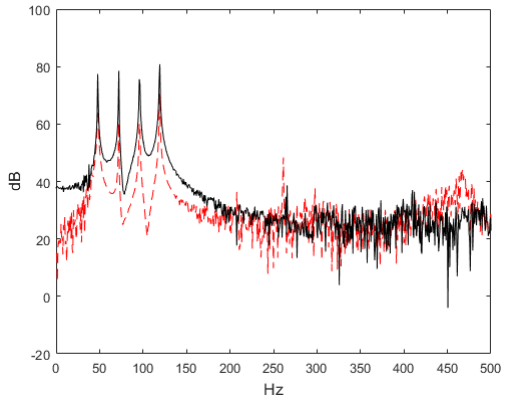

(d)

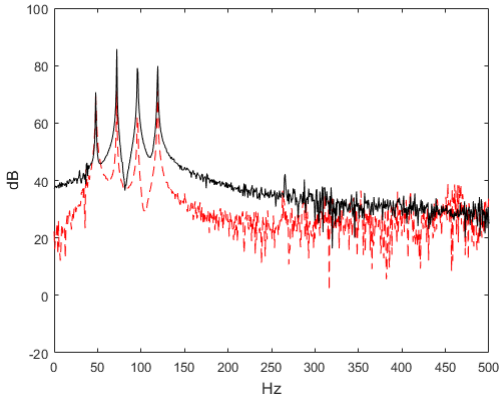

(e)

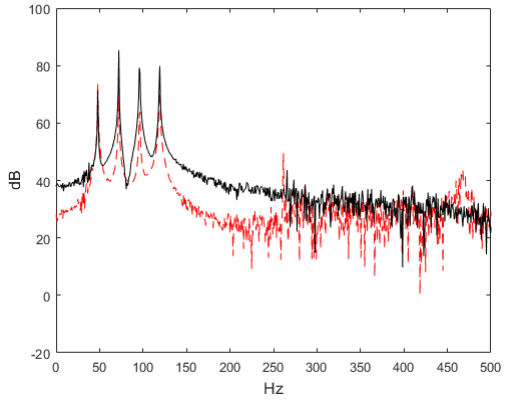

(f)

Figure 5.3: Frequency spectra measured 10 cm from the loudspeakers of seats A, C and E in the 2-dimensional model. Figures a), c) and e) correspond to architecture of cooperative adjacent loudspeakers, while figures b), d) and f) correspond to standalone systems each for one seat.

5.2.2 3D model

Since the solution with the adjacent loudspeakers cooperating with each other has important advantages, an additional 3D simulation has been held for this system. Due to limitations in computational resources, the 3D simulation has been held for only 4

	SPL reduction (dB)	Harmonic attenuation (dB)			
		48 Hz	72 Hz	96 Hz	119 Hz
Stand-alone systems					
Seats A-B	12	10	18	2	12
Seats C-D	16	4	18	17	10
Seats E-F	9	0	10	16	3
Cooperative systems					
Seats A-B	11	6	14	4	13
Seats C-D	15	10	17	16	10
Seats E-F	15	11	14	15	8

Table 5.1: SPL and BPF harmonic attenuation for the two ANC setups investigated in the 2-dimensional simulations.

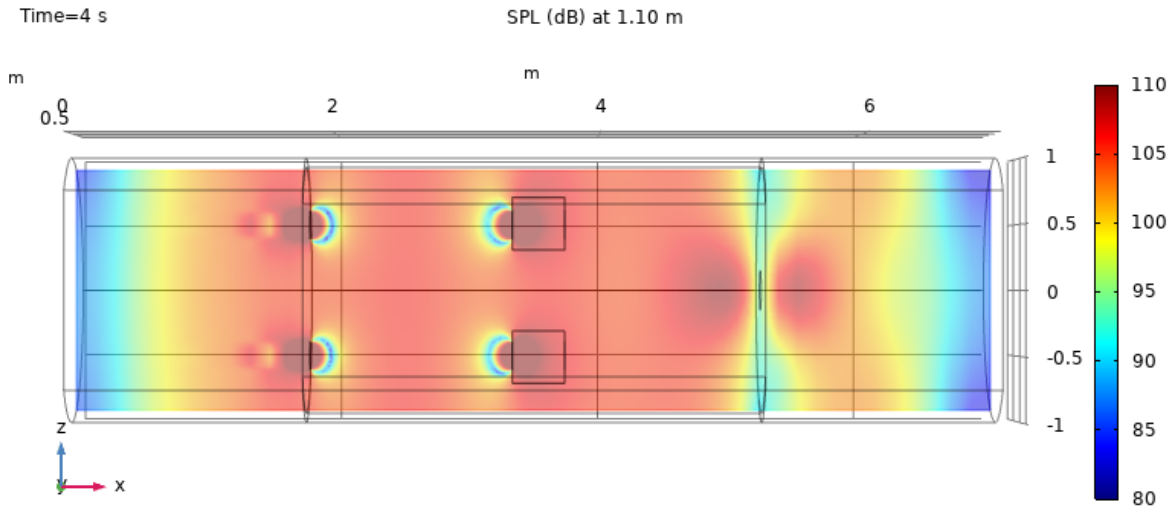

Figure 5.4: SPL distribution (dB) after the activation of ANC at the passenger's ears level (120 cm), for the 3D simulation

loudspeakers. The design of the model involved the creation of an air domain with semi-absorbing boundaries, which served as a representation of the cabin. Additionally, two Perfectly Matched Layers were incorporated at the front and rear ends of the cabin, respectively, to simulate the absorption of air in a long, corridor-like environment, such as an aircraft cabin. Further details on this model geometry are given in the Appendix A.2.2 of this dissertation.

The SPL reduction around the headrests is also presented in Figure 5.4. When the ANC was not activated, the overall SPL reached 105 dB in this simulation. When it was activated, the attenuation ranged from 8 dB to 19 dB forming a quiet zone of dimensions 20cm (length) x 38cm (width) x 25cm (height). The shape of the quiet zone was spherical, as depicted in Figure 5.5, and it was large enough to allow gentle head movements. In addition, at the passenger's ears level, which refer to height of 120 cm, the attenuation ranged from 12 dB to 19 dB. Similar results were obtained for the levels at 100 cm and

110 cm.

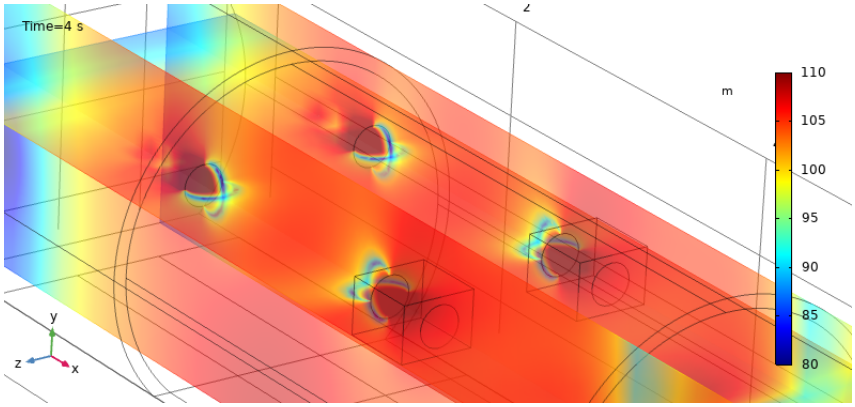

Figure 5.5: Shape of the quiet zones formed around the passenger headrests. The SPL is measured in dB.

Furthermore, the independent operation of opposing did not compromise their stability. Nevertheless, there was a slight increase in acoustic pressure in the areas between them, in case of non-cooperative systems. These conclusions are related to the geometry, which includes perfectly matched layers at the front and rear ends of the cabin. In the following paragraph, we will discuss the experimental evaluation of concurrent operation of separate ANC systems in an enclosure and draw conclusions accordingly.

5.3 Experimental evaluation

The experimental evaluation of the interaction between autonomous local ANC systems installed in a small enclosure was conducted in two phases. Initially, the interaction of the systems when they were mounted facing each other and exposed to a real-world acoustic disturbance, recorded within the cabin of a small tilt rotor aircraft, was assessed. Subsequently, the impact of four such systems on the overall sound field of the enclosure was investigated, when it was excited by low-frequency harmonic acoustic disturbances. All experimental evaluations were performed in the cabin mockup of a small aircraft at the Dynamics and Acoustics Laboratory.

5.3.1 Interaction between opposite-placed systems

At the outset of the evaluation of opposing local ANC systems (Figure 5.6a), only the first seat's active headrest was activated, and subsequently, the activation of the opposite system followed. In addition, the 2-input-2output mixed error FxLMS of section 2.5.1 was used as control algorithm for both systems. A reduction of 8 dB in the overall sound pressure level was achieved as illustrated in Figure 5.6b, and this reduction was consistent in both cases.

(a) Opposite local ANC systems in the small aircraft cabin mockup installed in the Dynamics and Acoustics Laboratory

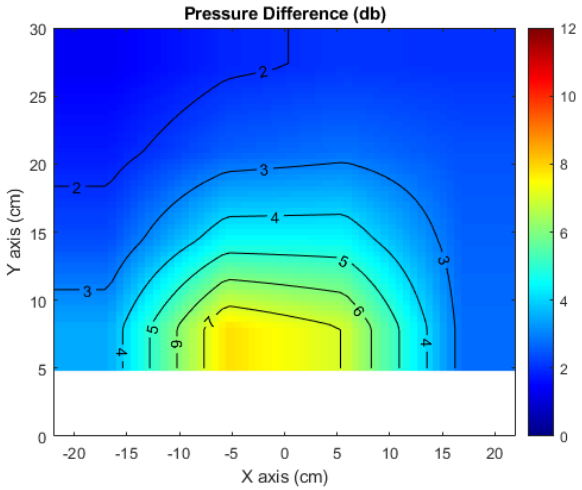

(b) Quiet zone at ear level when one system is activated

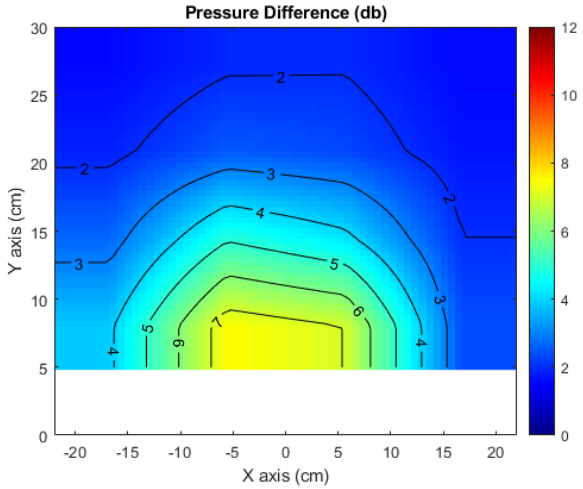

(c) Quiet zone at ear level when both opposing systems are activated

Figure 5.6: Opposing local ANC configuration and quiet zones in front of them

There was a slight improvement (about 0.5 dB) in performance when the system operated without interference from the opposing headrest (Figure 5.6b). In terms of the amplitude of main harmonic components, there was a reduction of 9 dB in the amplitude of the 119 Hz harmonic when the active headrest functioned as a stand-alone system. However, when both systems were active, the mitigation of the 119 Hz amplitude decreased to 7 dB. Another difference between the two spectra has to do with the harmonic at 48 Hz which was reduced by 5 dB more when both opposite headrests were activated. Conversely, the mitigation of the 72 Hz harmonic was reduced when the opposite active headrest was activated.

To sum up, although the attenuation of different harmonics varied when the opposing headrests were activated, both the overall SPL reduction and the system's stability were maintained in front of the headrests in the cabin mockup. This result matches the

simulation results even if there were no PML at the cabin ends in the experiment. Thus, it appears that two active headrests located opposite to each other can operate within a small enclosure with little decrease in performance. However, as we will see in the following section the acoustic pressure attenuation is limited through the quiet zone in front of the speakers and in some parts of the cabin there can be an amplification as demonstrated in the simulations of the two-dimensional model.

5.3.2 Four autonomous local ANC systems

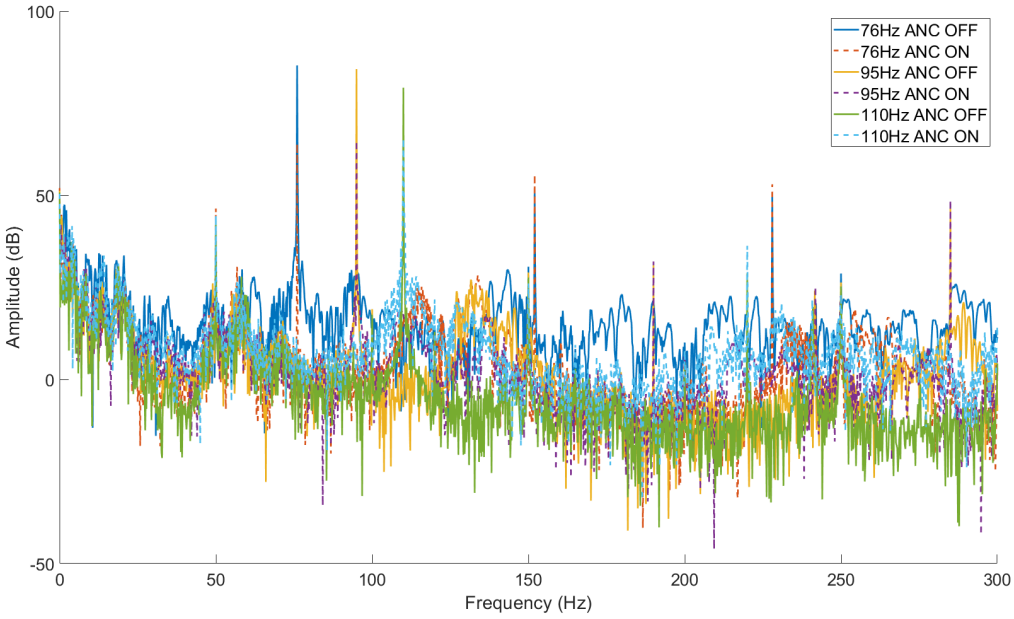

Figure 5.7: Frequency spectrums before and after the activation of four autonomous ANC systems, captured at the position of the error microphone for three harmonic acoustic disturbances at 76 Hz, 95 Hz and 110 Hz.

In this section, the performance of four local ANC systems is investigated when they operate simultaneously within the small aircraft cabin mockup. A single-input, single-output FxLMS algorithm was used for each individual system. In terms of hardware, four subwoofers and four microphones were used. The subwoofers were placed in the four corners of the cabin, as shown in Figure 5.10. In addition, single frequency harmonic acoustic disturbances that can be encountered in small aircraft cabins were used as noise sources for the system evaluation. Thus, harmonic disturbances with frequencies, 76 Hz, 95 Hz and 110 Hz, which have been occasionally identified in measuring campaigns of the Dynamics and Acoustics Laboratory, were selected.

The graph in Figure 5.7 depicts the frequency spectra, which were measured at the error microphone of system 1 (depicted in Figure 5.10a) under various conditions. Specifically, the spectra were obtained when the ANC was either enabled or disabled, and when

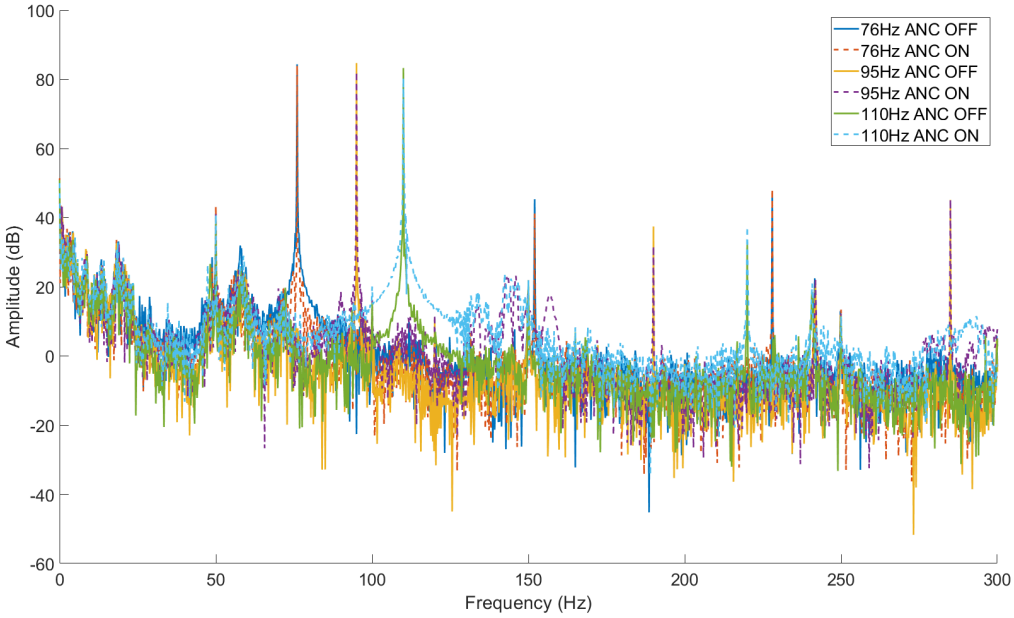

Figure 5.8: Frequency spectrums before and after the activation of four autonomous ANC systems, captured 20 cm from the error microphone for three harmonic acoustic disturbances at 76 Hz, 95 Hz and 110 Hz.

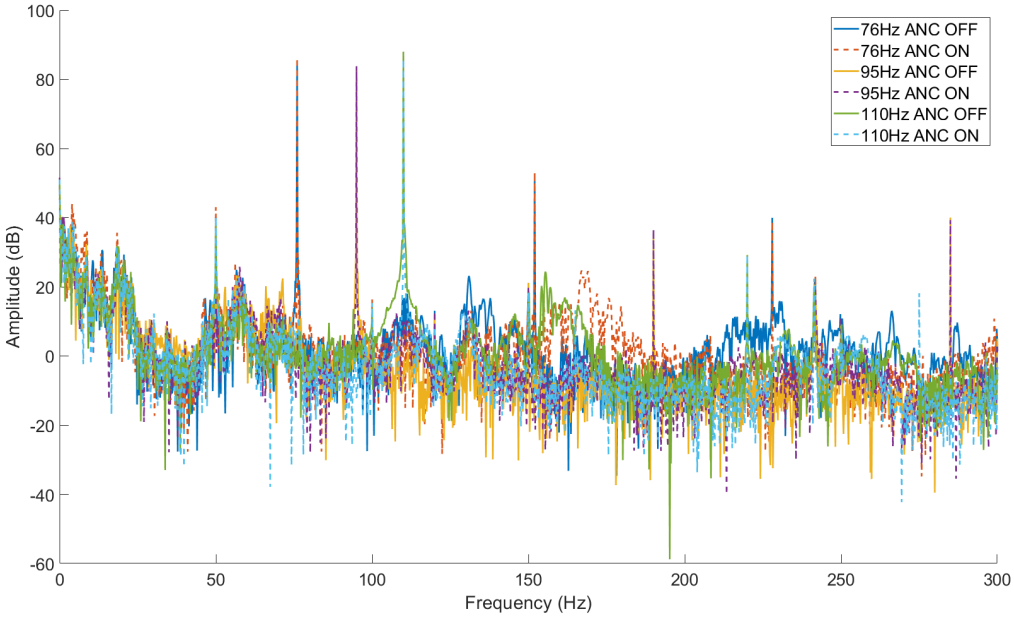

Figure 5.9: Frequency spectrums before and after the activation of four autonomous ANC systems, captured 40 cm from the error microphone for three harmonic acoustic disturbances at 76 Hz, 95 Hz and 110 Hz.

the cabin was excited by the aforementioned harmonic acoustic disturbances.

The results of the measurements at the three different frequencies indicate a substantial decrease in SPL, equal to or greater than 15 dB, when the frequency spectrums were

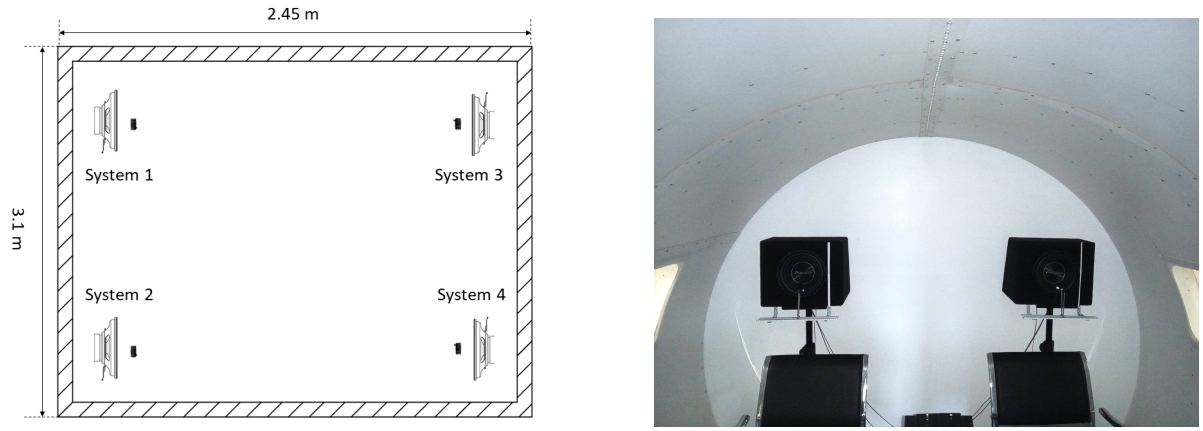

(a) (b)

Figure 5.10: a) Top view of the cabin mockup with four single-input single-output ANC systems, b) subwoofers of adjacent systems.

recorded at the error microphone. Specifically, the amplitude of the frequency at 75 Hz decreased by 15 dB, at 96 Hz by 19 dB, and at 110 Hz by 17 dB (Figure 5.7). Similar decreases were observed at the error microphones in front of the other systems (systems 2, 3, 4). When the frequency spectrum was recorded 20 cm in front of the error microphones, the SPL reduction was zero for the acoustic disturbance at 75 Hz, while it was only 2 dB at 96 Hz and 3 dB at 110 Hz (Figure 5.8). Additionally, when the measurement microphone was located 40 cm from the error microphone of system 1, an increase of 1 dB in SPL was observed at 76 Hz, a reduction of zero dB at 95 Hz, and a reduction of 2 dB at 110 Hz (Figure 5.9).

Furthermore, assuming the speed of sound at a temperature of $25°C$ to be 346.1 m/s, we can determine the wavelengths of the three acoustic disturbances. Consequently, the wavelength of 75 Hz is 4.55 m, the one of 96 Hz is 3.64 m, and the one of 110 Hz is 3.15 m. At a distance of 20 cm from the error microphone, which corresponds to $\lambda/23$ for 76 Hz, $\lambda/18$ for 95 Hz, and $\lambda/16$ for 110 Hz, the SPL attenuation is negligible or very small, causing no discernible effect on a human's perception. As a result, the autonomous ANC, randomly placed in the small enclosure of the cabin mockup, can create a quiet zone in front of each loudspeaker that extends almost $\lambda/10$ from the error microphone [52]. In other areas of the cabin, the SPL attenuation is very small or even exhibits areas of increased acoustic pressure. Finally, it is important to note that the simultaneous operation of four autonomous ANC systems within the cabin can result in the excitation of acoustic modes that are unrelated to external sound sources, which may negatively impact the noise reduction effect in the enclosure.

5.4 Concluding remarks

In this chapter, we examined the behaviour of several autonomous local ANC systems when operating simultaneously in the same enclosed space. Our findings, which were based on 2D and 3D simulations, demonstrated that a quiet zone is created in front of the speakers. However, when two adjacent systems cooperate, there are several advantages, including limiting the hardware used and keeping the SPL in cabin spaces away from the quiet zone at low levels. In contrast, when six stand-alone systems are operated simultaneously, an increase in acoustic pressure in the areas between them was observed. Furthermore, our experiments revealed that ANC systems placed opposite to each other at a distance of about 2 meters maintain their stability, although a small decrease in performance of 1-2 dB is observed. Finally, we found that placing local single channel systems in a random manner in an enclosure does not guarantee a global control of the sound field of the cabin. Therefore, alternative methods should be sought if global control is desired. In the following Chapter, a novel approach to global noise control is presented.

CHAPTER 6

Global ANC with Active Sound Absorbers

6.1 Introductory notes

In previous chapters, we have developed local ANC systems to create areas near passenger headrests in aircraft cabins or yachts with reduced acoustic pressure, which are called Quiet Zones. In Chapter 5, we also analyzed the interaction between these systems and their effects on the cabin's enclosed sound field, particularly in areas far from these zones. Thus, we discovered that the use of multiple stand-alone active headrests, along with the use of multiple actuators and sensors and the need for increased computational power, can result in increased acoustic pressure in some cabin areas, which can be a significant issue.

To overcome this problem, global ANC systems have been proposed that aim to reduce acoustic pressure throughout the entire cabin. One approach to global ANC involves minimizing the potential acoustic energy of the cabin by minimizing the sum of squares of a series of error signals. These signals are obtained using microphones placed at different positions of the enclosure, to observe the acoustic modes, which are responsible for the acoustic disturbance. An adaptive algorithm then calculates the antinoise signal, which drives the loudspeakers scattered throughout the cabin. Such systems have been evaluated during in-flight experiments, demonstrating good results [27], [67]. Several methods have also been suggested for optimizing the placement and quantity of microphones and speakers in global ANC systems [68], [118]–[120]. Moreover, a technique that explicitly predicts the sound field within an enclosure was compared with the optimum active noise

control sensor and actuator positioning method based on the modal analysis of an enclosure. This was found to be more accurate for realistic enclosures [121], and was employed to simulate the acoustics of a car cabin, demonstrating that a single optimized secondary source could couple efficiently with the single primary source [122].

Another approach has to do with the reduction of structure-borne noise. Extensive research has been conducted on the propagation of structure-borne noise in order to reduce acoustic pressure in cabins. A sensorless system that employs an electrically excited inertial actuator was proposed with the aim of reducing the sound power radiated from an aircraft trim panel [123]. Authors of [124] designed an active structural acoustic control system to mitigate helicopter gear meshing noise. Additionally, the authors of [15] mounted inertial force actuators on aircraft linings, achieving an SPL attenuation of approximately 10 dB in front of them. However, a drawback of these methods is that they cannot control airborne noise, despite the fact that air serves as an important propagation path for acoustic disturbances within aircraft cabins.

In this Chapter, the global ANC of an enclosed sound field is investigated using active sound absorbers, strategically located throughout an aircraft cabin mockup installed in the Dynamics and Acoustics laboratory. This approach can prove highly effective in the low frequency band, where a small enclosure is characterized by a low modal density. Sound absorbers aim to change the acoustic impedance of boundaries to achieve absorption [125]. A hybrid passive-active absorber based on the minimization of the acoustic pressure at the rear face of a porous layer was proposed in [126], with the goal of reducing noise transmitted out of an enclosure. Additionally, the authors of [71] investigated an electroacoustic absorber that combined sensor- and shunt-based techniques for damping low frequency modes in a waveguide. They achieved promising results that can potentially be replicated in a three-dimensional enclosure with appropriate modifications.

Other studies have also employed the wave separation method, which separates the sound waves into incident and reflected by using the p-p sound intensity measurement principle [127]. Thus, perfect absorption is achieved by minimizing the reflected components [128], [129]. Iwamoto et al. proposed a methodology that employs the damping of acoustic modes by absorbing reflected sound wave components to achieve global attenuation in a rectangular enclosure [130]. Meanwhile, an active wave control method for a small rectangular cavity using loudspeakers and microphones was also proposed and experimentally proven in another study [131]. Norambuena et al. demonstrated through three-dimensional simulations that low frequency sound fields inside rectangular rooms can be significantly attenuated by placing active sound absorbers based on the reflected wave minimization principle at the boundaries [10]. Heuchel et al. used loudspeakers and an array of microphones near the wall of a lecture hall to attenuate low frequency room modes [70]. The plane wave decomposition technique was used to perform wave separation, resulting in an SPL attenuation exceeding 10 dB in the frequency band between 30

and 120 Hz. Finally, Santillan et al. achieved the equalization of a rectangular room's low frequency response (up to 425 Hz) by filling a wall with loudspeakers and minimizing the cost function calculated using acoustic pressures measured by 76 microphones arranged in two planes in the center of the room [132].

Although the method of placing active sound absorbers has been used in order to equalize the low frequency response of small enclosures, it has never been used for attenuation of low frequency acoustic disturbances in small aircraft cabins. The fact that the acoustic disturbances in small propeller-driven aircrafts are characterized by low frequency harmonics of the Blade Passage Frequency, along with the acoustic mode sparsity in this frequency band, make sound field shape predictable. As a result, if active sound absorbers that are highly effective at low frequencies are strategically placed to equalize the dominant acoustic modes of the cabin, then a significant reduction in SPL can be achieved. This is the main idea behind the global ANC technique presented in this chapter. Its main advantages are: a) the reduction of acoustic pressure at locations remote from the system microphones, unlike conventional active noise control approaches that create quiet zones around them, b) the need of a small number of sensors and actuators and c) the relatively small portion of the cabin surface covered by sound absorbers, thereby meeting the weight restrictions of modern aircraft.

6.2 Active control of absorption coefficient

As mentioned in the previous section, the active sound absorbers, that are employed in the proposed methodology, are based on the active control of the absorption coefficient. This is achieved by decomposing the sound waves propagating into the enclosure into incident and reflected, and subsequently the minimization of the reflected component. This process is thoroughly described in the following lines.

A plane wave traveling through a long, narrow duct with a diameter much smaller than the wavelength and a rigid termination at one end can be considered as a one-dimensional sound field. By placing two microphones at a relatively close distance compared to the wavelength, the acoustic pressure at the midpoint can be separated into two components. The first component is due to the incident wave, while the second is due to the reflected wave. The two components are measured using the p-p sound intensity principle, which determines the acoustic pressure and particle velocity at the midpoint between the two microphones [133]. The following analysis is also presented by Zhu et al. [129]. The incident and reflected components are given by Eqs. 6.1 and 6.2.

$$p_i = \frac{1}{2}(p + \rho c u) \tag{6.1}$$

and

$$p_r = \frac{1}{2}(p - \rho c u) \tag{6.2}$$

where p_i and p_r are the acoustic pressures caused by the incident and the reflected wave respectively, ρ is the density of the propagation medium, c is the speed of sound and p, u are the acoustic pressure and the particle velocity at the midpoint of the two microphones, which can be computed from Eqs. 6.3 and 6.4.

$$p(t) = \frac{p_1(t) + p_2(t)}{2} \tag{6.3}$$

and

$$u(t) = \frac{1}{\rho d_p} \int_0^t (p_1(\tau) - p_2(\tau))\, d\tau \tag{6.4}$$

where d_p is the distance between the two microphones.

Thus, for a one-dimensional sound field, Eqs. 6.1-6.4 can be used to calculate the incident and reflected components of the acoustic pressure. Furthermore, the absorption coefficient at a given boundary for a plane wave of normal incidence is given by Eq. 6.5:

$$a = 1 - |R^2| \tag{6.5}$$

where R is the reflection factor given by Eq. 6.6.

$$R = \frac{p_r}{p_i} \tag{6.6}$$

The control of the absorption coefficient can be achieved by modifying the reflection factor. Let R_0 denote the desired reflection factor. Then the error that has to be minimized derives from Eqs. 6.6 and 6.7.

$$e(n) = R_0 - R = R_0 - \frac{p_r(n)}{p_i(n)} \tag{6.7}$$

where n denotes time in discrete signals. If the Mean Square Error criterion is used for the minimization of $e(n)$, the cost function is given by Eq. 6.8:

$$J = \mathbb{E}\{|e(n)|^2\} = \mathbb{E}\{|R_0 - \frac{p_r(n)}{p_i(n)}|^2\} \tag{6.8}$$

Furthermore, in order to achieve perfect absorption a must be equal to 1 and R_0 equal to 0. As a result, Eq. 6.8 becomes:

$$J = \mathbb{E}\{|\frac{p_r(n)}{p_i(n)}|^2\} \tag{6.9}$$

J is minimized when p_r is minimum. Thus, the cost function that has to be minimized in order to achieve maximum absorption derives from Eq. 6.10.

$$J_{abs} = \mathbb{E}\{|p_r(n)|^2\} = minimum \tag{6.10}$$

This optimization problem can be solved using the well-known FxLMS algorithm [129]. According to the FxLMS the coefficients of the N-length adaptive filter are computed from Eq. 6.11.

$$w(n+1) = w(n) - ux'(n)p_r(n) \tag{6.11}$$

where w is the vector of the FIR filter coefficients, u is the step size and $x'(n)$ is a synthesized reference signal filtered by the model of the secondary path with respect to the reflected component of the acoustic wave (Eq. 6.12).

The method for obtaining the secondary path model $s'(n)$ involves utilizing the LMS algorithm during a preliminary identification stage. During this process, the loudspeaker acts as an active absorber and reproduces a white noise signal, which is used as a reference for the LMS algorithm. Additionally, the acoustic pressure from the reflected wave (p_r) is employed in the computation of the identification error. It is important to note that in comparison to the identification process of the secondary path in Active Noise Cancellation systems, where the measured acoustic pressure at the cancellation point is used, p_r must be computed using Eq. 6.2 in the case of an Active Absorption system. Therefore, the filtered reference signal of Eq. 6.11 is derived from Eq. 6.12.

$$x'(n) = x(n) * s'(n) \tag{6.12}$$

where $x(n)$ is the reference sinusoidal signal. The frequency of the signal is the one where absorption is intended. In addition, * denotes the convolution operator. After this analysis, the driving signal of the active absorber derives from Eq. 6.13 as:

$$y(n) = w(n) * x(n) \tag{6.13}$$

6.3 Sound absorber positions in the cabin mockup

At low frequencies, where the wavelengths are roughly equivalent to the dimensions of the enclosure, the enclosed sound field is primarily influenced by the excitation of acoustic modes. In this context, the modal density is relatively low, which allows for an accurate estimation of the acoustic pressure distribution. This, in turn, can facilitate the effective application of Active Noise Control techniques, as outlined in the work of [134]. The acoustic pressure within an enclosure can be expressed as the sum of the mode shape functions, which are orthogonal. Therefore, if the acoustic modes that make a signifi-

cant contribution can be damped, then the acoustic pressure within the cabin of a small propeller-driven aircraft, which is primarily characterized by the low-frequency harmonics of the Blade Passage Frequency, can be reduced. An active absorber based on the wave separation method, as previously discussed, is effective for one-dimensional acoustic waves with normal incidence. In three dimensions, absorption can be achieved for waves propagating in the direction of the diaphragm's surface normal vector, as detailed in the research of [135]. This occurs as a result of the decomposition into incident and reflected waves, as well as the minimization of the reflected component in this particular direction.

Therefore, the subwoofers of the global ANC system, based on sound absorption, must be arranged in such a way that their diaphragms are perpendicular to the direction of wave propagation. In addition, they must be placed in both positive and negative directions to attain maximum absorption for a specific dimension [10]. To employ the wave separation method, a microphone pair must be placed in close proximity to the subwoofers. Following this, the FxLMS algorithm described in section 6.2 is applied. It is important to note, that the attenuation of the acoustic pressure can be increased, if the subwoofers are placed near a pressure maximum (antinode), as this is the location where the acoustic mode can be detected by the microphones of the active absorber [68]. By adhering to these guidelines, it is possible to determine the optimal positioning of the subwoofers based on the spectral characteristics of the low-frequency acoustic disturbance.

As previously stated, the knowledge of the shapes of acoustic modes is crucial for determining the optimal placement of active sound absorbers and attaining the maximum attenuation of acoustic pressure. Figure 6.1 depicts the first six mode shapes and their corresponding frequencies for an aircraft cabin mockup measuring 310 cm in length, 245 cm in width, and 200 cm in height, with sound-hard walls, installed in a laboratory. Given that this enclosure is a horizontal cylindrical segment, the acoustic pressure can be expressed as a combination of azimuthal and longitudinal acoustic modes. The order of the longitudinal modes is denoted by the parameter i, while the order of the azimuthal modes is represented by the parameter j. Moreover, the value of j affects the distribution of acoustic pressure. According to Figure 6.1, the first six modes correspond to $(i, j) = (1, 0), (0, 1), (1, 1), (0, 2), (1, 2), (2, 0)$. Finally, Figure 6.1 also indicates the location where the acoustic pressure attains its maximum value for each mode shape. With this information, it is possible to determine the positions of the active sound absorbers to achieve global attenuation of the acoustic pressure in the enclosure for low-frequency acoustic disturbances.

6.4 Computer simulation analysis

The method of active sound absorption described in section 6.3 was initially evaluated though FEM simulations using the Acoustics module of Comsol Multiphysics®. The

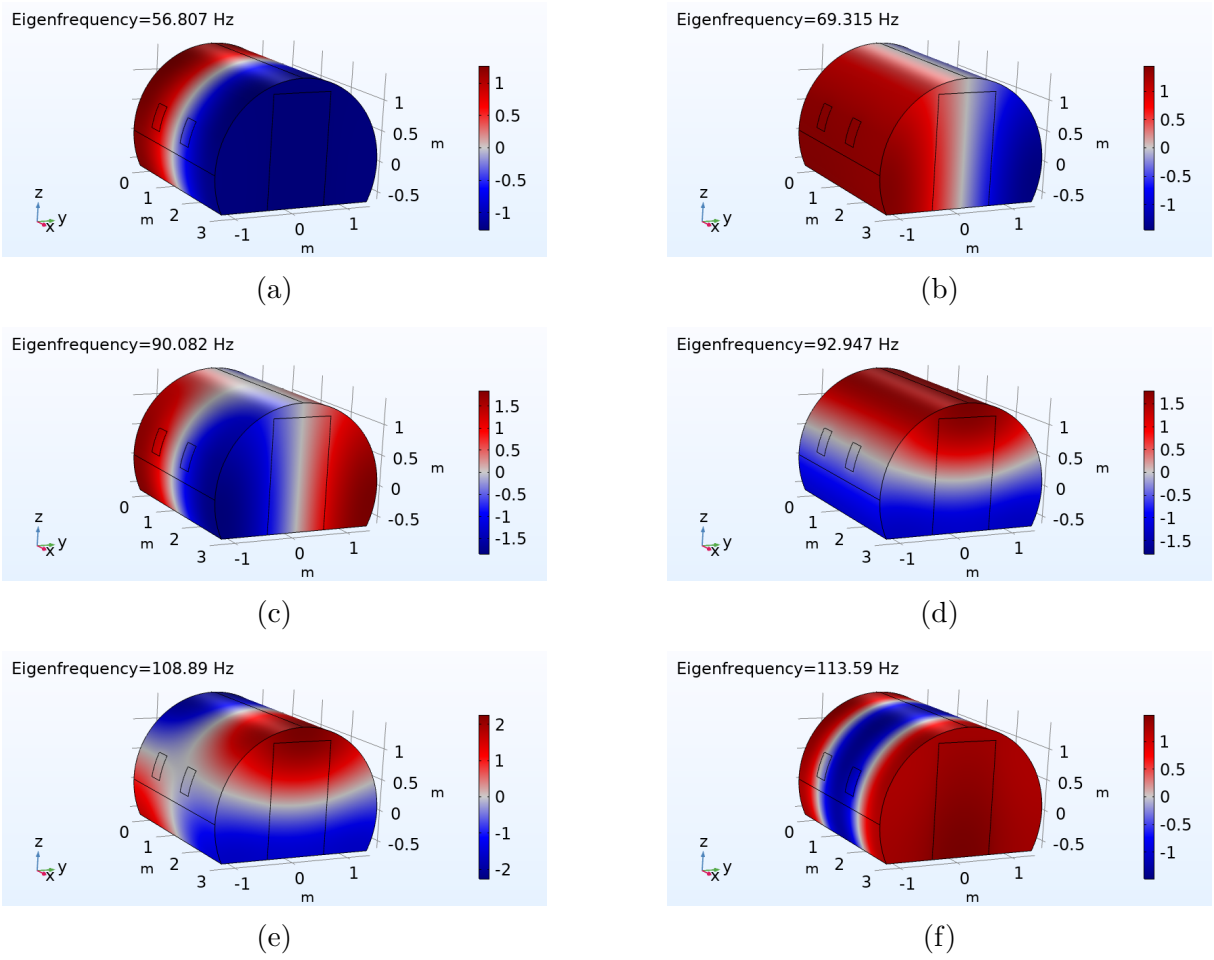

Figure 6.1: Acoustic modes of the aircraft cabin mockup up to 113 Hz and acoustic pressure distribution for each mode.

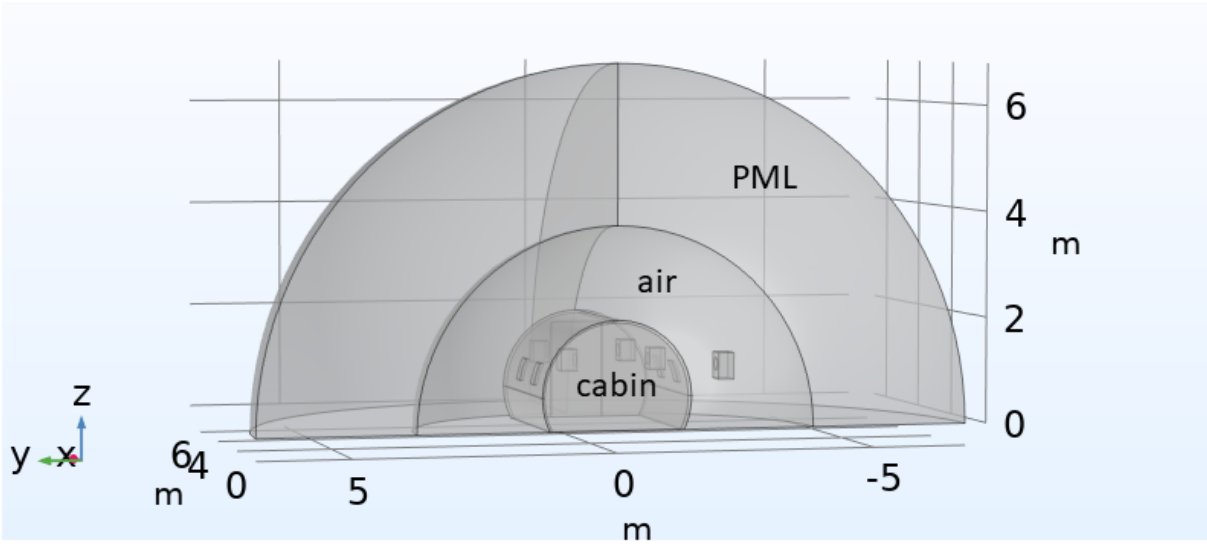

Figure 6.2: Geometry of the model developed for FEM simulations of the proposed method.

model's geometry, which is depicted in Figure 6.2 consisted of the cabin mockup, a quarter spherical domain of air and a Perfectly Matched Layer. In addition, four active absorbers were employed, in order to attenuate the acoustic disturbances that consisted of the first acoustic modes of the cabin mockup. Moreover, the wave separation method necessitated the placement of microphones at the same height as the center of the diaphragm of the active absorbers. More specifically, the distance between the diaphragm surface and the first microphone was set at 10 cm, while the distance between the two microphones was set at 3 cm. It is important to note that the distance should be small in comparison to the wavelength of the acoustic disturbances being absorbed, in order for the wave separation method to be applicable. Subsequently, the enclosure was excited by an external noise source positioned near it, and the acoustic disturbance was sinusoidal. Three of the cabin's acoustic resonances, namely (1,0), (0,1), and (0,2), as well as 110 Hz, were selected as the excitation frequencies.

In an enclosure with non-rigid walls, the acoustic resonances differ slightly from those of an enclosure with sound-hard boundaries [52], [136]. This is reflected in the first resonance of the aircraft cabin mockup model, which appeared at 61 Hz along the x-axis (Figure 6.3a) instead of the expected 56.807 Hz, corresponding to the hard-walled model (Figure 6.1a). When subjected to a sinusoidal acoustic disturbance at 61 Hz, the SPL attained a maximum value of 100 dB at both $x = 0$ and $x = L$, a realistic value for the interior of an aircraft cabin, according to [22], [137]. The active absorbers were positioned with the loudspeaker diaphragms perpendicular to the x-axis and near the maximum SPL locations, as detailed in Section 6.3. Furthermore, they were placed opposite to each other to provide absorption in both positive and negative directions [135].

The SPL attenuation at the x-y plane located at a height of 120 cm (Figure 6.3b) demonstrated a range of 12 to 20 dB when four active absorbers were enabled. As anticipated, the highest attenuation was observed at the midpoint between the two microphones used in the wave separation method, with the microphones placed at a height of 120 cm, corresponding to the level of a sitting passenger's head. The SPL across the cabin significantly decreased, as indicated by the SPL surfaces parallel to the x-z plane (Figure 6.3b). The maximum SPL of 88 dB was observed in areas near the walls of the cabin at x=0, L, while the minimum SPL of 62 dB was observed near the center of the cabin at x=L/2. The variation in acoustic pressure after the activation of the absorbers is related to the shape of the sound pressure field prior to their activation. Since the attenuation remains constant at 12 dB in remote areas of the cabin, the areas with the maximum SPL before the activation of the absorbers, maintained the highest values after their activation. Similarly, the areas with low SPL before activation experienced an even lower SPL afterward.

The second acoustic mode of the non-rigid walled cabin mockup was observed at 76 Hz and corresponded to $i = 0$ and $j = 1$. When the cabin was excited by this mode, the

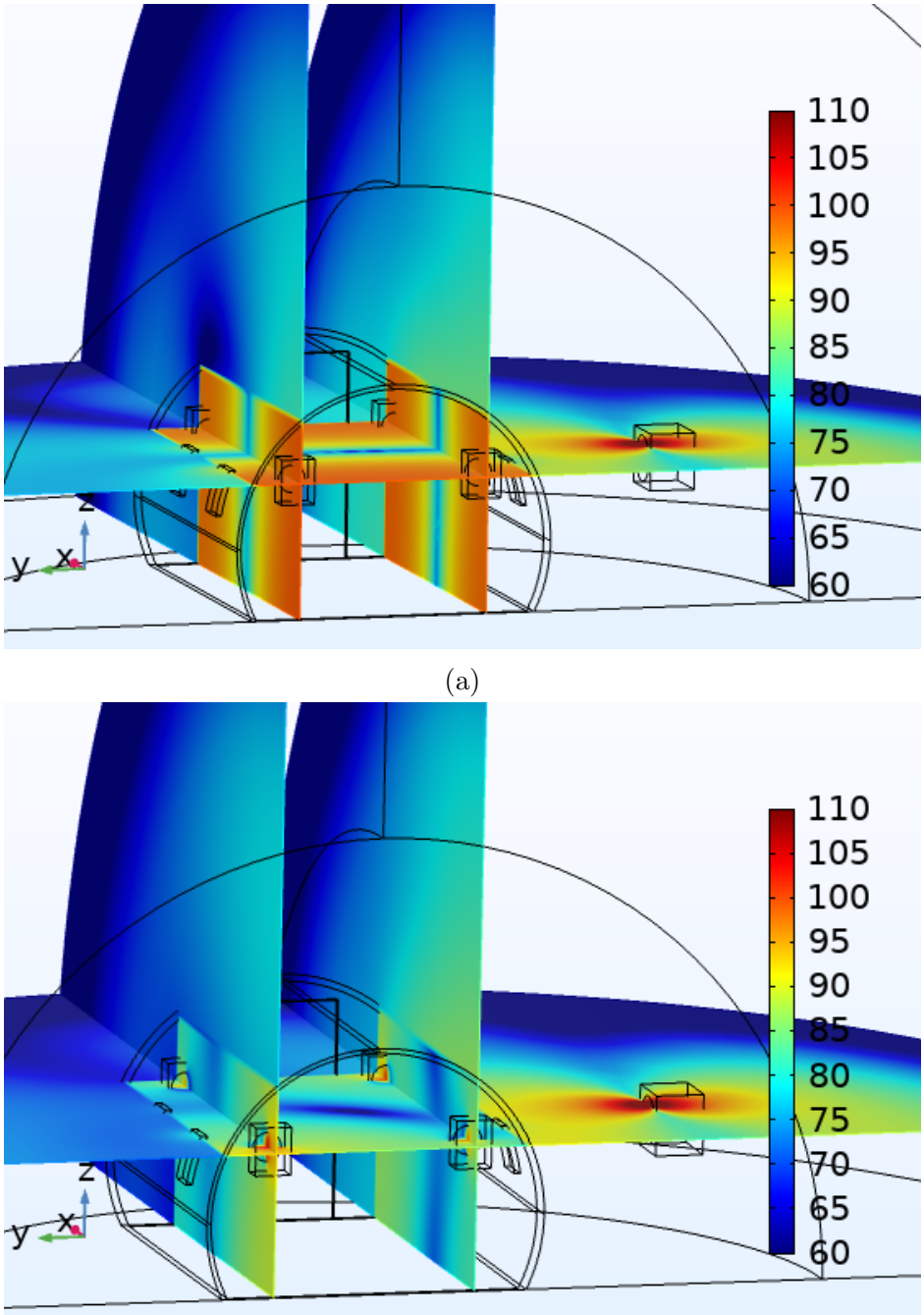

Figure 6.3: Sound Pressure Level (dB) in cabin model at two planes symmetrically located 0.85 m from x-z plane of symmetry and at one plane parallel to x-y plane (z=120 cm) (a) before and (b) after the activation of the sound absorbers. The cabin was excited by the longitudinal acoustic mode (1,0) at 61 Hz and diaphragms of active sound absorbers were set perpendicular to x-axis.

active absorbers were positioned on the cabin floor, where the maximum acoustic pressure was observed. The diaphragms were oriented perpendicular to the y-axis. Prior to the activation of the active absorbers, the maximum SPL in the cabin reached 104 dB near the walls (Figure 6.4a). Due to the acoustic mode shape, the SPL was lower in the cabin's

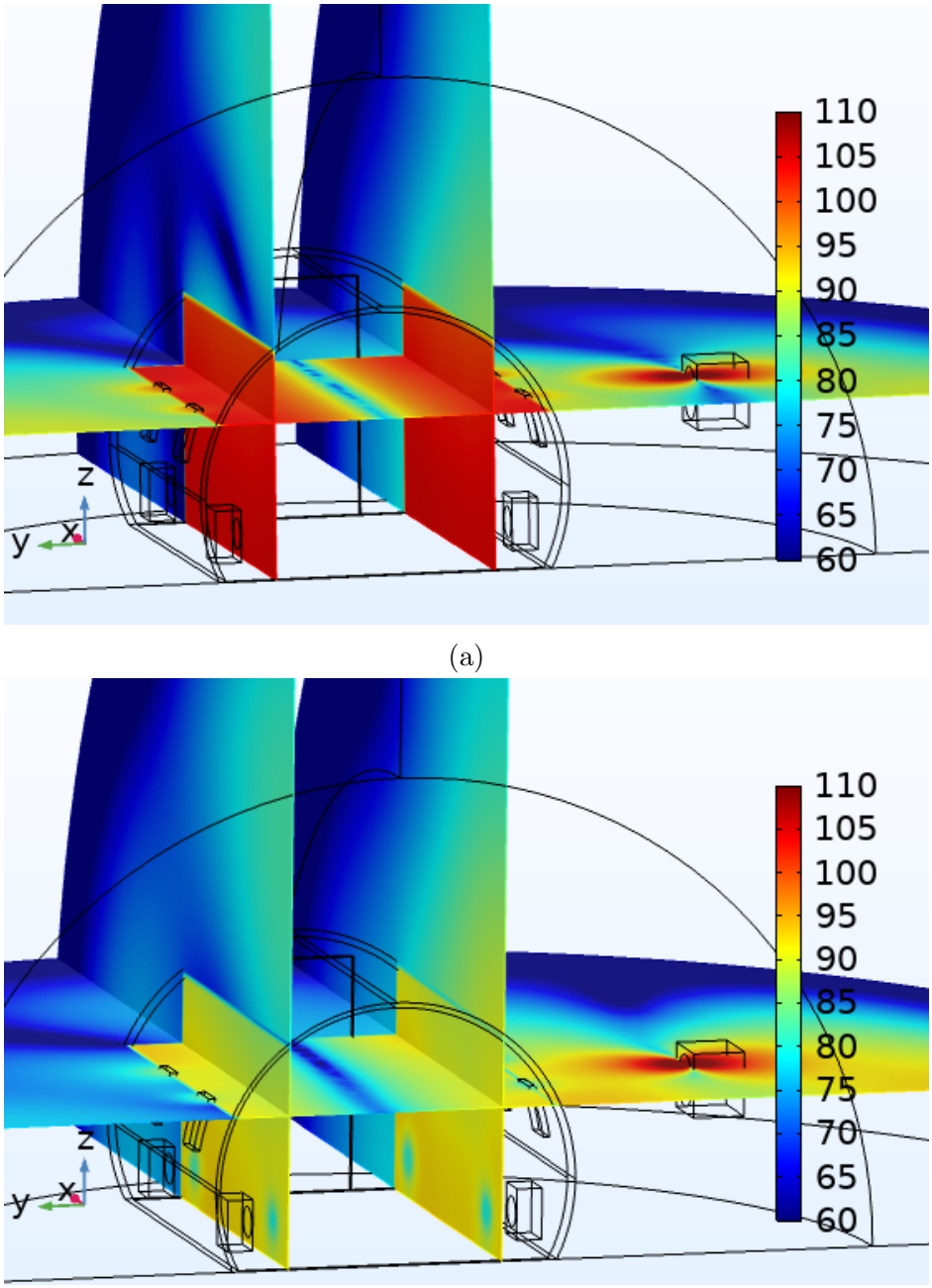

Figure 6.4: Sound Pressure Level (dB) in cabin model at two planes symmetrically located 0.85 m from x-z plane of symmetry and at one plane parallel to x-y plane (z=120 cm) (a) before and (b) after the activation of the sound absorbers. The cabin was excited by azimuthal acoustic mode (0,1) at 76 Hz and diaphragms of active sound absorbers were set perpendicular to y axis.

center, ranging from 75 dB to 81 dB. Following the activation of the absorbers, the global attenuation ranged from 13 to 24 dB. Additionally, at 120 cm, the SPL reduction reached 14 dB (Figure 6.4b), resulting in a significant global attenuation of the acoustic pressure.

Furthermore, when the cabin was excited by a 95 Hz sinusoidal acoustic disturbance that coincided with the resonance frequency of 92.947 Hz ($i = 0, j = 2$) of the sound-hard

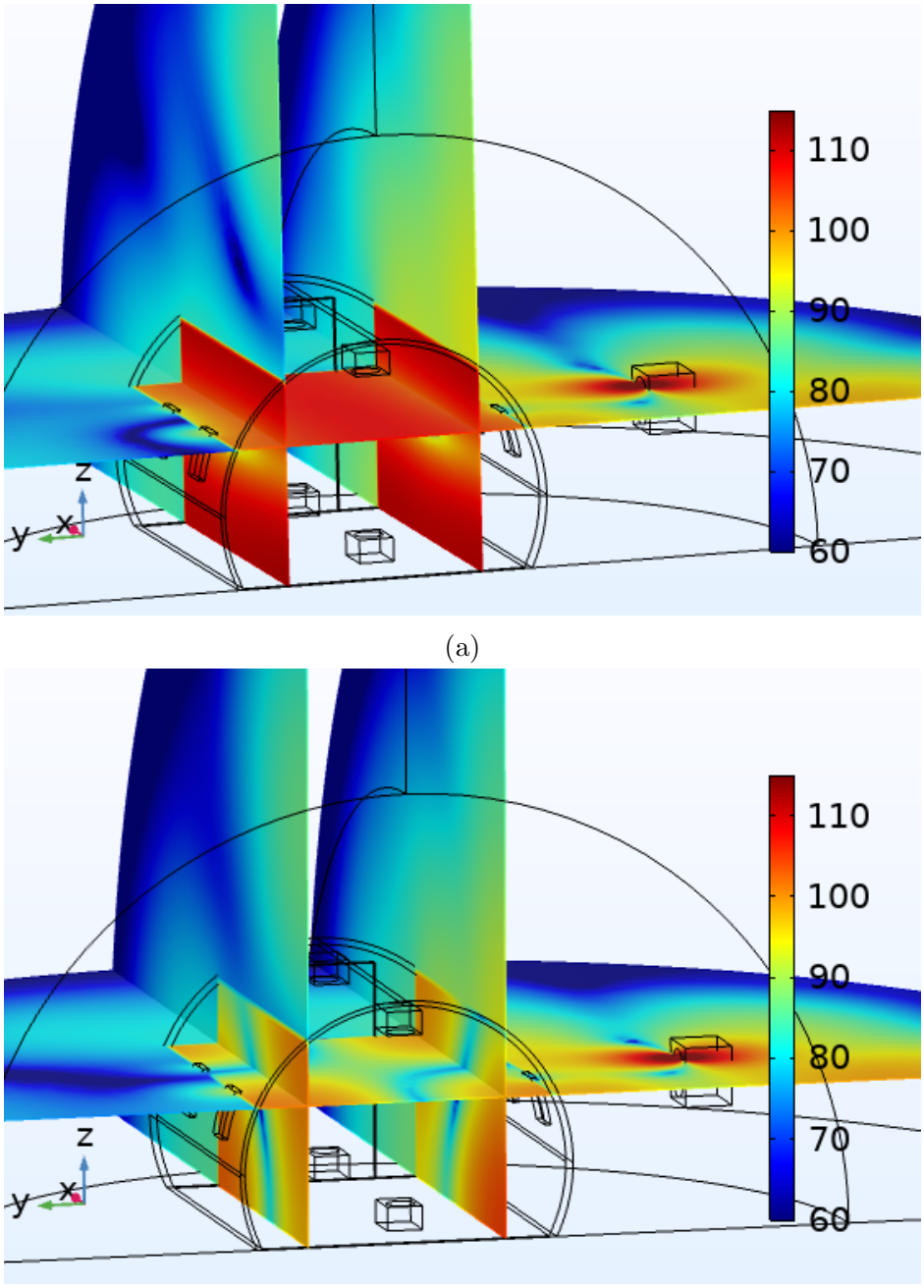

Figure 6.5: Sound Pressure Level (dB) in cabin model at two planes symmetrically located 0.85 m from x-z plane of symmetry and at one plane parallel to x-y plane (z=120 cm) (a) before and (b) after the activation of the sound absorbers. Cabin was excited by azimuthal acoustic mode (0,2) at 95 Hz and diaphragms of the active sound absorbers were set perpendicular to z axis.

walled cabin (Figure 6.1d), the SPL at a height of 120 cm ranged from 105 to 108 dB (Figure 6.5a). The active absorbers were placed in three different setups, with absorbing surfaces oriented perpendicularly to the x, y, or z axes, in order to discover which one was mare efficient in terms of SPL attenuation. The maximum attenuation was obtained when the absorbers were placed perpendicularly to the z-axis, with the y-coordinate set to

0, due to the shape of the acoustic field, as depicted in Figure 6.1d. The SPL attenuation within the cabin was primarily 20 dB (Figure 6.5b), but at the corners of the cabin it was only 4 dB, which can be attributed to the placement of the absorbers along the x-z (y=0) plane. To enhance the SPL attenuation in these areas of the cabin, additional absorbers should be placed nearby. It is important to note that the orientation of the additional loudspeakers must be carefully selected to achieve maximum acoustic pressure reduction, since absorption is achieved for the wave propagation component perpendicular to the loudspeaker diaphragm. While the installation of additional subwoofers improves performance, it also increases the overall system complexity, and the case of resonance at 95 Hz is not comparable to the other resonances when four subwoofers are utilized and therefore four subwoofers were employed.

Finally, the cabin was excited by a 110 Hz harmonic acoustic disturbance, as this frequency is usually encountered in small propeller-driven aircraft cabins. When the absorbing surfaces were again placed perpendicularly to z-axis, the acoustic pressure was significantly reduced. Thus, a global SPL attenuation of more than 10 dB was observed. Particularly, at the 120 cm z-plane, where SPL reached 95 dB, a reduction of more than 15 dB was observed following the activation of the sound absorbers. This particular absorber setup is efficient for this acoustic disturbance, because it performs damping to $(i = 0, j = 2)$ acoustic mode, which is the most significant in forming the shape of this particular sound field.

6.5 Experimental evaluation

The experimental evaluation took place in the cabin mockup for a 61 Hz sinusoidal acoustic disturbance. Four active sound absorbers were placed in the way depicted in Figure 6.3b, in order to achieve maximum SPL attenuation. Furthermore, 36 measurement microphones were selected to capture the acoustic pressure reduction prior to and subsequent to the activation of the active absorbers, as depicted in Figure 6.7. Along the x-axis, the distance between the measurement points and the absorber diaphragm was 30 cm for Points 1, 3, and 5, and 60 cm for Points 2, 4, and 6, respectively.

The distance between the measurement microphones and the floor of the cabin was 100 cm for Points 5 and 6, 120 cm for Points 3 and 4, and 140 cm for Points 1 and 2. As a result, the microphones were arranged in three planes that were parallel to the x-axis. Finally, 12 of the 36 measurement microphones were placed in the middle of the adjacent subwoofers in order to evaluate the attenuation of the acoustic pressure in areas of the cabin that were not directly in front of the diaphragms. These microphones were divided into two groups, with the front group denoted as F and the rear group indicated by R. Microphones F1-F6 were arranged in the same manner as the microphones in front of absorbers A and B, while microphones R1-R6 were placed in the same way as those in

Figure 6.6: The active absorber based on sound wave separation method

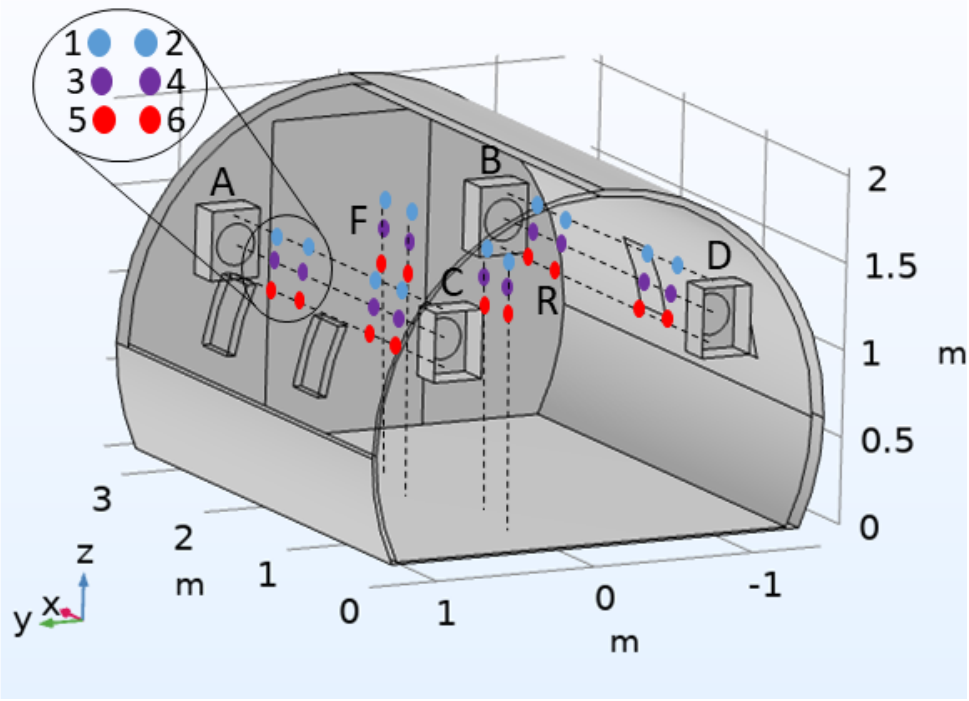

Figure 6.7: The 36 measurement microphones used for the monitoring of the performance of the proposed method. Each color corresponds to a z plane of the same height.

front of absorbers C and D.

The hardware utilized for the experimental evaluation of the active sound absorption method included four Pioneer® TS-A250S4 subwoofers, each rated at 400 Watts, and eight Shure® MX 183 omnidirectional microphones. Two of the microphones were situated in front of each subwoofer to implement the wave separation method (illustrated in Figure 6.6). The distance between the two microphones was set at 3cm, while the distance between the diaphragm of the subwoofer and the nearest microphone was 10cm, which aligns with the simulation configuration. To implement the algorithm that minimized the

reflected component of the acoustic wave, Python was utilized with the Motu® Ultralite AVB soundcard. The source code of both active absorption process and the secondary path modeling are presented in Appendix C.2 of this dissertation.

The evaluation of the proposed approach entails the progressive activation of four sound absorbers to assess the attenuation of sound pressure in each situation. Initially, only absorber A was activated, followed by the gradual activation of the other absorbers until they operated together. The SPL as well as the frequency spectra were measured at the 36 measurement points during the different scenarios. It is important to mention that the 61 Hz harmonic noise coincided with the longitudinal acoustic mode of the cabin mockup.

Activated sound absorbers	Attenuation (dB)		
	Min	Max	Avg
A	0	4	2.4
AB	3	8	6.4
ABC	7	10	7.8
ABCD	9	17	13.3

Table 6.1: Minimum, maximum and average attenuation of amplitude of 61 Hz acoustic disturbance during experimental evaluation of proposed methodology. Results were obtained from measurement of acoustic pressure at 36 different positions of cabin mockup when different number of active sound absorbers were activated.

As demonstrated in Table 6.1, the highest average amplitude attenuation of 13.3 dB was achieved among the 36 measurements when all four sound absorbers were activated. As shown in Figure 6.8, the frequency spectra captured by the monitoring microphones positioned 30 cm from the absorbing surfaces and 120 cm from the cabin floor for different numbers of activated absorbers reveal a maximum reduction of the 61 Hz amplitude when either three or four absorbers were activated. The amplitude reduction measured by Microphones A3, B3, and C3 was the same during the simultaneous operation of either three or four absorbers and reached 12 and 13 dB, respectively. However, the amplitude measured by measurement microphone D3 was further reduced by 7 dB when Sound Absorber D was activated, resulting in a total attenuation of 17 dB.

Additionally, when the monitoring microphones were positioned 60 cm from the diaphragms of the subwoofers, the amplitude reduction was less than that observed at 30 cm (as shown in Figure 6.9). The greatest reduction was achieved in front of absorber D, amounting to 14 dB, while it was 10, 11, and 10 dB at Positions A4, B4, and C4, respectively. Although the reduction of the harmonic amplitude was greater closer to the absorber diaphragms, as demonstrated in Figures 6.8 and 6.9, the final amplitude value was almost the same, resulting in an equalization of the acoustic pressure in front of each sound absorber. Moreover, at positions A4, B4, C4, and D4, the acoustic pressure was lowest when all four absorbers were activated, in contrast to Positions A3, B3, and C3,

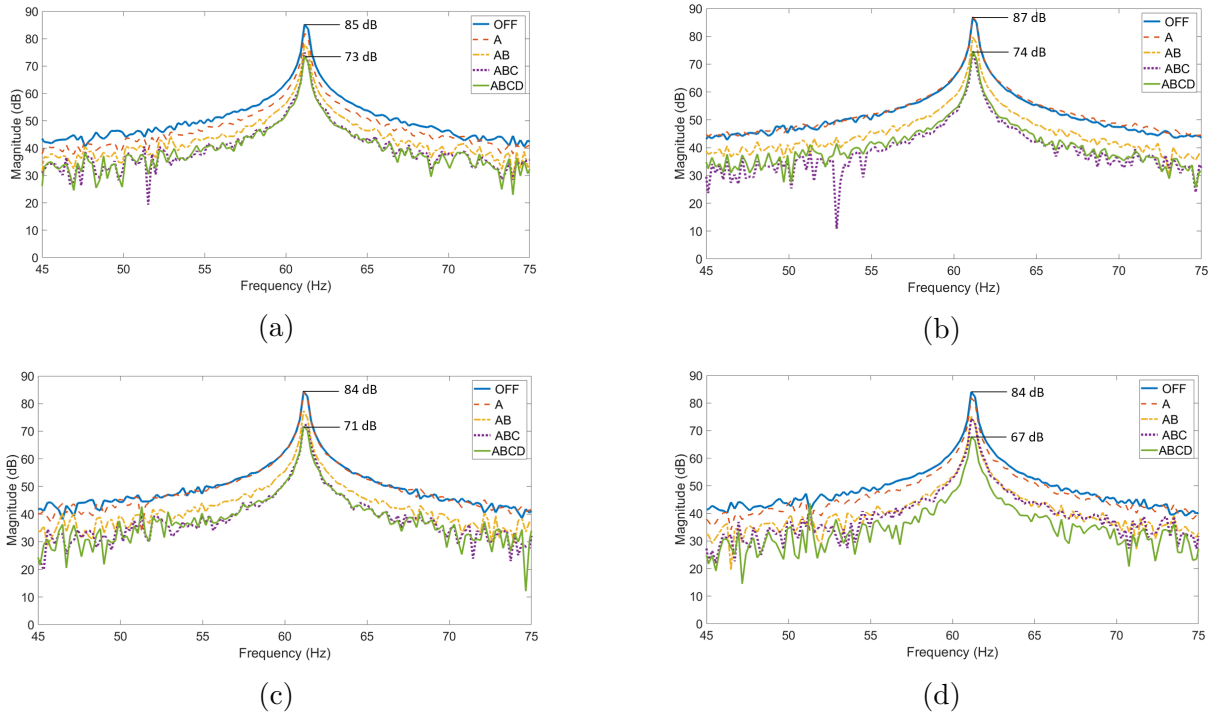

Figure 6.8: Frequency spectra captured by measurement microphones in front of sound absorbers (a) A, (b) B, (c) C and (d) D when they were gradually activated. "OFF" corresponds to the state when all absorbers were deactivated, "A" to the activation of absorber A, "AB" to the activation of both absorbers A and B etc. Measurement microphones were placed 30 cm from the subwoofer diaphragms and 120 cm from the cabin floor, which correspond to measurement microphones A3, B3, C3 and D3.

where the same harmonic amplitude was observed under both three and four activated absorbers.

Finally, the microphones located in the middle of the cabin (F1-F6 and R1-R6) measured a comparable reduction in acoustic pressure to those positioned in front of the absorbers (Figure 6.10). As a result, the amplitude of the 61 Hz peak was attenuated by 12, 10, 13, and 11 dB at Microphones F3, F4, R3, and R4, respectively, when all four absorbers were activated. This finding supports the contention that the proposed method effectively reduces the cabin acoustic pressure globally.

Moreover, the reduction in acoustic pressure at the monitoring locations 30 cm from the absorbers was greater when measured at points featuring a height of 120 cm, which coincides with the level at which the centers of the diaphragms of the loudspeakers are located. At heights of 100 and 140 cm, the reduction was less, as expected, as one moves away from the absorbing surface of the subwoofers along the z-axis. Between the 120 cm plane and the two other planes at 100 and 140 cm, a 2-5 dB difference in amplitude attenuation was observed. However, for most of the measurement positions, the harmonic amplitude attenuation exceeds 10 dB. Thus, even at locations farther from the subwoofer diaphragms, we observed that the amplitude decreased slightly and remained at low levels

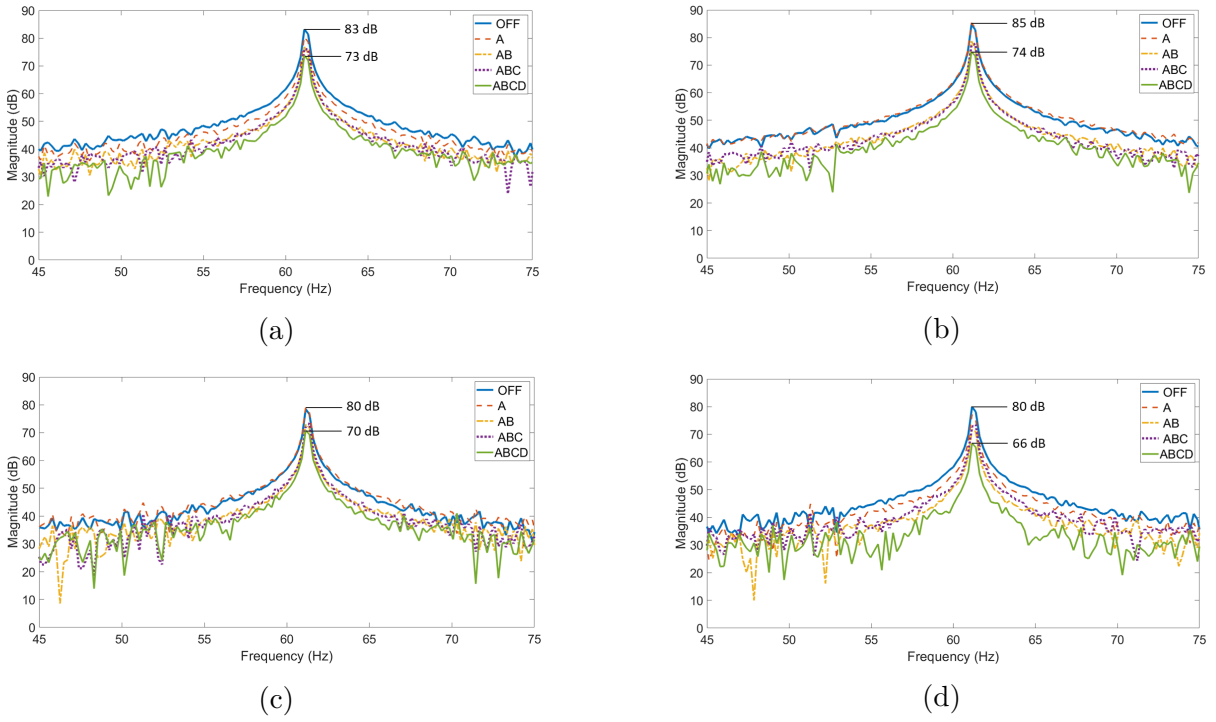

Figure 6.9: Frequency spectra captured by measurement microphones in front of sound absorbers (a) A, (b) B, (c) C and (d) D when they were gradually activated. "OFF" corresponds to the state when all absorbers were deactivated, "A" to the activation of absorber A, "AB" to the activation of both absorbers A and B etc. Measurement microphones were placed 60 cm from the subwoofer diaphragms and 120 cm from the cabin floor, which correspond to measurement microphones A4, B4, C4 and D4.

due to the effective damping of the longitudinal acoustic mode. Consequently, we can conclude that global attenuation was achieved.

6.6 Concluding remarks

In summary, employing active sound absorbers based on the wave separation method can effectively mitigate low-frequency harmonic acoustic disturbances in small aircraft cabins. The success of this method relies on the way of placement of the absorbers, which must be situated at pressure antinodes and oriented perpendicularly to the path of sound propagation. Initially, the shapes of the low frequency acoustic modes were determined both analytically and through the use of the Finite Element Method. Subsequently, simulations were executed to investigate the attenuation of acoustic pressure that can be achieved in an aircraft cabin mockup using various configurations of four active sound absorbers. The simulation outcomes indicated that by strategically placing the absorption boundaries, the SPL for a range of excitation frequencies of the enclosure, was significantly reduced. Although the sound pressure level attenuation was widespread throughout the cabin mockup, it was slightly greater in front of the absorbers and at the z-planes near

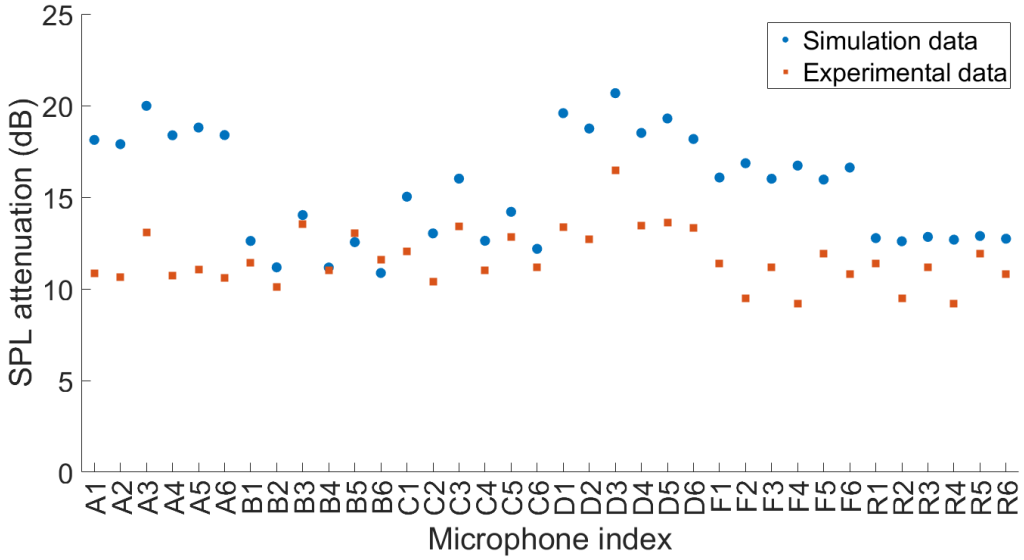

Figure 6.10: Comparison of the SPL attenuation obtained through the simulation (orange squares) and the experimental evaluation (blue dots) for 61 Hz harmonic excitation.

the height of the absorbing surface.

The outcomes of the proposed methodology were also experimentally corroborated to a satisfactory degree in an aircraft cabin mockup situated in the laboratory. When the cabin was excited by the first longitudinal mode at 61 Hz, significant global sound pressure level attenuation was documented, although it was lower at certain measurement points than the value predicted by the simulation model, as also demonstrated in Figure 6.10. Moreover, as the number of absorbers was increased, the performance generally improved. However, in an attempt to cover only a small portion of the interior surface area of the cabin and to limit the usage of hardware, four absorbers were found to be sufficient for addressing single frequency harmonic disturbances. The experimental data and simulation results demonstrated the viability and efficiency of the method for dealing with single frequency harmonic excitations.

CHAPTER 7

Conclusions

Research overview and basic concluding remarks

The aim of the research conducted in this PhD thesis was to develop methods and systems for the active control of low-frequency acoustic disturbances occurring in vehicle cabins, such as small aircraft and yachts, which deteriorate the acoustic comfort of passengers. Active Noise Control in these environments offers several advantages over conventional passive methods in terms of size and weight, making it a highly sought-after area of research and development for both manufacturers and researchers. However, key challenges such as enhancing acoustic pressure attenuation, increasing quiet zone size, lowering computational complexity, and ensuring the robustness of active systems have yet to be fully addressed, limiting their widespread use in real-world applications. To address these challenges, this thesis utilizes novel methods evaluated through a series of analytical models, simulation models, and real-time implementations in embedded digital signal processors, with the aim of providing a new perspective on both local and global ANC while focusing on practical real-world applications. The conclusions drawn are presented below for each concept addressed in this thesis:

- **Computational complexity of the control algorithm**

    1. The conventional multichannel FxLMS algorithm can be replaced with the computationally more efficient mixed error FxLMS in local Active Noise Control applications for headrests in transportation vehicles, such as aircraft and yachts, assuming low-noise acoustic disturbances, such as those found in the cabins of these vehicles.

2. The performance of mixed error FxLMS in terms of acoustic pressure reduction is comparable to that of conventional multichannel FxLMS, but the location of this reduction changes. Specifically, when the acoustic pressure at the error microphones is different, the maximum acoustic pressure attenuation is achieved between them. Hence, the position of the loudspeakers and microphones must be selected appropriately so that the maximum SPL reduction is close to the ears of the seat occupant.
3. The reduced computational resources required for the implementation of the proposed mixed FxLMS-based system can decrease the cost of the digital signal processor, resulting in a more cost-effective and easily implementable system.

- **Size and Location of the Quiet Zone**

1. The use of linear extrapolation to predict the acoustic pressure at ear locations of the seat occupant in combination with mixed-error FxLMS, led to the creation of a novel algorithm for local ANC systems for seat headrests called VEM-FxLMS. This method is capable of moving the quiet zone away from the error microphones with relative accuracy for low-frequency acoustic disturbances.
2. The relocation of the quiet zone also results in its enlargement, as when the error microphones are moved away from the speakers. The distance, that the quiet zone can be successfully moved and its size depends on the wavelength of the acoustic disturbance. Thus, the general rule is that the attenuation of disturbances with longer wavelengths, leads to quiet zones of larger diameter being relocated further away from the error microphones.
3. The use of the feedforward VEM-FxLMS in combination with a woofer, four error microphones and a reference microphone placed between the electric power generators of a yacht led to the creation of a local ANC that successfully mitigated the noise coming from the generators on the yacht's deck. This demonstrated the ability of the proposed method to perform efficiently in real-world conditions.

- **Performance of the control algorithm**

1. When instead of the linear FxLMS, an FLNN was used as the core of the control algorithm, a larger reduction of the harmonic amplitudes of the BPF of the rotor of a small tilt-rotor aircraft was achieved.
2. The FLNN-based algorithm successfully incorporated both the mixed-error approach and the acoustic pressure prediction technique at passenger ears,

based on linear extrapolation, resulting in a system that maintains stability and is characterized by relatively short convergence time.

3. The superior performance of the FLNN compared to the FxLMS can be attributed to its ability to perform the prediction task when the primary and secondary electroacoustic paths have non-minimum phase behavior. In addition, it performs better when the acoustic disturbances have stochastic characteristics, like the ones encountered in aircraft cabins.

- **Interaction of local ANC systems in small enclosures**

1. Separate standalone local ANC systems can operate simultaneously within a cabin, creating a quiet zone in the area in front of the speakers. In the case of the cabin mockup installed in the Dynamics and Acoustics Laboratory, four such systems operated simultaneously while maintaining their stability, with the distance between opposing positions being 2m. However, a slight drop in performance was observed compared to the case where each system operates without the presence of the others.
2. In the areas of the cabin away from the local quiet zones either no change in acoustic pressure or a slight increase was observed. Therefore, the random placement of local noise control systems does not imply global control of the enclosed sound field and in some cases may lead to an increase in the overall SPL.
3. When local ANC systems are installed in a small aircraft cabin setup, it is preferable that adjacent seats share one system with cooperating loudspeakers, to achieve better performance and minimize hardware and computing resources needed.

- **ANC with Active Sound Absorbers**

1. Four active sound absorbers, placed near the walls of a cabin with surface measuring $7.595m^2$ and height $2m$, are capable of producing a global attenuation of low-frequency acoustic disturbances greater than 10 dB. In some areas of the cabin, this attenuation can reach 24 dB.
2. The position of the absorbers is very important for the performance of the global ANC. In order to determine it, we need to approximate the shape of the acoustic modes of the enclosure; thus, the diaphragms should be perpendicular to the direction of wave propagation, when the mode we want to control is excited.
3. Installing sound absorbers along the boundaries of the enclosure is necessary to control several modes, to ensure both that there will always exist an ab-

sorber that is not placed at an acoustic pressure node and that the absorber diaphragms are perpendicular to the direction of wave propagation.

Further work

The research presented in this thesis deals with various issues of local and global ANC in vehicle cabins, leaving open several issues that need improvement and could be investigated in future studies.

The first and most important issue, that a future research work should focus on is the control algorithm and the investigation of artificial intelligence and machine learning methods to improve ANC performance, both in terms of acoustic pressure reduction and quiet zone size. Since the algorithmic problem of ANC is a combination of time series prediction and system identification tasks, neural networks are a very promising prospect. Especially, in cases where there are non-linearities in electroacoustic systems and non-harmonic components in acoustic disturbances, nonlinear algorithms present many advantages, as was also demonstrated by the superior performance of FLNN compared to the linear FxLMS. Thus, neural networks such as Recurrent Neural Networks and Convolutional Neural Networks, which are known for their good performance in similar tasks (speech enhancement and speech recognition) should be investigated for their performance in ANC in real-world conditions. Although some research has already been done, it is mostly limited to computer simulations, without creating embedded systems due to the computational burden, that makes the implementation of such a neural network difficult on a DSP. However, the evolution of both algorithms and embedded systems gives increasing possibilities in real-time implementation that need to be explored. For example, the Reservoir Computing method for RNN training, gives a new perspective that is to be explored in future work on the ANC task.

In addition, future research would focus on improving the practicality of the ANC system. This includes reducing the weight by creating smart ANC configurations and using lighter transducers. In addition, adapting the proposed methods to a feedback logic would eliminate the need for a reference signal in good correlation with the error signal. Therefore, the direction of these systems would be towards a plug and play logic that would increase practicality and thus attractiveness for commercial applications. Even in the case of reference microphones, however, there is a need for further research to determine their frequency and number in order to achieve optimal performance.

As far as global ANC using active sound absorbers is concerned, further research using more absorbers is needed to investigate the possibility of damping more acoustic modes. Furthermore, the behavior of the method in real-world acoustic disturbances, recorded in vehicle cabins, needs to be investigated. Another method to be explored in future research has to do with the structure borne noise of the cabin and its mitigation. This method is

called active vibration control and uses inertial actuators mounted on the fuselage linings in combination with microphones and accelerometers, in order to damp the vibrations transmitted through the fuselage to the cabin. Thus, it would be interesting to study how this approach works in comparison with the proposed local and global ANC systems. Overall, a comprehensive study of the combination of the aforementioned active methods of cabin noise mitigation, in order to create an integrated system with upgraded efficiency will be among the long-term objectives of the research work.

APPENDIX A

Simulation models

In the preceding chapters of this dissertation, the proposed ANC system configurations and control algorithms were evaluated by means of diverse simulation models. These models were either based on the k-space pseudospectral method or the widely used Finite Element Method (FEM). Appendix A provides comprehensive details regarding the implementation of the simulation models developed for this dissertation.

A.1 Models using k-Wave Matlab toolbox

The two-dimensional simulation models utilized for evaluating the VEM-FxLMS in Chapter 3 employed the k-Wave Matlab toolkit [138] as the implementation platform. This toolkit employs the k-space pseudospectral method to solve the wave equation in two dimensions and compute the acoustic pressure throughout a predefined domain. There are many numerical methods for solving partial differential equations, with numerous permutations for each method. The best approach depends on factors like computational domain size, frequencies of interest, medium properties, and boundary conditions. To assess ANC systems, a method that gives a time-domain solution of the wave equation for broadband acoustic waves in heterogeneous media is necessary. Classic finite difference and finite element methods require at least 10 grid points per acoustic wavelength for accuracy, leading to impractically large computational grids. For instance, a 3 MHz ultrasound image with 15 cm depth requires a 3D computational domain with over 10^11 grid elements, needing more than 400 GB of memory.

To address this, k-Wave uses the k-space pseudospectral method [139], combining spectral calculation of spatial derivatives with a temporal propagator in the spatial frequency domain (k-space). Unlike finite difference schemes that compute spatial gradients

locally, the Fourier collocation spectral method fits a Fourier series to all data, offering two main advantages: efficient amplitude calculation via the fast Fourier transform (FFT) and the need for only two grid points per wavelength. Therefore, the k-space pseudospectral method gives an effective alternative to FEM, that needs less computational resources. More details on this method are given in the k-Wave user's manual [94].

Firstly, when we create a new acoustic simulation in k-Wave we define parameters such as the size of the grid and each grid point, the properties of the propagation medium such as sound speed and density, and the points where there are speakers or microphones. Then one driving signal is assigned to each source and the problem is solved by calling the built-in function *kspaceFirstOrder2D*. The peculiarity of modeling an ANC system lies in the dynamic calculation of the antinoise signal, depending on the error and reference signals. Thus, the driving signal for the antinoise sources cannot be defined from the beginning. For this reason, the function *kspaceFirstOrder2D* was modified to dynamically calculate the antinoise signal. Therefore, the proposed control algorithms were incorporated in the aforementioned built-in function as illustrated in Figure A.2. This method enables us to calculate the suitable antinoise signal for any algorithm, such as single channel FxLMs or VEM-FxLMS, at each iteration. One of the significant advantages of this method is that the ANC is implemented in real-time, as it would be in a real-world application, which enhances the model's reliability compared to offline simulations.

Furthermore, the grid that is created depending on the simulation parameters is illustrated in Figure A.1. We observe the speakers, which can be represented as a sum of point sources and form arcs, thus simulating the speaker signal. In addition, barriers (e.g. walls) can be placed changing the properties of the propagation medium. Moreover, the microphones are modeled by one grid point. A drawback of this toolbox is nevertheless the inability to simulate reverberation phenomena in enclosed spaces, as well as phenomena related to the acoustic oscillation modes of an enclosure. Since such phenomena play a very important role when designing strategies for noise control in an enclosure, the need to develop models that take such phenomena into account emerged. Thus, in the following sections of the Appendix, such models are discussed.

A.2 FEM models

The Finite Element Method (FEM) is a numerical technique for solving complex problems in engineering and physics, particularly those involving partial differential equations. It works by dividing a large, complex problem into smaller, simpler parts called finite elements, which are then analyzed and assembled to model the entire system. This method allows for precise modeling of complex geometries and material properties. In acoustic simulations, FEM is advantageous because it can accurately capture the behavior of sound waves in heterogeneous media and complex structures, providing detailed insights

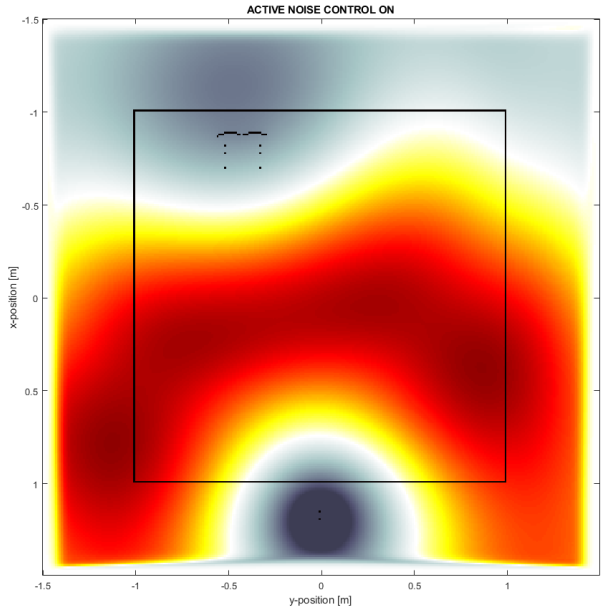

Figure A.1: k-Wave grid while simulating a 4in-2out VEM-FxLMS based ANC system.

into sound propagation, reflection, and absorption [140], [141]. This makes FEM an essential tool for designing quieter and more efficient acoustic environments and devices.

In this thesis three 3D models based on the finite element method were developed in Comsol Multiphysics ® platform [142] : one that models the open space, where there are very few reflections, one that represents a cabin that has no walls on its front and rear sides, thus simulating a long enclosure and a closed cabin. In all cases, particular attention was paid to the definition of the size of the finite elements, which is determined by the formula: $s = \frac{\lambda_{max}}{5}$, where λ_{max} is the wavelength of the lowest harmonic component of the simulated acoustic disturbance in the frequency spectrum. Moreover, the control algorithms that performed the ANC task were inserted into the model through global equations (Figure A.3a) that controlled the normal acceleration of the loudspeaker diaphragms. Each global equation was linked with a Matlab® function (Figure A.3b), through Comsol Matlab Livelink ® module [143].

A.2.1 Open space

The schematic representation of the open space model, as depicted in Figure A.4, was designed to mimic an anechoic chamber where reflections are absent. This model was employed in the simulation of Chapter 2, where the mixed error FxLMS algorithm was assessed for various loudspeaker arrangements. The model's architecture comprised a rectangular air domain with dimensions of 4 meters in width, 3 meters in length, and 4 meters in height, which was encompassed by a PML with thickness of 3 meters. The PML's thickness is determined by the wavelength of the lowest frequency component in the acoustic disturbance. In this model, the lowest frequency that we selected to solve the

```
480 -           if flags.compute_directivity && (flags.record_p || flags.record_I || flags.record_I_avg)
481 -               sensor_data.p(:, file_index) = directionalResponse(kgrid, sensor, sensor_mask_index, p_k);
482 -           end
483 -
484 -       end
485 -
486 -       %%%%%%%%%%%%%%%%%%%%%%%%%%%%%% ANC CODE- FxLMS %%%%%%%%%%%%%%%%%%%%%%%%
487 -       %%%%%%%%%%%%%%%%%%%%%%%%%%%%%%%%%%%%%%%%%%%%%%%%%%%%%%%%%%%%%%%%%%%%%%
488 -
489 -       %%added ANC code
490 -       if t_index<index_end
491 -           ref_mic=p(Nx-Nx/4-2,Ny/2);                    % reference microphone
492 -           Wx=[ref_mic Wx(1:flength-1)];                  % update the controller state
493 -           Wy=sum(Wx.*Ww);                               % calculate the controller output
494 -           antinoise_speaker_gain=1;
495 -           antinoise_speaker=antinoise_speaker_gain*Wy;
496 -           source.p(1,:)=[source.p(1,1:t_index) antinoise_speaker zeros(1,index_end-t_index-1)]; %driving signal of the antinoise
497                                                                                                   %source
498 -           error_mic_pressure=p(Nx/8+2,Ny/2);            % error mic
499 -           e_cont=error_mic_pressure;                    % measure the residue
500 -           Shx=[ref_mic Shx(1:flength-1)];               % update the state of Sh(z)
501 -           Xhx=[sum(Shx.*Shw) Xhx(1:flength-1)];         % calculate the filtered x(k)
502 -           Ww=Ww-mu*e_cont*Xhx;                          % adjust the controller weight according to FxLMS algorithm
503 -
504 -           %at the end of the algorithm keep the maximum pressure level at all
505 -           %grid
506 -           if (t_index>index_end-(3*(index_end/10)))
507 -               for i=1:1:Nx
508 -                 for j=1:1:Ny
509 -                     if abs(p(i,j))>abs(max_pressures(i,j))
510 -                             max_pressures(i,j)=abs(p(i,j));
511 -                     end
512 -                 end
513 -               end
514 -           end
515 -       end
```

(a)

```
489 -           if flags.compute_directivity && (flags.record_p || flags.record_I || flags.record_I_avg)
490 -               sensor_data.p(:, file_index) = directionalResponse(kgrid, sensor, sensor_mask_index, p_k);
491 -           end
492 -
493 -       end
494 -
495 -       %%%%%%%%%%%%%%%%%%%%%%%%%%%%%% VEM-FxLMS %%%%%%%%%%%%%%%%%%%%%%%%%%%%%%
496 -       %%%%%%%%%%%%%%%%%%%%%%%%%%%%%%%%%%%%%%%%%%%%%%%%%%%%%%%%%%%%%%%%%%%%%%
497 -
498 -       if t_index<index_end
499 -           ref=p(Nx/2, Ny/15-8); %determine the reference signal
500 -           Wx0=[ref Wx0(1:flength-1)]; %Wx0 is the reference buffer
501 -
502 -           %compute antinoise signal for the two antinoise sources
503 -           Wy=sum(Wx0.*Ww0);
504 -           antinoise_speaker_gain=1;
505 -           antinoise_speaker=antinoise_speaker_gain*Wy; % the same signal is used beacuase of geometrical symmetry
506                                                        % and lack of
507                                                        % reflections
508 -
509 -           %drive point sources with the proper signal
510 -           for i=1:14
511 -               source.p(i,:)=[source.p(i,1:t_index) antinoise_speaker zeros(1,index_end-t_index-1)];
512 -           end
513 -           error_mic_pressure=p(Nx-Nx/6-20,Ny/15+20+3);        % error mic 1
514 -           error_mic2_pressure=p(Nx-Nx/6-20-9,Ny/15+20+3);     % error mic 2
515 -           extr_mic_pressure=p(Nx-Nx/6-20,Ny/15+20+3+h);       % extrapolation mic 1
516 -           extr_mic2_pressure=p(Nx-Nx/6-20-9,Ny/15+20+3+h);    % extrapolation mic 2
517 -
518 -           %virtual error mics pressure estimation using linear extrapolation at position x
519 -           e_cont=(extr_mic_pressure-error_mic_pressure)*x/h+extr_mic_pressure;
520 -           e_cont2=(extr_mic2_pressure-error_mic2_pressure)*x/h+extr_mic2_pressure;
521 -
522 -           Xhx0=[sum(Wx0.*Shw) Xhx0(1:flength-1)]; % filter the reference with the mixed secondary path Shw
523 -           Ww0=Ww0-mu*Xhx0*(e_cont+e_cont2);       % weight update equation using mixed error FxLMS
```

(b)

Figure A.2: Matlab codes implementing a) single channel FxLMS and b) VEM-FxLMS as they are incorporated in *kspaceFirstOrder2D* built-in function of k-Wave.

wave equation was 72 Hz, corresponding to a wavelength of 4.8 meters. In order to achieve complete absorption, the PML thickness follows the formula $d_{PML} = \frac{6\lambda}{5}$. However, due to the substantial computational requirements of the model, we selected a smaller thickness

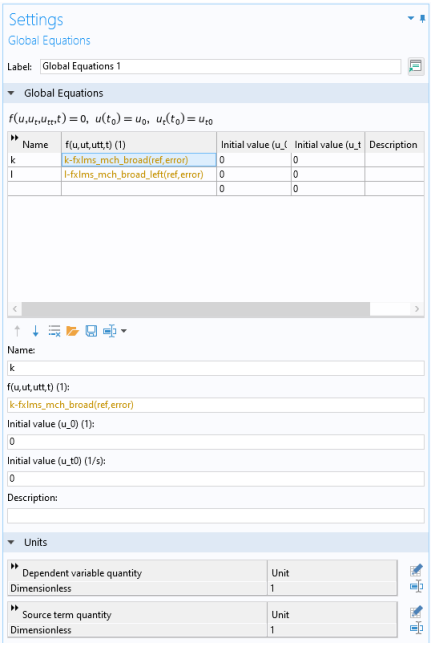

(a)

```
function out=fxlms_mch_broad(ref_mic,error_mic)
u=0.00001;  % step size
fl=200; %filter length
% load secondary path computed from previous identification stage
s_path=(load('C:\Users\el041\Documents\3d_sim\acta_acustica\spath_mixed_anc_2mics_opposite_30cm_right.txt'))';
persistent ref_buffer weights filtered_ref_buffer   % store the quantities computed by the model into
                                                    % persistent variables
if isempty(ref_buffer)
    ref_buffer=zeros(1,fl);
end
if isempty(weights)
    weights=zeros(1,fl);
end
if isempty(filtered_ref_buffer)
    filtered_ref_buffer=zeros(1,fl);
end
ref_buffer=[ref_mic ref_buffer(1:fl-1)];    % buffer where referenve signal is stored
out=sum(ref_buffer.*weights);               % antinoise signal
conv_error=error_mic;                       % error signal
filtered_ref_buffer=[sum(ref_buffer.*s_path) filtered_ref_buffer(1:fl-1)];  % filter ref buffer with seconary path
weights=weights-u*conv_error*filtered_ref_buffer;   % update adaptive filter weights
end
```

(b)

Figure A.3: a) Global equations in Comsol platform, b) Matlab function used as global equation.

than the recommended value without encountering any reflective interference that would significantly diminish the model's accuracy.

In addition, the time while the ANC was working was 3 seconds and the control algorithms were conventional multichannel FxLMS as well as mixed error FxLMS for comparison reasons. Furthermore, the mesh was different depending on the domain type of the model. For the PML, a swept mesh was used, which is is a type of structured or semi-structured mesh composed of prisms or hexahedrons. By structured, we mean a mesh where the interior mesh vertices are adjacent to the same number of elements. The mesh is structured in the sweep direction and then either structured or unstructured orthogonally to the sweep direction. For the air domain, a tetrahedral mesh was used, while the size of the tetrahedrons used for the loudspeakers diaphragms determined as extra fine.

A.2.2 Cabin with open ends

The open-ended cabin was designed to replicate the interior of an aircraft cabin, whose length is such that the reflections from the walls at the ends are not significant when we investigate the behavior of an ANC system. Therefore, two PML of thickness 1.8 m were placed at the front and rear end. In addition, the cabin's geometry was a cylindrical segment with dimensions of 1.5 meters in width, 3.45 meters in length, and 1.6 meters in height, which correspond to the cabin of a small tilt-rotor aircraft. The material of

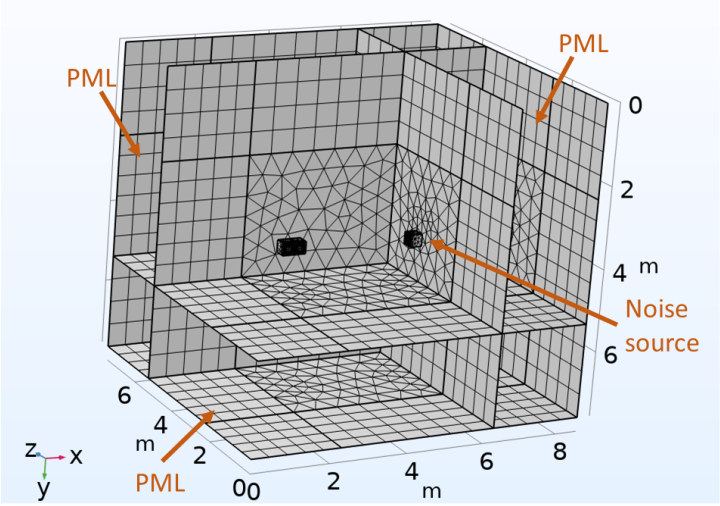

Figure A.4: Geometry and meshing of the open space model implemented in Comsol Multiphysics.

the outer shell was aluminum. The parameters of the selected material were sound speed $c = 6420m/s$ and density $rho = 2700kg/m^3$. The noise source was also placed at the rear end of the cabin, and it was modeled by a circle with 0.15 m diameter. Moreover, the global equations were inserted in the same way as in the open space model. The same principles were also followed for the determination of mesh size.

The open-ended model which is illustrated in Figure A.5 was employed in Chapter 5, where we examined the interaction between multiple ANC systems that coexist in an aircraft cabin. The 2-dimensional simulations in the same Chapter take place in a domain that is practically a top view of the three-dimensional model. In these simulations the loudspeakers were modeled as arcs ant the microphones as Domain point probes in similar way to the three-dimensional models. The big advantage of the two-dimensional simulations is the small complexity, which allows solving the model in a short time.

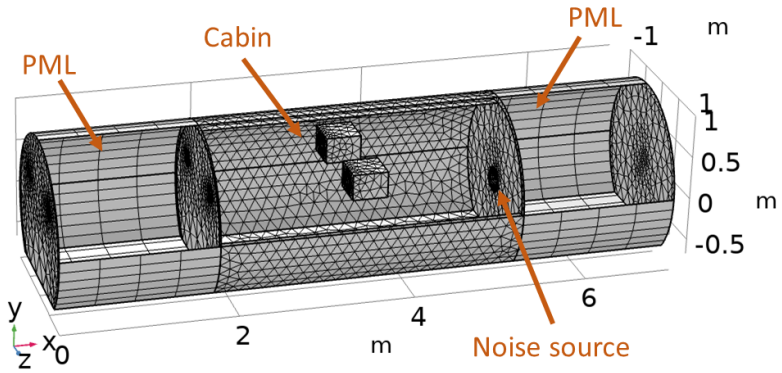

Figure A.5: Geometry and meshing of the model of the open-ended cabin implemented in Comsol Multiphysics.

A.2.3 Closed cabin

The closed cabin model was employed in simulations of Chapters 4 and 6 and modeled the small aircraft cabin mockup installed in the Dynamics and Acoustics Laboratory. The model of the cabin mockup was designed to have the same dimensions as the one installed in the laboratory (refer to Figure A.6) for the purpose of conducting experimental tests on the system. The material used for the horizontal cylindrical segment had an impact on the damping of the walls. MDF, which has a density of $\rho = 558kg/m^3$ and a sound speed of $c = 2177m/s$, was chosen for its similarity to the material used in the laboratory's mockup, as reported by [144]. In addition, a semi-spherical air domain and a PML were placed around the cabin to represent free space (refer to Figure A.6).

The loudspeakers were represented as circles with diameters of 40 cm for the noise source and 24 cm for the secondary sources. The driving signals derived from the selected control algorithm were introduced into the model by incorporating global equations that control the normal acceleration of the circular boundaries that represent the diaphragms of the subwoofers, as described by Figure A.3. Each of these equations included a Matlab function implementing the corresponding algorithm. Moreover, the communication between Comsol and Matlab was facilitated through Matlab Livelink® for each iteration of the time-dependent solver.

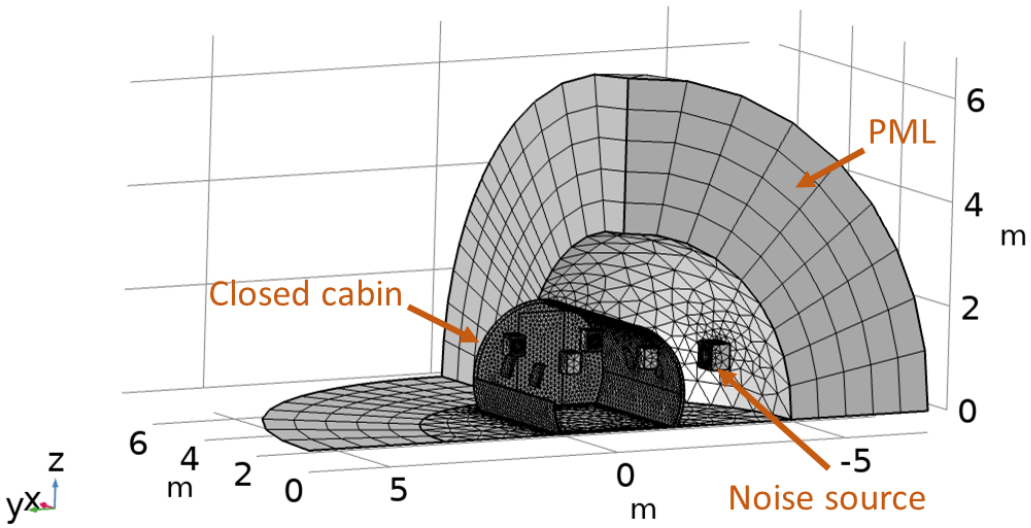

Figure A.6: Geometry and meshing of the model of the closed cabin implemented in Comsol Multiphysics.

APPENDIX B

Aircraft cabin mockup

The experimental evaluation of the ANC systems detailed in this dissertation was conducted in a wooden cabin mockup that was constructed in the Dynamics and Acoustics Laboratory. This mockup provided a small enclosed space with predefined acoustic properties, which was suitable for assessing an ANC system intended for installation in a similar small enclosed space, such as an aircraft cabin.

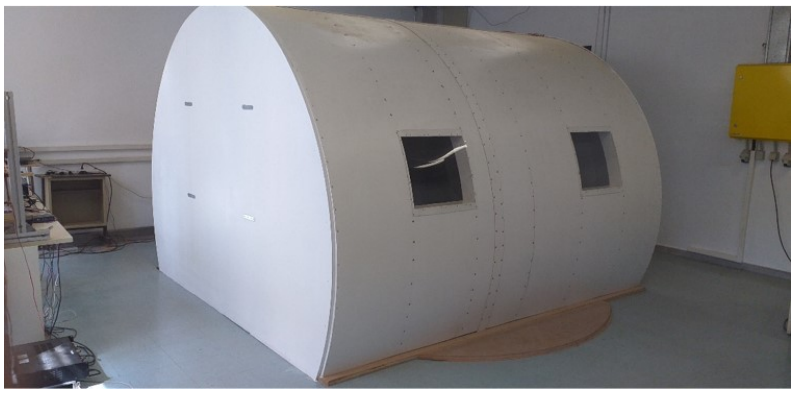

(a)

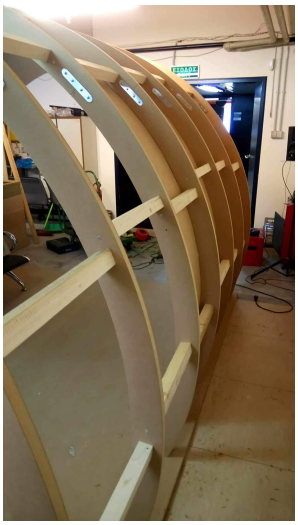

(b)

Figure B.1: a) Cabin mockup with dimensions of 310 cm length, 245 cm width, 200 cm height, b) The wooden frame of the mockup where the outer shell and rock wool panels were installed.

The shape of the mockup was a cylindrical segment that simulated a portion of an aircraft fuselage. Although it resembled an aircraft, the enclosed space could be used to evaluate an ANC system in any enclosure, including the cabin of a yacht. The most

significant difference between evaluating a system in an anechoic room and an enclosure lies in the presence of reflections on the boundaries of the cabin. Additionally, due to the small dimensions of the enclosure, low-frequency acoustic modes were excited, which could only be simulated in a cabin mockup with similar dimensions. Thus the experiments in this mockup gave an extra reliability to proposed systems regarding their functionality in real-world conditions.

In addition, two pieces of medium-density fiberboard measuring 3 centimeters in thickness were utilized to construct the flat side walls of the mockup. The curved surface, having a thickness of 10 centimeters, comprised of thin, flexible MDF panels that were fastened to a wooden frame. In addition, rock wool was inserted between the outer and inner panels. The dimensions of the mockup were specified as (length, L=310cm; width, W=245cm; and height, H=200cm) to replicate the cabin of a small aircraft. The reverberation times T_{30} in octave bands up to 500 Hz, as measured, are listed in Table B.1. Although these values are higher than those reported in the literature for actual aircraft cabins [145], they are within a realistic range.

Frequency (Hz)	63	125	250	500
T_{30} (s)	1.69	0.75	0.38	0.44

Table B.1: Measured reverberation times T_{30} for aircraft cabin mockup in octave bands.

APPENDIX C

DSP algorithm implementation

The control algorithms of this thesis were implemented on a National Instruments CompactRIO controller, illustrated in Figure C.1a and a Motu Ultralite AVB sound card, illustrated in Figure C.1b. In case of CompactRIO Labview® and Labview® FPGA were used as development platforms, while in case of the sound card the algorithm implementation was made in Python. In addition, the noise cancellation systems of Chapters 2, 3, 4 and 5 were implemented in CompactRIO while the active sound absorber algorithm of Chapter 6 was implemented in the sound card.

(a)

(b)

Figure C.1: a) CompactRIO-9030 DSP controller and b) Motu Ultralite AVB soundcard.

C.1 CompactRIO-9030

The cRIO-9030 controller, as shown in Figure C.1a, features (a) an Intel Atom 1.33 GHz real-time processor running NI Linux real-time operating system for fast FPGA and host controller communication and signal processing, (b) a Xilinx Kintex-7 type FPGA controller for high-speed control application, with fully customizable timing and 4 slots for analog I/O modules. Also, due to the built-in user interface capability with NI

Linux Real-Time, a local human-machine interface (HMI) is allowed to be implemented to simplify application development. The CompactRIO controller is ideal for complex digital signal processing applications. It has the capabilities required to integrate many parallel tasks into a single controller, ultimately reducing system cost, development time and complexity. Dual power supply inputs are supported with a wide range from 9 VDC to 30 VDC to ensure reliable operation in critical applications. A variety of connectivity options are also available, including Gigabit Ethernet, USB Hi-Speed host and serial ports.

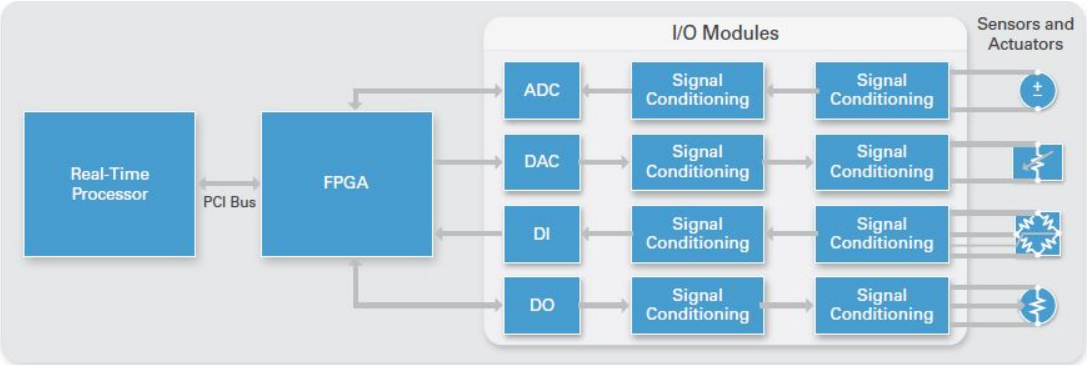

Figure C.2: Architecture of the cRIO 9030 [146].

For the analog to digital conversion of the signals, a NI 9220 module was used, which is illustrated in Figure C.3. The NI 9220 analog input module is suitable for installation in CompactRIO devices. It has 16 differential analog inputs, which can operate simultaneously and independently of each other. Each analog input channel provides a measurement range of ± 10 V and 16-bit resolution. The maximum sample rate per channel is 100 kS/s, and the maximum data rate is 3.2 MB/s when all channels are operating at the maximum sample rate.

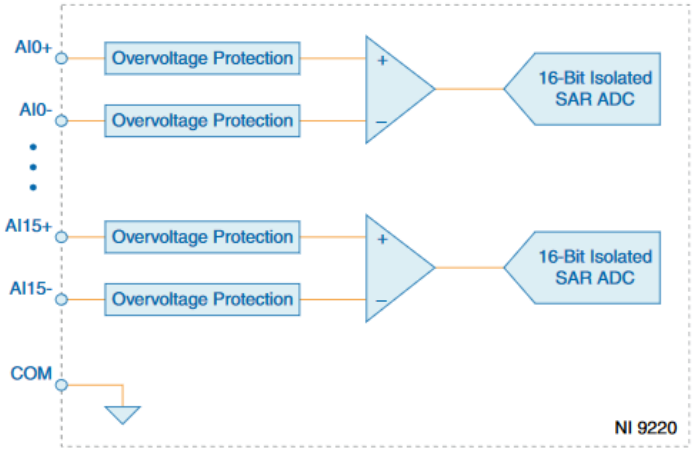

(a) (b)

Figure C.3: a) Analog to Digital converter (ADC) NI 9220, b) block diagram of NI9220 [147].

Moreover, the digital to analog conversion of the produced signals was carried out by NI 92 64 module, illustrated in Figure C.4. The NI-9264 analog output module is suitable for installation in CompactRIO devices. It has 16 differential channels of synchronous analog output, with a maximum sampling rate of 25 kS/s per channel. Each analog output channel has its own digital-to-analog converter (DAC), which can produce an output voltage signal with a maximum range of ± 10 V and a resolution of 16 bits. Each channel also has surged and short-circuit protection. In addition, each channel is connected to earth ground.

(a) (b)

Figure C.4: a) Digital to analog converter (DAC) NI 9264, b) block diagram of NI9264 [148].

The deployment of the algorithms featured a standard architecture that incorporated the implementation of the signal processing aspect on the Compact RIO FPGA using Labview version 2017. Subsequently, a user interface was developed within the real-time processor to enable users to configure various parameters, such as step size and filter length, as well as to visualize the real-time evolution of multiple signals, including the reference and error signals.

To provide a clearer illustration of the implementation of the ANC methods within the CompactRIO system, a block diagram of the mixed error FsLMS method outlined in Chapter 4 is presented. The A and B components of the diagram involve the initialization of certain memories and FIFOs. Next, in the C part of the diagram, the linear extrapolation-based acoustic pressure prediction technique described in Chapter 3 is implemented. Finally, in track D, the second-order FLNN is implemented using the built-in function *FXP Filtered-X LMS.vi*, which calculates the adaptive filter coefficients while accounting for the secondary path. By computing the sine and cosine of the reference signal, the filter bank version of the second-order FLNN can be executed.

The modeling process of the secondary path was also implemented in the FPGA part of the controller using the *FXP LMS.vi* built-in function, appropriately modified in order to fit the requirements of the proposed methods. For instance, the filter length as well as the step size, had to be modified according to each application needs. At first, a loop is running while the loudspeaker reproduces white noise, which is used as reference. In the meantime, the error signal is captured by the error microphone and the LMS algorithm is

updating the coefficients of the secondary path, until the modeling time has passed. The modeling time is a parameter determined by the user. Then the computed coefficients are stored in a FIFO in order to be visualized by the user interface and to be used in the noise-cancelling algorithm.

In the same way as in the noise cancellation algorithm a user interface was also implemented in order to enter the preferred parameters and to visualize the computed secondary paths and the convergence plots, in order to decide whether the secondary path modeling was accurate, as the accuracy of the secondary path modeling process is crucial for the ANC system's performance. The user interface communicates with the FPGA part of the code with FIFOs, which are a very common way of communication between the FPGA and the real-time processor of the CompactRIO. At the end of this appendix are presented selected block diagrams in Labview of some algorithms implemented in this thesis.

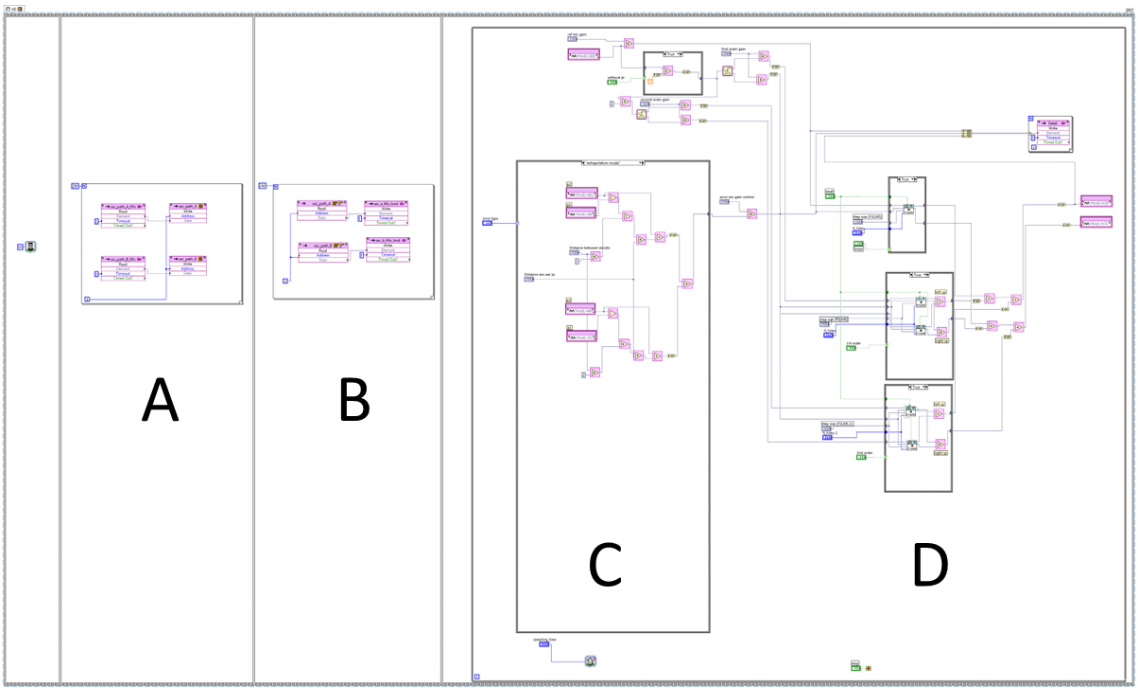

Figure C.5: Labview block diagram of the second order FLNN, as implemented for the FPGA part of the CompactRIO.

C.2 Motu Ultralite AVB soundcard

The MOTU UltraLite AVB is a versatile audio interface boasting 18 inputs and 18 outputs, allowing for extensive connectivity with support for sample rates up to 192 kHz. In this dissertation, the soundcard was accessed via Python in order to implement the active sound absorbers based on the wave separation technique into incident and reflected, using two closely spaced microphones. The sampling rate that was used was 44.1 kHz. In addition, the sounddevice python library [149] was used to play and record NumPy arrays

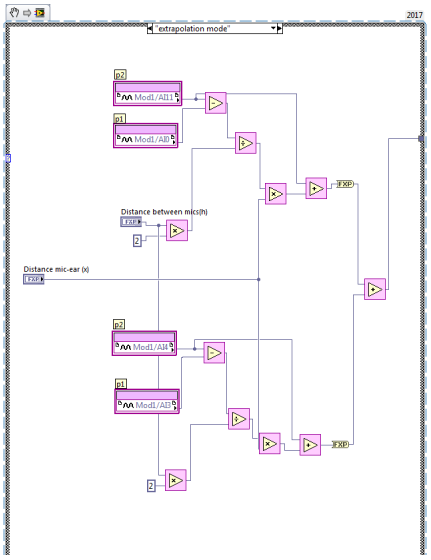

Figure C.6: The linear extrapolation based acoustic pressure prediction technique illustrated in C part of Figure C.5

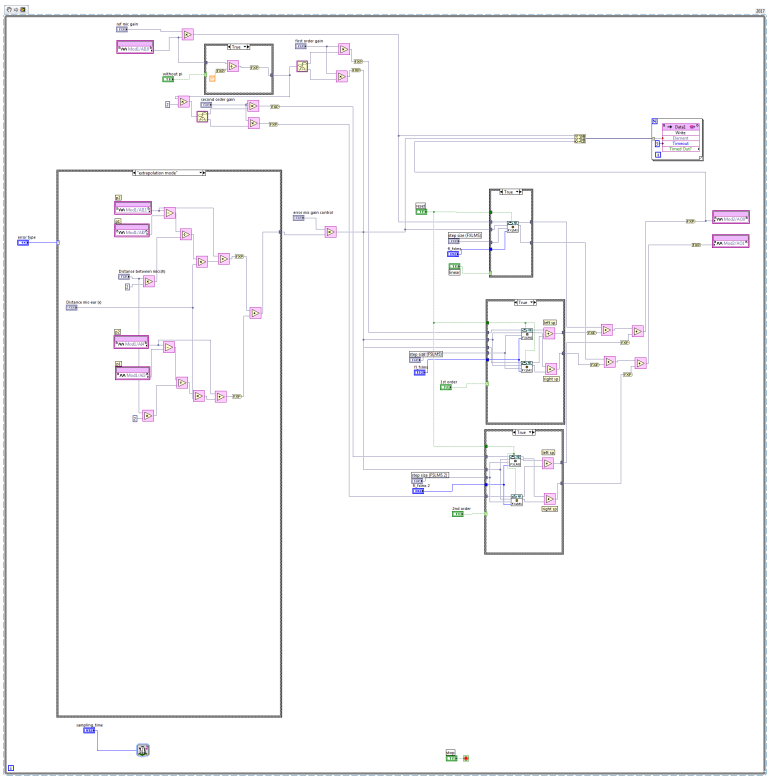

Figure C.7: The loop, which contains parts C and D of the diagram illustrated in Figure C.5 and implements the update equation of the non-linear adaptive filter coefficients.

containing audio signals. The update of the weights of the adaptive filter described in Chapter 6 is implemented by a callback function, which also computes in each iteration the driving signal for the active sound absorber. The Python code of this function is presented in Figure C.11. Before calculating the weights of the adaptive filter that implements the sound absorption task, the secondary path with respect to the reflected component of the

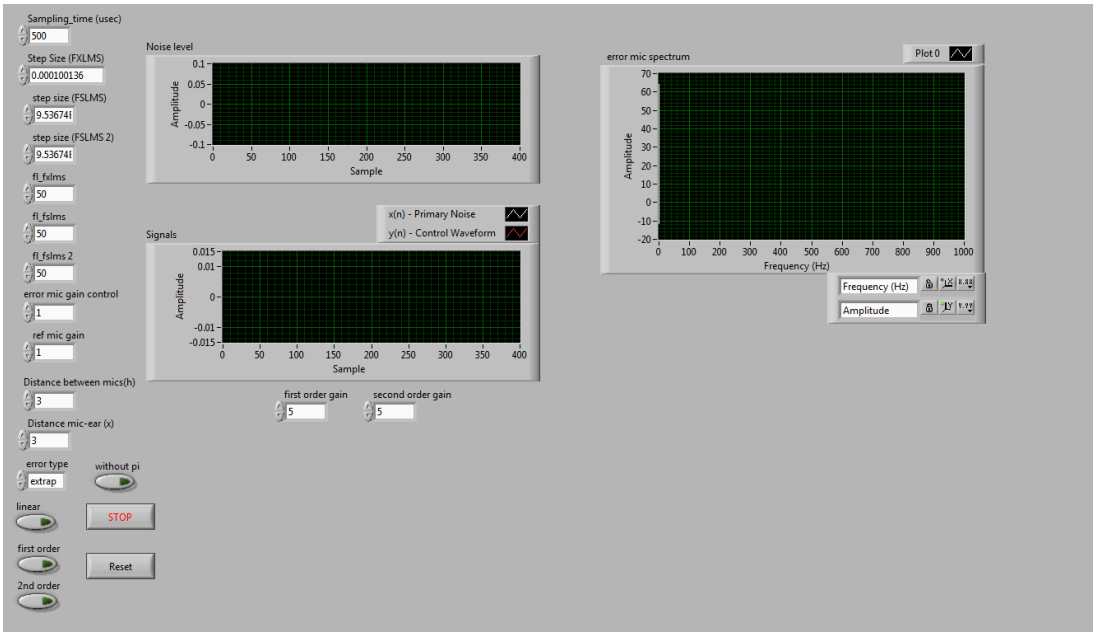

Figure C.8: The user interface, which is connected via FIFOs with the second order FLNN function, implemented in the FPGA platform of CompactRIO. The user interface is implemented in the real-time processor.

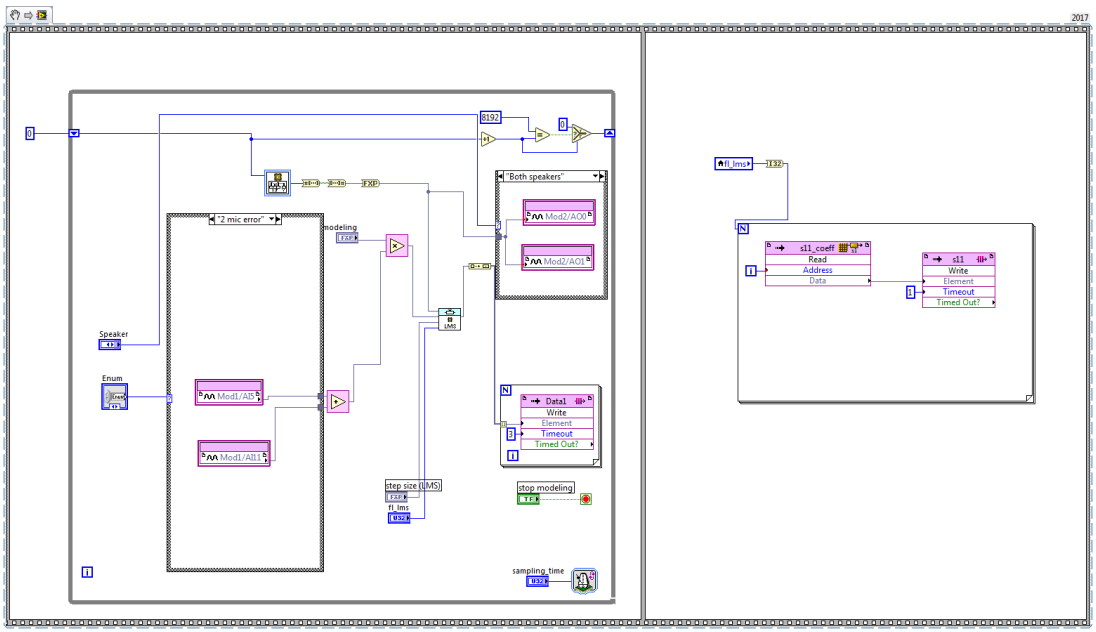

Figure C.9: Modeling procedure based on *FXP LMS.vi* built-in function.

acoustic wave has been determined. The Python code, wich for this process also uses a callback function and the sounddevice function library, is presented in Figure C.10.

```
try:
    samplerate = 48000
    #@jit
    def callback(indata, outdata, frames, time, status):
        ## here we define the variables as global variables
        ## this section is omitted

        # determine the input signals (microphones) used for active sound absorber implementation
        mic1=indata[2,0:1]
        mic2=indata[2,1:2]

        p_av=(mic1+mic2)/2
        alpha=mic1-mic2
        # use white noise as reference signal
        ref=0.9*np.random.rand(1,1)
        # drive the loudspeaker with white noise
        outdata[0,0:1]=ref; outdata[1,0:1]=ref; outdata[2,0:1]=ref; outdata[3,0:1]=ref; outdata[4,0:1]=ref;
        outdata[5,0:1]=ref; outdata[6,0:1]=ref; outdata[7,0:1]=ref; outdata[8,0:1]=ref; outdata[9,0:1]=ref;
        ref_buffer.appendleft(ref)
        ref_buffer_r=np.array(ref_buffer)
        output=np.dot(ref_buffer_r,s_path)
        alpha_buffer.appendleft(alpha)
        alpha_buffer_r=np.array(alpha_buffer)
        giota=np.sum(alpha_buffer_r)/(2*samplerate)+giota_buffer_r[1]
        giota_buffer.appendleft(giota)
        giota_buffer_r=np.array(giota_buffer)
        vel=giota_buffer_r[0]/mic_dist
        # compute the incident component of the sound wave
        p_incident_dc=(p_av+343*vel)/2
        p_incident_dc_buffer.appendleft(p_incident_dc)
        p_incident_dc_buffer_r=np.array(p_incident_dc_buffer)
        p_incident=p_incident_dc_buffer_r[0]-p_incident_dc_buffer_r[1]+0.8*p_incident_buffer_r[0]
        p_incident_buffer.appendleft(p_incident)
        p_incident_buffer_r=np.array(p_incident_buffer)
        #compute the reflected component of the sound wave
        p_reflected_dc=(p_av-343*vel)/2
        p_reflected_dc_buffer.appendleft(p_reflected_dc)
        p_reflected_dc_buffer_r=np.array(p_reflected_dc_buffer)
        p_reflected=p_reflected_dc_buffer_r[0]-p_reflected_dc_buffer_r[1]+0.8*p_reflected_buffer_r[0]
        p_reflected_buffer.appendleft(p_reflected)
        p_reflected_buffer_r=np.array(p_reflected_buffer)
        # define the error used during the minimiztion process
        conv_error=(r*p_incident-p_reflected)-output
        error_history.append(conv_error)
        # compute the coefficients of the secondary path
        s_path=np.add(s_path,u*conv_error*ref_buffer_r/(0.0001+np.sum(np.power(ref_buffer_r,2))))
    with sd.Stream(device=(input_device, output_device), channels=(2,1), callback=callback, blocksize=10,
                   samplerate=samplerate):
        print('#' * 50)
        print('press ctrl c to quit')
        print('#' * 50)
        input()
except KeyboardInterrupt:
    print("Keyboard Interrupt")
```

Figure C.10: Callback function implementing the modeling of the secondary path, which is used for the active sound absorption method described in Chapter 6.

```
try:
    samplerate = 48000
    #@jit
    def callback(indata, outdata, frames, time, status):
        ## here we define the variables as global variables
        ## this section is omitted
        mic1=indata[2,0:1]
        mic2=indata[2,1:2]
        ref=np.sin(2*np.pi*58*i/(4800))

        p_av=(mic1+mic2)/2
        alpha=mic1-mic2

        alpha_buffer.appendleft(alpha)
        alpha_buffer_r=np.array(alpha_buffer)
        giota=np.sum(alpha_buffer_r)/(2*samplerate)+giota_buffer_r[1]
        giota_buffer.appendleft(giota)
        giota_buffer_r=np.array(giota_buffer)
        vel=giota_buffer_r[0]/mic_dist

        # compute the incident component of sound wave
        p_incident_dc=(p_av+343*vel)/2
        p_incident_dc_buffer.appendleft(p_incident_dc)
        p_incident_dc_buffer_r=np.array(p_incident_dc_buffer)
        p_incident=p_incident_dc_buffer_r[0]-p_incident_dc_buffer_r[1]+0.8*p_incident_buffer_r[0]
        p_incident_buffer.appendleft(p_incident)
        p_incident_buffer_r=np.array(p_incident_buffer)

        # compute the output signal
        ref_buffer.appendleft(ref)
        ref_buffer_r=np.array(ref_buffer)
        out=np.dot(ref_buffer_r,weights)
        outdata[0,0:1]=gain*out; outdata[1,0:1]=gain*out; outdata[2,0:1]=gain*out; outdata[3,0:1]=gain*out; outdata[4,0:1]=gain*out;
        outdata[5,0:1]=gain*out; outdata[6,0:1]=gain*out; outdata[7,0:1]=gain*out; outdata[8,0:1]=gain*out; outdata[9,0:1]=gain*out;

        # compute the reflected component of sound wave
        p_reflected_dc=(p_av-343*vel)/2
        p_reflected_dc_buffer.appendleft(p_reflected_dc)
        p_reflected_dc_buffer_r=np.array(p_reflected_dc_buffer)
        p_reflected=p_reflected_dc_buffer_r[0]-p_reflected_dc_buffer_r[1]+0.8*p_reflected_buffer_r[0]
        p_reflected_buffer.appendleft(p_reflected)
        p_reflected_buffer_r=np.array(p_reflected_buffer)
        conv_error=(r*p_incident-p_reflected)

        #filter the reference signal with the secondary path
        f_ref=np.dot(ref_buffer_r,s_path)
        filtered_ref_buffer.appendleft(f_ref)
        filtered_ref_buffer_r=np.array(filtered_ref_buffer)
        error_history.append(conv_error)

        # weight update
        weights=np.add(weights,u*conv_error*filtered_ref_buffer_r/(0.00001+np.sum(np.power(filtered_ref_buffer_r,2))))
        i=i+1
    # drive the loudspeaker with the antinoise signal.
    with sd.Stream(device=(input_device, output_device), channels=(2,1), callback=callback, blocksize=10,
                           samplerate=samplerate):
        print('#' * 50)
        print('press ctrl c to quit')
        print('#' * 50)
        input()
except KeyboardInterrupt:
    print("Keyboard Interrupt")
```

Figure C.11: Callback function implementing the active sound absorber introduced in Chapter 6.

APPENDIX D

SPL measuring configuration

To measure the attenuation of sound pressure levels at the passenger's ears as well as to determine the size of the quiet zone in front of the active headrest systems studied in this thesis, a measuring setup consisting of a set of 16 observation microphones was implemented. These microphones were evenly distributed on a metallic grille, as shown in Figure D.1, to measure the sound pressure at a horizontal area up to $A = 0.5m \times 0.5m$.

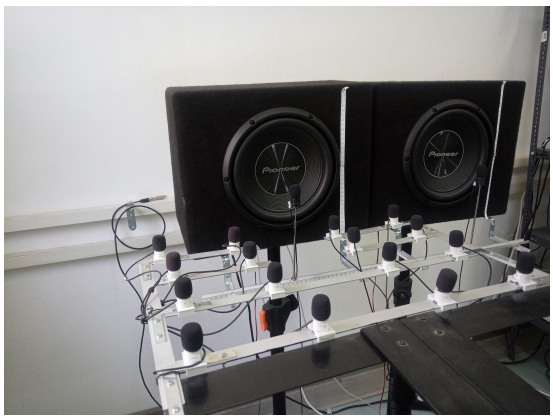

Figure D.1: The metallic grille, where 16 measurement microphones were mounted in order to monitor the acoustic pressure before and after the ANC activation.

The measured data were used to calculate the corresponding SPL. A linear interpolation of the calculated SPLs with resolution of 0.1 cm was implemented to form an SPL distribution on the entire horizontal area. Additionally, a vertical displacement of the grille was applied to build a 3D measurement grid consisting of horizontal planes. The DSP algorithm that processed the data measured from the measurement microphones was developed in National instruments® PXI 8820 controller and the ADC and DAC tasks were performed by PXI 6251 sampling card. Moreover, Labview® was employed to create

an application for real-time processing and monitoring of the obtained acoustic pressure signals. The user interface of this application is also illustrated in Figure D.2.

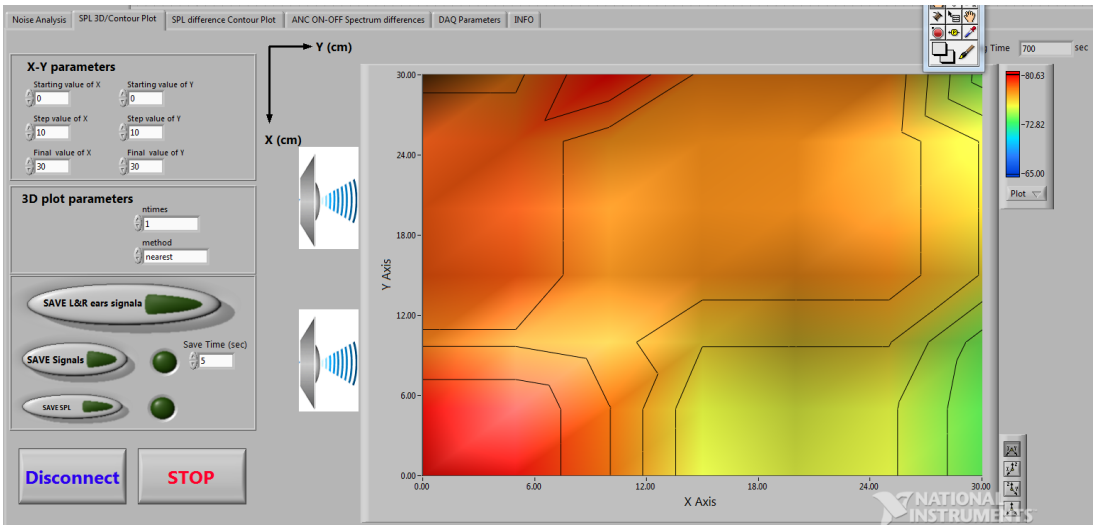

Figure D.2: User interface of the application used for the monitoring of acoustic pressure in front of the proposed ANC systems.

References

[1] P. Lueg, «Process of silencing sound oscillations», *U.S. patent No. 2,043,416.Application:8 March 1934. Patented:9 June 1936. Priority(Germany): 27 January 193*,

[2] D. Guicking, «On the invention of active noise control by Paul Lueg», *The Journal of the Acoustical Society of America*, vol. 87, no. 5, pp. 2251–2254, May 1990, ISSN: 0001-4966. DOI: 10.1121/1.399195. eprint: https://pubs.aip.org/asa/jasa/article-pdf/87/5/2251/11927142/2251_1_online.pdf. [Online]. Available: https://doi.org/10.1121/1.399195.

[3] H. F. Olson and E. G. May, «Electronic Sound Absorber», *The Journal of the Acoustical Society of America*, vol. 25, no. 6, pp. 1130–1136, Nov. 1953, ISSN: 0001-4966. DOI: 10.1121/1.1907249. eprint: https://pubs.aip.org/asa/jasa/article-pdf/25/6/1130/18731915/1130_1_online.pdf. [Online]. Available: https://doi.org/10.1121/1.1907249.

[4] B. Widrow, J. Glover, J. McCool, *et al.*, «Adaptive noise cancelling: Principles and applications», *Proceedings of the IEEE*, vol. 63, no. 12, pp. 1692–1716, 1975. DOI: 10.1109/PROC.1975.10036.

[5] B. Widrow, D. Shur, and S. Shaffer, «On adaptive inverse control», in *'15th Asilomar Conference Circuits, Systems Computers'*, 1981, pp. 185–89.

[6] M. Pawelczyk, «Adaptive noise control algorithms for active headrest system», *Control Engineering Practice*, vol. 12, no. 9, pp. 1101–1112, 2004, ISSN: 0967-0661. DOI: https://doi.org/10.1016/j.conengprac.2003.11.006. [Online]. Available: https://www.sciencedirect.com/science/article/pii/S0967066103002569.

[7] C.-Y. Chang, C.-T. Chuang, S. M. Kuo, and C.-H. Lin, «Multi-functional active noise control system on headrest of airplane seat», *Mechanical Systems and Signal Processing*, vol. 167, p. 108 552, 2022, ISSN: 0888-3270. DOI: https://doi.org/10.1016/j.ymssp.2021.108552.

[8] H. M. Lee, Y. Hua, Z. Wang, K. M. Lim, and H. P. Lee, «A review of the application of active noise control technologies on windows: Challenges and limitations», *Applied Acoustics*, vol. 174, p. 107 753, 2021, ISSN: 0003-682X. DOI: https://doi.org/10.1016/j.apacoust.2020.107753.

[9] B. Lam, W.-S. Gan, D. Shi, M. Nishimura, and S. Elliott, «Ten questions concerning active noise control in the built environment», *Building and Environment*, vol. 200, p. 107 928, 2021, ISSN: 0360-1323. DOI: https://doi.org/10.1016/j.buildenv.2021.107928.

[10] M. Norambuena, A. Jakob, and M. Möser, «Mathematical model for a multichannel active absorption system», *Acta Acustica united with Acustica*, vol. 99, pp. 905–916, 6 Nov. 2013, ISSN: 16101928. DOI: 10.3813/AAA.918670.

[11] B. Betgen and M.-A. Galland, «A new hybrid active/passive sound absorber with variable surface impedance», *Mechanical Systems and Signal Processing*, vol. 25, pp. 1715–1726, 5 Jul. 2011, ISSN: 08883270. DOI: 10.1016/j.ymssp.2010.12.006.

[12] D. Mylonas, A. Erspamer, C. Yiakopoulos, and I. Antoniadis, «Global control of propeller-induced aircraft cabin noise using active sound absorbers», *Journal of Sound and Vibration*, vol. 573, p. 118 213, 2024, ISSN: 0022-460X. DOI: https://doi.org/10.1016/j.jsv.2023.118213. [Online]. Available: https://www.sciencedirect.com/science/article/pii/S0022460X23006624.

[13] P. Cobo, A. Fernández, and O. Doutres, «Low-frequency absorption using a two-layer system with active control of input impedance», *The Journal of the Acoustical Society of America*, vol. 114, pp. 3211–3216, 6 Dec. 2003, ISSN: 0001-4966. DOI: 10.1121/1.1629306.

[14] K. An, J. Back, S.-K. Lee, S. Shin, and D. Jang, «Active vibration control for reduction of interior noise caused by r-mdps of electric power steering in electric vehicle», *Applied Acoustics*, vol. 211, p. 109 544, 2023, ISSN: 0003-682X. DOI: https://doi.org/10.1016/j.apacoust.2023.109544. [Online]. Available: https://www.sciencedirect.com/science/article/pii/S0003682X23003420.

[15] M. Misol, «Full-scale experiments on the reduction of propeller-induced aircraft interior noise with active trim panels», *Applied Acoustics*, vol. 159, p. 107 086, Feb. 2020, ISSN: 0003682X. DOI: 10.1016/j.apacoust.2019.107086.

[16] H. V. Fuchs, «Absorbers with active components», in *Applied Acoustics: Concepts, Absorbers, and Silencers for Acoustical Comfort and Noise Control: Alternative Solutions - Innovative Tools - Practical Examples*. Berlin, Heidelberg: Springer Berlin Heidelberg, 2013, pp. 89–99.

[17] I. Dimino and F. Aliabadi, *Active Control of Aircraft Cabin Noise*. IMPERIAL COLLEGE PRESS, 2015. DOI: 10.1142/p996. eprint: https://www.worldscientific.com/doi/pdf/10.1142/p996. [Online]. Available: https://www.worldscientific.com/doi/abs/10.1142/p996.

[18] J. Cheer, S. J. Elliott, and W. Jung, «Sound field control in the automotive environment», in *Automotive Acoustics Conference 2015*, W. Siebenpfeiffer, Ed., Wiesbaden: Springer Fachmedien Wiesbaden, 2019, pp. 158–175.

[19] C. L. Ferrari, J. Cheer, and M. Mautone, «Investigation of an engine order noise cancellation system in a super sports car», *Acta Acust*, vol. 7, 2023. DOI: 10.1051/aacus/2022060.

[20] G. Bernardini, C. Testa, and M. Gennaretti, «Tiltrotor cabin noise control through smart actuators», *Journal of Vibration and Control*, vol. 22, pp. 3–17, 1 Jan. 2016, ISSN: 1077-5463. DOI: 10.1177/1077546314526919.

[21] A. D. Marano, T. Polito, M. Guida, *et al.*, «Tiltrotor acoustic data acquisition and analysis», *Aerotecnica Missili and Spazio*, vol. 100, pp. 111–122, 2 Jun. 2021, ISSN: 0365-7442. DOI: 10.1007/s42496-021-00075-5.

[22] J. Wilby, «Aircraft interior noise», *Journal of Sound and Vibration*, vol. 190, no. 3, pp. 545–564, 1996, ISSN: 0022-460X. DOI: https://doi.org/10.1006/jsvi.1996.0078. [Online]. Available: https://www.sciencedirect.com/science/article/pii/S0022460X96900784.

[23] D. Mylonas, A. Erspamer, C. Yiakopoulos, and I. Antoniadis, «An extrapolation-based virtual sensing technique of improving the control performance of the fxlms algorithm in a maritime environment», *Applied Acoustics*, vol. 193, p. 108 756, 2022, ISSN: 0003-682X. DOI: https://doi.org/10.1016/j.apacoust.2022.108756. [Online]. Available: https://www.sciencedirect.com/science/article/pii/S0003682X2200130X.

[24] J. Cheer and S. J. Elliott, «Active noise control of a diesel generator in a luxury yacht», *Appl Acoust*, vol. 105, pp. 209–214, 2016. DOI: 10.1016/j.apacoust.2015.12.007.

[25] E. D. Simshauser and M. E. Hawley, «The Noise-Cancelling Headset—An Active Ear Defender», *The Journal of the Acoustical Society of America*, vol. 27, no. 1 Supplement, pp. 207–207, Jan. 1955, ISSN: 0001-4966. DOI: 10.1121/1.1917899.

[26] S. Elliott, A. Curtis, A. Bullmore, and P. Nelson, «The active minimization of harmonic enclosed sound fields, part iii: Experimental verification», *Journal of Sound and Vibration*, vol. 117, no. 1, pp. 35–58, 1987, ISSN: 0022-460X. DOI: https://doi.org/10.1016/0022-460X(87)90434-2.

[27] C. Dorling, G. Eatwell, S. Hutchins, C. Ross, and S. S.C.G., «A demontration of active noise reduction in an aircraft cabin», *Journal of Sound and Vibration*, vol. 128, pp. 358–360, 1989. DOI: 10.1038/s41598-018-23531-y. [Online]. Available: https://doi.org/10.1038/s41598-018-23531-y.

[28] F. Orduña-Bustamante and P. A. Nelson, «An adaptive controller for the active absorption of sound», *The Journal of the Acoustical Society of America*, vol. 91, no. 5, pp. 2740–2747, May 1992, ISSN: 0001-4966. DOI: 10.1121/1.403779. [Online]. Available: https://doi.org/10.1121/1.403779.

[29] D. Das and G. Panda, «Active mitigation of nonlinear noise processes using a novel filtered-s lms algorithm», *IEEE Transactions on Speech and Audio Processing*, vol. 12, no. 3, pp. 313–322, 2004. DOI: 10.1109/TSA.2003.822741.

[30] Y.-L. Zhou, Q.-Z. Zhang, X.-D. Li, and W.-S. Gan, «Analysis and dsp implementation of an anc system using a filtered-error neural network», *Journal of Sound and Vibration*, vol. 285, no. 1, pp. 1–25, 2005, ISSN: 0022-460X. DOI: https://doi.org/10.1016/j.jsv.2004.08.007. [Online]. Available: https://www.sciencedirect.com/science/article/pii/S0022460X04006364.

[31] S. J. Elliott, W. Jung, and J. Cheer, «Head tracking extends local active control of broadband sound to higher frequencies», *Scientific Reports*, 2018. DOI: 10.1038/s41598-018-23531-y. [Online]. Available: https://doi.org/10.1038/s41598-018-23531-y.

[32] R. Han, M. Wu, C. Gong, *et al.*, «Combination of robust algorithm and head-tracking for a feedforward active headrest», *Applied Sciences (Switzerland)*, vol. 9, 9 May 2019, ISSN: 20763417. DOI: 10.3390/app9091760.

[33] M. L. N. S. Karthik, S. Pradhan, and N. V. George, «Performance evaluation of an active headrest system using a filtered-x least mean square/fourth algorithm with virtual sensing», *The Journal of the Acoustical Society of America*, vol. 154, no. 5, pp. 2878–2891, Nov. 2023, ISSN: 0001-4966. DOI: 10.1121/10.0022329. eprint: https://pubs.aip.org/asa/jasa/article-pdf/154/5/2878/18201554/2878_1_10.0022329.pdf. [Online]. Available: https://doi.org/10.1121/10.0022329.

[34] L. Yin, Z. Zhang, M. Wu, *et al.*, «Adaptive parallel filter method for active cancellation of road noise inside vehicles», *Mechanical Systems and Signal Processing*, vol. 193, p. 110 274, 2023, ISSN: 0888-3270. DOI: https://doi.org/10.1016/j.ymssp.2023.110274. [Online]. Available: https://www.sciencedirect.com/science/article/pii/S0888327023001814.

[35] X. Liang, J. Yao, L. Luo, W. Zhu, W. Zhang, and Y. Wang, «A new proportionate filtered-x rls algorithm for active noise control system», *Sensors (Basel)*, vol. 22, no. 12, p. 4566, 2022. DOI: 10.3390/s22124566.

[36] A. Zeb, A. Mirza, and S. A. Sheikh, «Filtered-x rls algorithm based active noise control of impulsive noise», in *2015 7th International Conference on Modelling, Identification and Control (ICMIC)*, 2015, pp. 1–5. DOI: 10.1109/ICMIC.2015.7409414.

[37] Z. Zhang, M. Wu, C. Gong, L. Yin, and J. Yang, «Adjustable structure for feedback active headrest system using the virtual microphone method», *Applied Sciences (Switzerland)*, vol. 11, 11 Jun. 2021, ISSN: 20763417. DOI: 10.3390/app11115033.

[38] X. Shen, W.-S. Gan, and D. Shi, «Alternative switching hybrid anc», *Applied Acoustics*, vol. 173, p. 107 712, 2021, ISSN: 0003-682X. DOI: https://doi.org/10.1016/j.apacoust.2020.107712. [Online]. Available: https://www.sciencedirect.com/science/article/pii/S0003682X20308161.

[39] L. Lu, K.-L. Yin, R. C. de Lamare, *et al.*, «A survey on active noise control in the past decade–part ii: Nonlinear systems», *Signal Processing*, vol. 181, p. 107 929, 2021, ISSN: 0165-1684. DOI: https://doi.org/10.1016/j.sigpro.2020.107929. [Online]. Available: https://www.sciencedirect.com/science/article/pii/S0165168420304734.

[40] J. Seo, K. Kim, and S. Nam, «Nonlinear anc using a third-order volterra filter with an ldlt-fap algorithm», *IFAC Proceedings Volumes*, vol. 41, no. 2, pp. 7566–7569, 2008, 17th IFAC World Congress, ISSN: 1474-6670. DOI: https://doi.org/10.3182/20080706-5-KR-1001.01279. [Online]. Available: https://www.sciencedirect.com/science/article/pii/S147466701640162X.

[41] L. Tan and J. Jiang, «Adaptive volterra filters for active control of nonlinear noise processes», *IEEE Transactions on Signal Processing*, vol. 49, no. 8, pp. 1667–1676, 2001. DOI: 10.1109/78.934136.

[42] L. Luo, J. Sun, B. Huang, and X. Jiang, «A modified fslms algorithm for nonlinear anc», in *2016 Asia-Pacific Signal and Information Processing Association Annual Summit and Conference (APSIPA)*, 2016, pp. 1–4. DOI: 10.1109/APSIPA.2016.7820859.

[43] S. Kuo and H.-T. Wu, «Nonlinear adaptive bilinear filters for active noise control systems», *IEEE Transactions on Circuits and Systems I: Regular Papers*, vol. 52, no. 3, pp. 617–624, 2005. DOI: 10.1109/TCSI.2004.842429.

[44] X. Guo, J. Jiang, J. Chen, S. Du, and L. Tan, «Bibo-stable implementation of adaptive function expansion bilinear filter for nonlinear active noise control», *Applied Acoustics*, vol. 168, p. 107 407, 2020, ISSN: 0003-682X. DOI: https://doi.org/10.1016/j.apacoust.2020.107407. [Online]. Available: https://www.sciencedirect.com/science/article/pii/S0003682X20305119.

[45] M. Scarpiniti, D. Comminiello, R. Parisi, and A. Uncini, «A collaborative filter approach to adaptive noise cancellation», in *Neural Nets and Surroundings: 22nd Italian Workshop on Neural Nets, WIRN 2012, May 17-19, Vietri sul Mare, Salerno, Italy*, B. Apolloni, S. Bassis, A. Esposito, and F. C. Morabito, Eds. Berlin, Heidelberg: Springer Berlin Heidelberg, 2013, pp. 101–109, ISBN: 978-3-642-35467-0. DOI: 10.1007/978-3-642-35467-0_11. [Online]. Available: https://doi.org/10.1007/978-3-642-35467-0_11.

[46] D. Shi, B. Lam, K. Ooi, X. Shen, and W.-S. Gan, «Selective fixed-filter active noise control based on convolutional neural network», *Signal Processing*, vol. 190, p. 108 317, 2022, ISSN: 0165-1684. DOI: https://doi.org/10.1016/j.sigpro.2021.108317. [Online]. Available: https://www.sciencedirect.com/science/article/pii/S0165168421003546.

[47] H. Zhang and D. Wang, «Deep anc: A deep learning approach to active noise control», *Neural Networks*, vol. 141, pp. 1–10, 2021, ISSN: 0893-6080. DOI: https://doi.org/10.1016/j.neunet.2021.03.037. [Online]. Available: https://www.sciencedirect.com/science/article/pii/S0893608021001258.

[48] A. S. M, R. Biradar, and P. V. Joshi, «Implementation of an active noise cancellation technique using deep learning», in *2022 International Conference on Inventive Computation Technologies (ICICT)*, 2022, pp. 249–253. DOI: 10.1109/ICICT54344.2022.9850807.

[49] K. Zhang, G. Lyu, and X. Luo, «A deep recurrent neural network controller for nonlinear active noise control systems», in *2020 IEEE 6th International Conference on Computer and Communications (ICCC)*, 2020, pp. 2393–2396. DOI: 10.1109/ICCC51575.2020.9345164.

[50] Y.-J. Jang, J. Park, W.-C. Lee, and H.-J. Park, «A convolution-neural-network feedforward active-noise-cancellation system on fpga for in-ear headphone», *Applied Sciences*, vol. 12, no. 11, 2022, ISSN: 2076-3417. DOI: 10.3390/app12115300. [Online]. Available: https://www.mdpi.com/2076-3417/12/11/5300.

[51] D. Shi, W.-S. Gan, B. Lam, and S. Wen, «Feedforward selective fixed-filter active noise control: Algorithm and implementation», *IEEE/ACM Transactions on Audio, Speech, and Language Processing*, vol. 28, pp. 1479–1492, 2020. DOI: 10.1109/TASLP.2020.2989582.

[52] P. Nelson and S. Elliot, *Active Control of Sound*. London: Academic Press Limited, 1992.

[53] S. Kuo and D. Morgan, «Active noise control: A tutorial review», *Proceedings of the IEEE*, vol. 87, no. 6, pp. 943–973, 1999. DOI: 10.1109/5.763310.

[54] R. Corsaro, «Inflatable lightweight low-frequency loudspeaker», *The Journal of the Acoustical Society of America*, vol. 110, pp. 2671–2671, Nov. 2001, ISSN: 0001-4966. DOI: 10.1121/1.4777127. [Online]. Available: https://doi.org/10.1121/1.4777127.

[55] J. Han, J. H. Lang, and V. Bulović, «An ultrathin flexible loudspeaker based on a piezoelectric microdome array», *IEEE Transactions on Industrial Electronics*, vol. 70, no. 1, pp. 985–994, 2023. DOI: 10.1109/TIE.2022.3150082.

[56] D. Moreau, B. Cazzolato, A. Zander, and C. Petersen, «A review of virtual sensing algorithms for active noise control», *Algorithms*, vol. 1, pp. 69–99, 2 Dec. 2008, ISSN: 19994893. DOI: 10.3390/a1020069.

[57] J. Buck, S. Jukkert, and D. Sachau, «Performance evaluation of an active headrest considering non-stationary broadband disturbances and head movement», *The Journal of the Acoustical Society of America*, vol. 143, pp. 2571–2579, 5 May 2018, ISSN: 0001-4966. DOI: 10.1121/1.5034767.

[58] C. D. Petersen, A. C. Zander, B. S. Cazzolato, and C. H. Hansen, «A moving zone of quiet for narrowband noise in a one-dimensional duct using virtual sensing», *The Journal of the Acoustical Society of America*, vol. 121, pp. 1459–1470, 3 Mar. 2007, ISSN: 0001-4966. DOI: 10.1121/1.2431583.

[59] A. Roure and A. Albarrazin, «The remote microphone technique for active noise control», in *Proceedings of the INTER-NOISE and NOISE-CON Congress and Conference*, vol. 5, 1999, pp. 1233–1244.

[60] C. Lei, J. Xu, J. Wang, C. Zheng, and X. Li, «Active headrest with robust performance against head movement», *Journal of Low Frequency Noise, Vibration and Active Control*, vol. 34, pp. 233–250, 3 Jun. 2015, ISSN: 1461-3484. DOI: 10.1260/0263-0923.34.3.233.

[61] M. Ferrer, A. Gonzalez, M. de Diego, and G. Pinero, «Computationally efficient version of the affine projection algorithm for multichannel active noise control», in *Processing Workshop Proceedings, 2004 Sensor Array and Multichannel Signal*, 2004, pp. 561–565. DOI: 10.1109/SAM.2004.1503011.

[62] S. Gaiotto, A. Laudani, G. M. Lozito, and F. R. Fulginei, «A computationally efficient algorithm for feedforward active noise control systems», *Electronics*, vol. 9, no. 9, 2020, ISSN: 2079-9292. DOI: 10.3390/electronics9091504. [Online]. Available: https://www.mdpi.com/2079-9292/9/9/1504.

[63] W. Chen, Z. Liu, L. Hu, *et al.*, «A low-complexity multi-channel active noise control system using local secondary path estimation and clustered control strategy for vehicle interior engine noise», *Mech Syst Signal Process*, vol. 204, 2023. DOI: 10.1016/j.ymssp.2023.110786.

[64] S. Park and D. Park, «Low-power fpga realization of lightweight active noise cancellation with cnn noise classification», *Electronics*, vol. 12, no. 11, 2023, ISSN: 2079-9292. DOI: 10.3390/electronics12112511. [Online]. Available: https://www.mdpi.com/2079-9292/12/11/2511.

[65] A. Leva and L. Piroddi, «Fpga-based implementation of high-speed active noise and vibration controllers», *Control Engineering Practice*, vol. 19, no. 8, pp. 798–808, 2011, ISSN: 0967-0661. DOI: https://doi.org/10.1016/j.conengprac.2011.04.006. [Online]. Available: https://www.sciencedirect.com/science/article/pii/S0967066111000724.

[66] D. Mylonas, A. Erspamer, C. Yiakopoulos, and I. Antoniadis, «A low computational complexity local active noise control system for adjacent aircraft seats», in *Forum Acusticum Proceedings*, Torino, Italy, 2023. DOI: 10.61782/fa.2023.0022.

[67] S. Elliot, P. Nelson, I. Stothers, and C. Boucher, «In-flight experiments on the active control of propeller-induced cabin noise», *Journal of Sound and Vibration*, vol. 140, no. 2, pp. 219–238, 1990, ISSN: 0022-460X. DOI: https://doi.org/10.1016/0022-460X(90)90525-5. [Online]. Available: https://www.sciencedirect.com/science/article/pii/0022460X90905255.

[68] S. ELLIOTT, «9 - optimisation of transducer location», in *Signal Processing for Active Control*, ser. Signal Processing and its Applications, S. ELLIOTT, Ed., London: Academic Press, 2001, pp. 411–438, ISBN: 978-0-12-237085-4. DOI: https://doi.org/10.1016/B978-012237085-4/50011-9. [Online]. Available: https://www.sciencedirect.com/science/article/pii/B9780122370854500119.

[69] H. Lissek, R. Boulandet, and R. Fleury, «Electroacoustic absorbers: Bridging the gap between shunt loudspeakers and active sound absorption», *The Journal of the Acoustical Society of America*, vol. 129, no. 5, pp. 2968–2978, May 2011, ISSN: 0001-4966. DOI: 10.1121/1.3569707. eprint: https://pubs.aip.org/asa/jasa/article-pdf/129/5/2968/13951213/2968_1_online.pdf. [Online]. Available: https://doi.org/10.1121/1.3569707.

[70] F. M. Heuchel, E. Fernandez-Grande, F. T. Agerkvist, and E. Shabalina, «Active room compensation for sound reinforcement using sound field separation techniques», *The Journal of the Acoustical Society of America*, vol. 143, pp. 1346–1354, 3 Mar. 2018, ISSN: 0001-4966. DOI: 10.1121/1.5024903.

[71] E. Rivet, S. Karkar, and H. Lissek, «Broadband low-frequency electroacoustic absorbers through hybrid sensor-/shunt-based impedance control», *IEEE Transactions on Control Systems Technology*, vol. 25, pp. 63–72, 1 Jan. 2017, ISSN: 1063-6536. DOI: 10.1109/TCST.2016.2547981.

[72] S. Adachi and H. Sano, «Application of two-degree-of-freedom type active noise control using imc to road noise inside automobiles», in *Proceedings of 35th IEEE Conference on Decision and Control*, vol. 3, 1996, 2794–2795 vol.3. DOI: 10.1109/CDC.1996.573537.

[73] S. M. Kuo, Y.-R. Chen, C.-Y. Chang, and C.-W. Lai, «Development and evaluation of light-weight active noise cancellation earphones», *Applied Sciences*, vol. 8, no. 7, 2018, ISSN: 2076-3417. DOI: 10.3390/app8071178. [Online]. Available: https://www.mdpi.com/2076-3417/8/7/1178.

[74] C. Gong, M. Wu, J. Guo, Z. Zhang, Y. Cao, and J. Yang, «Multichannel narrowband active noise control system with a frequency estimator based on dft coefficients», *Journal of Sound and Vibration*, vol. 521, p. 116 660, 2022, ISSN: 0022-460X. DOI: https://doi.org/10.1016/j.jsv.2021.116660. [Online]. Available: https://www.sciencedirect.com/science/article/pii/S0022460X21006726.

[75] J. Su, J. Nie, and S. Chen, «Application of an improved wide–narrow-band hybrid anc algorithm in a large commercial vehicle cabine», *Scientific Reports*, vol. 14, no. 1, p. 10 470, 2024. DOI: 10.1038/s41598-024-60979-7. [Online]. Available: https://doi.org/10.1038/s41598-024-60979-7.

[76] F. Yang, A. Gupta, and S. M. Kuo, «Parallel multi-frequency narrowband active noise control systems», in *2009 IEEE International Conference on Acoustics, Speech and Signal Processing*, 2009, pp. 253–256. DOI: 10.1109/ICASSP.2009.4959568.

[77] R. Roy and T. Kailath, «Esprit-estimation of signal parameters via rotational invariance techniques», *IEEE Transactions on Acoustics, Speech, and Signal Processing*, vol. 37, no. 7, pp. 984–995, 1989. DOI: 10.1109/29.32276.

[78] S. Johansson, «Active control of propeller-induced noise in aircraft-algorithms and methods», Ph.D. dissertation, Blekinge Institute of Technology, Ronneby, Sweden, 2020.

[79] S. Kuo and D. Morgan, «5 - multiple-channel active noise control», in *Active Noise Control Systems-Algorithms and DSP Implementations*, ser. Series in Telecommunications and Signal Processing, New York: Wiley, 1996, pp. 158–167.

[80] S. C. Douglas, «Fast implementations of the filtered-x lms and lms algorithms for multichannel active noise control», *IEEE Transactions on Speech and Audio Processing*, vol. 7, pp. 454–465, 1999. DOI: 10.1109/89.771315.

[81] D. Shi, W. S. Gan, J. He, and B. Lam, «Practical implementation of multichannel filtered-x least mean square algorithm based on the multiple-parallel-branch with folding architecture for large-scale active noise control», *IEEE Transactions on Very Large Scale Integration (VLSI) Systems*, vol. 28, pp. 940–953, 2020. DOI: 10.1109/TVLSI.2019.2956524.

[82] C. Shi and Y. Kajikawa, «A partial-update minimax algorithm for practical implementation of multi-channel feedforward active noise control», in *16th International Workshop on Acoustic Signal Enhancement (IWAENC)*, 2018, pp. 1–15. DOI: 10.1109/IWAENC.2018.8521376.

[83] D. Shi, B. Lam, J. Ji, X. Shen, C. K. Lai, and W. S. Gan, «Computation-efficient solution for fully-connected active noise control window: Analysis and implementation of multichannel adjoint least mean square algorithm», *Mech Syst and Signal Process*, vol. 199, 2023. DOI: 10.1016/j.ymssp.2023.110444.

[84] C. Y. Ho, L. Liu, K. K. Shyu, S. M. Kuo, and C. Y. Chang, «Time-division multiple reference approach for multiple-channel active noise control system», *J. Sound Vib*, vol. 495, 2021. DOI: 10.1016/.

[85] T. Murao, C. Shi, W. S. Gan, and M. Nishimura, «Mixed-error approach for multichannel active noise control of open windows», *Applied Acoustics*, vol. 127, pp. 305–315, Dec. 2017, ISSN: 1872910X. DOI: 10.1016/j.apacoust.2017.06.024.

[86] J. Garcia-Bonito, S. J. Elliott, and C. C. Boucher, «Generation of zones of quiet using a virtual microphone arrangement», *The Journal of the Acoustical Society of America*, vol. 101, pp. 3498–3516, 6 Jun. 1997, ISSN: 0001-4966. DOI: 10.1121/1.418357.

[87] W. Jung, S. J. Elliott, and J. Cheer, «Combining the remote microphone technique with head-tracking for local active sound control», *The Journal of the Acoustical Society of America*, vol. 142, pp. 298–307, 1 Jul. 2017, ISSN: 0001-4966. DOI: 10.1121/1.4994292.

[88] J. Buck and D. Sachau, «Active headrests with selective delayless subband adaptive filters in an aircraft cabin», *Mechanical Systems and Signal Processing*, vol. 148, p. 107 164, 2021, ISSN: 0888-3270. DOI: https://doi.org/10.1016/j.ymssp.2020.107164. [Online]. Available: https://www.sciencedirect.com/science/article/pii/S0888327020305501.

[89] Z. Zhang, M. Wu, L. Yin, *et al.*, «Robust parallel virtual sensing method for feedback active noise control in a headrest», *Mechanical Systems and Signal Processing*, vol. 178, p. 109 293, 2022, ISSN: 0888-3270. DOI: https://doi.org/10.1016/j.ymssp.2022.109293. [Online]. Available: https://www.sciencedirect.com/science/article/pii/S0888327022004344.

[90] S. K. Behera, D. P. Das, and B. Subudhi, «Head movement immune active noise control with head mounted moving microphones», *The Journal of the Acoustical Society of America*, vol. 142, pp. 573–587, 2 Aug. 2017, ISSN: 0001-4966. DOI: 10.1121/1.4996125.

[91] D. Petersen, A. C. Zander, B. S. Cazzolato, and C. H. Hansen, «Optimal virtual sensing for active noise control in a rigid-walled acoustic duct», *The Journal of the Acoustical Society of America*, vol. 118, pp. 3086–3093, 5 Nov. 2005, ISSN: 0001-4966. DOI: 10.1121/1.2047127.

[92] C. D. Kestell, B. S. Cazzolato, and C. H. Hansen, «Active noise control in a free field with virtual sensors», *The Journal of the Acoustical Society of America*, vol. 109, pp. 232–243, 1 Jan. 2001, ISSN: 0001-4966. DOI: 10.1121/1.1326950.

[93] B. Cazzolato, «Sensing systems for active control of sound transmission into cavities», Ph.D. dissertation, Department of Mechanical Engineering, The University of Adelaide, 1999.

[94] B. Treeby, B. Cox, and J. Jaros, *K-wave user manual version 1.1*, Accessed: 2024-06-08, 2016. [Online]. Available: http://www.k-wave.org/manual/k-wave_user_manual_1.1.pdf.

[95] N. V. George and G. Panda, «Advances in active noise control: A survey, with emphasis on recent nonlinear techniques», *Signal Processing*, vol. 93, pp. 363–377, 2 Feb. 2013, ISSN: 01651684. DOI: 10.1016/j.sigpro.2012.08.013.

[96] M. Costa, J. Bermudez, and N. Bershad, «Stochastic analysis of the filtered-x lms algorithm in systems with nonlinear secondary paths», *IEEE Transactions on Signal Processing*, vol. 50, no. 6, pp. 1327–1342, 2002. DOI: 10.1109/TSP.2002.1003058.

[97] A. C. Sicuranza, «Nonlinear multichannel active noise control», in *Advances in Nonlinear Signal and Image Processing*, S. Marshall and G. Sicuranza, Eds., Hindawi Publishing Corporation, 2006, pp. 169–203.

[98] T. Matsuura, T. Hiei, H. Itoh, and K. Torikoshi, «Active noise control by using prediction of time series data with a neural network», in *Proceedings of IEEE International Conference on Systems, Man, and Cybernetics*, vol. 3, 1995, pp. 2070–2075.

[99] S. K. Behera, D. P. Das, and B. Subudhi, «Functional link artificial neural network applied to active noise control of a mixture of tonal and chaotic noise», *Applied Soft Computing Journal*, vol. 23, pp. 51–60, 2014, ISSN: 15684946. DOI: 10.1016/j.asoc.2014.06.007.

[100] R. Walia and S. Ghosh, «Design of active noise control system using hybrid functional link artificial neural network and finite impulse response filters», *Neural Computing and Applications*, vol. 32, no. 7, pp. 2257–2266, Apr. 2020, ISSN: 1433-3058. DOI: 10.1007/s00521-018-3697-5. [Online]. Available: https://doi.org/10.1007/s00521-018-3697-5.

[101] K.-L. Yin, Y.-F. Pu, and L. Lu, «Hermite functional link artificial-neural-network-assisted adaptive algorithms for iov nonlinear active noise control», *IEEE Internet of Things Journal*, vol. 7, no. 9, pp. 8372–8383, 2020. DOI: 10.1109/JIOT.2020.2989761.

[102] B. Chen, S. Yu, Y. Yu, and R. Guo, «Nonlinear active noise control system based on correlated emd and chebyshev filter», *Mechanical Systems and Signal Processing*, vol. 130, pp. 74–86, 2019, ISSN: 0888-3270. DOI: https://doi.org/10.1016/j.ymssp.2019.04.059. [Online]. Available: https://www.sciencedirect.com/science/article/pii/S0888327019302961.

[103] D. P. Das, D. J. Moreau, and B. S. Cazzolato, «A nonlinear active noise control algorithm for virtual microphones controlling chaotic noise», *The Journal of the Acoustical Society of America*, vol. 132, pp. 779–788, 2 Aug. 2012, ISSN: 0001-4966. DOI: 10.1121/1.4731227.

[104] D. P. Das, D. J. Moreau, and B. S. Cazzolato, «Nonlinear active noise control for headrest using virtual microphone control», *Control Engineering Practice*, vol. 21, pp. 544–555, 4 Apr. 2013, ISSN: 09670661. DOI: 10.1016/j.conengprac.2012.11.007.

[105] Y.-H. Pao and Y. Takefuji, «Functional-link net computing: Theory, system architecture, and functionalities», *Computer*, vol. 25, no. 5, pp. 76–79, 1992. DOI: 10.1109/2.144401.

[106] L. Luo, Z. Bai, W. Zhu, and J. Sun, «Improved functional link artificial neural network filters for nonlinear active noise control», *Applied Acoustics*, vol. 135, pp. 111–123, 2018, ISSN: 0003-682X. DOI: https://doi.org/10.1016/j.apacoust.2018.01.021. [Online]. Available: https://www.sciencedirect.com/science/article/pii/S0003682X17306242.

[107] J. Ren, Q. Song, X. Wang, and X. Yang, «Chebyshev functional link neural network integrating fir filter architecture for power amplifier linearization», in *2022 IEEE International Conference on Consumer Electronics (ICCE)*, 2022, pp. 1–5. DOI: 10.1109/ICCE53296.2022.9730573.

[108] F. G. Lasaki, H. Ebrahimi, and M. Ilie, «A novel lagrange functional link neural network for solving variable-order fractional time-varying delay differential equations: A comparison with multilayer perceptron neural networks», *Soft Computing*, vol. 27, no. 17, pp. 12 595–12 608, 2023, ISSN: 1433-7479. DOI: 10.1007/s00500-023-08494-1. [Online]. Available: https://doi.org/10.1007/s00500-023-08494-1.

[109] D. M. Sahoo and S. Chakraverty, «Functional link neural network approach to solve structural system identification problems», *Neural Computing and Applications*, vol. 30, no. 11, pp. 3327–3338, 2018, ISSN: 1433-3058. DOI: 10.1007/s00521-017-2907-x. [Online]. Available: https://doi.org/10.1007/s00521-017-2907-x.

[110] V. Patel, V. Gandhi, S. Heda, and N. V. George, «Design of adaptive exponential functional link network-based nonlinear filters», *IEEE Transactions on Circuits and Systems I: Regular Papers*, vol. 63, no. 9, pp. 1434–1442, 2016. DOI: 10.1109/TCSI.2016.2572091.

[111] P. P. Das, R. Bisoi, and P. Dash, «Time series forecasting using fuzzy functional link neural network trained by improved second order levenberg-marquardt algorithm», in *2015 IEEE Power, Communication and Information Technology Conference (PCITC)*, 2015, pp. 827–833. DOI: 10.1109/PCITC.2015.7438110.

[112] D. P. Das, S. R. Mohapatra, A. Routray, and T. K. Basu, «Filtered-s lms algorithm for multichannel active control of nonlinear noise processes», *IEEE Transactions on Audio, Speech and Language Processing*, vol. 14, pp. 1875–1880, 5 Sep. 2006, ISSN: 15587916. DOI: 10.1109/TSA.2005.858543.

[113] «Path identification for active noise control (piano), horizon 2020». (2023), [Online]. Available: https://piano-project.eu/scope/.

[114] L. Luo and W. Zhu, «Fast-convergence hybrid functional link artificial neural network for active noise control with a mixture of tonal and chaotic noise», *Digital Signal Processing: A Review Journal*, vol. 106, Nov. 2020, ISSN: 10512004. DOI: 10.1016/j.dsp.2020.102846.

[115] G. L. Sicuranza and A. Carini, «On the bibo stability condition of adaptive recursive flann filters with application to nonlinear active noise control», *IEEE Transactions on Audio, Speech and Language Processing*, vol. 20, pp. 234–245, 1 2012, ISSN: 15587916. DOI: 10.1109/TASL.2011.2159788.

[116] A. BenSaïda, «A practical test for noisy chaotic dynamics», *SoftwareX*, vol. 3-4, pp. 1–5, 2015, ISSN: 2352-7110. DOI: https://doi.org/10.1016/j.softx.2015.08.002. [Online]. Available: https://www.sciencedirect.com/science/article/pii/S2352711015000096.

[117] F. Félix, M. de Castro Magalhães, and G. de Souza Papini, «An improved anc algorithm for the attenuation of industrial fan noise», *Journal of Vibration Engineering and Technologies*, 2020. DOI: 10.1007/s42417-020-00225-2.

[118] F. Fahroo and M. A. Demetriou, «Optimal actuator/sensor location for active noise regulator and tracking control problems», *Journal of Computational and Applied Mathematics*, vol. 114, no. 1, pp. 137–158, 2000, ISSN: 0377-0427. DOI: https://doi.org/10.1016/S0377-0427(99)00293-9. [Online]. Available: https://www.sciencedirect.com/science/article/pii/S0377042799002939.

[119] G. Charalampopoulos, S. Mouzakitis, and C. Provatidis, «Gradient optimisation methods for the positioning of active noise control actuators in enclosures», *International Journal of Acoustics and Vibrations*, vol. 9, pp. 163–174, Dec. 2004. DOI: 10.20855/ijav.2004.9.4165.

[120] S. Mouzakitis, «Simulation of noise attenuation systems», Ph.D. dissertation, National Technical University of Athens, 2006. DOI: 10.12681/eadd/17022. [Online]. Available: http://hdl.handle.net/10442/hedi/17022.

[121] C. Provatidis, S. Mouzakitis, and G. Charalampopoulos, «Optimum positioning of active noise control sensors and actuators in enclosures with significant damping properties», *Acta Acustica united with Acustica*, vol. 91, pp. 846–859, Sep. 2005.

[122] C. G. Provatidis, S. T. Mouzakitis, and G. Charalampopoulos, «Simulation of active noise control in enclosures using direct sound field prediction», *Journal of Computational Acoustics*, vol. 17, pp. 83–107, 2009. DOI: 10.1142/S0218396X09003859.

[123] R. Boulandet, M. Michau, P. Micheau, and A. Berry, «Aircraft panel with sensorless active sound power reduction capabilities through virtual mechanical impedances», *Journal of Sound and Vibration*, vol. 361, pp. 2–19, Jan. 2016, ISSN: 0022460X. DOI: 10.1016/j.jsv.2015.09.042.

[124] X. Ma, Y. Lu, and F. Wang, «Active structural acoustic control of helicopter interior multifrequency noise using input-output-based hybrid control», *Journal of Sound and Vibration*, vol. 405, pp. 187–207, Sep. 2017, ISSN: 0022460X. DOI: 10.1016/j.jsv.2017.05.051.

[125] O. Lacour, M. Galland, and D. Thenail, «Preliminary experiments on noise reduction in cavities using active impedance changes», *Journal of Sound and Vibration*, vol. 230, pp. 69–99, 1 Feb. 2000, ISSN: 0022460X. DOI: 10.1006/jsvi.1999.2614.

[126] J.-B. Dupont and M.-A. Galland, «Active absorption to reduce the noise transmitted out of an enclosure», *Applied Acoustics*, vol. 70, pp. 142–152, 1 Jan. 2009, ISSN: 0003682X. DOI: 10.1016/j.apacoust.2007.12.008.

[127] F. Fahy, *Sound Intensity*. CRC Press, 2017, ISBN: 9781135822026. [Online]. Available: https://books.google.gr/books?id=HSSpDwAAQBAJ.

[128] F. Orduña-Bustamante and P. A. Nelson, «An adaptive controller for the active absorption of sound», *The Journal of the Acoustical Society of America*, vol. 91, pp. 2740–2747, 5 May 1992, ISSN: 0001-4966. DOI: 10.1121/1.403779.

[129] H. Zhu, R. Rajamani, and K. A. Stelson, «Active control of acoustic reflection, absorption, and transmission using thin panel speakers», *The Journal of the Acoustical Society of America*, vol. 113, pp. 852–870, 2 Feb. 2003, ISSN: 0001-4966. DOI: 10.1121/1.1534834.

[130] H. Iwamoto, N. Tanaka, and A. Sanada, «Noise reduction in a rectangular enclosure using active wave control», *Journal of Environment and Engineering*, vol. 6, pp. 107–118, 1 2011, ISSN: 1880-988X. DOI: 10.1299/jee.6.107.

[131] H. Iwamoto, N. Tanaka, and A. Sanada, «Wave-filter-based approach for generation of a quiet space in a rectangular cavity», *Mechanical Systems and Signal Processing*, vol. 100, pp. 570–587, Feb. 2018, ISSN: 08883270. DOI: 10.1016/j.ymssp.2017.07.050.

[132] A. O. Santillán, C. S. Pedersen, and M. Lydolf, «Experimental implementation of a low-frequency global sound equalization method based on free field propagation», *Applied Acoustics*, vol. 68, no. 10, pp. 1063–1085, 2007, ISSN: 0003-682X. DOI: https://doi.org/10.1016/j.apacoust.2006.05.010.

[133] F. Jacobsen and H.-E. Bree, «A comparison of two different sound intensity measurement principles», *Journal of The Acoustical Society of America - J ACOUST SOC AMER*, vol. 118, Sep. 2005. DOI: 10.1121/1.1984860.

[134] Pham Vu, Thach and Lissek, Hervé, «Low frequency sound field reconstruction in a non-rectangular room using a small number of microphones», *Acta Acust.*, vol. 4, no. 2, p. 5, 2020. DOI: 10.1051/aacus/2020006. [Online]. Available: https://doi.org/10.1051/aacus/2020006.

[135] M. Norambuena, «Active control of sound absorption», Ph.D. dissertation, Berlin Institute of Technology, 2012.

[136] A. Pierce, *Acoustics: An Introduction to Its Physical Principles and Applications*. Springer, 2019, ISBN: 978-3-030-11214-1. DOI: https://doi.org/10.1007/978-3-030-11214-1.

[137] S. A. Bagherzadeh and M. Salehi, «Assessment of cabin noise contributing factors of a turbo-propeller airplane using emd and ssa signal decomposition methods», *Applied Acoustics*, vol. 178, p. 108 020, 2021, ISSN: 0003-682X. DOI: https://doi.org/10.1016/j.apacoust.2021.108020. [Online]. Available: https://www.sciencedirect.com/science/article/pii/S0003682X21001134.

[138] B. E. Treeby and B. T. Cox, «K-wave: Matlab toolbox for the simulation and reconstruction of photoacoustic wave-fields», *Journal of Biomedical Optics*, vol. 15, no. 2, p. 021 314, 2010. DOI: 10.1117/1.3360308.

[139] B. E. Treeby, J. Jaros, A. P. Rendell, and B. T. Cox, «Modeling nonlinear ultrasound propagation in heterogeneous media with power law absorption using a k-space pseudospectral method», *Journal of the Acoustical Society of America*, vol. 131, no. 6, pp. 4324–4336, 2012. DOI: 10.1121/1.4712021.

[140] N. Atalla and F. Sgard, *Finite Element and Boundary Methods in Structural Acoustics and Vibration*. Boca Raton, Florida: CRC Press, 2015, ISBN: 9781138749177.

[141] M. Petyt, «Finite element techniques for acoustics», in *Theoretical Acoustics and Numerical Techniques*, P. Filippi, Ed. Vienna: Springer Vienna, 1983, pp. 51–103, ISBN: 978-3-7091-4340-7. DOI: 10.1007/978-3-7091-4340-7_2. [Online]. Available: https://doi.org/10.1007/978-3-7091-4340-7_2.

[142] COMSOL vr 5.5, *COMSOL Mltiphysics Reference Manual*, Accessed: 2024-06-10, 2020. [Online]. Available: https://doc.comsol.com/5.5/doc/com.comsol.help.comsol/COMSOL_ReferenceManual.pdf.

[143] COMSOL vr 5.5, *LiveLink for MATLAB User's Guide*, Accessed: 2024-06-10, 2020. [Online]. Available: https://doc.comsol.com/5.4/doc/com.comsol.help.llmatlab/LiveLinkForMATLABUsersGuide.pdf.

[144] J. Smardzewski, T. Kamisiński, D. Dziurka, *et al.*, «Sound absorption of wood-based materials», *Holzforschung*, vol. 69, no. 4, pp. 431–439, 2015. DOI: doi:10.1515/hf-2014-0114. [Online]. Available: https://doi.org/10.1515/hf-2014-0114.

[145] M. Misol, «Experiment on noise reduction aircraft with active sidewall panels.», in *Proc. 25th International Congress on Sound and Vibration*, Hiroshima, Japan, Jan. 2018.

[146] N. Instruments, *Crio-9030 specifications*, Accessed: 2024-06-12, 2024. [Online]. Available: https://www.ni.com/docs/en-US/bundle/crio-9030-specs/page/specs.html.

[147] N. Instruments, *Ni-9220 getting started guide*, Accessed: 2024-06-12, 2024. [Online]. Available: https://www.ni.com/docs/en-US/bundle/ni-9220-getting-started/page/overview.html.

[148] N. Instruments, *Ni-9264 getting started guide*, Accessed: 2024-06-12, 2024. [Online]. Available: https://www.ni.com/docs/en-US/bundle/ni-9264-getting-started/page/overview.html.

[149] Matthias Geier, *Python-sounddevice*, https://github.com/spatialaudio/python-sounddevice/, Accessed: 2024-06-13, 2024.

[150] I. Dimino, C. Colangeli, J. Cuenca, P. Vitiello, and M. Barbarino, «Active noise control for aircraft cabin seats», *Applied Sciences*, vol. 12, no. 11, 2022, ISSN: 2076-3417. DOI: 10.3390/app12115610. [Online]. Available: https://www.mdpi.com/2076-3417/12/11/5610.

Εκτενής περίληψη

Συστήματα Τοπικού και Ολικού Ενεργητικού Ελέγχου Θορύβου σε Οχήματα

1. Εισαγωγή

Ο Ενεργητικός Έλεγχος Θορύβου (ΕΕΘ) περιλαμβάνει μια ομάδα τεχνικών που χρησιμοποιούνται για τον μετριασμό της ακουστικής πίεσης και σε αντίθεση με τις παθητικές συμβατικές μεθόδους, δε χρησιμοποιούν φυσικά εμπόδια για τον σκοπό αυτό. Αντίθετα, βασίζονται στη δημιουργία ακουστικών κυμάτων που έχουν ως αποτέλεσμα την ακύρωση ή την απορρόφηση των ανεπιθύμητων ακουστικών διαταραχών. Έτσι, μπορούμε να χωρίσουμε τις μεθόδους ΕΕΘ σε αυτές που βασίζονται στην ακύρωση θορύβου και σε αυτές που βασίζονται στην απορρόφηση του ακουστικού κύματος. Η έννοια της ενεργητικής ακύρωσης θορύβου διατυπώθηκε για πρώτη φορά από τον Paul Lueg [1] στις αρχές του 1933. Βασίζεται στην αρχή της καταστροφικής συμβολής δυο κυμάτων, σύμφωνα με την οποία το πλάτος ενός ακουστικού κύματος μπορεί να μηδενιστεί αν συναντηθεί με ένα κύμα ίδιου πλάτους και αντίθετης φάσης. Παρόλα αυτά, τεχνολογικοί περιορισμοί δεν επέτρεψαν για πολύ καιρό την ευρεία εφαρμογή του ΕΕΘ σε πραγματικές συνθήκες [2], μέχρι που οι Olson και May πρότειναν την ιδέα του Ενεργητικού Απορροφητή ήχου [3], που η αρχή λειτουργία του βασίζονταν στην ιδέα του Lueg. Μια ακόμα σημαντική ανακάλυψη σε αυτόν τον τομέα ήρθε από τον Widrow με την εισαγωγή των αλγορίθμων LMS [4] και FxLMS [5] το 1975 και το 1981 αντίστοιχα, οι οποίοι ακόμη και σήμερα εξακολουθούν να αποτελούν σημείο αναφοράς για τα συστήματα Ενεργητικής Ακύρωσης Θορύβου.

Στις μέρες μας, πολλά τέτοια συστήματά έχουν ενσωματωθεί σε εμπορικά διαθέσιμα ακουστικά, ενώ στο μέλλον φαίνεται ότι τέτοια συστήματα θα ενσωματωθούν σε μια ποικιλία συσκευών, όπως προσκέφαλα ακύρωσης θορύβου [6], [7], ενεργά παράθυρα [8] και ενεργά φράγματα θορύβου [9]. Από την άλλη πλευρά, οι τεχνικές Ενεργητικής Απορρόφησής Θορύβου (ΕΑΘ) έχουν σχεδιαστεί για να αλλάζουν την ακουστική σύνθετη αντίσταση μιας

επιφάνειας προκειμένου να επιτευχθεί ηχοαπορρόφηση, η οποία μπορεί να οδηγήσει στη μείωση της ακουστικής πίεσης σε έναν κλειστό χώρο. Στα πλαίσια αυτά, έχουν προταθεί ποικίλες μέθοδοι για την τροποποίηση της ακουστικής σύνθετης αντίστασης, συμπεριλαμβανομένης της αλλαγής της ηλεκτρικής αντίστασης του μεγαφώνου που δρα σαν ενεργός απορροφητής ή της αλλαγής του συντελεστή απορρόφησης με υπολογισμό και ελαχιστοποίηση της ανακλώμενης συνιστώσας ενός ηχητικού κύματος μπροστά από το μεγάφωνο. Τέλος, υπάρχει μια κατηγορία μεθόδων γνωστών ως Ενεργητικός Έλεγχος Δονήσεων (ΕΕΔ), οι οποίες στοχεύουν στη μείωση της ακουστικής πίεσης μέσω της μείωσης των δονήσεων που μεταδίδονται διαμέσου των δομικών στοιχείων.

Μια κατηγορία εφαρμογών των συστημάτων ΕΕΘ έχουν να κάνουν με τη μείωση της ακουστικής πίεσης σε καμπίνες οχημάτων, αντιμετωπίζοντας τα υψηλά επίπεδα θορύβου που προέρχονται από τον κινητήρα και την αλληλεπίδραση με τα στοιχεία του περιβάλλοντος, όπως τον αέρα και τα κύματα [24], [150]. Οι παραδοσιακές παθητικές μέθοδοι όπως η μόνωση με ηχοαπορροφητικά υλικά είναι λιγότερο αποτελεσματικές σε χαμηλές συχνότητες [16], μιας και περιλαμβάνουν διατάξεις με μεγάλο πάχος και βάρος που έρχονται σε αντίθεση με την τάση μείωσης του βάρους κατά την κατασκευή οχημάτων. Αυτή η πρόκληση έχει οδηγήσει σε μεγαλύτερο ενδιαφέρον για τα συστήματα ΕΕΘ, τα οποία στοχεύουν στον μετριασμό του θορύβου, ελαχιστοποιώντας ταυτόχρονα το βάρος και το κόστος του οχήματος. Η μείωση του βάρους άλλωστε είναι ταυτόχρονα μια σημαντική παράμετρος για τη βιομηχανία αεροσκαφών αφού συντελεί στη μείωση της κατανάλωσης καυσίμου και συνακόλουθα των εκπομπών αερίων του θερμοκηπίου.

Συνεπώς, η παρούσα διδακτορική διατριβή εστιάζει σε συστήματα ΕΕΘ σε καμπίνες μικρών αεροσκαφών και σκαφών αναψυχής, που έχουν γίνει αντικείμενο πιο περιορισμένης έρευνας σε σχέση με τις καμπίνες των επιβατηγών αυτοκινήτων [18], [19]. Έτσι, διερευνάται η αποτελεσματικότητα των ΕΕΘ στην ακύρωση χαμηλόσυχνων αρμονικών και χαοτικών ακουστικών διαταραχών, που οφείλονται στους κινητήρες και τους έλικες των αεροσκαφών καθώς και στις μηχανές και τις γεννήτριες των σκαφών αναψυχής. Η παρούσα μελέτη προτείνει ακόμα καινοτόμες μεθόδους για τη μετακίνηση και την επέκταση των ζωνών ησυχίας μέσα στις καμπίνες, τη βελτίωση της απόδοσης των υπαρχόντων αλγορίθμων ελέγχου και επιπλέον εστιάζει στην πρακτική υλοποίηση των προτεινόμενων συστημάτων, εξετάζοντας ζητήματα όπως η υπολογιστική πολυπλοκότητα και η εγκατάσταση σε μικρούς χώρους.

2. Καινοτομία

Στα πλαίσια της παρούσας διδακτορικής διατριβής αναπτύχθηκαν δυο νέοι αλγόριθμοι ελέγχου για συστήματα ΕΕΘ, οι οποίοι εστιάζουν στην ακύρωση χαμηλόσυχνων ακουστικών διαταραχών γύρω από το προσκέφαλο των θέσεων αεροσκαφών και πλοίων. Η μία μέθοδος εστιάζει στη μεγέθυνση και τη μετακίνηση της ζώνης όπου έχουμε μεγάλη μείωση του επιπέδου θορύβου (ζώνη ησυχίας), κοντά στα αυτιά του επιβάτη, ενώ η άλλη χρησιμοποιεί

ένα μη γραμμικό φίλτρο που βασίζεται σε ένα νευρωνικό δίκτυο FLNN για να βελτιώσει την απόδοση ενός συστήματος ΕΕΘ. Και οι δύο προτεινόμενες μέθοδοι εστιάζουν στην υλοποίηση σε πραγματικές εφαρμογές και ως εκ τούτου ιδιαίτερη έμφαση δίνεται στη μείωση της υπολογιστικής πολυπλοκότητας, ώστε να είναι δυνατή η υλοποίηση σε έναν επεξεργαστή ψηφιακού σήματος. Εκτός από τις δυο καινοτόμες μεθόδους, παρουσιάζεται μια συστηματική μελέτη του ακουστικού πεδίου που διαμορφώνεται μέσα σε έναν κλειστό χώρο μικρής επιφάνειας, όταν λειτουργούν ταυτόχρονα πολλά αυτόνομα συστήματα. Τέλος, για πρώτη φορά επιχειρείται ο συνολικός έλεγχος του ακουστικού πεδίου που σχηματίζεται σε έναν κλειστό χώρο που προσομοιώνει καμπίνα αεροσκάφους, μέσω ενεργών απορροφητών ήχου. Οι απορροφητές αυτοί είναι ένας συνδυασμός ηχείων και μικροφώνων που βασίζουν τη λειτουργία τους στον διαχωρισμό ενός ακουστικού κύματος σε προσπίπτον και ανακλώμενο μέρος και τον συνακόλουθο μηδενισμό του ανακλώμενου.

3. Ο αλγόριθμος FxLMS μικτού σφάλματος

Ο πιο συνηθισμένος αλγόριθμος ελέγχου που χρησιμοποιείται σε συστήματα ΕΕΘ πολλών εισόδων πολλών εξόδων είναι ο συμβατικός πολυκαναλικός FxLMS [26]. Ο αλγόριθμος αυτός αποτελεί μια προσαρμογή του γραμμικού αλγορίθμου LMS στο πρόβλημα την ενεργής ακύρωσης θορύβου, συμπεριλαμβάνοντας στην ανάλυση το δευτερογενές ηλεκτρο-ακουστικό μονοπάτι. Έτσι ο αλγόριθμος ελέγχου γίνεται ευσταθής μιας και εξουδετερώνονται οι πόλοι που εισάγει το εν λόγω σύστημα. Από εκεί και έπειτα, η λειτουργά του αλγορίθμου αυτού βασίζεται στην ελαχιστοποίηση του αθροίσματος των τετραγώνων των στιγμιαίων σημάτων σφάλματος που συλλέγονται από M μικρόφωνα. Έτσι για ένα πολυκαναλικό σύστημα με ένα σήμα αναφοράς και K ηχεία, οι συντελεστές του γραμμικού προσαρμοστικού φίλτρου που προκύπτει από τον συμβατικό FxLMS δίνονται από την ακόλουθη εξίσωση:

$$\mathbf{w}_k(n+1) = \mathbf{w}_k(n) - \mu \sum_{m=1}^{M} \mathbf{x}'_{km}(n) e_m(n), \quad k = 1, 2, ..., K. \tag{1}$$

όπου μ είναι η παράμετρος που επηρεάζει την ταχύτητα σύγκλισης και x'_{km} είναι το σήμα αναφοράς φιλτραρισμένο από ένα μοντέλο το δευτερογενούς μονοπατιού από το k ηχείο στο m μικρόφωνο σφάλματος. Το μοντέλο αυτό υπολογίζεται σε μια φάση μοντελοποίησης, που προηγείται της λειτουργίας του ΕΕΘ. Κατά τη φάση αυτή, το κάθε ηχείο αναπαράγει λευκό θόρυβο που χρησιμοποιείται σαν σήμα αναφοράς, και το αντίστοιχο μικρόφωνο σφάλματος καταγράφει το σήμα που πέρασε μέσα από το δευτερογενές μονοπάτι. Έπειτα, ο αλγόριθμος LMS χρησιμοποιείται για τη μοντελοποίησή του μονοπατιού.

Συνεπώς, για τον υπολογισμό των συντελεστών της εξίσωσης 1, χρειάζεται ο υπολογισμός της συνέλιξης ανάμεσα στο σήμα αναφοράς και το μοντέλο του αντίστοιχου δευτερογενούς μονοπατιού. Αυτή η πράξη είναι ιδιαιτέρως κοστοβόρα από υπολογιστικής σκοπιάς. Επιπλέον, το υπολογιστικό κόστος αυξάνεται πολύ, όταν στο σύστημα ΕΕΘ περιλαμβάνονται

πολλά ηχεία και μικρόφωνα σφάλματος.

Από την άλλη, η προσέγγιση μικτού σφάλματος περιορίζει τις συνελίξεις σε μια για καθένα από τα ηχεία που χρησιμοποιούνται. Έτσι η εξίσωση υπολογισμού των συντελεστών του προσαρμοστικού φίλτρου που προκύπτει από τον FxLMS μικτού σφάλματος δίνεται από την εξίσωση 2:

$$\mathbf{w}_k(n+1) = \mathbf{w}_k(n) - \mu \mathbf{x'}_{k,mix}(n) e_{mix}(n), \quad k = 1, 2, ..., K. \tag{2}$$

όπου μ είναι και πάλι η παράμετρος που επηρεάζει την ταχύτητα σύγκλισης, $x'_{k,mix}$ είναι το σήμα αναφοράς φιλτραρισμένο από το μικτό δευτερογενές μονοπάτι και e_{mix} είναι το άθροισμα των στιγμιαίων σημάτων σφάλματος. Επίσης, το μοντέλο του μικτού δευτερογενούς μονοπατιού υπολογίζεται όπως και στη συμβατική εκδοχή του FxLMS, με τη διαφορά ότι σαν σήμα σφάλματος λαμβάνεται ξανά το άθροισμα των σημάτων των M μικροφώνων.

3.1 Προσομοιώσεις

Για την αξιολόγηση του αλγορίθμου FxLMS μικτού σφάλματος σε εφαρμογές τοπικών συστημάτων ΕΕΘ διενεργήθηκαν τρισδιάστατες προσομοιώσεις χρησιμοποιώντας τη μέθοδο πεπερασμένων στοιχείων. Για ένα σύστημα δύο εισόδων δύο εξόδων, ο εν λόγω αλγόριθμος δημιουργεί παρόμοιες ζώνες ησυχίας με τον συμβατικό FxLMS, τόσο ως προς τη μείωση των επιπέδων θορύβου, όσο και ως προς το σχήμα, στην περίπτωση που τα μικρόφωνα σφάλματος μετρούν σχεδόν ίδιες ακουστικές πιέσεις, όπως απεικονίζεται στο Σχήμα 1α΄. Σε αντίθετη περίπτωση, όταν οι ακουστικές πιέσεις διαφέρουν, η μέγιστη μείωση της ακουστικής πίεσης παρατηρείται στο μέσο ανάμεσα στα δυο μικρόφωνα σφάλματος. Οι παραπάνω διαπιστώσεις προϋποθέτουν την παραδοχή ότι το μήκος κύματος των ακουστικών διαταραχών είναι σημαντικά μεγαλύτερο σε σχέση με την απόσταση ανάμεσα στα μικρόφωνα σφάλματος.

Επιπλέον, εξετάστηκε ένα σύστημα 3 εισόδων-2 εξόδων, που σκοπός του ήταν η μείωση των επιπέδων θορύβου μπροστά από τα προσκέφαλα δυο διπλανών θέσεων καμπίνας αεροσκάφους. Στην περίπτωση αυτή παρατηρήθηκε ότι με τη χρήση του FxLMS μικτού σφάλματος μπορεί να επιτευχθεί μια μείωση των επιπέδων θορύβου από 18 έως 20 dB μπροστά από κάθε θέση, με μια ζώνη ησυχίας αρκετά μεγάλη ώστε να καλύψει ελαφρές κινήσεις του κεφαλιού του επιβάτη, όπως απεικονίζεται στο Σχήμα 1β΄. Τέλος, πρέπει να σημειώσουμε ότι η ακουστική διαταραχή που χρησιμοποιήθηκε στις προσομοιώσεις και των δυο συστημάτων αποτελούνταν από τρεις αρμονικές συνιστώσες της συχνότητας BPF ενός μικρού αεροσκάφους που μελετήθηκε στα πλαίσια της παρούσα διατριβής. Η συχνότητα αυτή παρουσιάζονταν στα 24 Hz και κατά συνέπεια οι αρμονικές συνιστώσες βρίσκονταν στα 72, 96 και 120 Hz.

Τέλος, όσο αφορά στο υπολογιστικό κόστος, αυτό είναι σημαντικά μειωμένο αφού και για τα δυο συστήματα παραμένει στις 1501 πράξεις πολλαπλασιασμού και πρόσθεσης για τον FxLMS μικτού σφάλματος. Αντίθετα, ο συμβατικός FxLMS απαιτεί 2502 και 3503

πράξεις για τα συστήματα 2 εισόδων-2 εξόδων και 3 εισόδων-2 εξόδων αντίστοιχα, για κάθε επανάληψη. Στους παραπάνω υπολογισμούς υποτέθηκε ότι ο αριθμός των συντελεστών των προσαρμοστικών φίλτρων είναι 250.

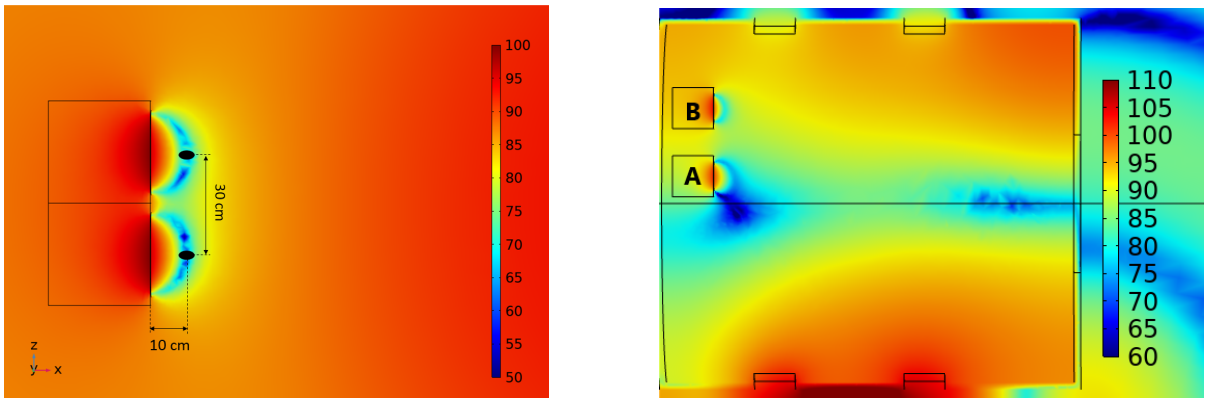

(α′) (β′)

Σχήμα 1: α′) Ζώνη ησυχίας μπροστά από τα δυο ηχεία ενός συστήματος ΕΕΘ 2 εισόδων-2 εξόδων που χρησιμοποιεί τον αλγόριθμο FxLMS μικτού σφάλματος, όταν οι ακουστικές πιέσει στα μικρόφωνα σφάλματος είναι σχεδόν ίδιες. β′) Οι ζώνες ησυχίας μπροστά από τις θέσεις A και B του αεροσκάφους, όταν χρησιμοποιείται το σύστημα 3 εισόδων-2 εξόδων.

3.2 Πειραματική αξιολόγηση

Η πειραματική αξιολόγηση του συστήματος 3 εισόδων-2 εξόδων διενεργήθηκε στο ομοίωμα καμπίνας αεροσκάφους που είναι εγκατεστημένο στο Εργαστήριο Δυναμική και Ακουστικής (Σχήμα 2α′) για δυο διπλανές θέσεις (Σχήμα 2β′). Η συνθετική ακουστική διαταραχή δημιουργήθηκε μέσω του συνδυασμού τριών ημιτονοειδών συνιστωσών στα 72, 96 και 120 Hz, καθώς και λευκού θορύβου χαμηλού πλάτους. Η πηγή θορύβου τοποθετήθηκε σε κοντινή απόσταση από το ομοίωμα της καμπίνας και ένα μικρόφωνο που ήταν τοποθετημένο σε απόσταση $5cm$ από την πηγή κατέγραφε το σήμα αναφοράς. Για τη μέτρηση της ακουστικής πίεσης μπροστά από τα δύο καθίσματα, χρησιμοποιήθηκαν συνολικά 16 μικρόφωνα, τοποθετημένα σε ένα πλέγμα που κάλυπτε μια περιοχή εμβαδού $30cm$ επί $25cm$. Χρησιμοποιήθηκε επιπλέον, η γραμμική παρεμβολή για την εκτίμηση των επιπέδων ακουστικής πίεσης σε σημεία μεταξύ των θέσεων μέτρησης. Και για τα δύο καθίσματα, η μέγιστη εξασθένιση του επιπέδου θορύβου επιτεύχθηκε $10cm$ μακριά από τα μικρόφωνα σφάλματος, γεγονός που συμπίπτει με τα αποτελέσματα της προσομοίωσης. Πιο συγκεκριμένα η μείωση της SPL έφτασε τα 15,5 dB μπροστά από το κάθισμα A και τα 13 dB μπροστά από το κάθισμα B. Επιπλέον, η μείωση των πλατών των επιμέρους αρμονικών κυμάνθηκε από 10 έως 22 dB μπροστά από τη θέση A και από 4 έως 20 dB μπροστά από τη θέση B.

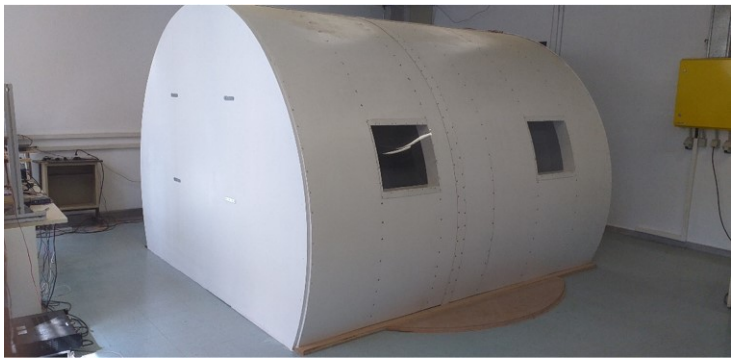

(α′)

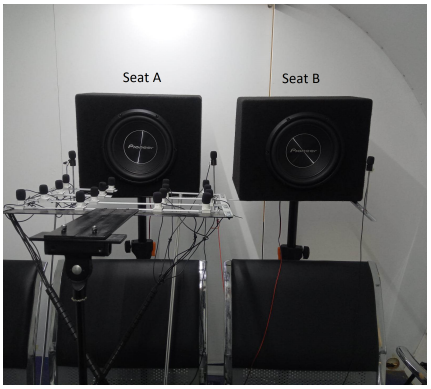

(β′)

Σχήμα 2: α′) Το ομοίωμα καμπίνας αεροσκάφους, εγκατεστημένο στο εργαστήριο Δυναμικής και Ακουστικής. β′) Δύο διπλανές θέσεις στο ομοίωμα καμπίνας αεροσκάφους, όπου εφαρμόστηκε το σύστημα 3 εισόδων-2 εξόδων.

4. Ο αλγόριθμος VEM-FxLMS

Τα συστήματα ΕΕΘ της προηγούμενης ενότητας πετυχαίνουν τη μεγαλύτερη μείωση της ακουστικής πίεσης, είτε γύρω από τα μικρόφωνα σφάλματος, είτε στην περιοχή ανάμεσά τους. Το γεγονός αυτό μπορεί να αποτελέσει πρόβλημα σε περιπτώσεις που τα μικρόφωνα δεν μπορούν να τοποθετηθούν κοντά στα αυτιά του επιβάτη, λόγω χωροταξικών περιορισμών. Τότε χρειάζεται μια μέθοδος που να μετακινεί τη ζώνη ησυχίας μακρυά από τα μικρόφωνα, ώστε η μέγιστη μείωση των επιπέδων θορύβου να επιτυγχάνεται στην περιοχή ενδιαφέροντος. Στην κατεύθυνση αυτή, η παρούσα ενότητα παρουσιάζει μια νέα μέθοδο που συνδυάζει τον αλγόριθμο FxLMS μικτού σφάλματος με μια μέθοδο πρόβλεψης της ακουστικής πίεσης σε κοντινή απόσταση από τα μικρόφωνα σφάλματος, που βασίζεται στη μέθοδο της γραμμικής παρέκτασης. Σύμφωνα με τη μέθοδο αυτή, η ακουστική πίεση στα αυτιά του επιβάτη για χαμηλόσυχνες ακουστικές διαταραχές υπολογίζεται από την εξίσωση 3 :

$$e_{vk}(n) = \frac{e_{pk2}(n) - e_{pk1}(n)}{a} x + e_{pk2}(n), \quad \text{for } \kappa{=}1{,}2 \tag{3}$$

όπου e_{pk1}, e_{pk2} είναι τα σήματα σφάλματος από τα ζεύγη μικροφώνων που χρησιμοποιούνται για τη γραμμική παρέκταση, όπως απεικονίζονται στο Σχήμα 3, a είναι η απόσταση των μικροφώνων κάθε ζεύγους και x είναι η απόσταση από το μακρινό μικρόφωνο κάθε ζεύγους μέχρι τη θέση που επιδιώκουμε την μετακίνηση της ζώνης ησυχίας.

Για τον σχηματισμό της εξίσωσης υπολογισμού των συντελεστών του προσαρμοστικού φίλτρου του VEM-FxLMS, υπολογίζουμε το εικονικό μικτό σφάλμα από την εξίσωση 4:

$$e_{v,mix}(n) = \sum_{k=1}^{2} e_{vk}(n) =$$
$$\frac{e_{p12}(n) + e_{p22}(n) - e_{p11}(n) - e_{p21}(n)}{a} x + e_{p12}(n) + e_{p22}(n) = \tag{4}$$
$$\frac{e_{p2,mix}(n) - e_{p1,mix}(n)}{a} x + e_{p2,mix}(n)$$

Έπειτα οι συντελεστές υπολογίζονται από την εξίσωση 5. Επιπλέον, το μοντέλο του δευτερογενούς μονοπατιού υπολογίζεται όπως και στον αλγόριθμο FxLMS μικτού σφάλματος λαμβάνοντας όμως υπόψη τα σήματα e_{p12}, e_{p22}.

$$\mathbf{w}_k(n+1) = \mathbf{w}_k(n) - \mu \mathbf{x'}_{k,mix}(n) e_{v,mix}(n), \quad k = 1, 2, ..., K. \tag{5}$$

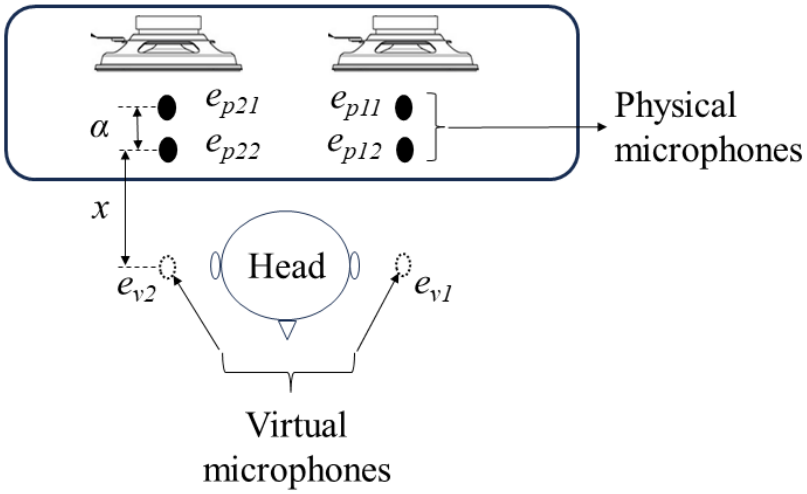

Σχήμα 3: Κάτοψη του ενεργού προσκέφαλου που αποτελείται από 2 ηχεία και 4 φυσικά μικρόφωνα, τα οποία χρησιμοποιούνται για την εκτίμηση της ακουστικής πίεσης σε δύο εικονικές θέσεις.

4.1 Προσομοιώσεις

Κατά τη διάρκεια της προσομοίωσης του VEM-FxLMS στον υπολογιστή, χρησιμοποιήθηκαν δύο αρχιτεκτονικές ΕΕΘ. Η πρώτη χρησιμοποίησε ένα μεγάφωνο και τέσσερα φυσικά μικρόφωνα (4 είσοδοι-1 έξοδος), ενώ η δεύτερη χρησιμοποίησε δύο μεγάφωνα και τέσσερα φυσικά μικρόφωνα (4 είσοδοι-2 έξοδοι), όπως απεικονίζεται στα Σχήματα 4α′ και 4β′. Επιπλέον, χρησιμοποιήθηκε η βιβλιοθήκη συναρτήσεων k-Wave του MATLAB για την προσομοίωση της διάδοσης του ακουστικού κύματος σε ελεύθερο πεδίο. Τα αποτελέσματα της προσομοίωσης έδειξαν ότι επιτυγχάνεται σημαντική μείωση του θορύβου έως και 30 dB σε μια περιοχή μακριά από τη φυσική θέση του μικροφώνου σφάλματος, η οποία εξαρτάται από την παράμετρο x που είναι η απόσταση της εικονικής θέσης από το πιο απομακρυσμένο

φυσικό μικρόφωνο. Σε αυτό το σημείο πρέπει να σημειώσουμε ότι στον συμβατικό FxLMS επιτυγχάνεται παρόμοια μείωση θορύβου σε μια περιοχή κοντά στη φυσική θέση του μικροφώνου σφάλματος όταν χρησιμοποιείται τόσο ένα σύστημα 4 εισόδων-1 εξόδου όσο και ένα σύστημα 4 εισόδων-2 εξόδων. Ωστόσο, η εξασθένιση του θορύβου δε φτάνει στα αυτιά των επιβατών και, επομένως, η παραγόμενη ζώνη ησυχίας δε βρίσκεται στο επιθυμητό σημείο.

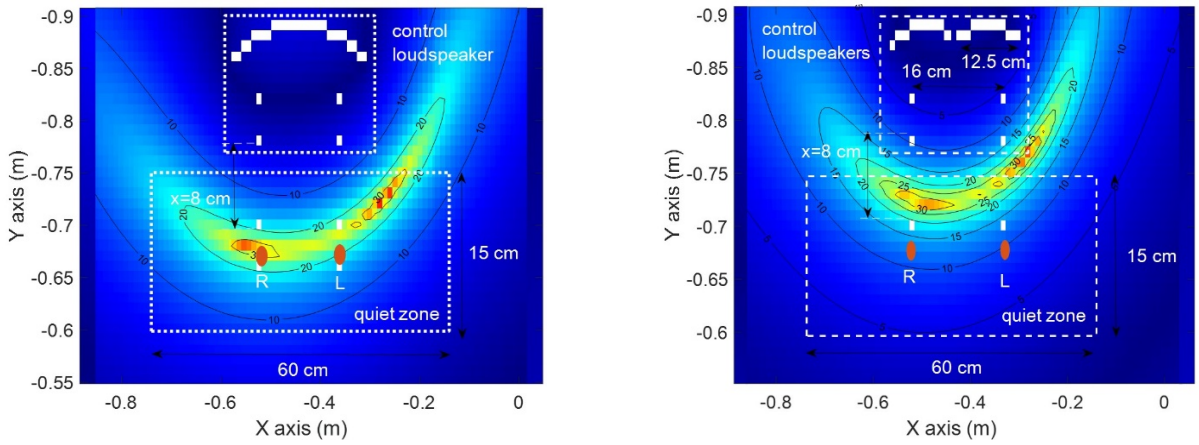

(α′) (β′)

Σχήμα 4: Μετακίνηση της ζώνης ησυχίας κατά $8cm$ όταν έχουμε σύστημα: α′) 4 εισόδων-1 εξόδου και β′) 4 εισόδων-2 εξόδων.

4.2 Πειραματική αξιολόγηση

Τα εν λόγω συστήματα αξιολογήθηκαν στο ομοίωμα καμπίνας του εργαστηρίου και έπειτα το σύστημα ΕΕΘ 4 εισόδων-1 εξόδου τοποθετήθηκε στο κατάστρωμα ενός σκάφους αναψυχής προκειμένου να διαπιστωθεί αν μπορεί να εξουδετερώσει το θόρυβο που παράγεται από τις ηλεκτρογεννήτριες. Συνεπώς, η μέθοδος VEM-FxLMS αξιολογήθηκε και σε πραγματικές συνθήκες. Στην περίπτωση των εργαστηριακών δοκιμών, η ακουστική διαταραχή ήταν ένα πολυτονικό συνθετικό σήμα μαζί με λευκό θόρυβο πλάτους 30 dB. Όταν το ΕΕΘ ήταν απενεργοποιημένο, το επίπεδο θορύβου κυμαινόταν από 80 έως 85 dB σε κάθε ένα από πέντε επίπεδα μέτρησης. Όταν το σύστημα ενεργοποιήθηκε παρατηρήθηκε μείωση του επιπέδου θορύβου που κυμαίνεται από 17 έως 24 dB απευθείας στα αυτιά του επιβάτη. Αυτό το αποτέλεσμα προήλθε με τον καθορισμό της παραμέτρου x στα $32cm$.

Στην περίπτωση της λειτουργίας στο κατάστρωμα του σκάφους αναψυχής, παρατηρήθηκε πτώση του πλάτους της αρμονικής στα 52 Hz της τάξης των 25 dB (βλ. Σχήμα 5), όταν η παράμετρος x ήταν $15cm$. Επιπλέον, ο όγκος της ζώνης ησυχίας όπου τα επίπεδα θορύβου παρουσίασαν πτώση άνω των 10 dB είχε διαστάσεις $60cm \times 45cm \times 40cm$. Ως αποτέλεσμα, η ζώνη ησυχίας των 10 dB, κατά τη χρήση του αλγορίθμου VEM-FxLMS, επεκτάθηκε από τις θέσεις των μικροφώνων σφάλματος έως και $45cm$ μακριά από αυτά. Επιπλέον, καταγράφηκαν παρόμοιες μετρήσεις για τα επίπεδα μέτρησης πάνω και κάτω από το μεσαίο επίπεδο, με

αποτέλεσμα μιας περιοχής με μείωση του επιπέδου θορύβου κατά 10 dB με ύψος $40cm$ κατά μήκος του άξονα z.

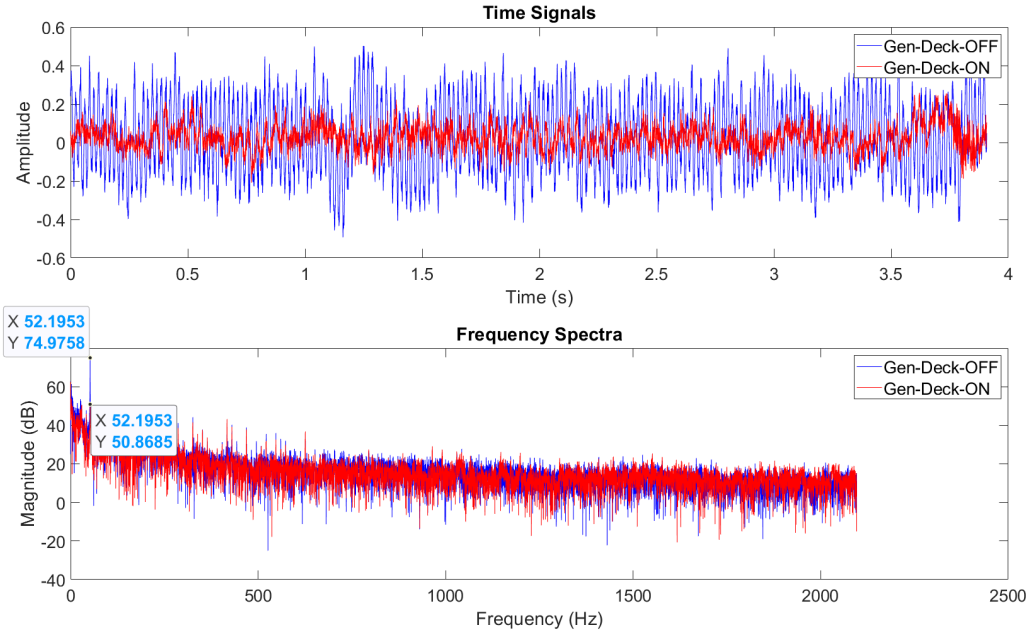

Σχήμα 5: Σήματα στο πεδίο του χρόνου και φάσματα συχνοτήτων όταν το σύστημα ΕΕΘ με βάση τον VEM-FxLMS λειτούργησε στο κατάστρωμα ενός σκάφους αναψυχής σε πραγματικές συνθήκες. Η απόσταση μεταξύ του μικροφώνου σφάλματος και του μικροφώνου μέτρησης ήταν $15cm$.

5. Μη γραμμικός ΕΕΘ βασισμένος σε ένα FLNN

Στις προηγούμενες ενότητες συζητήθηκαν γραμμικοί αλγόριθμοι για συστήματα ΕΕΘ και δόθηκε ιδιαίτερη προσοχή στη μείωση της υπολογιστικής πολυπλοκότητας και στη δημιουργία και τη μετατόπιση των περιοχών, όπου επιτυγχάνεται μείωση της ακουστικής πίεσης σε ικανοποιητικό βαθμό. Ωστόσο, οι αλγόριθμοι που βασίζονται στον FxLMS είναι εγγενώς γραμμικοί και συνήθως έχουν μειωμένη απόδοση όταν χρησιμοποιούνται για τη μοντελοποίηση ηλεκτροακουστικών συστημάτων όπου υπάρχουν ισχυρές μη γραμμικότητες [95] ή όταν χρησιμοποιούνται για την πρόβλεψη χρονοσειρών που αποτελούν μείγμα αρμονικών και χαοτικών στοιχείων.

Οι μη γραμμικότητες στα συστήματα ΕΕΘ μπορούν να προκύψουν από τα μικρόφωνα, τα ηχεία ή τους ενισχυτές, που εμπλέκονται κυρίως στο δευτερογενές μονοπάτι. Η παρουσία συχνοτήτων με μεγάλα πλάτη στον πρωτογενή θόρυβο μπορεί ακόμα να προκαλέσει κορεσμό σε συσκευές χαμηλής ισχύος, όπως τα μικρόφωνα αναφοράς και σφάλματος. Η επίδραση των μη γραμμικοτήτων που οφείλονται σε αυτά τα στοιχεία έχει μελετηθεί σε βάθος στην εργασία των Costa et al.[96], η οποία δείχνει ότι η παρουσία ακόμη και μιας μικρής μη γραμμικότητας μπορεί να επηρεάσει την ικανότητα μετριασμού του θορύβου.

Λύση σε αυτό το ζήτημα προσπαθούν να δώσουν τα μη γραμμικά προσαρμοστικά φίλτρα, τα οποία είναι πιο αποτελεσματικά στην απόσβεση των ευρυζωνικών ακουστικών διαταραχών που χαρακτηρίζονται από τον συνδυασμό αρμονικών και χαοτικών συνιστωσών, οι οποίες διαδίδονται μέσω μη γραμμικών ηλεκτροακουστικών διαδρομών. Σε αυτή την ενότητα παρουσιάζεται ένας μη γραμμικός αλγόριθμος βασισμένος σε ένα FLNN με ημιτονοειδή επέκταση (βλ. Σχήμα 6), που ενσωματώνει ακόμα τις τεχνικές των προηγούμενων ενοτήτων, όσο αφορά στη χρήση του μικτού σφάλματος και της γραμμικής παρέκτασης.

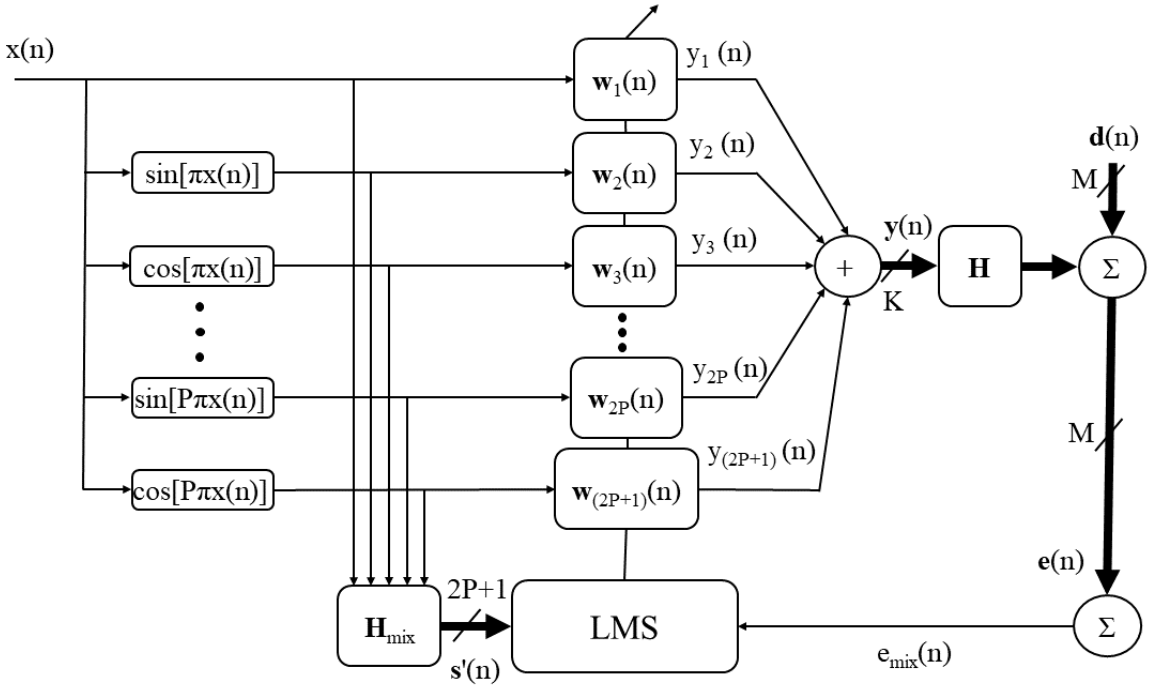

Σχήμα 6: Μπλοκ διάγραμμα του αλγορίθμου FLNN που εκνωματώνει την τεχνική του μικτού σήματος σφάλματος για ένα πολυκαναλικό ΕΕΘ με K μεγάφωνα και M μικρόφωνα. Το διευρυμένο σήμα αναφοράς που φιλτράρεται από το δευτερεύον μονοπάτι μικτού σφάλματος H_{mix} συμβολίζεται με $s'(n)$.

5.1 Προσομοιώσεις

Για την αξιολόγηση της προτεινόμενης μεθόδου, έλαβαν χώρα τόσο προσομοιώσεις σύγκλισης του αλγορίθμου, όσο και ακουστικές προσομοιώσεις χρησιμοποιώντας τη μέθοδο πεπερασμένων στοιχείων. Καταρχήν, στις προσομοιώσεις σύγκλισης, η απόδοση του FLNN δεύτερης τάξης ξεπερνά αυτή των άλλων αλγορίθμων και για τα τέσσερα σήματα που χρησιμοποιήθηκαν. Τα σήματα αυτά ήταν δύο καταγραφές της ακουστικής διαταραχής στην καμπίνα ενός μικρού αεροσκάφους κλίνοντος στροφείου, ένα χαοτικό σήμα λογιστικού τύπου και ένα μείγμα τονικών στοιχείων και λευκού θορύβου. Για το χαοτικό σήμα λογιστικού τύπου, η διαφορά μεταξύ γραμμικών και μη γραμμικών συστημάτων είναι πιο έντονη, υποδεικνύοντας ότι η μέθοδος που βασίζεται στο FLNN μπορεί να προβλέπει καλύτερα χρονοσειρές, όπου

υπάρχουν χαοτικά στοιχεία (βλ. Σχήμα 7α′). Επιπλέον, η ακουστική προσομοίωση έδειξε ότι η μέθοδος της γραμμικής παρέκτασης για τη μετακίνηση της ζώνης ησυχίας, λειτουργεί αποτελεσματικά, όχι μόνο μετακινώντας αλλά και μεγεθύνοντας την περιοχή με ικανοποιητική πτώση των επιπέδων θορύβου, όπως καταδεικνύεται και στο Σχήμα 7β′. Έτσι, για μια συνθετική ακουστική διαταραχή που αποτελείται από τρεις αρμονικές της συχνότητας διέλευσης της έλικας (BPF) στα 48, 72 και 96 Hz, η μέγιστη εξασθένιση του επιπέδου θορύβου φτάνει τα 25 dB (από περίπου 93 σε 68 dB).

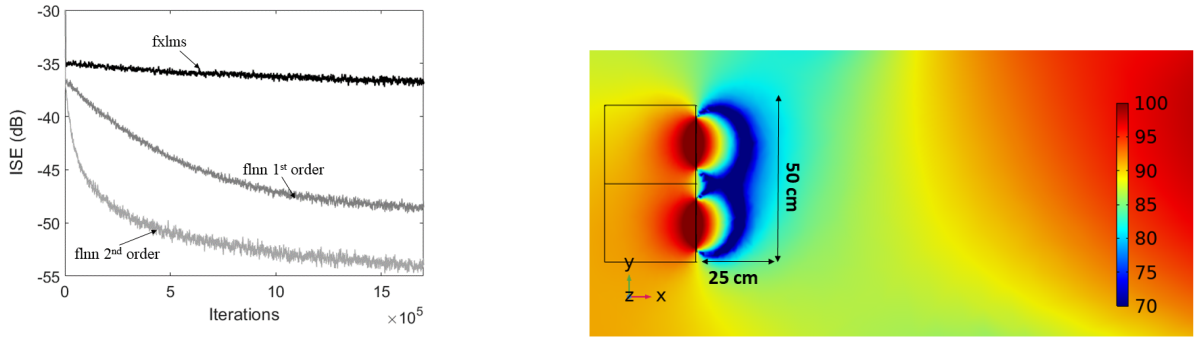

(α′) (β′)

Σχήμα 7: α′) Στιγμιαίο τετραγωνικό σφάλμα του FxLMS και του FLNN πρώτης και δεύτερης τάξης, όταν το σήμα αναφοράς είναι χαοτικό, λογιστικού τύπου. β′) Ζώνη ησυχίας που σχηματίζεται με τον συνδυασμό του FLNN και την γραμμική παρέκταση.

5.2 Πειραματική αξιολόγηση

Η πειραματική αξιολόγηση της προτεινόμενης μη γραμμικής μεθόδου περιελάμβανε τη δοκιμή της για πραγματικά σήματα που καταγράφηκαν σε καμπίνες μικρών ελικοφόρων αεροσκαφών και αεροσκαφών κλίνοντος στροφείου καθώς και σε καμπίνα ελικοπτέρου και σκάφους αναψυχής. Όλα τα πειραματικά τεστ έγιναν στο ομοίωμα καμπίνας αεροσκάφους που είναι εγκατεστημένο στο εργαστήριο. Στην περίπτωση της καταγραφής από το αεροσκάφος κλίνοντος στροφείου, η μέθοδος που βασίζεται στο FLNN δεύτερης τάξης έδειξε καλύτερη απόδοση από τον FxLMS στις 1/3 οκτάβες με κεντρικές συχνότητες 53 και 60 Hz, όπου επιτυγχάνει 3-4 dB μεγαλύτερη μείωση της ηχοστάθμης (βλ. Σχήμα 8α′). Η διαφορά αυτή προκύπτει από τη μεγαλύτερη μείωση ορισμένων αρμονικών και τον μετριασμό των χαοτικών συνιστωσών. Το πλάτος της αρμονικής των 48 Hz μειώθηκε κατά 12 dB και 17 dB στο δεξί και το αριστερό αυτί αντίστοιχα όταν χρησιμοποιήθηκε ως αλγόριθμος ελέγχου ο FLNN δεύτερης τάξης αντί για 1 dB όταν εφαρμόστηκε ο FxLMS. Επιπλέον, η απόδοση του FLNN είναι ανώτερη στην περίπτωση των συχνοτήτων στα 163 και 280 Hz. Η ανώτερη απόδοση του FLNN οφείλεται στην ικανότητά του να προβλέπει χαοτικές διαταραχές και να μοντελοποιεί καλύτερα φυσικά συστήματα με μη γραμμικότητες.

Επιπλέον, στην περίπτωση του μικρού ελικοφόρου αεροσκάφους παρατηρήθηκε σημαντική μείωση της ακουστικής πίεσης στο φάσμα συχνοτήτων από τα 60 έως τα 140 Hz, και για

τα δύο σημεία μέτρησης που αντιστοιχούν στα δύο αυτιά των επιβατών. Οι μεγαλύτερες μειώσεις παρατηρήθηκαν στις συνιστώσες των 62 και 124 Hz, οι οποίες ήταν 14 και 17 dB αντίστοιχα για το δεξί αυτί και 14 και 15 dB για το αριστερό αυτί. Τα παραπάνω συμπεράσματα απεικονίζονται στο Σχήμα 8β΄. Στην περίπτωση του ελικοπτέρου, η μείωση της ηχοστάθμης ήταν μεγαλύτερη για τις υψηλότερες αρμονικές συνιστώσες, όπως η αρμονική στα 52 Hz, η οποία παρουσίασε εξασθένιση 11 dB. Επιπλέον, η μείωση του πλάτους ήταν 14 dB στο αριστερό αυτί και 15 dB στο δεξί αυτί του επιβάτη στα 78 Hz. Επιπλέον, οι αρμονικές στα 92 και 115 Hz παρουσίασαν μείωση πλάτους κατά 19 και 18 dB στο αριστερό αυτί και 16 και 22 dB στο δεξί αυτί, αντίστοιχα. Τέλος, για τον θόρυβο του σκάφους αναψυχής παρατηρήθηκε μείωση της ηχοστάθμης που κυμάνθηκε από 14 έως 16 dB.

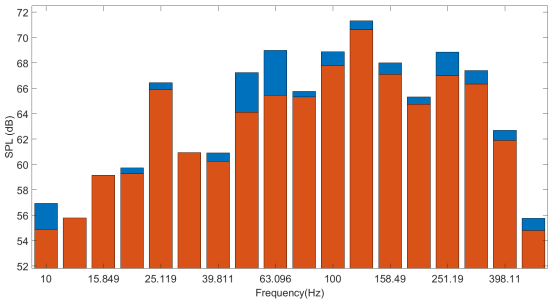

(α΄)

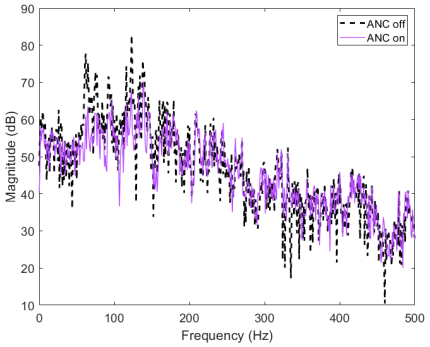

(β΄)

Σχήμα 8: α΄) Διαφορά της ηχοστάθμης για τις διάφορες 1/3 οκτάβες όταν το ΕΕΘ χρησιμοποιεί τον FxLMS (μπλέ) ή τον FLNN δεύτερης τάξης (πορτοκαλί). β΄) Φάσμα συχνοτήτων πριν και μετά την ενεργοποίηση του FLNN για το σήμα της καμπίνας του μικρού ελικοφόρου αεροσκάφους.

6. Αλληλεπίδραση τοπικών συστημάτων ΕΕΘ σε μικρούς χώρους

Οι προηγούμενες ενότητες επικεντρώθηκαν σε αρχιτεκτονικές και αλγορίθμους συστημάτων ΕΕΘ που είναι κατάλληλοι για ένα ενεργό σύστημα προσκέφαλου σε οχήματα, όπως μικρά αεροσκάφη και σκάφη αναψυχής, για τον μετριασμό των ακουστικών διαταραχών γύρω από το κεφάλι του επιβάτη. Η προσέγγιση αυτή βασίζεται στην τοπική επίδραση ξεχωριστών συστημάτων, καθώς η εξασθένιση της ακουστικής πίεσης λαμβάνει χώρα εντός μιας συγκεκριμένης ζώνης ησυχίας. Κατά συνέπεια, η προσέγγιση αυτή αναφέρεται ως τοπικός ΕΕΘ. Ωστόσο, η τυχαία τοποθέτηση πολλών τοπικών συστημάτων σε έναν μικρό χώρο, όπως μια καμπίνα σκάφους αναψυχής ή αεροσκάφους, δεν εγγυάται το τρόπο που θα επηρεαστεί το ηχητικό πεδίο σε άλλες θέσεις εντός του χώρου, οι οποίες βρίσκονται μακριά από τις ζώνες ησυχίας. Σε αυτή την ενότητα, χρησιμοποιούμε προσομοιώσεις που βασίζονται στη μέθοδο πεπερασμένων στοιχείων, καθώς και πειράματα για να διερευνήσουμε την αλληλεπίδραση

μεταξύ τοπικών συστημάτων ΕΕΘ. Συγκεκριμένα, αξιολογούμε δύο αρχιτεκτονικές: στην πρώτη, κάθε θέση διαθέτει ένα αποκλειστικό σύστημα ΕΕΘ, ενώ στη δεύτερη γειτονικές θέσεις μοιράζονται ένα πολυκαναλικό σύστημα, όπως περιγράφηκε στην Ενότητα 3.

6.1 Προσομοιώσεις

Τόσο δισδιάστατες, όσο και τρισδιάστατες προσομοιώσεις έλαβαν χώρα για την αξιολόγηση της απόδοσης των τοπικών συστημάτων ΕΕΘ, όταν λειτουργούν ταυτόχρονα σε ένα χώρο που προσομοιώνει την καμπίνα ενός αεροσκάφους κλίνοντος στροφείο με ανοιχτά τα άκρα στην εμπρός και πίσω πλευρά, ώστε να προσομοιωθεί το μεγάλο μήκος. Η ακουστική διαταραχή που δημιουργήθηκε στην πλατφόρμα Comsol περιλάμβανε τέσσερις αρμονικές στα 48, 72, 96 και 119 Hz, που μοιάζουν με την πραγματική διαταραχή στο εσωτερικό του αεροσκάφους και σαν αλγόριθμος ελέγχου επιλέχθηκε ο μη γραμμικός αλγόριθμος που βασίζεται στο FLNN δεύτερης τάξης. Στην περίπτωση των γειτονικών μεγαφώνων που ανήκουν στο ίδιο πολυκαναλικό σύστημα με 2 εισόδους και 2 εξόδους (βλ. Σχήμα 9α΄), η μείωση της ηχοστάθμης έφτασε στα τα 19 dB μπροστά από ορισμένα καθίσματα. Σε σύγκριση με την αρχιτεκτονική ΕΕΘ έξι αυτόνομων συστημάτων, οι ζώνες ησυχίας μπροστά από τα καθίσματα ήταν μεγαλύτερες και πιο ομοιόμορφες. Επιπλέον, η περιοχή όπου η πτώση της ηχοστάθμης ήταν μεγαλύτερη των 10 dB ήταν πιο εκτεταμένη και δεν υπήρχαν πλέον περιοχές όπου παρατηρήθηκε αύξηση της ακουστικής πίεσης. Τέλος, η ζώνη ησυχίας μπροστά από τα μεσαία καθίσματα επεκτάθηκε στην περιοχή μεταξύ των δύο προσκέφαλων, με αποτέλεσμα τη μείωση της ηχοστάθμης κατά 6 dB.

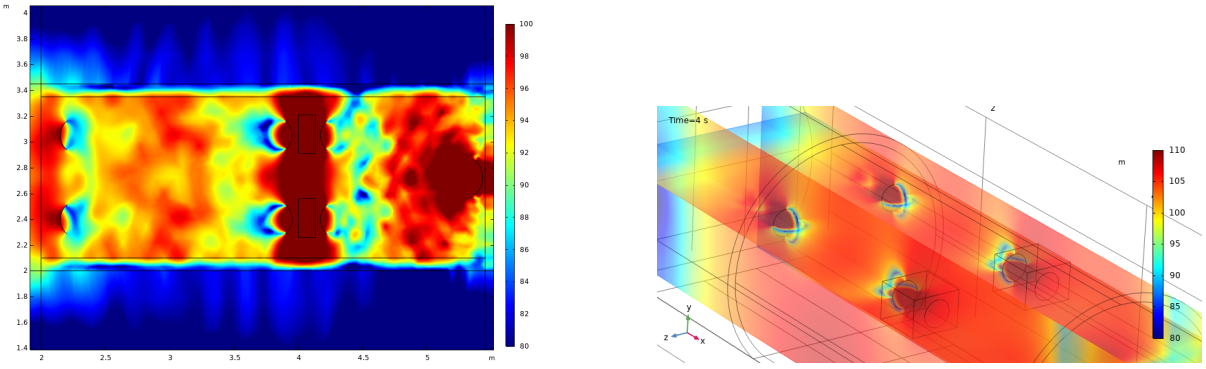

(α΄) (β΄)

Σχήμ 9: α΄) Κατανομή της ηχοστάθμης, όταν χρησιμοποιείται η αρχιτεκτονική 2 εισόδων-2 εξόδων, με συνεργαζόμενα γειτονικά συστήματα . β΄) Τρισδιάστατη απεικόνιση των ζωνών ησυχίας μπροστά από τα επιμέρους τοπικά συστήματα ΕΕΘ.

Δεδομένου ότι η λύση με τα γειτονικά ηχεία που συνεργάζονται μεταξύ τους έχει σημαντικά πλεονεκτήματα, πραγματοποιήθηκε μια πρόσθετη τρισδιάστατη προσομοίωση για αυτό το σύστημα. Η μείωση της ηχοστάθμης γύρω από τα προσκέφαλα παρουσιάζεται στο Σχήμα 9β΄. Όταν το ΕΕΘ δεν ήταν ενεργοποιημένο, η ηχοστάθμη έφτασε τα 105 dB σε αυτή την

προσομοίωση. Όταν ενεργοποιήθηκε, η εξασθένιση κυμάνθηκε από 8 έως 19dB σχηματίζοντας μια ζώνη ησυχίας διαστάσεων $20cm \times 38cm \times 25cm$. Επιπλέον, το σχήμα της ζώνης ησυχίας ήταν σφαιρικό και το μέγεθος της ήταν αρκετό, ώστε να επιτρέπει ήπιες κινήσεις του κεφαλιού του επιβάτη.

6.2 Πειραματική αξιολόγηση

Η πειραματική αξιολόγηση της αλληλεπίδρασης μεταξύ αυτόνομων τοπικών συστημάτων ΕΕΘ εγκατεστημένων στο ομοίωμα καμπίνας πραγματοποιήθηκε σε δύο φάσεις. Αρχικά, αξιολογήθηκε η αλληλεπίδραση των συστημάτων όταν αυτά ήταν τοποθετημένα το ένα απέναντι από το άλλο και εκτέθηκαν σε μια πραγματική ακουστική διαταραχή, η οποία καταγράφηκε εντός της καμπίνας του αεροσκάφους κλίνοντος στροφείου. Στη συνέχεια, διερευνήθηκε η επίδραση τεσσάρων τέτοιων συστημάτων στο συνολικό ηχητικό πεδίο της καμπίνας, όταν αυτό διεγείρεται από αρμονικές ακουστικές διαταραχές χαμηλής συχνότητας.

Στην περίπτωση που δύο αυτόνομα συστήματα λειτουργούν απέναντι το ένα στο άλλο, όπως απεικονίζεται στο Σχήμα 10, παρόλο που η εξασθένιση των διαφόρων αρμονικών διαφέρει από την περίπτωση όπου καθένα λειτουργεί μόνο του, τόσο η μείωση της συνολικής ηχοστάθμης όσο και η ευστάθεια του συστήματος διατηρούνταν μπροστά από τα προσκέφαλα. Το αποτέλεσμα αυτό ταιριάζει με τα αποτελέσματα της προσομοίωσης, παρόλο που στην προσομοίωση τα άκρα της καμπίνας ήταν ανοιχτά. Έτσι, φαίνεται ότι δύο ενεργά προσκέφαλα τοποθετημένα το ένα απέναντι από το άλλο μπορούν να λειτουργήσουν μέσα σε ένα μικρό περίβλημα με μικρή μείωση της απόδοσης.

Σχήμα 10: Τοπικά συστήματα ΕΕΘ, τοποθετημένα απέναντι το ένα στο άλλο, μέσα στο ομοίωμα καμπίνας μικρού αεροσκάφους που έχει εγκατασταθεί στο Εργαστήριο Δυναμικής και Ακουστικής.

Στην περίπτωση των τεσσάρων συστημάτων που λειτουργούν ταυτόχρονα στο εσωτερικό της καμπίνας, τα αποτελέσματα των μετρήσεων σε τρεις διαφορετικές συχνότητες υποδεικνύουν σημαντική μείωση της ηχοστάθμης, ίση ή μεγαλύτερη από 15 dB, όταν τα φάσματα

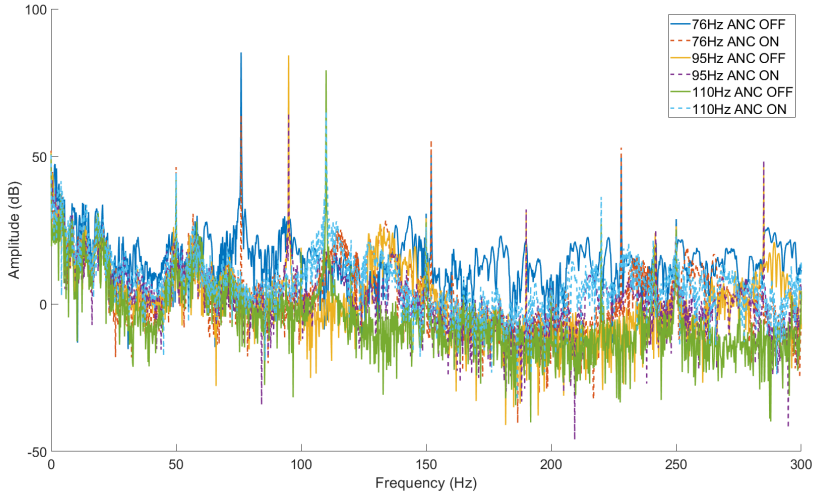

Σχήμα 11: Φάσματα συχνοτήτων πριν και μετά την ενεργοποίηση τεσσάρων αυτόνομων συστημάτων ΕΕΘ, καταγεγραμμένα στη θέση του μικροφώνου σφάλματος για τρεις αρμονικές ακουστικές διαταραχές στα 76 Hz, 95 Hz και 110 Hz.

συχνοτήτων καταγράφηκαν πάνω στο μικρόφωνο σφάλματος (βλ. Σχήμα 11). Συγκεκριμένα, το πλάτος της συχνότητας στα 75 Hz μειώθηκε κατά 15 dB, στα 96 Hz κατά 19 dB και στα 110 Hz κατά 17 dB. Παρόμοιες μειώσεις παρατηρήθηκαν στα μικρόφωνα σφάλματος μπροστά από τα άλλα συστήματα. Όταν το φάσμα συχνοτήτων καταγράφηκε $20cm$ μπροστά από τα μικρόφωνα σφάλματος, η πτώση της ηχοστάθμης ήταν μηδενική για την ακουστική διαταραχή στα 75 Hz, ενώ ήταν μόνο 2 dB στα 96 Hz και 3 dB στα 110 Hz. Επιπλέον, όταν το μικρόφωνο μέτρησης βρισκόταν σε απόσταση $40cm$ από το μικρόφωνο σφάλματος σε ένα από τα τέσσερα συστήματα, παρατηρήθηκε αύξηση της ηχοστάθμης κατά 1 dB στα 76 Hz, μείωση κατά μηδέν dB στα 95 Hz και μείωση κατά 2 dB στα 110 Hz.

7. Ολικός ΕΕΘ με χρήση Ενεργών Απορροφητών Ήχου

Σε αυτή την ενότητα διερευνάται ο ολικός ΕΕΘ σε ένα κλειστό χώρο, με τη χρήση ενεργών απορροφητών ήχου, στρατηγικά τοποθετημένων στο ομοίωμα καμπίνας αεροσκάφους που έχει εγκατασταθεί στο εργαστήριο Δυναμικής και Ακουστικής. Αυτή η προσέγγιση μπορεί να αποδειχθεί ιδιαίτερα αποτελεσματική στη ζώνη χαμηλών συχνοτήτων, όπου το ακουστικό πεδίο χαρακτηρίζεται από χαμηλή πυκνότητα ακουστικών τρόπων ταλάντωσης. Έτσι, οι απορροφητές ήχου αποσκοπούν στην αλλαγή της ακουστικής αντίστασης των ορίων της καμπίνας, με στόχο την απόσβεση των κυρίαρχων τρόπων ταλάντωσης, που οδηγεί στη μείωση της συνολικής ηχοστάθμης της καμπίνας [125].

Αν και η μέθοδος τοποθέτησης ενεργών ηχοαπορροφητών έχει χρησιμοποιηθεί για την εξισορρόπηση της απόκρισης χαμηλών συχνοτήτων μικρών δωματίων, δεν έχει χρησιμοποι-

ηθεί ποτέ για την εξουδετέρωση των χαμηλόσυχνων ακουστικών διαταραχών σε καμπίνες μικρών αεροσκαφών. Το γεγονός ότι οι ακουστικές διαταραχές σε μικρά ελικοφόρα αεροσκάφη χαρακτηρίζονται από αρμονικές της συχνότητας διέλευσης των πτερυγίων της έλικας, σε συνδυασμό με την αραιή κατανομή των ακουστικών τρόπων ταλάντωσης σε αυτή τη ζώνη συχνοτήτων, καθιστούν το σχήμα του ηχητικού πεδίου προβλέψιμο. Κατά συνέπεια, εάν τοποθετηθούν σε κατάλληλα σημεία ενεργοί απορροφητές ήχου που είναι ιδιαίτερα αποτελεσματικοί στις χαμηλές συχνότητες για να εξισορροπήσουν τους κυρίαρχους ακουστικούς τρόπους της καμπίνας, τότε μπορεί να επιτευχθεί σημαντική μείωση της ηχοστάθμης. Αυτή είναι η βασική ιδέα πίσω από την μέθοδο συνολικού ΕΕΘ που παρουσιάζεται σε αυτή την ενότητα.

Οι ενεργοί απορροφητές ήχου που χρησιμοποιούνται στην προτεινόμενη μεθοδολογία βασίζονται στον ενεργητικό έλεγχο του συντελεστή απορρόφησης, μπροστά από το διάφραγμα ενός ηχείου. Αυτό επιτυγχάνεται με τον διαχωρισμό του ηχητικού κύματος σε προσπίπτον και ανακλώμενο, και στη συνέχεια με την ελαχιστοποίηση της ανακλώμενης συνιστώσας (βλ. Σχήμα 12). Για τον διαχωρισμό αυτών των συνιστωσών χρησιμοποιείται η μέθοδος p-p για τη μέτρηση της έντασης του ηχητικού κύματος. Για να εφαρμοστεί η μέθοδος αυτή απαιτείται η τοποθέτηση δύο μικροφώνων με μικρή απόσταση μεταξύ τους, μπροστά από το διάφραγμα του ηχείου. Έπειτα το ηχείο, που λειτουργεί σαν ενεργός ηχοαπορροφητής οδηγείται από ένα σήμα που προκύπτει ελαχιστοποιώντας την ανακλώμενη συνιστώσα μέσω ενός προσαρμοστικού αλγορίθμου όπως ο FxLMS [28]. Στο σημείο αυτό έγκειται και η σημαντικότερη διαφορά της τεχνικής της ενεργητικής απορρόφησης σε σχέση με την τεχνική της ενεργητικής ακύρωσης θορύβου, όπου ελαχιστοποιείται η ακουστική πίεση που μετριέται από ένα μικρόφωνο σφάλματος.

Σχήμα 12: Ο ενεργός απορροφητής ήχου με δύο μικρόφωνα, που εφαρμόζει τη μέθοδο p-p για το διαχωρισμό του ακουστικού κύματος σε προσπίπτον και ανακλώμενο.

7.1 Προσομοιώσεις

Οι προσομοιώσεις που βασίστηκαν στη μέθοδο πεπερασμένων στοιχείων διενεργήθηκαν προκειμένου να διαπιστωθεί η αποτελεσματικότητα της μεθόδου ολικού ΕΕΘ, όσο αφορά το μέγεθος της ηχομείωσης στο εσωτερικό της καμπίνας. Για την υλοποίηση της, χρησιμοποιήθηκαν τέσσερις ηχοαπορροφητές οι οποίοι τοποθετήθηκαν σε διαφορετικά σημεία, έχοντας το διάφραγμα των ηχείων τους στραμμένο σε διαφορετικό προσανατολισμό ανάλογα με τη συχνότητα της αρμονικής διαταραχής.

Όταν η συχνότητα της ακουστικής διαταραχής ήταν τα 61 Hz, οι ενεργοί απορροφητές τοποθετήθηκαν με τα διαφράγματα των ηχείων κάθετα στον άξονα x και κοντά στις περιοχές με τη μέγιστη ηχοστάθμη. Η μείωση της ηχοστάθμης στο σύνολο της καμπίνας, στο επίπεδο x-y που βρίσκεται σε ύψος 120 cm κυμάνθηκε από 12 έως 20 dB όταν ενεργοποιήθηκαν οι τέσσερις απορροφητές, όπως άλλωστε φαίνεται στο Σχήμα 13α′). Όπως αναμενόταν, η υψηλότερη μείωση παρατηρήθηκε στο μέσο μεταξύ των δύο μικροφώνων, με τα μικρόφωνα τοποθετημένα σε ύψος 120 cm, που υποτέθηκε ότι αντιστοιχεί στο επίπεδο του κεφαλιού ενός καθιστού επιβάτη.

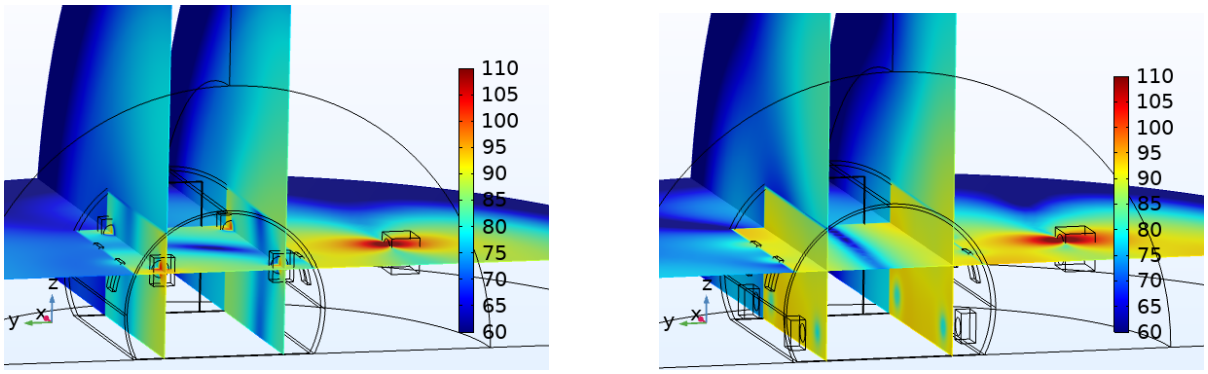

(α′) (β′)

Σχήμα 13: Μείωση της ηχοστάθμης στην καμπίνα αεροσκάφους σε δύο επίπεδα που βρίσκονται συμμετρικά σε απόσταση 0,85 m από το επίπεδο συμμετρίας x-z και σε ένα επίπεδο παράλληλο προς το επίπεδο x-y (z=120 cm) για αρμονική ακουστική διαταραχή συχνότητας α′) 61 Hz και β′) 76 Hz.

Όταν η καμπίνα διεγέρθηκε από μια αρμονική διαταραχή στα 76 Hz, που συμπίπτει με τον δεύτερο ακουστικό τρόπο ταλάντωσης, οι ενεργοί απορροφητές τοποθετήθηκαν στο δάπεδο της καμπίνας, όπου παρατηρήθηκε η μέγιστη ακουστική πίεση. Τα διαφράγματα ήταν προσανατολισμένα κάθετα στον άξονα y. Πριν από την ενεργοποίηση των ενεργών απορροφητών, η μέγιστη ηχοστάθμη στην καμπίνα έφτασε τα 104 dB κοντά στα τοιχώματα. Λόγω της μορφής του ηχητικού πεδίου, η ηχοστάθμη ήταν χαμηλότερη στο μέσο της καμπίνας, και κυμαίνονταν από 75 έως 81 dB. Μετά την ενεργοποίηση των απορροφητών, η συνολική μείωσή της κυμάνθηκε από 13 έως 24 dB (βλ. Σχήμα 13β′). Επιπλέον, σε ύψος 120 cm από το δάπεδο, η μείωση έφτασε τα 14 dB , που αποτελεί μια ικανοποιητική ηχομείωση.

Στην περίπτωση της ακουστική διαταραχής στα 95 Hz, που αποτελεί τον τέταρτο ακουστικό τρόπο ταλάντωσης της καμπίνας, παρατηρήθηκε μια μείωση της ηχοστάθμης κατά 20 dB, όταν τα ηχεία τοποθετήθηκαν με το διάφραγμά τους κάθετα προς τον άξονα z. Τέλος, όταν η συχνότητα της ακουστικής διαταραχής ήταν 110 Hz, η οποία απαντάται συχνά σε μικρά ελικοφόρα αεροσκάφη παρατηρήθηκε πτώση μεγαλύτερη των 15 dB στο επίπεδο με ύψος 120 cm από το δάπεδο της καμπίνας.

7.2 Πειραματική αξιολόγηση

Η πειραματική αξιολόγηση έλαβε χώρα στο ομοίωμα της καμπίνας για ημιτονοειδή ακουστική διαταραχή στα 61 Hz. Τέσσερις ενεργοί ηχοαπορροφητές τοποθετήθηκαν με τον τρόπο που περιγράφηκε στην προηγούμενη ενότητα. Επιπλέον, επιλέχθηκαν 36 μικρόφωνα μέτρησης για να καταγράψουν τη μείωση της ακουστικής πίεσης πριν και μετά την ενεργοποίηση των ενεργών απορροφητών. Για την εφαρμογή του αλγορίθμου που ελαχιστοποιεί την ανακλώμενη συνιστώσα του ακουστικού κύματος, χρησιμοποιήθηκε η Python με το Motu® Ultralite AVB κάρτα ήχου. Η αξιολόγηση της προτεινόμενης προσέγγισης περιλαμβάνει την προοδευτική ενεργοποίηση τεσσάρων ηχοαπορροφητών για την αξιολόγηση της εξασθένισης της ηχητικής πίεσης σε κάθε κατάσταση. Η υψηλότερη μέση εξασθένιση πλάτους 13,3 dB επιτεύχθηκε μεταξύ των 36 μετρήσεων όταν ενεργοποιήθηκαν και οι τέσσερις ηχοαπορροφητές. Επιπλέον η μέγιστη μείωση του πλάτους της αρμονικής στα 61 Hz έφτασε τα 17 dB, μπροστά από έναν από τα τέσσερα ηχεία (βλ. Σχήμα 14). Επίσης, πρέπει να σημειωθεί ότι μείωση της ηχοστάθμης μεγαλύτερη των 10 dB ανιχνεύθηκε από όλα τα μικρόφωνα μέτρησης, ανεξάρτητα από το σημείο που ήταν τοποθετημένα στην καμπίνα, καταδεικνύοντας μια συνολική μείωση του θορύβου, όπως άλλωστε ήταν και η επιδίωξη της προτεινόμενης μεθόδου.

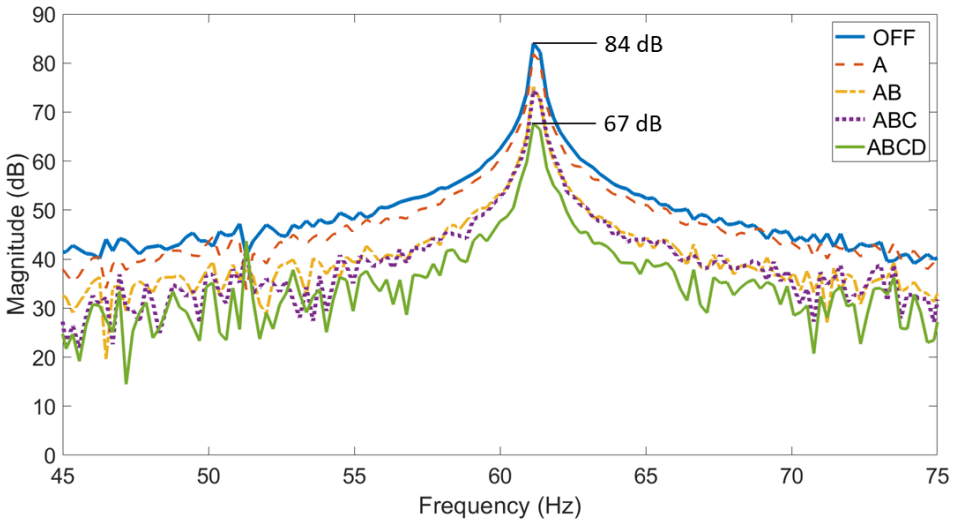

Σχήμα 14: Μέγιστη μείωση του πλάτους της αρμονικής στα 61 Hz, 30 cm μπροστά από έναν από του 4 απορροφητές.

8. Συμπεράσματα

Η έρευνα που διεξήχθη σε αυτή τη διδακτορική διατριβή είχε ως στόχο την ανάπτυξη μεθόδων για τον ενεργητικό έλεγχο χαμηλόσυχνων ακουστικών διαταραχών στις καμπίνες μεταφορικών μέσων, όπως μικρά αεροσκάφη και σκάφη αναψυχής, προκειμένου να βελτιωθεί η ακουστική άνεση των επιβατών. Η ενεργή ακύρωση θορύβου σε αυτά τα περιβάλλοντα προσφέρει πλεονεκτήματα σε σχέση με τις συμβατικές παθητικές μεθόδους, όσον αφορά στο μέγεθος και το βάρος, καθιστώντας την ένα τομέα έντονης έρευνας και ανάπτυξης για κατασκευαστές και ερευνητές. Ωστόσο, βασικές προκλήσεις όπως βελτίωση της απόδοσης όσο αφορά στη μείωση της ακουστικής πίεσης, η αύξηση του μεγέθους της ζώνης ησυχίας, η μείωση της υπολογιστικής πολυπλοκότητας και η διασφάλιση της ευρωστίας των συστημάτων αυτών σε ποικίλες συνθήκες δεν έχουν ακόμα πλήρως αντιμετωπιστεί, περιορίζοντας την ευρεία χρήση τους σε πραγματικές εφαρμογές. Για να αντιμετωπιστούν αυτές οι προκλήσεις, η παρούσα διατριβή εισάγει νέες μεθόδους που αξιολογούνται μέσω αναλυτικών μοντέλων, μοντέλων προσομοίωσης και υλοποιήσεων σε πραγματικό χρόνο σε ενσωματωμένους επεξεργαστές ψηφιακού σήματος, με στόχο να παρέχει μια νέα ματιά τόσο στον τοπικό όσο και στον συνολικό Ενεργητικό Έλεγχο Θορύβου σε μικρούς χώρους, δίνοντας έμφαση σε πρακτικές εφαρμογές σε πραγματικές συνθήκες.

Τα κύρια ευρήματα περιλαμβάνουν: α) την προσαρμογή του αλγορίθμου mixed-error FxLMS σε εφαρμογές τοπικού ΕΕΘ για προσκέφαλα θέσεων μέσων μεταφοράς, ο οποίος προσφέρει παρόμοια μείωση θορύβου με τις παραδοσιακές μεθόδους με χαμηλότερες απαιτήσεις σε υπολογιστική ισχύ και κόστος, β) έναν αλγόριθμο VEM-FxLMS για την επέκταση και μεγέθυνση των ζωνών ησυχίας μακριά από τα μικρόφωνα σφάλματος, ο οποίος είναι ιδιαίτερα αποτελεσματικός σε πραγματικές συνθήκες, το οποίο αποδείχθηκε όταν εγκαταστάθηκε στο κατάστρωμα ενός σκάφους αναψυχής, γ) έναν αλγόριθμο ελέγχου βασισμένο σε ένα FLNN δεύτερης τάξης που παρουσιάζει μεγαλύτερη αποτελεσματικότητα σε σχέση με τον γραμμικό FxLMS, όταν πρόκειται για την αντιμετώπιση μη γραμμικών ηλεκτροακουστικών συστημάτων και στοχαστικών ακουστικών διαταραχών. Επίσης, προέκυψε το συμπέρασμα ότι πολλαπλά αυτόνομα συστήματα ΕΕΘ μπορούν να λειτουργούν ταυτόχρονα σε μικρούς κλειστούς χώρους με μια μικρή μείωση στην απόδοση όσο αφορά στην ηχομείωση που επιτυγχάνεται στη ζώνη ησυχίας κάθε συστήματος και με μια μικρή αύξηση της ηχοστάθμης σε περιοχές μακριά από τις ζώνες αυτές. Τέλος, διαπιστώθηκε ότι η χρήση ενεργών ηχοαπορροφητών σε συγκεκριμένες θέσεις στην καμπίνα ενός μικρού αεροσκάφους, μπορεί να μειώσει σημαντικά το επίπεδο χαμηλόσυχνου θορύβου σε ολόκληρο το χώρο, αν μπορέσει να επιτευχθεί απόσβεση των κύριων τρόπων ταλάντωσης που διεγείρονται από τις αυτές τις ακουστικές διαταραχές.

Τέλος, όσο αφορά στη μελλοντική έρευνα πάνω στα συστήματα ΕΕΘ, αυτή μπορεί να περιλαμβάνει: α) τη βελτίωση των αλγορίθμων ελέγχου, χρησιμοποιώντας τεχνικές τεχνητής νοημοσύνης και μηχανικής μάθησης, για την αύξηση της απόδοσης όσο αφορά στη μείωση

της ηχοστάθμης όσο και στην αύξηση του μεγέθους της ζώνης ησυχίας. Τα νευρωνικά δίκτυα, ειδικά τα Αναδρομικά (RNN) και τα Συνελικτικά Νευρωνικά Δίκτυα (CNN), είναι πολλά υποσχόμενες τεχνολογίες, ειδικά για την αντιμετώπιση των μη γραμμικοτήτων στα ηλεκτρακουστικά συστήματα και των μη αρμονικών διαταραχών, αν και η υλοποίησή τους σε επεξεργαστές ψηφιακού σήματος, παραμένει πρόκληση λόγω των υψηλών υπολογιστικών απαιτήσεων. Η μελλοντική έρευνα πρέπει επίσης να επικεντρωθεί στην πρακτικότητα των συστημάτων ΕΕΘ, μειώνοντας το βάρος και αναπτύσσοντας έξυπνες διατάξεις και ελαφρύτερους επενεργητές (ηχεία) χρησιμοποιώντας τεχνολογίες, όπως τα μεταϋλικά. Επίσης, η προσαρμογή των προτεινόμενων μεθόδων σε λογική ανάδρασης θα μπορούσε να εξαλείψει την ανάγκη για σήμα αναφοράς, καθιστώντας τα συστήματα πιο ελκυστικά για εμπορικές εφαρμογές. Επιπλέον, χρειάζεται περαιτέρω έρευνα όσο αφορά στο συνολικό ΕΕΘ με ενεργούς ηχοαπορροφητές και στην ανάπτυξη μεθόδων καταπολέμησης του θορύβου που μεταδίδεται μέσα από τα δομικά στοιχεία μιας καμπίνας. Έτσι, ο συνδυασμός αυτών των μεθόδων θα μπορούσε να οδηγήσει στη δημιουργία ενός ολοκληρωμένου συστήματος με αυξημένη αποδοτικότητα σε πραγματικές συνθήκες λειτουργίας.